



Fabrication of Organic Radar Absorbing Materials

A Report on the TIF Project

Paul Saville

Trisha Huber

Darren Makeiff

Defence R&D Canada – Atlantic

Technical Report

DRDC Atlantic TR 2005-124

May 2005

This page intentionally left blank.

Fabrication of Organic Radar Absorbing Materials

A Report on the TIF Project

Paul Saville

Trisha Huber

Darren Makeiff

Defence R&D Canada – Atlantic

Technical Report

DRDC Atlantic TR 2005-124

May 2005

Author

Paul Saville

Paul Saville

Approved by

[Signature]

Terry Foster

Head Dockyard Laboratory Pacific

Approved for release by

[Signature]

Kirk Foster

DRP Chair

Terms of release: The information contained herein is proprietary to Her Majesty and is provided to the recipient on the understanding that it will be used for information and evaluation purposes only. Any commercial use including use for manufacture is prohibited. Release to third parties of this publication or information contained herein is prohibited without the prior written consent of Defence R&D Canada.

© Her Majesty the Queen as represented by the Minister of National Defence, 2005

© Sa majesté la reine, représentée par le ministre de la Défense nationale, 2005

Abstract

The fabrication of microwave absorbing materials requires the ability to make materials with well-controlled properties such as shape, thickness, permittivity and permeability. The ability to measure the permittivity and permeability is an essential requirement for designing an optimised absorber. And good optimisations codes are required in order to achieve the best possible absorber designs. In this report, the results from a Technology Investment Funded project on the fabrication of organic radar absorbing materials are presented. The absorbing phase used was based in conducting polymers, which were synthesised and characterised for control and correlation of absorptive properties. The materials made were characterised through measurement of their conductivity and permittivity at microwave frequencies. Methods were then developed for optimising the design of microwave absorbers. A portion of the TIF also focussed on the development of radar cross section modelling software with the capability of determining the radar cross section of a platform with absorbing patches applied.

Résumé

La fabrication de matériaux absorbant les hyperfréquences exige la capacité de créer des matériaux dont les propriétés sont bien contrôlées, par exemple la forme, l'épaisseur, la permittivité et la perméabilité. La capacité de mesurer la permittivité et la perméabilité est essentielle pour la conception d'un absorbant optimisé. Et de bons codes d'optimisation sont nécessaires pour obtenir le meilleur modèle d'absorbant possible. Le présent rapport décrit les résultats d'un projet sur la fabrication de matériaux organiques absorbants radar, financé par le Fonds d'investissement technologique. La phase absorbante utilisée fait appel à des polymères conducteurs, qui ont été synthétisés et caractérisés pour le contrôle et la corrélation de propriétés absorbantes. Les matériaux fabriqués ont été caractérisés en mesurant leur conductivité et leur permittivité aux hyperfréquences. Des méthodes ont ensuite été définies pour optimiser la conception des absorbants. Une partie du projet portait aussi sur le développement d'un logiciel de modélisation de section efficace radar, capable de déterminer la section efficace radar d'une plate-forme munie de pièces absorbantes.

This page intentionally left blank.

Executive summary

Introduction

Radar is a very sensitive long-range detection technique that is deployed in many locations and on many platforms including missiles. The signature received by a radar from a target is determined by the radar cross section of the target. Low radar cross section means that a platform is less detectable and can operate at closer ranges. The factors affecting radar cross section are the target's shape, size and the materials from which it is manufactured. Radar cross section reduction relies on shaping, low reflectivity materials and on the use of radar absorbing materials. Absorbers have been fabricated using different materials and designs. Here the results from the development of a materials research program into the fabrication of organic radar absorbing materials are reported.

Results

Conducting polymers present some useful properties compared to other conductive materials used in fabricating absorbers, such as low density and the ability to tune the conductivity based on synthetic and manufacturing conditions. Correlations have been made between the material's properties and synthesis conditions. Characterisation techniques have been developed at microwave frequencies. The properties at microwave frequencies are required for optimum design of radar absorbers. Design optimisation techniques have been developed for determining the best possible absorber design for multilayered absorbers.

Significance

DRDC now has the initial technology required for the fabrication of broadband radar absorbing materials. A considerable wealth of knowledge has been developed in the synthetic control of materials microwave properties and the ability to measure these at microwave frequencies. The technology to design optimised absorber has also been established.

Future plans

Development of strict control of material properties is required and a study on the stability of the conductive properties in the end product is required. Effort will also be extended to developing methodology for the fabrication of large area material for the purpose of free space characterisation and reflectivity measurements. The technology for making these measurements already partially exists within the existing measurement facilities. Optimisation techniques need to be extended to optimise absorbers as a function of incident angle, layer thickness, spacer permittivity and for capacitive-inductive inclusions. After these steps the development of circuit analog materials, structural absorbers and dynamic absorbers will produce further improvements in the ability to reduce a platform's radar cross section.

Saville, P.. 2005. Fabrication of Organic Radar absorbing Materials: A Report on the TIF Project. DRDC Atlantic TR 2005 - 124 DRDC Atlantic.

Sommaire

Introduction

Le radar est un outil de détection longue portée très sensible qui est utilisé dans de nombreux environnements et sur un grand nombre de plates-formes, y compris des missiles. La signature reçue d'une cible est déterminée par la section efficace radar de celle-ci. Une faible section efficace radar rend une plate-forme moins détectable et permet de l'utiliser à des distances plus courtes. Les facteurs qui influent sur la section efficace radar sont la forme, la taille et la composition matérielle de la cible. On peut réduire la section efficace radar d'une cible en conformant celle-ci de manière adéquate, et en utilisant des matériaux à faible réflectivité et des matériaux absorbants radar. Les absorbants ont été fabriqués dans différents matériaux et selon diverses conceptions. Nous présentons ici les résultats du développement d'un programme de recherche sur les matériaux en ce qui concerne la fabrication de matériaux organiques absorbants radar.

Résultats

Les polymères conducteurs présentent des propriétés utiles comparativement à d'autres matériaux conducteurs utilisés dans la fabrication d'absorbants, par exemple faible densité et conductivité réglable selon les conditions de synthèse et de fabrication. Des corrélations ont été établies entre les propriétés des matériaux et les conditions de synthèse. Des techniques de caractérisation des propriétés aux hyperfréquences ont été développées. Ces propriétés sont nécessaires à l'optimisation de la conception des absorbants radar. Des techniques d'optimisation de la conception ont été développées pour déterminer le meilleur modèle d'absorbant multicouche possible.

Portée

RDDC possède maintenant la technologie initiale nécessaire à la fabrication de matériaux absorbants radar à large bande. D'importantes connaissances ont été acquises en ce qui concerne le contrôle synthétique des propriétés hyperfréquences des matériaux et la capacité de mesurer ces propriétés aux hyperfréquences. La technologie de conception d'absorbants optimisés a également été établie.

Recherches futures

Il est nécessaire de développer des moyens de contrôle strict des propriétés des matériaux et d'effectuer une étude sur la stabilité des propriétés conductrices du produit final. Des efforts seront également déployés en vue d'établir des méthodes de fabrication de matériaux à grande surface aux fins de la caractérisation en espace libre et de l'établissement de mesures de réflectivité. La technologie nécessaire pour ces mesures existe déjà en partie dans les installations de mesure en place. Les techniques d'optimisation doivent être étendues afin d'optimiser les absorbants en fonction de

l'angle d'incidence, de l'épaisseur de couche, de la permittivité des éléments intercalaires et aux fins d'inclusions capacitatives et inductives. Une fois ces étapes réalisées, le développement de matériaux de type circuit analogique, d'absorbants structuraux et d'absorbants dynamiques continuera d'accroître le capacité de réduire la section efficace radar des plates-formes.

Saville, P.. 2005. Fabrication de matériaux organiques absorbants radar : rapport sur le projet du FIT. DRDC Atlantic TR 2005 –124. RDDC Atlantique.

Table of contents

Abstract.....	i
Executive summary	iii
Sommaire.....	v
Table of contents	vii
List of figures	xv
Acknowledgements	xxvii
1. Introduction	1
1.1 Materials.....	1
1.2 Property Measurement.....	2
1.3 Absorber Design.....	2
1.4 RCS	2
1.5 Report Layout.....	3
2. Radar Absorbing Materials Review	4
2.1 A History of RAM Development	4
2.2 Theory Reflectivity Minimisation	7
2.3 Types of Radar Absorbing Material	8
2.3.1 Graded Interfaces – Impedance Matching.....	8
2.3.1.1 Pyramidal Absorbers.....	9
2.3.1.2 Tapered Loading Absorbers.....	9
2.3.1.3 Matching Layer Absorbers.....	10
2.3.2 Resonant Materials	11
2.3.2.1 Dallenbach (Tuned) Layer Absorber	11
2.3.2.2 Salisbury Screen.....	13
2.3.2.3 Jaumann	14
2.3.3 Circuit Analog RAM.....	15
2.3.4 Magnetic RAM.....	19

2.3.5	Adaptive RAM (Dynamically adaptive RAM)	19
2.4	Recursion Relationship for Calculating the Reflectivity	20
2.5	Transmission Line Theory	21
2.6	Techniques for Optimisation of Radar Absorbing Materials	23
2.6.1	The Dallenbach Layer	23
2.6.2	Salisbury Screen	24
2.6.2.1	Optimised Design of Salisbury Screens	24
2.6.3	Jaumann Layers	25
2.6.4	Optimisation of Jaumann Layers	25
2.6.4.1	Maximally Flat Design	25
2.6.4.2	Tschebyscheff (Equal-Ripple) Design	26
2.6.4.3	Gradient Methods	27
2.6.4.4	Optimisation of Jaumann Layers: Genetic Algorithm	28
2.6.4.5	Optimisation of Jaumann Layers: Other methods (Finite Element, FDTD and Taguchi Methods)	30
2.7	Absorbing Materials	30
2.7.1	Carbon	30
2.7.2	Metal and Metal Particles	30
2.7.3	Conducting Polymers	31
2.7.4	Polypyrrole	31
2.7.4.1	Polypyrrole-Polymer Composites	31
2.7.4.2	Polypyrrole-Fabric Composites	32
2.7.4.3	Conducting Polymer Latex	33
2.7.5	Polyaniline	34
2.7.5.1	Polyaniline Fibres	34
2.7.6	Other Conducting Polymers	34
2.7.7	Tubules and Filaments	35
2.7.8	Chiral Materials	35
2.8	Shielding	36
2.9	Conclusion	37
2.10	References	37
3.	Reflectivity from Materials	48

3.1	Interaction of Electromagnetic Radiation with Matter	48
3.1.1	Maxwell's Equations	49
3.1.2	The Wave Equation	51
3.2	Reflection from an Interface.....	53
3.3	Practical Details: Reflection from an Interface	57
3.3.1	Reflectivity from a Single Layer	59
3.3.2	Practical Details: Reflection from a Layer	63
3.3.3	Magnetic Material	73
3.4	Reflection from Multiple Layers	74
3.5	Conclusions	81
3.6	Future Work	81
3.7	References	83
4.	Organic Radar Absorbing Materials.....	84
4.1	Conducting Polymers	84
4.2	Polyaniline.....	85
4.2.1	Effect of Synthetic Parameters on Conductivity: Polyaniline	88
4.2.2	Effect of Substituents on Conductivity: Polyaniline	91
4.2.3	Effect of Processing Parameters on Permittivity: Polyaniline.....	92
4.2.4	Polyaniline-Carbon Nanostructure Composites	97
4.2.5	Polyaniline Summary	98
4.2.6	Future Work: Polyaniline	98
4.2.7	References	99
4.3	Polypyrrole	99
4.3.1	Review of Polypyrrole: Synthesis	100
4.3.1.1	Electropolymerisation of Pyrrole	102
4.3.1.2	Chemical Polymerisation of Pyrrole	103
4.3.2	Processability.....	104
4.3.2.1	Solutions.....	104
4.3.2.2	Composites-Chemical Preparation.....	104
4.3.2.3	Copolymers and Graft Copolymers	105
4.3.2.4	Composites-electrochemical	105
4.3.2.5	Composite Blends	105

4.3.2.6	Textiles.....	106
4.3.2.7	Conducting Polymer-Textile Formation	106
4.3.2.8	Stability of Conducting Polymer Coated Textiles.....	108
4.3.2.9	Microwave Properties of Conducting Polymer Coated Textiles	109
4.3.2.10	Polypyrrole - Latex	109
4.3.2.11	Improved Adhesion to Inorganic Substrates	111
4.3.2.12	Tubules/Fibres.....	111
4.3.3	Polypyrrole Stability.....	111
4.3.4	Material Characterisation	114
4.3.4.1	Spectroscopy of Polypyrrole	114
4.3.4.2	IR-Raman spectroscopy of polypyrrole	114
4.3.4.3	Characterisation of Polypyrrole's Permittivity and Conductivity at Microwave Frequencies.....	115
4.3.4.4	Conducting Nature of Polypyrrole.....	116
4.3.4.5	Temperature Dependence of Conductivity	117
4.3.4.6	Frequency Dependence	117
4.3.4.7	Conductivity of Composites.....	119
4.3.5	Polypyrrole use in Radar Absorbing Materials	120
4.3.5.1	Dallenbach Layers / Polypyrrole Composites.....	120
4.3.5.2	Stability	121
4.3.6	Experimental	122
4.3.6.1	Synthesis of Conducting Polypyrrole Powder	122
4.3.6.2	Formation of Polypyrrole Coated Fabric	122
4.3.6.3	Polypyrrole Pellet Formation	123
4.3.6.4	Coating Formulation	124
4.3.6.5	Conductivity Measurements.....	124
4.3.6.6	Permittivity Measurements	125
4.3.6.7	Weathering	125
4.3.7	Results	125
4.3.7.1	Galvanostatic Polymerisation of Pyrrole and Control of Film Thickness	125
4.3.7.2	Effect of pH on the Conductivity of Electrodeposited Polypyrrole	126

4.3.7.3	Effect of Electrolyte Type on Conductivity	127
4.3.7.4	Electrodeposition onto Pyrrole Coated Fabric	129
4.3.7.5	Undoping of Polypyrrole Films	129
4.3.7.6	Polypyrrole Powders	129
4.3.7.7	Effect of Pellet Density	129
4.3.7.8	Effect of Powder Milling	130
4.3.7.9	Effect of Dopant on Pellet Conductivity	131
4.3.7.10	Effect of Dopant to Monomer Concentration Ratio.....	133
4.3.7.11	Effect of Fabric Type	133
4.3.7.12	The Effect of Aging and Acid on Polypyrrole Coated Fabric	142
4.3.7.13	Effect of Aging and Temperature on Pellet Conductivity	144
4.3.7.14	IR Study of Polypyrrole Pellets.....	147
4.3.7.15	Thermal Analysis of Polypyrrole Powders	148
4.3.7.16	Polypyrrole Coatings.....	148
4.3.7.17	Polypyrrole Powder Milling and Particle Dispersion ...	148
4.3.7.18	DC Conductivity of Polypyrrole Coatings	149
4.3.7.19	Permittivity of Polypyrrole Coatings	150
4.3.7.20	Weathering of Polypyrrole Coatings.....	153
4.3.8	Conclusions	154
4.3.9	Future Work: Polypyrrole.....	155
4.3.10	References	155
4.4	Stable Conducting Polymers	161
4.4.1	Sulfur-Bridged Thiophenes	162
4.4.1.1	Synthesis of sulfur-bridged thiophenes	162
4.4.1.2	Chemical Polymerizations of sulfur-bridged thiophenes:Synthesis	163
4.4.1.3	Conductivity Studies	165
4.4.1.4	Optical Properties of de-doped Poly-4	166
4.4.1.5	Electrochemistry of sulfur-bridged thiophenes:Oxidation Potentials	167
4.4.1.6	Electropolymerization of sulfur-bridged monomer 1.....	168
4.4.1.7	Electropolymerization of sulfur-bridged monomer 4.....	168

4.4.1.8	Electropolymerization of sulfur-bridged monomer 11.....	171
4.4.1.9	Electropolymerization of other sulfur-bridged monomers	172
4.4.1.10	Conclusions and Future Work.....	173
4.4.2	Phosphorus-Bridged Thiophenes.....	174
4.4.2.1	Synthesis of phosphorus-bridged thiophenes.....	174
4.4.2.2	Synthesis of metal complexes of P-bridged thiophenes...	175
4.4.2.3	Electrochemistry of P-bridged thiophenes and their metal complexes	175
4.4.2.4	Conclusions and Future Work.....	176
4.4.3	Silicon-Bridged Thiophenes.....	177
4.4.3.1	Synthesis of silicon-bridged thiophenes.....	177
4.4.3.2	Electrochemistry of silicon-bridged thiophenes.....	177
4.4.3.3	Conclusions and Future Work.....	180
4.4.4	Amine-Bridged Thiophenes	181
4.4.4.1	Synthesis of phenylamine-bridged thiophenes.....	181
4.4.4.2	Electrochemistry of phenylamine-bridged thiophenes:Electrochemistry of triarylamine model compounds	181
4.4.4.3	Electrochemistry of tris-EDOT/amine 1	182
4.4.4.4	Electrochemistry of bis-EDOT/amine 2.....	185
4.4.4.5	Conclusions and Future Work.....	188
4.4.5	Conclusions: Organic Materials	188
4.4.6	Future Work	188
4.4.7	References	188
5.	Permittivity and Permeability Measurement Techniques.....	190
5.1	Overview	191
5.2	Method Selection.....	191
5.3	Transmission – Reflection Method	192
5.4	Reflection – Two Position Method.....	195
5.5	Calibration of Network Analyzer	197
5.6	Uncertainty Analysis	198
5.6.1	Reflection-Transmission Method	198
5.6.2	Reflection – Two Positions Method	201
5.7	Measurement Results.....	201

5.7.1	Low Loss Materials (Batch 1)	201
5.7.2	PPy Materials	204
5.8	Conclusions	211
5.9	Future Work	211
5.10	References	211
6.	Absorber Design: The Genetic Algorithm.....	213
6.1	Optimisation of Jaumann Layers: Genetic Algorithm.....	213
6.2	The Genetic Algorithm.....	215
6.2.1	Initiation	216
6.2.2	Selection	216
6.2.2.1	Decimation Selection	216
6.2.2.2	Roulette Wheel Selection.....	217
6.2.2.3	Tournament Selection	217
6.2.3	Crossover.....	217
6.2.4	Mutation	217
6.2.5	The New Generation	218
6.2.6	Simple Genetic Algorithm.....	218
6.2.7	Elitism	218
6.2.8	Steady State Genetic Algorithms.....	218
6.2.9	Pareto Genetic Algorithms	218
6.3	RAM Design using Resistive Sheets and the Genetic Algorithm	219
6.3.1	Front Protective Layer.....	225
6.3.2	Spacer Permittivity	227
6.3.3	Higher Permittivity with Protective Layer	229
6.4	Conclusions	230
6.5	Future Research	231
6.6	References	232
7.	Circuit Analog Materials	233
7.1	Modeling Software	234
7.2	Results and Discussion	236
7.3	Conclusion.....	242
7.4	Reference.....	242

8. Summary and Future Work	243
Appendix A	244
8.1 Publications related to Research.....	244
8.2 Conference Presentations	245
Appendix B.....	247
Appendix C: Experimental Synthesis of Sulfur-Bridged Thiophenes.....	263
Appendix D: Phosphorous-Bridged Thiophenes Experimental.....	267
Appendix E: Silicon-Bridged Thiophenes Experimental	270
Appendix F: Amine-Bridged Thiophenes	271
Appendix G:	272
List of symbols/abbreviations/acronyms/initialisms	273
Distribution list.....	277

List of figures

Figure 2.1. Pyramidal Absorber	9
Figure 2.2. Tapered Loading Absorber, type a) smooth type b) stepped.	10
Figure 2.3. Matching Layer	11
Figure 2.4. Dallenbach Layer	12
Figure 2.5. Salisbury Screen.....	14
Figure 2.6. Jaumann Layers.....	15
Figure 2.7. Circuit Analog Sheet of crosses. The spacing between the elements gives rise to a capacitance, and the length, to an inductance. The resistive component is a result of the lossy material.	16
Figure 2.8. Transmission line circuit for a Salisbury Screen with a Circuit Analog sheet. Z_L is the load impedance. For an absorber on a perfect electrical conductor the load impedance is a short circuit and thus equal to zero. Z_1 is the impedance of the spacer. There will be a finite thickness for the sheet and circuit analog material.	17
Figure 2.9. Reflectivity from Jaumann absorber layers.....	21
Figure 2.10. Multisection transmission line.	22
Figure 3.1. Reflection and refraction at an interface between two media with refractive indices N_i and N_t . The x-axis points into the page as does E_{\perp} , which is represented by the X in the circles. E_{\parallel} is in the plane of incidence.	53
Figure 3.2. Reflectivity of 10 GHz microwaves from water ($\epsilon_r = 81$, $\mu_r = 1$ and $\sigma = 0$) and earth ($\epsilon_r = 6$, $\mu_r = 1$ and $\sigma = 0$, red = R, blue = R_{\perp} , green = R_{\parallel}). As θ_i tends to 90, R tends to 1 so smooth surfaces will appear as perfect reflectors.....	59
Figure 3.3. Reflection and refraction from a single layer. The E^r and E^t fields in the incident and transmitting media (N_i and N_t) are defined as being the sum of all waves arising from multiple reflections in the middle media (N_m)......	60
Figure 3.4. The optical path difference between the two reflected waves is $\Lambda = AB + BC - AD$. When this is equal to $1/2 \lambda$ the waves are 180° out of phase and destructive interference results in a minimum.	64
Figure 3.5. Total reflectivity from a non-absorbing layer (Incident medium is air, Layer $\epsilon_r = 9$, $\mu_r = 1$ and $\sigma = 0$, and substrate $\epsilon_r = 2.25$, $\mu_r = 1$ and $\sigma = 0$, normal incidence) as a	

function of the ratio of the optical path length difference to wavelength. The reflectivity has a finite value at the minima due to the difference in dielectric constants of the air and substrate layers.^[2] 65

Figure 3.6. Total reflectivity as a function of frequency and Incident angle for a single 0.9375 cm thick non lossy layer with $\epsilon_r = 2.56$, $\mu_r = 1.0$ and $\sigma = 0$, surrounded by air. The minimum in reflectivity shifts to higher frequency due to a decrease in optical path length difference as the incident angle increases. 66

Figure 3.7. Total reflectivity as a function of frequency and incident angle for a single 0.4688 cm thick non lossy layer with $\epsilon_r = 2.56$, $\mu_r = 1.0$ and $\sigma = 0$, incident medium of air and transmitted medium with $\epsilon_r = 8$, $\mu_r = 1.0$ and $\sigma = 0$. The minimum in reflectivity again shifts to higher frequency due to a decrease in optical path length difference as the incident angle increases. Reflectivity also approaches 1 as incident angle increases. The transmittance = 1-R. 67

Figure 3.8. Total reflectivity of a lossy layer as a function of frequency and incident angle. System has the same parameters as modelled in Figure 3.7, however, the permittivity of the layer is now $\epsilon_r = 2.56-0.5i$. The effect of the absorption is to damp the reflectivity at higher frequency, due to the longer optical pathlength. As the frequency tends to infinity, the reflectivity tends to that from the first interface assuming an infinite medium (ie $R=0.0576$). 68

Figure 3.9. Total reflectivity from the film of Figure 3.8 mounted on a perfect electrical conductor (PEC). The overall reflectivity is much higher than seen in Figure 3.8, especially at low frequencies where the layer thickness is small in comparison to the wavelength. Again reflectivity approaches the infinite medium reflectivity (reflectivity from an interface). 69

Figure 3.10. Total reflectivity from the material in Figure 3.9 mounted on a PEC as a function of film thickness. Notice the relationship between frequency and thickness. 70

Figure 3.11. Total reflectivity of the film in Figure 3.7 as a function of film conductivity with $\epsilon_r' = 2.56$ on a PEC. Notice that the minimum reflectivity for this case results from a conductivity of about 1.1 S/m. For larger values of ϵ_r' , the minimum occurs at higher.. 71

Figure 3.12. Total reflectivity from three hypothetical absorbing materials. Red, $d = 0.25$ cm, $\epsilon_r' = 9.5$ and $\sigma = 2.2$ S/m, Blue $d = 0.083$ cm, $\epsilon_r' = 81$ and $\sigma = 6.4$ S/m and Green $d = 0.01$ cm, $\epsilon_r' = 5700$ and $\sigma = 53$ S/m. Incident medium is air, and supporting medium is a PEC. 72

Figure 3.13. A special case arises for a material with equal permittivity and permeability. The impedance of material and air are matched and the reflectivity at zero incident angle is a linear function of the film thickness. (air/ $d=0.004$ m, $\epsilon_r= 3.9-0.5i$, $\mu_r=3.9-0.5i$ /PEC). 73

Figure 3.14. Comparison of the total reflectivity from an electric (red) and a hybrid, electric-magnetic (blue) absorber. The reflectivity is lower over most of the frequency range for

the hybrid material (Red air/d=0.001875 m, $\epsilon_r=16-5.8i$, $\mu_r=1$ /PEC, Blue air/d=0.001875 m, $\epsilon_r=16-5.8i$, $\mu_r=10-3.6i$ /PEC).....	74
Figure 3.15. Reflectivity from a Salisbury Screen (blue) and a Dallenbach layer (red), optimised for a minimum at 10 GHz. The bandwidth of the Salisbury screen is seen to be larger than that of the Dallenbach layer. (parameters Dallenbach Layer air/ absorber d=0.0024 m, $\epsilon_r'=10$, s=2.2 S/m./ PEC. Salisbury Screen, air/ absorber d=0.0001 m, $\epsilon_r'=20$, s=27 S/m, spacer d= 0.0055 m, $\epsilon_r'=1.05$ / PEC). The bandwidth is 2.2 GHz for the Salisbury Screen and 0.8 GHz for the Dallenbach layer at a reflectivity of -20 dB. ...	76
Figure 3.16. Reflectivity from a Salisbury Screen as a function of the layer impedance. Red = 377 ohms, Blue = 300 ohms, green = 200 ohms. This repeats figure 8.9 of reference ^[6]	77
Figure 3.17. Reflectivity from Jaumann structures with 1(red), 2(blue) and 3(green) resistive sheets. The spacers are 0.00655 m thick and the resistive sheets are 0.1 mm thick with ϵ_r' of 9.....	78
Figure 3.18. Reflectivity from three layer Jaumann centered at 10 GHz with reflectivity below -20 dB. Parameters as per Table 3.1.....	79
Figure 4.1. Common conducting polymers,(top-bottom) polythiophene, polypyrrole and polyaniline.....	85
Figure 4.2. Variable Oxidation State Octamers of Aniline.....	86
Figure 4.3. Acid Doping of Polyaniline: The Formation of Charge Carriers	87
Figure 4.4. Conductivity as a Function of Dopant Structure	89
Figure 4.5. Conductivity and Yield as a Function of Oxidant: Monomer Ratio	90
Figure 4.6. Conductivity as a Function of Acid Concentration.....	91
Figure 4.7. Conductivity as a Function of Mole % Aniline in Feed Stock.....	92
Figure 4.8. A Typical Plot of Permittivity as a Function of Frequency	94
Figure 4.9. Permittivity, Loss Tangent, and Conductivity as a Function of Plasticizer Content.	95
Figure 4.10. Permittivity, Loss Tangent, and Conductivity as a Function of Heating Time ...	96
Figure 4.11. Permittivity, Loss Tangent, and Conductivity as a Function of Polyaniline Loading	96
Figure 4.12. SEM Images of a) as received MWNT, and b) Polyaniline – MWNT Composite	97

Figure 4.13. TEM Images of a) as received MWNT, and b) Polyaniline – MWNT Composite	97
Figure 4.14. Conductivity as a Function of MWNT Content	98
Figure 4.15. Oxidative polymerisation of pyrrole to polypyrrole proceeds via a one electron oxidation of pyrrole to a radical cation, which subsequently couples with another radical cation to form the 2,2'-bipyrrole. This process is then repeated to form longer chains.	100
Figure 4.16. Chemical structures of polypyrrole In neutral aromatic and quinoid forms and in oxidized polaron and bipolaron forms.....	101
Figure 4.17. Polypyrrole/PTSA film thickness as a function of polymerisation time at constant current. Polymerisation temperature 1°C, current density $\sim 3 \text{ mA/cm}^2$, $0.4 < \text{pH} < 11.4$	126
Figure 4.18. Polypyrrole/PTSA film conductivity as a function of initial electrolyte pH.....	127
Figure 4.19. Conductivity as a Function of Dopant Concentration for Electrochemically Synthesized Polypyrrole Films. The conductivity of NSA-1 and NSA-2 doped films decreases at higher concentrations due to the a gellation of the electrolyte (b).	128
Figure 4.20. Conductivity of pressed polypyrrole pellets as a function of pellet density. Dopant is NSA-1.	130
Figure 4.21. Top, conductivity of polypyrrole pellets pressed from powders milled in different ways. Bottom, same plots with the conductivity normalised by the density. Dopant used AQDSA.	131
Figure 4.22. Top, conductivity of pressed polypyrrole pellets as a function of dopant. Bottom, normalised conductivity (conductivity/density) of the same pellets.	132
Figure 4.23. Effect of dopant to monomer ratio on the conductivity (normalised for density) of pressed polypyrrole pellets. Dopant ion NSA-1.	133
Figure 4.24. Cotton Fabric Samples before and after coating with polypyrrole. The cotton textiles have different weaves and densities and are made from spun fibres.	134
Figure 4.25. Polyester fabric samples before and after coating with polypyrrole. Polyester #1 and #2 have similar densities and are woven from rovings (a loosely associated bundle of untwisted filaments) of about 35 filaments. Polyester #2 had been previously treated in a corona. Polyester #3 has a density more than 50% less than the other polyesters and is woven from spun fibres.....	135
Figure 4.26. Polyamide and Glass tissues before and after coating with polypyrrole. These textiles are made from randomly oriented single filament fibres. The glass fibres are sized while the polyamide fibres appear to be fused.....	136

Figure 4.27. For synthetic fibres the conductivity is proportional to the density of polypyrrole in the composite fabric (ie mass of polypyrrole per unit volume of fabric). Data from Table 4.5. Natural cotton fibres present a higher surface area and absorb more reactants from solution.	138
Figure 4.28. Comparison of the measured imaginary component of the permittivity, ϵ'' , to theoretical value calculated from the static conductivity. Within the uncertainty most points fall on the theoretical line. Uncertainties in the imaginary component are on the order of 5-10%.	140
Figure 4.29. Plot of ϵ'' vs ϵ' for the average values from the glued and taped samples at 10 GHz. Figure 4.31a shows a linear fit to the data with slope, $\tan \delta$, of 2.5. Figure 4.31b shows the data fitted to a nonlinear section at lower values of ϵ'' and a linear section for the higher values.....	141
Figure 4.30. Conductivity (a) and normalised conductivity ($\sigma/\sigma_{\text{initial}}$) (b) as a function of aging time.....	143
Figure 4.31. Decrease in conductivity for polypyrrole doped with different ions at -18° C. 144	
Figure 4.32. Room temperature decrease in conductivity as a function of time for polypyrrole doped with different ions.....	145
Figure 4.33. Decrease in normalised conductivity as a function of time for polypyrrole doped with different ions at 85° C.	146
Figure 4.34. Spectra for Three Temperatures.....	147
Figure 4.35. Conductivity of some alkyd#1-polypyrrole coatings with the same formulation. Conductivity of pressed pellets of polypyrrole powder was 31 S/cm for black line and 19 S/cm for the other series.....	150
Figure 4.36. Real and Imaginary components of the permittivity as a function of the wt% polypyrrole in alkyd#1 coating. All formulations originate from the same batch of polypyrrole made with NSA-1. ϵ'_r , blue squares, ϵ''_r , red circles.	151
Figure 4.37. Real and Imaginary components of the permittivity as a function of the wt% polypyrrole in the polyurethane non-skid coating. Top graph, hand mixed, bottom graph speed mixed. Dopant NSA-1.....	152
Figure 4.38. Permittivity of PPy/AQDSA-Alkyd#2 coatings as a function of weathering time. Blue markers – 5 wt% red markers 3 wt% polypyrrole. Solid markers the real component of the permittivity and open markers the imaginary component.....	153
Figure 4.39. Synthesis of 1-5.....	162
Figure 4.40. Synthesis of 6-8.....	163

Figure 4.41. Synthesis of 9-10.....	163
Figure 4.42. Synthesis of 11.	163
Figure 4.43. Reaction of model compound 12 with FeCl ₃	165
Figure 4.44. Synthesis of EDOT/4 based copolymers.....	165
Figure 4.45. Synthesis of doped Poly4 and its reduction to undoped state.	166
Figure 4.46. UV-Vis of poly4 after reduction with hydrazine.....	166
Figure 4.47. UV-Vis of poly8/FeCl ₃	167
Figure 4.48. Putative electropolymerization of 1.	168
Figure 4.49. Electropolymerization of 4 in CH ₂ Cl ₂ .(a) 1 st scan....(e) 40 th scan. Y-axis units are in microAmps.	169
Figure 4.50. CV of Poly4 at different scan rates. (a) 0.05 V/s (b) 0.1 V/s (c) 0.2 V/s (d) 0.4 V/s (e) 0.8 V/s (f) 1 V/s. Y-axis units are in microAmps.....	170
Figure 4.51. Reduction of Poly4 on ITO electrode at different potentials. (a) 1.3 V (b) 0.5 V (c) 0.2 V (d) 0 V (e) -0.2 V	170
Figure 5.52. Potential-dependent conductivity of Poly4. Y-axis units are in microAmps. ...	171
Figure 4.53. Electronic spectrum of poly11 in (a) doped and (b) undoped forms.....	172
Figure 4.54. Putative electropolymerization of both 4 and 11.....	172
Figure 4.55. Proposed synthesis of Poly4 derivatives with improved processing properties.173	
Figure 4.56. Synthesis of EDOT-substituted phosphines 1-5.....	174
Figure 4.57. Synthesis of Mo complexes of 1-5.....	175
Figure 4.58. Synthesis of EDOT silanes 3 and 4.....	177
Figure 4.59. CV of Poly1 (solid line) and Poly4 (dashed line). Y-axis units are in microAmps.	178
Figure 4.60. Solution absorption spectra of polymers derived from 1-4.....	180
Figure 4.61. Synthesis of EDOT amines 1-3.....	181
Figure 4.62. Oxidation of triarylaminines.	182
Figure 4.63. CV of tris-EDOT amine 1.	182

Figure 4.64. Electropolymerization of tris-EDOT amine 1.....	183
Figure 4.65. CV of poly1 at scan rates: (a) 0.01, (b) 0.025, (c) 0.05, (d) 0.1, (e) 0.15, (f) 0.2 V/s	183
Figure 4.66. CV of Poly1 after one cycle (solid line) and 100 cycles (dashed line).	184
Figure 4.67. UV-Vis spectra of poly1 at different potentials: (a) +1.1V...(d) -1.0V vs. Ag/AgCl.	185
Figure 4.68. CV of bis-EDOT amine 2.....	185
Figure 4.69. Electropolymerization of bis-EDOTamine 2. Y-axis units are in microAmps.	186
Figure 4.70. CV of film of Poly2.....	187
Figure 4.71. Absorption spectra of Poly2 at (a)+1.0V, (b) 0V, and (c)-1V vs Ag/AgCl.	187
Figure 5.1. Network analyser and waveguide used for measuring S-parameters and fitting permittivity.....	190
Figure 5.2. Sample placement in the waveguide for transmission – reflection measurements and the equivalent circuit for derivation of the relationship between the measured data and sample parameters.	194
Figure 5.3. Placements of the test sample in the reflection – two-position method	195
Figure 5.4. Circuit for derivation of the relationship between the scattering parameters and the permittivity and permeability for the T2P method.....	196
Figure 5.5. The dielectric constant (blue) and loss factor (red); sample B2.....	201
Figure 5.6. The dielectric constant (blue) and loss factor (red); sample CN.....	202
Figure 5.7. The dielectric constant (blue) and loss factor (red); sample T3	203
Figure 5.8. The dielectric constant (dark blue, dielectric loss factor (pale blue), permeability, real part (red) and magnetic loss factor (pale red); sample MN.....	204
Figure 5.9. Permittivity of 12.4% sample.....	206
Figure 5.10. Permittivity of 18% sample.....	207
Figure 5.11. Permittivity of 24.8% sample.....	208
Figure 5.12. Permittivity of 42% sample.....	209
Figure 5.13. Permittivity of 56.8% sample.....	210

Figure 6.1. Reflectivity from Jaumann absorber layers.....	213
Figure 6.2. Reflectivity of different absorbers over the frequency range for N= 1, 3, 5, and 7 (a) and N= 2, 4, and 6 (b). These absorbers were optimised using the Bandwidth objective function. ϵ_r spacer = 1.0.....	220
Figure 6.3. Bandwidth of the absorber increases with the number of resistive sheets, N and approaches the maximum bandwidth, (1.81). The bandwidth objective function (solid line) converges on absorber designs with larger bandwidths than does the reflectivity objective function (dashed line). ϵ_r spacer = 1.0.....	221
Figure 6.4. Bandwidth as a function of sheet resistance for a Salisbury Screen as determined using the bandwidth objective function. The maximum bandwidth for this absorber is about 0.25 and occurs at a slightly lower sheet resistance (369 Ω /sq) than that which yields the minimum reflectivity (ie 377 Ω /sq), ϵ_r spacer = 1.0.....	222
Figure 6.5. Bandwidth as a function of sheet resistance for a 2-layer Jaumann absorber as determined using the bandwidth and reflectivity objective functions (Eq 13). Significant bandwidth is achieved for a small range of R1 (Black dots) compared to R2 (Blue dots), the resistive sheet at the air/absorber interface. The maximum bandwidth for this 2-layer absorber is 0.87. Figure 6.5a includes all absorber designs for generations 1-10 while Figure b shows only generation 10. ϵ_r spacer = 1.0.....	223
Figure 6.6. Resistance profile for a 6 layer Jaumann absorber optimised using the reflectivity and bandwidth objective functions. Generation 4 (a), and 1-50 (b). ϵ_r spacer = 1.0.....	224
Figure 6.7. Bandwidth improvement as a function of a protective layer at the air/absorber interface. ϵ_r spacer = 1.1. Absorbers optimised using the bandwidth objective function. Solid line absorber with protective layer, dashed line absorber without.....	225
Figure 6.8. The maximum bandwidth is achieved over a wide range of sheet resistances, even for the Salisbury Screen, when a protective layer is placed at the air/absorber interface. ϵ_r spacer = 1.1, bandwidth objective function.....	226
Figure 6.9. The optimised resistance profile for a seven layer absorber with a protective layer. ϵ_r spacer = 1.1.....	226
Figure 6.10. Reflectivity profiles for Salisbury screen designs with different spacer permittivity. ϵ_r = 1.1 (solid line), 2 (dotted line) and 3 (dashed line).....	227
Figure 6.11. Bandwidth vs sheet resistance for one and two layer absorber designs with a spacer permittivity of ϵ_r spacer = 2. The genetic algorithm converges on absorber designs where the bandwidth is smaller than found for lower permittivity materials.....	228
Figure 6.12. Bandwidth vs sheet resistance for a three layer absorber design with a spacer permittivity of ϵ_r spacer = 2. The optimum absorber is not achieved with an external sheet resistance of 50 k Ω /sq.....	229

Figure 6.13. Bandwidth vs sheet resistance (a) for a Salisbury screen with a spacer permittivity of ϵ_r , spacer = 2, and a protective layer. The optimum absorber design has a much wider bandwidth and appears to have the same reflectivity profile (b) as a two-layer absorber with no protective sheet.	230
Figure 7.1. View of one structure with Vezzuto software.	234
Figure 7.2. Equivalent circuit for the FSS. Admittance of the FSS is Y_L	235
Figure 7.35. Variation of the impedance as a function of the element (cross) length. Material 1.	237
Figure 7.36. Dependence of the resistance (red) and the reactance (black) on the gap width. Material 1, $f=10\text{GHz}$	238
Figure 7.37. Resistance at the resonant frequency for the different materials (for structure B6 on the left side, and for structure C1 on the right side).	238
Figure 7.38. Resonant frequency as a function of the permittivity and the conductivity.	239
Figure 7.3. Cross dimensions and equivalent impedance plotted in the Smith chart (structure A1).	247
Figure 7.4. Resistance and reactance (structure A1).	247
Figure 7.5. Cross dimensions and equivalent impedance plotted in the Smith chart (structure A2).	248
Figure 7.6. Resistance and reactance (structure A2).	248
Figure 7.7. Cross dimensions and equivalent impedance plotted in the Smith chart (structure A3).	249
Figure 7.8. Resistance and reactance (structure A3).	249
Figure 7.9. Cross dimensions and equivalent impedance plotted in the Smith chart (structure B1).	250
Figure 7.10. Resistance and reactance (structure B1).	250
Figure 7.11. Cross dimensions and equivalent impedance plotted in the Smith chart (structure B2).	251
Figure 7.12. Resistance and reactance (structure B2).	251
Figure 7.13. Cross dimensions and equivalent impedance plotted in the Smith chart (structure B3).	252
Figure 7.14. Resistance and reactance (structure B3).	252

Figure 7.15. Cross dimensions and equivalent impedance plotted in the Smith chart (structure B4).....	253
Figure 7.16. Resistance and reactance (structure B4).....	253
Figure 7.17. Cross dimensions and equivalent impedance plotted in the Smith chart (structure B5).....	254
Figure 7.18. Resistance and reactance (structure B5).....	254
Figure 7.19. Cross dimensions and equivalent impedance plotted in the Smith chart (structure B6).....	255
Figure 7.20. Resistance and reactance (structure B6).....	255
Figure 7.21. Cross dimensions and equivalent impedance plotted in the Smith chart (structure B7).....	256
Figure 7.22. Resistance and reactance (structure B7).....	256
Figure 7.23. Cross dimensions and equivalent impedance plotted in the Smith chart (structure B8).....	257
Figure 7.24. Resistance and reactance (structure B8).....	257
Figure 7.25. Cross dimensions and equivalent impedance plotted in the Smith chart (structure B9).....	258
Figure 7.26. Resistance and reactance (structure B9).....	258
Figure 7.27. Cross dimensions and equivalent impedance plotted in the Smith chart (structure C1).....	259
Figure 7.28. Resistance and reactance (structure C1).....	259
Figure 7.29. Cross dimensions and equivalent impedance plotted in the Smith chart (structure C2).....	260
Figure 7.30. Resistance and reactance (structure C2).....	260
Figure 7.31. Cross dimensions and equivalent impedance plotted in the Smith chart (structure C3).....	261
Figure 7.32. Resistance and reactance (structure C3).....	261
Figure 7.33. Cross dimensions and equivalent impedance plotted in the Smith chart (structure C4).....	262
Figure 7.34. Resistance and reactance (structure C4).....	262

List of tables

Table 3.1. Material Thickness and Properties for Jaumann Layers.....	80
Table 4.1: Dopant Structure.....	89
Table 4.2. IR and Raman absorption frequencies.....	115
Table 4.3. Dopants and Acronym.....	122
Table 4.4. Fabric description.....	123
Table 4.5. Polypyrrole coated textile properties.....	137
Table 4.6. Measured parameters for various fabrics as a function of whether they were glued or taped to the acrylic block for microwave measurements.....	139
Table 4.7. Summary of Fabric Aging.....	142
Table 4.8. Diffusion coefficients calculated from loss of conductivity of polypyrrole pellets doped with different ions.....	146
Table 4.9. Results of chemical polymerization of sulfur-bridged thiophenes by FeCl ₃	164
Table 4.10. Elemental analyses for FeCl ₃ polymerized 1 and 4.....	164
Table 4.11. Conductivity of EDOT/4 copolymers.....	165
Table 4.12. Electrochemical and optical properties of sulfur-bridged thiophenes.....	168
Table 4.13. Electrochemical and optical properties of sulfur-bridged thiophene polymers..	173
Table 4.14. Oxidation peak potentials of EDOT phosphines and their metal complexes.	176
Table 4.15. Electrochemical and optical properties of EDOT silanes 1-4.....	178
Table 4.16. Electrochemical and absorption data for polymers derived from 1-4.....	179
Table 4.17. Optical properties of Poly1 films at different potentials.....	184
Table 4.18. Optical properties of Poly2 at different potentials.....	188
Table 5.1. . Samples measured, batch of February 2001.....	205

Table 5.2. Polynomial representation of the material permittivity - coefficients	210
Table 6.1. Algorithm for a simple genetic algorithm.	215
Table 6.2. Absorber thicknesses and fractional bandwidths.....	221
Table 7.1. Material properties, permittivity and conductivity.	236
Table 7.2. Dimension influence for structures A.....	240
Table 7.3. Dimension influence for structures B.....	241

Acknowledgements

The authors would like to acknowledge the contribution of the following people Maria Stuchly, Robin Hicks, Bob Pakneys, Satish Kashyap, Sandra Neville, Terry Foster, Mary Diep, Andrew Leslie, David Edwards, Mike Kopac, and Geoffrey Blenkinsop.

This page intentionally left blank.

1. Introduction

This paper reports the results from a Technology Investment Funded (TIF) project entitled Fabrication of Organic Radar Absorbing Materials. When this project was proposed Defence R&D Canada had no program investigating materials for use as microwave absorbers. The literature was reporting interesting properties of conducting polymers that would be suitable for use in microwave absorbers. These materials would circumvent problems with conventional absorber materials, such as weight and a tendency to corrode. At the same time scientists at DRDC Ottawa had been working on modelling the radar cross section of CF platforms, and had a requirement for developing their own code Radar Cross Section (RCS) code.

The aim of this project was to develop the capability to design and create improved radar absorbing materials (RAM) for reduction of the radar cross section of Canadian Naval platforms. Four enabling technologies were identified as being key to the success of this project. These technologies were:

1. Materials: Synthesis of stable conducting polymers.
2. Property Measurement: Development of measurement methods to obtain optical properties of conducting polymer films at microwave frequencies.
3. Absorber Design: Use of measured optical properties to find optimal RAM designs, and
4. RCS Modelling: Determination of RCS, hotspots and RCS reduction with RAM for CF platforms.

Research into each of these technologies was undertaken as part of the TIF.

1.1 Materials

There are two classes of materials that are used for the absorption of electromagnetic energy: magnetic materials and conductive materials. Ferrites and carbonyl iron have been used for these purposes, resulting in heavy materials that are unstable to corrosion. There are no practical organic magnetic materials existing today, however, conducting polymers are feasible contenders for use as microwave absorbers.

In this part of the project investigations were made into several areas of conductive material fabrication: Synthetic control of conductive polymer properties, formulation of the conductive polymer into useful materials while still controlling the properties and stabilisation of these properties. Polypyrrole and polyaniline were chosen for study, as they are inexpensive, easy to synthesize and relatively stable conducting polymers. Typically these polymers are synthesized in powder form and so they must be formulated into a coating, or composite, ie in the form of a carrier so that the

material can be applied where and how it is needed. Stability of material properties is related to the degradation of absorber performance. Chemical processes that result in the loss of polymer conductivity must be minimized to ensure adequate absorber lifetime. The stability of the conducting polymers is investigated and new conducting polymers are synthesized with the aim of improving stability.

1.2 Property Measurement

The permittivity and permeability of a material are required in order to describe how electromagnetic waves interact with matter. Specifically these parameters are required for the calculation of the reflectivity from a material, and are therefore the key requirements needed to design an absorber. These properties are frequency dependent and there must be determined over the frequency range over which an absorber is to operate.

In this part of the project a method was developed for determining the permittivity and permeability of a material. This allowed the materials fabricated in the laboratory to be characterized and correlated against synthetic and fabrication conditions. It also provided material properties that could be used for modelling optimum absorber designs.

1.3 Absorber Design

The design of an effective absorber requires the combination of material properties and the physical structure of the absorber. For a single layer this problem can be analytically solved. More complex, broadband absorbers require the use of optimisation techniques as the problem becomes complex and nonlinear. The goal when using an optimisation routine is to find the global minimum, and not to converge on local minima solutions. Another goal of optimisation routines is to consider optimum solutions against a number of design functions. For absorbers, the design requirements usually are the lowest reflectivity over the widest bandwidth. However, absorber thickness and weight are also important considerations. Multi-objective optimisation finding the global optimum is effectively handled using the Genetic Algorithm.

In this part of the project the Genetic Algorithm was used to design multilayered Jaumann absorbers using resistive sheets. This method can also be applied to the design of absorbers based on a database of available materials.

1.4 RCS

The radar cross section is a measure of the how much electromagnetic radiation is scattered from an object. The magnitude of the RCS is indicative of the objects detectability. Reducing the RCS reduces the detection range of a platform. The optimum means of reducing the RCS of an object is in the design phase, where low scattering materials and angular shapes can be used to reduce the signal returned to a

radar receiver. The RCS of a platform can be determined on a range, in an anechoic chamber with a scale model, or by modelling. DRDC Ottawa required their own RCS modelling code so that they knew what the code did and could modify it to contain finer detail.

In this part of the project a modelling code was developed to determine the RCS of a ship starting with a CAD design of the structure. The ships structure is sectioned into triangular facets. These facets are adjustable in size so that regions containing fine detail can be studied at higher resolution than broad monotonic regions. Rays are traced from a microwave transmitter and back to the receiver, where physical optics are applied to calculate the reflected electromagnetic field. The RCS can be determined over the surface of the platform from any angle, highlighting hotspots. The RCS of the hotspots can be reduced by application of RAM and the RCS recalculated.

This code should be useful in the design of CF platforms with reduced RCS, or in the reduction of the RCS of existing platforms by determining the best location for applying RAM patches.

This RCS work is not discussed further in this report, as DRDC Ottawa will report on it when the code is completed.

1.5 Report Layout

In the first part of this report radar absorbing materials are reviewed looking at the historical development of absorbers, the types of absorbers, absorber optimisation, and materials (Section 2). The physics of the interaction of electromagnetic waves with matter is developed with practical considerations for absorbers in Section 3. In Section 4, the synthesis and fabrication of conducting polymers and materials are reported and correlated to their optical properties. Permittivity and permeability measurement techniques are explained in Section 5 and absorber design optimisation is presented in Section 6. Section 7 reports the modelling of the reflectivity from circuit analog materials using FDTD simulation.

2. Radar Absorbing Materials Review

Exploitation of the electromagnetic spectrum for detection purposes extends from the ultra violet through visible, infrared, microwave and radio frequencies. The theory of physical optics has aided in the advancement of these detection methods. Conversely detection avoidance through camouflage, or signature reduction, exploits the same theory of physical optics to minimise reflections, emissions and hence detection. It is a combination of optics and materials that lead to signature reduction.

The detectability of a target is measured in terms of the radar cross section (RCS). The RCS is a property of the targets size, shape and the material from which it is fabricated and is a ratio of the incident and reflected power. For targets that are small in comparison to the radiation wavelength Rayleigh scattering occurs. Large objects, compared to the wavelength, result in optical scattering including diffraction and specular scattering. For these large objects geometrical optics with diffraction theory (geometrical theory of diffraction) are used to determine the RCS. When the object size is on the order of the wavelength of the radiation, Mie scattering occurs which is characterized by creeping waves.

There are four methods of reducing the radar cross section; shaping, active loading, passive loading and distributed loading. Shaping is the primary method of reducing the backscattered signal. Although shaping is very important, it redirects the radiation through specular reflection hence increasing the probability of detection from bistatic radars. Active and passive loading aims to reduce the scattering from hotspot regions through the application of patches. Active materials detect the incident radiation and emit signals of equal amplitude and opposite phase to cancel the signal, while passive materials are designed to modify the surface impedance so as to cancel the scattered signal. The fourth method, distributed loading involves covering the surface with a radar absorbing material that has imaginary components of permittivity and/or permeability (ie the electric or magnetic fields of the radiation couple with the material properties and energy is consumed).

In this paper the field of microwave (radar) absorbing materials (RAM) is reviewed with consideration of the historical development, physical theory, design optimisation and materials behind these devices.

2.1 A History of RAM Development

The development of Radar absorbing materials has been reviewed in several papers^[1-6] and Books.^[7-9] Exploitation of radar absorbing materials started in the 1930's shortly after the advent of radar. Absorber design has incorporated materials with different loss mechanisms and has made use of physical optics to optimise absorption over wide bandwidths. Absorbers therefore come with many different shapes and structures, ranging from thick pyramidal structures, to multilayers and single coatings. Microwave absorbing materials have been used in commercial settings, for anechoic

chambers and for reducing the reflected signals from buildings and superstructures around radar installations. Current communication technologies at microwave frequencies are driving the development of absorbers and frequency selective surfaces. This section gives a brief review of the historical development of RAM, and referral to subsequent sections will help illustrate the devices, materials and structures being discussed here. Also due to the secret nature of RAM development some details are sketchy or not published.

Research into electromagnetic wave absorbers started in the 1930's,^[2,8] with the first patent appearing in 1936 in the Netherlands.^[10] This absorber was a quarter-wave resonant type using carbon black as a lossy resistive material and Titanium dioxide for its high permittivity to reduce the thickness.

During World War II, Germany, concerned with radar camouflage for submarines, developed "Wesch" material, a carbonyl iron powder loaded rubber sheet about 0.3 inches thick and a resonant frequency at 3 GHz. The front surface of this material was waffled to produce a larger bandwidth. They also produced the Jaumann Absorber, a multilayer device of alternating resistive sheets and rigid plastic. This device was about 3 inches thick with resistances decreasing exponentially from the front to the back. This device achieved a reduction in the reflectivity of -20 dB over 2-15 GHz. America, during this period, led by Halpern at MIT Radiation Laboratory developed materials known as "HARP" for Halpern Anti Radiation Paint. The airborne version, known as MX-410, had a thickness of 0.025 inches for X-band resonance. The base dielectric had a high permittivity of 150 due to loading with highly oriented disk shaped aluminium flakes suspended in a rubber matrix and carbon black for loss. This material offered a 15-20 dB reduction in reflectivity. Shipborne absorbers were 0.07 inch thick (X-band) iron particle loaded rubber with a permittivity of 20 and enough permeability to produce resonance broadening.^[11,12] At the same time the resonant Salisbury Screen was developed with about 25% bandwidth at resonance.^[13] Production of Salisbury screens was aided by the US Rubber Company marketing a resistive cloth called Uskon. Another absorber design that arose at this time was a long pyramidal structure with the inside coated with Salisbury Screen and the apex in the direction of propagation. The multiple reflections from the absorber resulted in high attenuation.^[14] The importance of ferrites was known. With the exceptions of the Jaumann device and the inverted pyramid, these devices are typically narrow band.

The postwar period (1945-1950) was characterized by the development of broadband absorbers using sharp pointed geometric shapes that produce a gradual transition into the absorbing material. These materials found application in anechoic chambers.^[15-18] Materials investigated for microwave attenuation include carbon loaded plaster of paris, graphite, iron oxide, powdered iron, powdered aluminum and copper, steel wool, water, powdered "Advance" and "Constantin" and metal wires.^[19] Binders included various plastics and ceramics, while supports with a lot of air at the interface included foams, fibres and "excelsior". More functional lossy broadband materials were created with a flat surface by using patterned flat layered resistive sheets that reproduced the pyramidal, or conical structures of above.^[12]

The 1950's saw the commercial production of RAM called "Spongex", based on carbon coated animal hair, by the Sponge Products Company, (later to become a division of B.F. Goodrich Company). This material, 2 inches thick, resulted in -20 dB attenuation in the reflectivity over 2.4-10 GHz for normal incidence. 4 and 8 inch versions also produced for lower frequencies. This company was later joined by, Emerson and Cuming Inc and McMillan Industrial Corporation, in the manufacture of absorbers. Research into circuit analog devices was started by Severin and Meyer during this decade.^[1,2,20,21] The term circuit analog comes from the use of circuit theory to represent the components/processes occurring in the absorber, and hence to model the reflectivity. This technique was adopted from research programs on acoustical absorbers. Severin and Meyer made experimental absorbers based on resistance loaded loops, slots in resistive foil, resistance loaded dipoles, strips of resistive material with various orientations, strips of magnetic material with various orientations, surface shaping and magnetic loading of resonant materials. This started a new field of research into frequency selective surfaces (FSS).^[22]

The 60's and 70's saw continuing work on circuit analog materials,^[9] and significant absorber thickness reductions were demonstrated using ferrite underlayers.^[23] Pyramidal shaped absorbers were being used for anechoic chambers achieving -60 dB at near normal incidence. Control of the fabrication of Jaumann layers was demonstrated by screen printing,^[24] and absorbers were being made from foams, netlike structures, knitted structures, or honeycomb and coated with a paint containing particulate or fibrous carbon, evaporated metal or nickel chromium alloy.^[25] Interesting, though not practical one patent describes an absorbers that employing a plasma to absorb the microwaves. The plasma was generated by a radioactive substance requiring about 10 Curies/cm²!^[26]

The 1980's. The absorber design process is improved by optimization techniques.^[27-29] Bandwidth improvement of Jaumann absorbers was evaluated by using graded layers^[6,30] and different resistive profiles to achieve maximum bandwidths. Computers and transmission line models were used to calculate reflectivity from material properties, and for frequency selective surfaces which can be represented as equivalent circuits, the transmission line model are applied.^[5] Circuit analog materials are designed^[31] and the scattering of these materials is analysed based on the Floquet theorem.^[32] Materials continue to use carbon black or graphite, carbonyl iron and ferrites, though now artificial dielectrics are being made by adding inclusions such as rods, wires, disc and spheres.^[6] Helical inclusions are found to improve absorption and resulted in research into chiral materials.^[33] Mixing theory is used to calculate the desired permittivity and permeability of these new materials. Conducting polymers appear as potential radar absorbing materials.

The 1990's and on to today has seen more optimisation techniques for Jaumann structures including genetic algorithm optimisation.^[34-40] Circuit analog and frequency selective surfaces continue to big in the literature.^[20,31,32,35,40-49] Conducting polymers and composite materials with these are found along with conducting polymer coated fibres and fabrics for creating devices.^[50-84] A new class of absorbers that find their roots in conducting polymers is that of dynamic RAM,^[85-89] where the resonant

frequency of the absorber is tuneable through variation of resistive and capacitive elements in the absorber.

2.2 Theory Reflectivity Minimisation

The theory behind the interaction of electromagnetic radiation with matter is discussed in detail in section 3. In this section several points for reflectivity minimization are considered.

In an attempt to minimise the reflection from a surface it is useful to consider the physical equations that represent the reflection process. There are three conditions that result in a minimum reflectivity.

The first equation of interest is that describing the reflection coefficient at an interface.

$$r = \frac{\eta_M - \eta_o}{\eta_M + \eta_o} = \frac{Z_M - Z_o}{Z_M + Z_o} \quad 2.1$$

where r is the reflection coefficient and η the admittance of the propagating medium (subscript o for incident medium or air and M for the substrate). The admittance in this equation can be replaced with the intrinsic impedance ($Z = 1/\eta$). The reflection coefficient falls to zero when $\eta_M = \eta_o$, or in other words the material in the layer is impedance matched to the incident medium. The intrinsic impedance of free space is effectively given by

$$Z_o = \frac{\mathbf{E}}{\mathbf{H}} = \sqrt{\frac{\mu_o}{\epsilon_o}} \approx 377 \text{ohms} \quad 2.2$$

where \mathbf{E} and \mathbf{H} are the electric and magnetic field vectors and μ_o and ϵ_o are the permeability and permittivity of free space. Thus a material with an impedance of 377 ohms will not reflect microwaves if the incident medium is free space.

Perfect impedance matching can also be realised if the electric permittivity and the magnetic permeability are equal. This gives the second condition that results in a minimum in the reflection coefficient. In this case equation 2.1 is rewritten as

$$r = \frac{\frac{Z_M}{Z_o} - 1}{\frac{Z_M}{Z_o} + 1} \quad 2.3$$

The normalized intrinsic impedance is

$$\frac{Z_M}{Z_o} = \sqrt{\frac{\mu_r^*}{\varepsilon_r^*}} \quad 2.4$$

where $\varepsilon_r^* = \frac{\varepsilon' - i\varepsilon''}{\varepsilon_o}$ and $\mu_r^* = \frac{\mu' - i\mu''}{\mu_o}$, the prime and double prime superscripts represent the real and imaginary components of the complex numbers, respectively. If the incident medium is free space and the reflectivity is zero, then it follows that $\mu_r^* = \varepsilon_r^*$. The implication is if both the real and imaginary parts of the permittivity and permeability are equal, then the reflectivity coefficient is zero.

The third consideration is the attenuation of the wave as it propagates into the absorbing medium. The power of the wave decays exponentially with distance, x , by the factor $e^{-\alpha x}$. α is the attenuation constant of the material and can be expressed as

$$\alpha = -\sqrt{\varepsilon_o \mu_o} \omega (a^2 + b^2)^{1/4} \sin\left(\frac{1}{2} \tan^{-1}\left(-\frac{a}{b}\right)\right) \quad 2.5$$

where $a = (\varepsilon_r' \mu_r' - \varepsilon_r'' \mu_r'')$ and

$$b = (\varepsilon_r' \mu_r'' + \varepsilon_r'' \mu_r').$$

To get a large amount of attenuation in a small thickness, α must be large, which implies that ε_r' , ε_r'' , μ_r' and μ_r'' must be large. It is noted here that this condition must be tempered with the first condition (equation 2.1), where large values of permittivity and permeability would result in a large reflection coefficient.

2.3 Types of Radar Absorbing Material

It is useful to consider how the theory in section 2.2 have been put into practice by considering the types of absorbers that have been produced.^[1,2,5,6] Absorbers can be classified into impedance matching and resonant absorbers, though it will be shown in the following discussion that many absorbers have features of both of these classifications. These features typically are a graded interface to match impedance or a gradual transition in material properties for impedance matching, and tuned or so called quarter wavelength resonant layers. Discussion of absorber optimisation is reserved for section 2.6.

2.3.1 Graded Interfaces – Impedance Matching

As seen in equation 2.1, a propagating wave that impinges upon an interface will experience some reflection that is proportional to the magnitude of the impedance step between incident and transmitting media. From this consideration three classes of

impedance matching RAM, pyramidal, tapered and matched, have been developed to reduce the impedance step between the incident and absorbing media. For complete attenuation of the incident wave one or more wavelengths of material are required, making them bulky and adding weight.

2.3.1.1 *Pyramidal Absorbers*

Pyramidal absorbers^[2,17] are typically thick materials with pyramidal or cone structures extending perpendicular to the surface in a regularly spaced pattern. Pyramidal absorbers were developed so that the interface presents a gradual transition in impedance from air to that of the absorber. The height and periodicity of the pyramids tend to be on the order of one wavelength. For shorter structures, or longer wavelengths, the waves are effectively met by a more abrupt change in the impedance. Pyramidal absorbers thus have a minimum operating frequency above which they provide high attenuation over wide frequency and angle ranges. These absorbers provide the best performance. The disadvantage of pyramidal absorbers is their thickness and tendency to be fragile. They are usually used for anechoic chambers. A more robust flat “pyramidal” absorber has been fabricated using multilayers with a pyramidal type structure being described by resistive sheets.^[18]

Pyramidal and wedge shaped absorbers have been designed using a Tschebyshev transformer technique^[90] and have been investigated with Finite Element Methods.^[91]

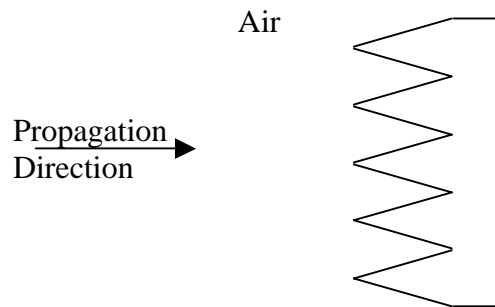


Figure 2.1. *Pyramidal Absorber*

2.3.1.2 *Tapered Loading Absorbers*

This material is typically a slab composed of a low loss material mixed with a lossy material. The lossy component is homogeneously dispersed parallel to the surface, with a gradient perpendicular to the surface and increasing into the material.^[12,17] One type of material includes an open celled foam or 3-d plastic net, dipped or sprayed with lossy material from one side, or allowed to drain and dry.^[92] It is difficult to

reproducibly fabricate a gradient in this manner. A second type is composed of homogeneous layers with increasing loading in the direction of propagation (ie. The gradient is created as a step function) see Figure 2.2.

The advantage of these materials is that they are thinner than the pyramidal absorbers. The disadvantage is that they have poorer performance and it is best to vary the impedance gradient over one or more wavelengths.

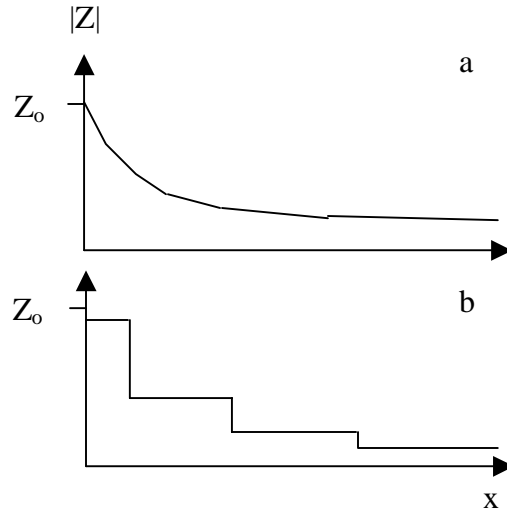


Figure 2.2. Tapered Loading Absorber, type a) smooth type b) stepped.

2.3.1.3 Matching Layer Absorbers

The matching layer absorber attempts to reduce the thickness required for the gradual transition materials. This absorber places a transition absorbing layer between the incident and absorbing media. The transition layer has thickness and impedance values that are between the two impedances to be matched (ie the absorber and incident media). The idea is to have the combined impedance from the first and second layers to equal the impedance of the incident medium, Figure 2.3. This matching occurs when the thickness of the matching layer is one quarter of a wavelength of the radiation in the layer and

$$Z_2 = \sqrt{Z_1 Z_3} \quad 2.6$$

The impedance matching occurs then only at the frequency that equals the optical thickness. This makes the matching layer materials narrow band absorbers. These absorbers are made using an intermediate impedance and quarter wavelength thickness for absorption at microwave frequencies.

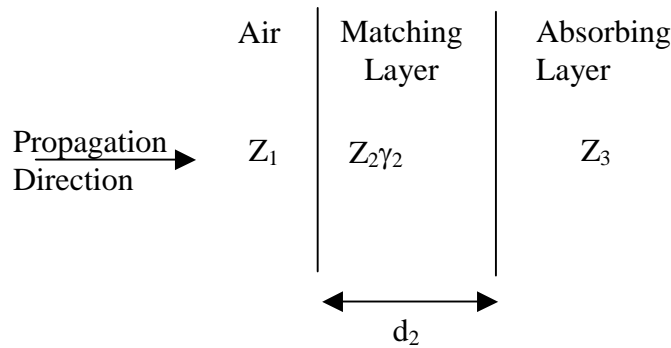


Figure 2.3. Matching Layer

2.3.2 Resonant Materials

Resonant materials are also called tuned or quarter wavelength absorbers and include Dallenbach layers, Salisbury Screen and Jaumann layers. In this class of materials the impedance is not matched between incident and absorbing media and the material is thin so that not all the power is absorbed. This arrangement results in reflection and transmission at the first interface. The reflected wave undergoes a phase reversal of π . The transmitted wave travels through the absorbing medium and is reflected from a metal backing. This second reflection also results in a phase reversal of π before the wave propagates back to the incident medium. If the optical distance travelled by the transmitted wave is an even multiple of $\frac{1}{2}$ wavelengths then the two reflected waves will be out of phase and destructively interfere. If the magnitude of the two reflected waves is equal then the total reflected intensity is zero.

2.3.2.1 Dallenbach (Tuned) Layer Absorber

A Dallenbach layer,^[93] is a homogeneous absorber layer placed on a conducting plane. The layer's thickness, permittivity and permeability are adjusted so that the reflectivity is minimised for a desired wavelength. The Dallenbach layer relies on destructive interference of the waves reflected from the first and second interfaces. For the reflectivity to result in a minimum, the effective impedance of the layer, Z_L , must equal the incident impedance Z_0 .

$$Z_L = Z_2 \tanh \gamma_2 d_2 \quad 2.7$$

However, since Z_L is complex and Z_0 real there is a requirement that the sum of the phase angles in Z_2 and $\tanh \gamma_2 d_2$ is zero (destructive interference) and the product of their magnitudes is equal to Z_0 . In the design of a tuned layer there are five properties to play with, ϵ' , ϵ'' , μ' , μ'' and d .

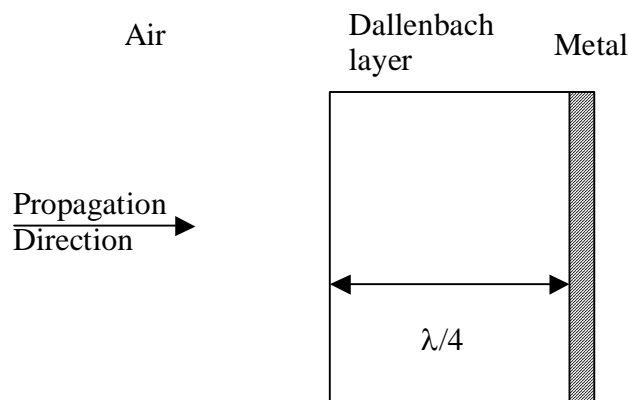


Figure 2.4. Dallenbach Layer

The reflectivity from Dallenbach layers has been simulated using CAD software called Touchstone and found to agree well with exact methods of calculating the reflectivity.^[94]

Optimisation of Dallenbach layers has been investigated^[95] and shown that it is not possible to obtain a broadband absorber with only one layer, however several layers stacked together showed increased bandwidth.^[96] A modified Powell method has been used to optimise reflectivity as a function of incident angle and frequency.^[97]

Dallenbach layers have been patented based on ferrite materials.^[96] The use of two or more layers with different absorption bands will increase the absorption bandwidth. Dallenbach layers have also been made with silicone rubber sheets filled with silicon carbide, titanium dioxide and carbon black.^[98] The bandwidth of standard ferrite absorbers have been improved through a two layer absorber design, with a ferrite layer at the air/absorber interface and a layer containing ferrite and short metal fibres at the absorber/metal interface. The fibre length is chosen to have a frequency near the required absorption frequency f_0 , (ie for 8-13 GHz the fibre length was 1-4 mm for 60 μm diameter wire). The impedance of the wires shifts from being capacitive when the frequency is less than f_0 of the fibres, to inductive for $f > f_0$. Impedance is at a minimum at f_0 and the induced current is at a maximum. Between f_0 and $\frac{1}{2} f_0$ the fibre has a capacitive reactance and for $f < \frac{1}{2} f_0$ the fibre resistance becomes small and the reactance is capacitive only. At f_0 the fibre length is nearly $\frac{1}{2} \lambda$ in the matrix.^[99] The ferrite layer acts as an impedance matching layer as well as absorber. Performance is better than -20 dB over 8-12 GHz and up to 45 degrees with an overall thickness of 4.6 mm. Design curves for Dallenbach layers have been considered.^[100] Multilayer Dallenbach devices have been designed using a Lagrangian optimization method with constrained variable.^[101] This method has also been used for the design of tapered and $\frac{1}{4}$ wavelength absorbers. A general solution for a single layer absorber is given along with design curves.^[102] Ferrite samples have been prepared and characterized for the lower frequency regions (100-200 MHz) with reflectivity profiles.^[103]

Although devices can be fabricated with large bandwidths, it is not known whether the maximum bandwidth possible has been achieved. The ultimate thickness to bandwidth ratio of radar absorbers has been calculated for different RAM types.^[104] At -10 dB reflectance the thickness of a multilayer dielectric slab cannot be less than $\lambda_{\max}/17.2$, where λ_{\max} is the maximum wavelength at which the reflectance is -10 dB. For a nonmagnetic Dallenbach layer with this reflectance, the best thickness/ $\Delta\lambda$ is 1/3.2 whereas for a narrow-band absorber the ratio is 1/13.9. This indicates that the largest possible bandwidth of a narrow-band dielectric absorber is about 4.4 times larger than that of a nonmagnetic Dallenbach screen of the same thickness.

2.3.2.2 Salisbury Screen

The Salisbury Screen (patented 1952)^[13] is also a resonant absorber, however, unlike the tuned absorbers it does not rely on the permittivity and permeability of the bulk layer. The Salisbury Screen consists of a resistive sheet placed an odd multiple of $\frac{1}{4}$ wavelengths in front of a metal (conducting) backing usually separated by an air gap. A material with higher permittivity can replace the air gap. This decreases the required gap thickness at the expense of bandwidth. In terms of transmission line theory, the quarter wavelength transmission line transforms the short circuit at the metal into an open circuit at the resistive sheet. The effective impedance of the structure is the sheet resistance. (If the gap is a half wavelength then the short circuit reappears and perfect reflection occurs). If the sheet resistance is 377 ohms/square (ie the impedance of air), then good impedance matching occurs. An analogue of the electrical screen would be to place a magnetic layer on the metal surface, resulting in a thinner device.^[5,27] The -20 dB bandwidth of the Salisbury Screen at the resonant frequency is about 25%.

Salisbury screens have been fabricated and the reflectivity calculated.^[71,105-109] Initial structures were made of canvas on plywood frames with a colloidal graphite coating on the canvas.^[14] Conducting polymers have been considered in the design of Salisbury screens.^[110] The reflectivity has calculated, using the optical matrix method, as a function of conducting polymer thickness, spacer thickness and incident angle.

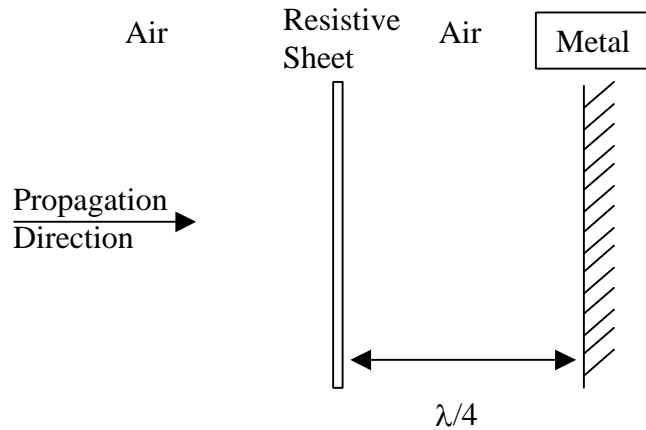


Figure 2.5. Salisbury Screen

2.3.2.3 Jaumann

Jaumann layers (1943)^[1] are a method of increasing the bandwidth of the Salisbury screen, the simplest form of a Jaumann device. The first device consisting two equally spaced resistive sheets in front of the conducting plane was mathematically shown to produce two minima in the reflectivity, thus increasing the bandwidth. Multilayer Jaumann devices consisting of low loss dielectric sheets separating poorly conductive sheets (with conductivity increase towards metal plane) were described and the reflectivity calculated(1948).^[1]

Resistive layers have been formulated using powdered carbon (25 weight %) in a phenol-formaldehyde, cellulose or polyvinyl acetate binder with polyethylene foams as spacers.^[24] Silk screening the resistive layers has been shown to produce better control of thickness and resistance. A six-layer device was capable of about 30 dB decrease in the reflectivity from 7-15 GHz.

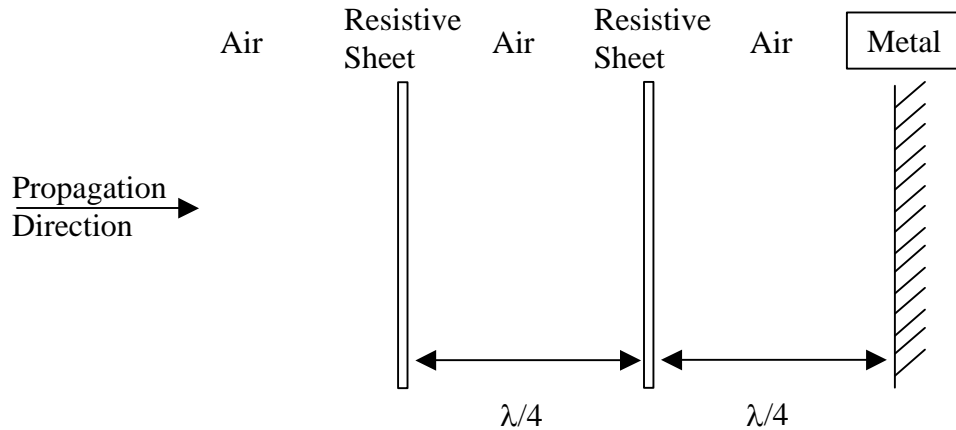


Figure 2.6. Jaumann Layers

The first calculations demonstrating that conducting polymers could be used as Jaumann absorbers occurred in 1991,^[111,112] and the first measurements of Jaumann absorbers incorporating conducting polymers occurred in 1992.^[106,113] Resistive polypyrrole films were grown electrochemically or by chemical methods using paper or fabrics as a support.^[105,107,109,113] Touchstone software has been used to model the reflectivity from conducting polymer materials, using Transmission line modelling. Simple RC networks have been used to fit the measured reflectivity.^[106-109] Methods for optimisation of Jaumann absorbers are considered in section 2.6.3.

2.3.3 Circuit Analog RAM

Improvement can be made on the bandwidth and attenuation of the resonant absorbers (Jaumann layers and Salisbury screen) by employing materials that take advantage of other loss mechanisms. The Salisbury screen and Jaumann layers were initially designed using purely resistive sheets. Replacement of the resistive sheets with materials also containing capacitance and inductance gives added scope for making broadband absorbers. Resistive-capacitive materials have been made in the form of conducting polymer coated fibers,^[114] and resistive-inductive materials have been made with helical metal coils imbedded in a dielectric layer.^[115] However, the field of circuit analog absorbers generally refers to materials where the resistive sheet has been replaced with lossy materials deposited in geometric patterns on a thin lossless sheet.^[1] The thickness of the lossy material determines the effective resistance and the shape, geometry and spacing of the patterns control the effective inductance and capacitance. These materials show improved reflectivity and bandwidth performance and tend to be thinner absorbers.

A simplistic view of how a circuit analog material work is shown in Figure 2.7. The resistive loss comes from the conductivity of the material used for the patterns. The spacing between the elements of the patterns gives rise to a capacitance and the length of the element gives rise to an inductance.^[22]

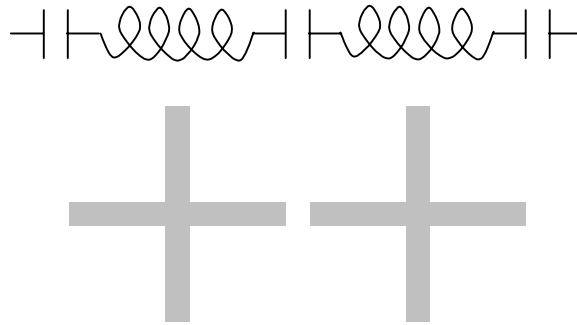


Figure 2.7. Circuit Analog Sheet of crosses. The spacing between the elements gives rise to a capacitance, and the length, to an inductance. The resistive component is a result of the lossy material.

The circuit analog equivalent of a Salisbury screen can be treated with transmission line theory (Section 2.5). The circuit analog sheet is modelled as a series circuit containing elements of resistance, capacitance and inductance, Figure 2.8. By varying the spacing between elements and element size the input impedance of the device can be tuned to that of free space.^[1] The bandwidth of a simple Salisbury Screen made from dipoles was measured to be 44% at -10dB Reflectivity. Lower reflectivity was obtained using a dielectric spacer compared to air.

$$Z_s = R_s + j\omega L_s + \frac{1}{j\omega C_s} \quad 2.8$$

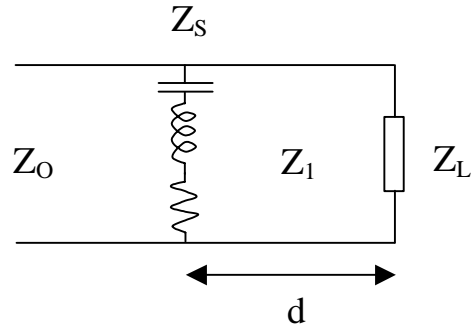


Figure 2.8. Transmission line circuit for a Salisbury Screen with a Circuit Analog sheet. Z_L is the load impedance. For an absorber on a perfect electrical conductor the load impedance is a short circuit and thus equal to zero. Z_1 is the impedance of the spacer. There will be a finite thickness for the sheet and circuit analog material.

The first artificial lossy materials were based on magnetic absorbers as these can be placed against the metal surface, resulting in thinner absorbers than the electrical analogs, which are spaced $\frac{1}{4}$ wavelength from the metal surface. These artificial magnetic materials were formed from an array of loop antennas distributed on the surface of a metal plate. This arrangement produces an impedance that can be tuned to match free space by varying the surface density of the loops and by varying the resistance of the resonator which absorbs the energy from the antenna. The resistive load was in the form of a few mg of iron powder.^[1,20,21] This was an anisotropic material that resulted in different reflection coefficients depending on the magnetic field polarization; only absorbing when the magnetic field vector has a component in the direction of the magnetic dipoles represented by the loop antennas. A second device was based on the pyramidal absorber material with resistive cards placed perpendicular to the metal plate and parallel to the E field direction.^[1,21] The resistive cards acted as a waveguide below the cutoff frequency if spaced at less than $\frac{1}{2}$ wavelength and the surface resistivity was low. For such an arrangement, the incident wave does not penetrate into the absorber and is reflected. Thus spacings larger than $\frac{1}{2}$ wavelength are needed. Results show maximum attenuation when the spacer separation is a little larger than half the wavelength. The reflectivity's dependence on incident angle depends on the resistive card spacing. For specular reflection the reflectivity is a smoothly increasing function with angle. The periodic structure causes diffraction, so that there are maxima in the reflectivity at specular and off-specular angles. Diffraction can be avoided by having pyramids of different lengths. These absorbers are very thick.

A frequency selective surface, FSS, is similar to a circuit analog absorber, however the patterned elements are made from metallic materials. FSS are typically used as bandpass filters for radomes. A FSS acts differently from a circuit analog absorber. Consider a FSS of metallic dipoles or slots with a dielectric spacer of $\frac{1}{4}$ wavelength or more. The dipoles act as short circuits and slots act as open circuits. The resonant

frequency of a slotted layer varies around $\frac{f_o}{\sqrt{\epsilon_r}}$, while for dipoles f_o is independent of

dielectric slab thickness. Stacking frequency selective surfaces improves transmission or reflection bandwidth. Placing dielectric slabs on either side of a FSS also increases bandwidth, insensitivity to angle of incidence and falloff.^[22] Three dielectrics and two screens produces good results. With the outer dielectric layers made of the same material (ϵ_r), a constant bandwidth over a wide angle of incidence and polarization is realised. The middle slab determines the flatness of the top of the bandpass.

Due to the complexity of patterns there are no simple means to model and optimise circuit analog and frequency selective surfaces. Transmission line models for broadband microwave absorbers have been used to analytically solve for the reflectivity.^[116] The transmission through periodically perforated conducting screens has been treated using Babinet's principle.^[117] Resistive and metallic strips were modelled using the spectral-Galerkin method.^[118] These strips represent a grating in free space. The repeat spacing of the strips (periodicity), results in a minimum reflectivity for normal incidence, when equal to the wavelength. Transmission line models for strip gratings have been made and applied to circuit analog Salisbury screens made by replacing the screen with a resistive grating and the base conductor by a conductive grating. This device is polarisation sensitive, absorbing TE and transmitting TM polarised waves.^[119] A method for determining the scattering from a device made from periodic arrays of resistive dipoles and crossed dipoles has been developed.^[32] This study was built on the spectral domain (spectral-Galerkin) methods of Mitra^[118,120,121] for frequency selective surfaces, which was extended to include resistive surfaces. Perfectly conducting patterns arrayed on the surface with a periodicity larger than the wavelength, show an influence from a ground plane (ie Salisbury Screen Configuration). If the periodicity is smaller than the wavelength, the ground plane is screened and has little influence.

One of the first patents on FSS for microwave absorption describes a multilayer grid device, where resistive grids are spaced with increasing mesh in the direction of propagation.^[122] Another early patent reports the use of multilayered arrays of disks or squares.^[49] Two patents have been issued for Jaumann type circuit analog absorber designs.^[31,48] These designs are reported to reflect less than -15 dB over a bandwidth of 2-18 GHz. FSS's are printed using silk screening and result in conductors ca 0.18 inches thick on Mylar sheets 0.03 inches thick. Resistances of the conductive elements ranged from 0.04 to 1.5 ohms/square. It also has been reported^[22] that the use of vapour deposited resistive sheets, optical masking and etching produced much better control over reproducibility. Another patent discusses a novel polymeric material blended with conducting materials such as carbon, metal powder, ferrites or conducting polymers.^[123] The conductivity of this material was controlled and holes punched in the material with a certain period. Several of these layers were arranged into a metal terminated device and the reflectivity measured. The effect of conducting disks has been considered.^[124] An array of conducting disks will increase the effective thickness of an absorber by introducing a capacitive admittance. The resonant thickness of the layer decreases as the disk diameter increases to the periodicity of the disks. Thinner absorbers are achievable with the same bandwidth. The capacitance of

an array of disks is frequency dependant and harmonics are eliminated. Two layer Jaumann devices made with disks were also shown to reduce the absorber thickness. The effective permittivity of dielectric honeycombs has been studied. Mention is also made of dipole crosses and perforated materials.^[125]

FDTD methods have been used to model the reflectivity from a FSS.^[126] A checkerboard design of lossy dielectric and magnetic material was studied and indicated the possibility of achieving absorbers with better than -25 dB over a bandwidth of 5 to 40 GHz. Composite frequency selective surfaces laminated with radar absorbing material (a chopped carbon fibre layer) have been made and their reflectivity measured.^[127] The measured results were compared against theoretical predictions made using micro genetic algorithms.^[34] Fractal like FSS have been studied and optimised using genetic algorithms.^[128]

2.3.4 Magnetic RAM

Magnetic absorber have been based on carbonyl iron and hexaferrites. These materials have absorb in the MHz and GHz ranges. The resonance frequency is related to particle size. Optical properties of M-Type Hexaferrites have been measured and reflection losses calculated.^[129,130] These materials can be tuned to absorb at higher frequencies (5-20 GHz) based on particle size and sintering temperature. Optical parameters for a single layer of carbonyl iron loaded in polychloroprene rubber have been measured and then used to calculate the reflectance of this material. The results compared favourably with reflectivity measurements.^[131] Dallenbach layers have been patented based on ferrite materials.^[96] At least two layers with different absorption bands are used to increase the absorption bandwidth. They have also been patented based on silicone rubber sheets filled with silicon carbide, titanium dioxide and carbon black.^[98] The bandwidth of standard ferrite absorbers have been improved through a two layer absorber design, with a ferrite layer at the air/absorber interface and a layer containing ferrite and short metal fibres at the absorber/metal interface. The fibre length is chosen to have a frequency near the required absorption frequency f_o , (ie for 8-13 GHz the fibre length was 1-4 mm for 60 μ m diameter wire). The impedance of the wires shifts from being capacitive when the frequency is less than f_o of the fibres, to inductive for $f > f_o$. Impedance is at a minimum at f_o and the induced current is at a maximum. Between f_o and $\frac{1}{2} f_o$ the fibre has a capacitive reactance and for $f < \frac{1}{2} f_o$ the fibre resistance becomes small and the reactance is capacitive only. At f_o the fibre length is nearly $\frac{1}{2} \lambda$ in the matrix.^[99] The ferrite layer acts as an impedance matching layer as well as absorber. Performance is better than -20 dB over 8-12 GHz and up to 45 degrees with an overall thickness of 4.6 mm.

2.3.5 Adaptive RAM (Dynamically adaptive RAM)

The potential to make adaptive absorbers has been explored. Mechanical devices that change the spacer thickness using a lossless dielectric fluid filled cell behind the resistive sheet have been explored, (see GB patent 9302394.3 1993). More practical methods have looked at tuning the absorption by changing the sheet impedance.^{[85-}

89,132-138] [22] This methodology is akin to circuit analog materials where the capacitance and resistance of the impedance sheet can be tuned.

2.4 Recursion Relationship for Calculating the Reflectivity

The following is a simple procedure for calculating the reflectivity from a multilayer material. Each layer is defined by three parameters: the thickness, complex permittivity and permeability, Figure 2.9. A recursion formula is used to calculate the reflectivity at the air/absorber interface. In this strategy the layers are numbered 1 to n starting at the first layer next to the perfect electrical conductor, PEC, and the interfaces are numbered 0 to n starting at the PEC/first layer interface (Figure 2.9). The recursion formula, expressed below, starts by calculating the reflectivity from interface $i = 1, 2, 3, \dots, n$, where at interface n the reflectivity coefficient from the whole absorber, is obtained.

$$\Gamma_i = \frac{\tilde{\Gamma}_i + \Gamma_{i-1} e^{-2jk_{i-1}t_{i-1}}}{1 + \tilde{\Gamma}_i \Gamma_{i-1} e^{-2jk_{i-1}t_{i-1}}} \text{ for } i > 0 \quad 2.9$$

where k_i is the component of the wave vector normal to the interface,

$$k_i = 2\pi f \sqrt{\mu_i \varepsilon_i - \sin^2 \theta_i} \quad 2.10$$

$\tilde{\Gamma}_i$ is the reflection coefficient from interface i, and is dependent on the polarisation such that

$$\tilde{\Gamma}_i^{TE} = \frac{\mu_{i-1} k_i - \mu_i k_{i-1}}{\mu_{i-1} k_i + \mu_i k_{i-1}} \text{ for } i > 0 \quad 2.11$$

$$\tilde{\Gamma}_i^{TM} = \frac{\varepsilon_i k_{i-1} - \varepsilon_{i-1} k_i}{\varepsilon_i k_{i-1} + \varepsilon_{i-1} k_i} \text{ for } i > 0 \quad 2.12$$

For the PEC/first layer interface,

$$\tilde{\Gamma}_i^{TE/TM} = -1 \text{ for } i = 0. \quad 2.13$$

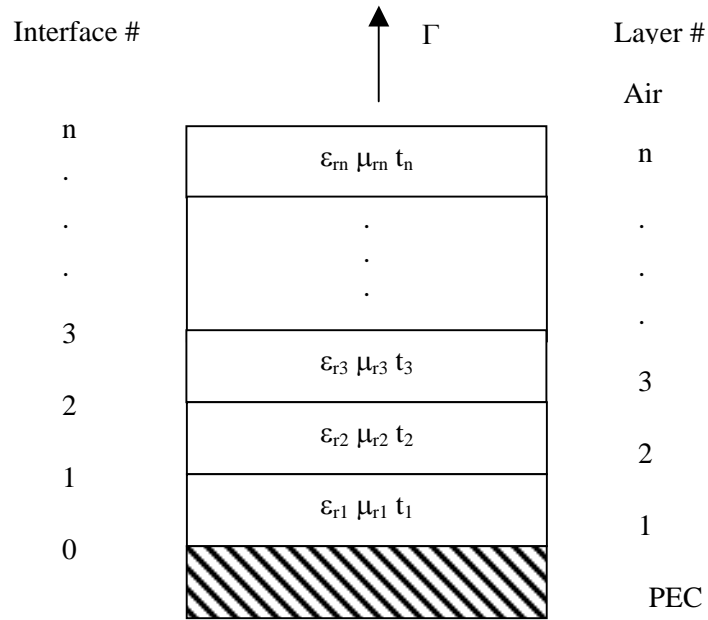


Figure 2.9. Reflectivity from Jaumann absorber layers

2.5 Transmission Line Theory

Transmission Line theory, has been used to model and optimise absorbers and essentially follows the logic of the previous section. A multisection transmission line is shown in Figure 2.10. The layer electrical lengths, L , are given by

$$L_i = \frac{n_i l_i}{\lambda_o} = \frac{l_i}{\lambda_i}, \quad \text{for } i = 1, 2, \dots, M. \quad 2.14$$

where λ_i is the wavelength of section i .

The phase thickness of a section, δ , is then

$$\delta_i = \beta_i l_i = 2\pi L_i \frac{f}{f_o} = 2\pi L_i \frac{\lambda_o}{\lambda}, \quad \text{for } i = 1, 2, \dots, M. \quad 2.15$$

The wave impedances, \bar{Z}_i , are continuous across the interfaces and are related by the recursion relationship

$$\bar{Z}_i = Z_i \frac{\bar{Z}_{i+1} + jZ_i \tan \delta_i}{Z_i + j\bar{Z}_{i+1} \tan \delta_i}, \quad \text{for } i = M, \dots, 1. \quad 2.16$$

The recursion is started with $\bar{Z}_{M+1} = Z_L$. The reflection coefficients from the left of each interface are then

$$\Gamma_i = \frac{\bar{Z}_i - Z_{i-1}}{\bar{Z}_i + Z_{i-1}} \quad 2.17$$

and the values of Γ_i are obtained by the recursion relationship

$$\Gamma_i = \frac{\rho_i + \Gamma_{i+1} e^{-2j\delta_i}}{1 + \rho_i \Gamma_{i+1} e^{-2j\delta_i}}, \quad \text{for } i = M, \dots, 1. \quad 2.18$$

The recursion is started at $\Gamma_{M+1} = \Gamma_L = \frac{Z_L - Z_M}{Z_L + Z_M}$, and ρ_i is the reflectivity coefficient at the interface, calculated from

$$\rho_i = \frac{Z_i - Z_{i-1}}{Z_i + Z_{i-1}}, \quad \text{for } i = 1, 2, \dots, M+1, \text{ and } Z_{M+1} = Z_L. \quad 2.19$$

When the load at the end of the transmission line is a short circuit, $Z_L = 0$.

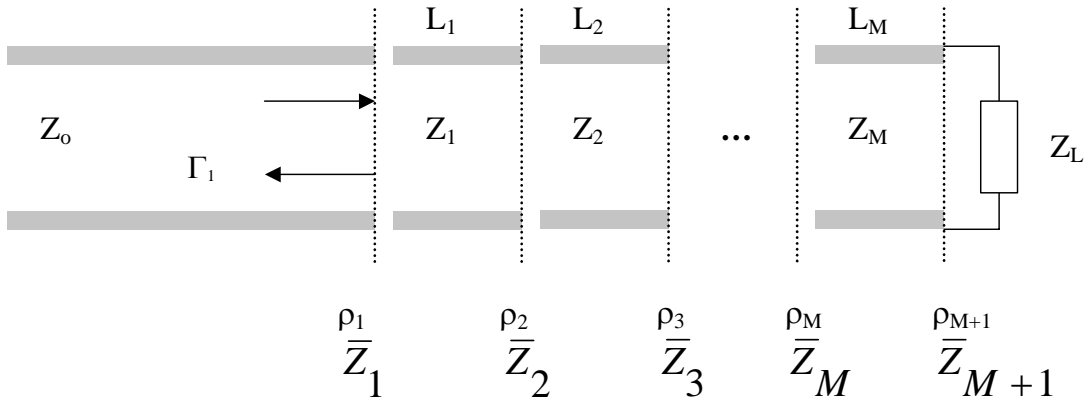


Figure 2.10. Multisection transmission line.

2.6 Techniques for Optimisation of Radar Absorbing Materials

The absorption of microwaves by a material depends on the properties of the material and its structure. One technique used to produce low reflectivity is to match the impedance of the electromagnetic radiation at the air-absorber interface, allowing the electromagnetic radiation to propagate into the absorber. Another technique used is to create destructive interference between the electromagnetic waves reflecting from different layers of the absorber. This class of absorbers are called resonant absorbers with examples being Dallenbach layers, Salisbury Screens and Jaumann layers. The reflectivity from these absorbers can be calculated if the thickness, permittivity and permeability of all layers are known. The procedure is to calculate the reflection and transmission coefficients for each layer, based on the permittivity and permeability, and then recursively propagate the electromagnetic field through the absorber. One technique used for microwave reflection from radar absorbers on perfect electrical conductors, PEC, is the recursion formulation.^[139] In this case the recursion analysis starts at PEC surface and works back through the absorber to the air/absorber interface.

Although it is possible to calculate the reflectivity from an absorber, it is only feasible to analytically solve for the optimum absorber properties over a few layers.^[27,140] Multilayer structures are described by a large number of variables and the mathematics become too complex to solve. Some strategies have been proposed for creating good absorbers by grading the impedance of the layers,^[27,28] however, these are not the optimum absorbers that can be achieved, in terms of minimum reflection over the widest possible bandwidth.

Numerical optimisation techniques can be used for solving for the best absorber.^[29,140] Techniques such as Conjugate Gradient, Quasi-Newton and Simplex methods tend to find local minima and do not work well if the objective functions are non differentiable or discontinuous. These methods tend to be dependent on the starting point/initial guess used. More global techniques include Random Walk, Simulated Annealing and Genetic Algorithm methods. These techniques do not take advantage of local solution-space information, resulting in slower convergence. The convergence, however, is near to the global minimum.

In this paper optimisation techniques for absorber design are reviewed with a focus on Genetic Algorithm methods. The Genetic Algorithm is reviewed along with objective functions that have been applied to absorber design. In the next sections three types of layered absorbers are reviewed. The simplest is the single Dallenbach layer, while the Salisbury Screen consists of two layers, a resistive sheet and a low dielectric spacer. Multiple Salisbury Screens stacked together form the Jaumann absorber.

2.6.1 The Dallenbach Layer

The Dallenbach layer is a resonant absorber that also uses the bulk of its material for absorption. A number of the Dallenbach layers specifically incorporate magnetic materials, or a combination of conductive and magnetic. Design curves for

permittivity and permeability values have been calculated.^[100,102] The Kramers-Kronig relationship has been investigated to see if it places a limitation on the bandwidth of Dallenbach layers.^[95] This study also attempted to use simulation to determine the maximum bandwidths achievable for multilayer (Dallenbach) absorbing structures. The ultimate thickness to bandwidth ratio for a radar absorber has been analytically calculated.^[104] Multilayer Dallenbach devices have been designed using a Lagrangian optimization method with constrained variable.^[101] A general solution for a single layer absorber is given along with design curves.^[102]

2.6.2 Salisbury Screen

The Salisbury Screen (patented 1952)^[13] is the simplest layered resonant absorber consisting of a resistive sheet placed an odd multiple of $\frac{1}{4}$ wavelengths in front of a metal (conductive) backing, separated by an air gap (Figure 2.5). A low dielectric material is often used to replace the air gap, reducing the gap thickness at the expense of bandwidth. The Salisbury Screen has been examined in terms of transmission line theory. The quarter wavelength transmission line transforms the short circuit at the metal into an open circuit at the resistive sheet. The effective impedance of the structure is the sheet resistance. If the sheet resistance is 377 ohms/square (ie the impedance of air), then good impedance matching occurs and a reflective null appears at a frequency corresponding to the spacer thickness. The magnetic analogue of the electrical screen would place a magnetic layer on the metal surface, resulting in a thinner device.^[5,27] Initial Salisbury Screens were made of canvas on plywood frames with a colloidal graphite coating on the canvas.^[14]

2.6.2.1 Optimised Design of Salisbury Screens

Several strategies have been used for the design of the Salisbury screen.^[27,141] The thickness of the optimal Salisbury screen can be calculated when the sheet resistance is equal to the impedance of free space (Z_0). The absorber thickness is given by

$$d = \frac{1}{Z_0 \sigma} \quad 2.20$$

where σ is the conductivity of the sheet. Two approximations are made regarding the resistive layer: The first is that the layer is electrically thin ($1 \gg k_0 d \sqrt{|\epsilon^*|}$ where k_0 is $2\pi/\lambda_0$ and d is the resistive layer thickness), and the second approximation is that the loss in the layer originates from the conductivity and $\epsilon'' \gg \epsilon'$.^[141] For practical devices these approximations may not be realistic with the result that the resonant frequency shifts to smaller values as the resistive sheet thickness, or ϵ' is increased. This was shown using a transmission line model with a RCL circuit representing the Salisbury screen.^[141] The thickness of the resistive sheet for optimum absorption has an inverse relationship to the sheet conductivity.^[8]

The bandwidth of Salisbury Screens can be maximised given the maximum acceptable reflectivity.^[142] The optimum sheet resistance was calculated to be 377 ohms/sq for the lowest reflectivity, while the optimum resistance, R_{sopt} , for a given reflectivity limit is given by

$$R_{sopt} = Z_o \frac{1 - \Gamma_{cutoff}}{1 + \Gamma_{cutoff}} \quad 2.21$$

where Γ_{cutoff} is the maximum acceptable reflectivity. Analytically it was also shown that bandwidth decreases with increasing permittivity of the spacing layer.

2.6.3 Jaumann Layers

Jaumann layers are a method of increasing the bandwidth of the Salisbury screen, the simplest form of a Jaumann device. The number of layers is proportional to the bandwidth of the absorber. For instance, a device consisting of two equally spaced resistive sheets in front of a conducting plane (Figure 2.6) was mathematically shown to produce two minima in the reflectivity, increasing the absorber's bandwidth over the Salisbury screen.^[1] A seven layered Jaumann device consisting of resistive sheets, with increasing conductivity towards the metal plane, and separated by uniformly thick low loss dielectric sheets was also described and the reflectivity calculated.^[1]

2.6.4 Optimisation of Jaumann Layers

Optimisation of Jaumann absorbers is complex due to the number of parameters involved, which increase as the number of layers increase. Empirical procedures and numerical optimization techniques^[28] have been used for designing Jaumann absorbers.

Two analytical techniques have been used to optimise Jaumann absorbers up to a stack of three resistive sheets. These techniques are called the Maximally Flat or binomial design and the Tschebyscheff polynomial, or equal-ripple design after the shape of the reflectivity curve.

2.6.4.1 Maximally Flat Design

The objective of maximally flat design, or binomial expansion, is to have the flattest possible bandpass in the frequency region of interest. This is achieved by stacking up several Salisbury screens.^[27] An approximate expression for such a quarter wave stack is

$$\Gamma = \Gamma_0 + \Gamma_1 e^{-2j\theta} + \Gamma_2 e^{-4j\theta} + \dots + \Gamma_n e^{-2nj\theta} = \sum_{n=0}^N \Gamma_n e^{-2nj\theta} \quad 2.22$$

where Γ_n is the reflection coefficient from an interface and

$$\theta = \beta_n d_n = \frac{2\pi}{\lambda_n} \frac{\lambda_{n_o}}{4} = \frac{\pi f}{2f_o}$$

The summation on the right hand side of equation 3 can be expanded in a Taylor series in frequency so that the form is $\Gamma = A + Bf + \dots$. It is desirable to have the

reflectivity at the center frequency of the band equal to zero, and $\frac{dR}{df} = 0$ for the flat

bandpass. The material properties are then solved for that set the coefficient A and B to 0. This technique has been extended to 3 resistive sheets and explored for magnetic and electric materials.^[27] The bandwidth was found to increase over that of the Salisbury screen and with the bandwidth increasing as the admittance of the spacer decreases. The bandwidth of an absorber, with an outer magnetic and inner electric screen, increases with admittance. For this case the reflectivity does not necessarily reach a maximum ($R=1$). With two magnetic screens, one on the surface of the conductor and one a distance in front of the conductor plane, the reflectivity is independent of the separation of the second magnetic layer if the normalized complex magnetic impedance is $1/Y$. This is due to the first screen absorbing all the radiation. However, there is a frequency dependence that requires the second screen for compensation and the bandwidth was calculated to increase. A three-screen Jaumann device was shown to have a larger bandwidth than the two-screen device. The three-screen device was also shown to reduce the reflectivity for incidence angles up to 60 degrees.

2.6.4.2 Tschebyscheff (Equal-Ripple) Design

In this design strategy the interference fringes from the quarter wavelength spaced resistive sheets are forced to approximate an equal amplitude ripple, with one ripple for each resistive layer. This is achieved by replacing the summation in equation 3 with a Tschebyscheff polynomial.^[140]

$$\Gamma = e^{-jN\theta} \frac{T_N \sec \theta_m \cos \theta}{T_N \sec \theta_m} \quad 2.23$$

where

$$T_N \sec \theta_m = p_m^{-1} \quad 2.24$$

p_m is the ripple magnitude in dB, N is the number of ripples and layers,

$$\theta = \frac{\pi}{2(1+F)} \text{ and } F = \frac{f - f_o}{f_o}.$$

This method yields a wider bandwidth than the corresponding maximally flat solution. Tshebyscheff polynomials are also used to optimize the bandwidth of a Jaumann device.^[140] This study showed that choosing the optimal spacer had a big influence on the bandwidth of the absorber. The Tshebyscheff technique has also been applied to the design of tapered absorbers.^[90]

2.6.4.3 Gradient Methods

The analytical approach of using binomial, maximally flat design and polynomial, Tshebyscheff design was only found to be suitable up to a stack of 3 and 5 resistive sheets, respectively. For larger stacks up to 20 resistive sheets a Newton-Raphson method is used to solve for maximally flat and equi-ripple designs.^[28,29] The optimum maximum relative dielectric constant of the spacer tends to 1.0 as the number of layers increases.

The optimal control method has been used to optimise absorber design and has been compared to solutions from simulated annealing for the purpose of overcoming local optimum traps.^[143] In simulated annealing the coating is subdivided into a large number of thin layers with fixed thicknesses. Each layer is assigned a material chosen from a predefined set of available materials. The optimal solution is found through iterative random perturbations of the material. Choices for each layer and evaluations are based on the metropolis criterion. This optimization technique usually leads to thinner, less reflective material than the optimal control approach.

A number of objective functions were formulated for optimizing the absorber properties. For instance the objective function for reflectivity performance of an absorber, OF , could be the mean reflectivity evaluated across the frequency band

$$OF = \frac{1}{n} \sum_{i=1}^n R(f_i) \quad 2.25$$

where R is the reflectivity as a function of the frequency, f_i , and n is the number of frequency points across the band. A variation on this objective function is to optimise the reflectivity in comparison to a target reflectivity, R_c ,

$$OF = \frac{1}{n} \sum_{i=1}^n |R(f_i) - R_c(f_i)| \quad 2.26$$

A final objective function, includes weights for different regions of the frequency spectrum

$$OF = \sum_{i=1}^n p_i |R(f_i) - R_c(f_i)| \quad 2.27$$

where $\sum p_i = 1$ and $p_i > 0$. This function permits the reduction in reflectivity for different frequencies.

If more than one objective function is to be optimised for then a weighting factor, α , is used to combine the weighting factors into a single expression,

$$OF = \alpha OF_1 + (1 - \alpha) OF_2 \quad 2.28$$

Modified Powell Algorithm (does not rely on explicit gradient information)

All these methods rely on local characteristics and so converge to local optima.

2.6.4.4 Optimisation of Jaumann Layers: Genetic Algorithm

The above optimization methods have produced significant increases in bandwidth and reduction in reflectivity. These methods, however, do not produce the optimal absorbing material, based on a number of factors such as minimum thickness or weight, or whether the solution is a local or global minimum. For these reasons, the Genetic Algorithm (GA) has been investigated as an optimization technique for RAM. Use of the GA is explored in this section and the GA method is reviewed in Section 4.

A review of the use of genetic algorithms in engineering electromagnetics provides a good description of the genetic algorithm with some examples including the design of microwave absorbers.^[38] Genetic Algorithms were first used in 1993 for the optimization of Jaumann absorbers^[144-146] and built on the approaches used for the optimal control method.^[143] A set of available materials, their frequency dependent optical properties (permittivity and permeability), and the layer thicknesses were used to define a population of absorbers. A genetic algorithm was used to optimise the absorber design against objective functions including reflectivity, thickness and weight. Both TE and TM polarisations of the reflection coefficient were calculated as well, in order to optimise the absorber as a function of incident angle as well. The reflectivity was calculated using a recursion relationship and the permittivity, permeability of the materials. Pareto fronts for the thickness vs reflectivity were presented.^[139] Several Pareto Genetic Algorithms were compared with the non-dominated sorting genetic algorithm, NSGA, producing the best results.^[139]

The genetic algorithm has also been used to optimise Jaumann absorbers based on transmission line theory.^[88,147-150] Absorber bandwidth was shown to increase rapidly as a function of the number of resistive layers before asymptotically approaching the maximum bandwidth as the layer number approached infinity.^[149] The optimum sheet resistance profile, assumed to have an exponential form,^[30] was shown to have a sigmoid form with the resistance of the outer layers asymptotically approaching a maximum sheet resistance.^[88,147,149] In these studies the bandwidth was studied as a function of both polarisations so that the absorbers could be optimized for incident angle as well. The bandwidth was defined as

$$BW = 2 \frac{(f_u - f_l)}{(f_u + f_l)} \quad 2.29$$

and the objective function for the combined polarisations as

$$OF = \frac{BW_{//} BW_{\perp}}{(|BW_{//} - BW_{\perp}| + 1)} \quad 2.30$$

The optimised bandwidth for both polarisations was found to be less than that for normal incidence or one polarisation. At oblique incidences up to about 30 degrees the optimum bandwidth was found to remain fairly constant (near the value at normal incidence) before decreasing.^[88] It was found that a two-stage strategy was useful in optimising absorber design. In the first stage an objective function based on the sum of the reflectivity below -20 dB was used to ensure that the -20 dB bandwidth was non-zero. Then in stage two, objective function sought to maximize the bandwidth and ensure that the reflectivity was still below -20 dB.^[88] Absorbers with a protective skin were also optimised^[88] and it was found that with proper choice of the outer layer material the absorber acted as if it had another resistive sheet and therefore had a wider bandwidth. With more than two resistive sheets, shinned absorbers could not be optimised below the -20 dB reflectivity limit, though the bandwidth could be improved for higher reflectivity targets.

The design of active (dynamic) radar absorbers has been investigated by using the genetic algorithm to optimise the absorption over different frequency bands by varying the sheet resistance, the spacer thickness or the spacer permittivity.^[88]

Resistive sheets with capacitive properties have been used for making absorbers.^[109] The optimal design of resistive-capacitive material based microwave absorbers has been studied using the genetic algorithm and transmission line theory.^[36,151] The use of adaptive mutation has been explored to get out of local minima and to protect designs that are near the global minimum.^[37] The genetic algorithm was also applied to the design of magnetic Dallenbach layers.^[152]

A unique absorber design has been proposed and optimised using a genetic algorithm, where patches of material are organised to form a sheet.^[153] These patches are either of the same material with different thicknesses or different materials with the same or different thicknesses.

A variant of the genetic algorithm, the microgenetic algorithm has been used for optimising frequency selective surfaces and circuit analog absorbers.^[34,35,154] The microgenetic algorithm uses a small randomly generated population for optimisation in the usual manner for a genetic algorithm. Convergence occurs in a few generations and the fittest individual is added to those from previous generations. A new population is then randomly selected. Narrow band Salisbury Screens with circuit analog patterns replacing the resistive sheet have also been considered.^[155-157]

2.6.4.5 Optimisation of Jaumann Layers: Other methods (Finite Element, FDTD and Taguchi Methods)

Scattering from cylindrical absorbers has been modelled using finite element method, FEM, and for single layer Jaumann (Salisbury Screen) the numerical method gives results similar to the analytic result.^[158]

Preliminary FDTD calculations of the RCS of tapered Salisbury Screens and Jaumann layers have shown that the performance of these devices is not limited by resonant behaviour.^[159]

The Taguchi method of optimization was used as a means of exploring less parameter space to explore the sensitivity and interaction of parameters in the design of planar and curved Jaumann Absorbers.^[160]

2.7 Absorbing Materials

Many of the early materials included conductive carbon or metal powder formulations as these were readily available conducting materials.

2.7.1 Carbon

Absorbers for anechoic chambers were originally made, by coating mats of curled animal hair with carbon black impregnated neoprene. The front surface has then been moulded into geometric forms (ie pyramids) or the amount of lossy material was increased as a function of depth into the mat by dipping.^[1,17] Carbon black and fibrous carbon has been incorporated into Dallenbach layers.^[10,14,25,98]

Percolation networks of randomly distributed graphite-type microsphere inclusions have been theoretically studied as a function of permittivity and frequency for RAM applications.^[161] Multiple-scattering effects were noted to increase the effective absorptivity through scattering losses.

2.7.2 Metal and Metal Particles

Broad band absorbers have been made from solid aluminum metallic particles or dielectric filled metallic shells in the shape of spheroids (oblate or prolate) dispersed in a matrix.^[162] Iron oxide, powdered iron, powdered aluminum and copper, steel wool, water, powdered “Advance” and “Constantin”, evaporated metal or nickel chromium alloy and metal wires.^[19,25]

2.7.3 Conducting Polymers

In a polymer such as polypyrrole, partial oxidation of the polymer (doping) causes it to become conducting through the formation of polarons and bipolarons; the charge carriers along the chains. The conductivity of a conducting polymer is modelled by phonon assisted hopping between the randomly distributed localized states (that result from the partial oxidation).^[163]

One of the inherent problems with conducting polymers is that they are typically intractable. Some of them can be compressed into shapes, such as polyaniline, PANI. Formation of composites with thermoplastic materials is another method. Polypyrrole, PPy, has been polymerised on the surface of PVA, PVC and within it to form composites. Emulsion polymerisation has also been used. PANI is soluble in solvents such as DMF, or the solubility of monomers has been increased by chemical modification though usually at the expense of conductivity. Textile materials have been used as substrates for a number of materials and have been coated with conducting polymers by soaking them with oxidant and then exposing them to monomer.^[52] This procedure was also reversed soaking in the monomer and then adding oxidant.^[72] The first investigation of PANI and PPy deposition onto fabric by an *in situ* polymerization technique was reported in 1989.^[59]

2.7.4 Polypyrrole

Polypyrrole by itself does not have great physical properties and so most of the useful materials are composites of polypyrrole and other materials such as latex, fibres or polymer blends. Polypyrrole finds great use due to its relative stability in air.

2.7.4.1 Polypyrrole-Polymer Composites

The frequency response of polypyrrole-PMMA composites has been studied in the range of 10 kHz to 8 GHz.^[164] The imaginary component of the permittivity, and hence the conductivity, were observed to be frequency dependent. At low frequencies, below 10^5 Hz, the conductivity displays percolative behaviour and does not depend on the frequency. Subtraction of the direct current conductivity reveals a relaxation at frequencies up to 10^9 Hz. This work shows the dependence of the imaginary component of the permittivity on the ac and dc conductivity. At frequencies above 1 GHz, the conductivity is dominated by the ac conductivity resulting from the hopping mechanism of charge transport in the conducting polymer. It was shown that the ac conductivity in the composites is an intrinsic property of the conducting polymer independent of the polypyrrole concentration.

One of the few references that presents permittivity, conductivity and reflectivity data for polypyrrole, shows that processing has a great effect on the final product.^[165] Polypyrrole/PVC composite was compressed and melt injected into sheets. The compressed material was macroscopically conductive with $\epsilon'' \propto K\omega^{-s} = \frac{\sigma(\omega)}{\omega\epsilon_0}$,

where K is a constant and the conductivity is frequency dependent. The melt-injected material was macroscopically insulating with Maxwell-Wagner type relaxation. The relaxation frequency is given by $f_r = \frac{\sigma_2}{2\pi\epsilon_o(2\epsilon_1' + \epsilon_2')}$, where the subscript 1 denotes the properties of the matrix and 2 the conducting phase. The compressed material is difficult to make into a tuned absorber, while the melt injected material readily forms a resonant Dallenbach layer.^[165] This material shows a very narrow absorption with more than -40 dB reflectivity.

Dallenbach layers have also been made from polypyrrole doped with *p*-toluene sulphonic acid sodium salt, or 5-sulfosalicylic acid dehydrate.^[81,166] The chemically prepared powder was dispersed in a commercial paint, or milled with natural rubber and moulded into flat sheets and both were applied to an aluminum backing panel. These materials show resonance absorption if the content of the conductive powder is not below the percolation threshold. The percolation threshold for these materials was 2-4% due to the high aspect ratio of the PPy. Mixing was noted to destroy the fibrous nature, resulting in thresholds up to 16%. The rubber composites, and inclusion of conducting fibres that did not produce a macroscopically conductive material, still had a reasonable high value of ϵ'' and were therefore useful in making Dallenbach layers. A hybrid dielectric/magnetic material was also made using carbonyl iron, however, extra bandwidth was not realised for this material.^[81,166] Powder processing was noted to have an influence on the final material properties.

Materials with conductive gradients have been made.^[166] Phenolic foam, with a pore size on the order of 1 μm , was soaked in aqueous ferric chloride and then exposed to pyrrole vapour from one side. The gradient was obtained by controlling the exposure time. Uniformly coated foam was prepared by immersing the oxidant doped foam in an aqueous pyrrole solution and flowing the pyrrole solution through the foam. The permittivity of the foam was measured and showed very low values of ϵ_r' in the range of 1-2 and good values of ϵ_r'' in the range of 0.5-10. Two problems are associated with vapour polymerization, a thick coating on one surface of the foam and poorly conducting polymer doped with chloride from the ferric chloride. The wet method produced a material with better properties and a gradient could be induced into the material. It was noted that a 15 mm thick foam prepared in this manner^[166] performed better than other published gradient absorbers.^[25,167]

2.7.4.2 Polypyrrole-Fabric Composites

Several materials have been formed by polymerising pyrrole in the presence of a fabric or fibres. Pyrrole has been oxidatively polymerised with ferric chloride in the presence of paper (cellulose)^[52,168] to form a PPy coated paper composite. Through manipulation of the chemistry and deposition time, the electrical conductivity of the composite could be carefully controlled. Absorbers were fabricated from these

materials and measured.^[106] The same techniques have been applied to cotton and polyester fabrics.^[107] Modelling the phase and amplitude of reflected microwaves from the composite has allowed values of the resistance and capacitance of the fabric sheets to be determined as a function of fabric type and PPy loading.^[105-109] The resistance decreases with loading while capacitance increases to maximum at about 2 to 3 mg cm⁻². At low loadings the PPy coating is smooth (hence decrease in R and increase in C). At higher loadings the coating becomes more particulate results in short circuits between fibres (hence a decrease in C).^[105] Another feature of the PPy-fabrics occurs when asymmetrical weaves are used. This results in different properties based on the polarisation of the microwaves to the weave.^[105] The use of polypyrrole coated fabrics (including glass fibres) enables the formation of structural RAM. The properties of the fabric-coated materials were modelled and made as Salisbury Screens and Jaumann layers.^[105,108,109]

PPy-fabrics have been marketed by Milliken & Company under the trademark Contex®. These have been used as nets for microwave attenuation (trademark Intrigue®)^[67] and as Salisbury screens and Jaumann absorbers.^[108] Other applications have been realised by patterning the polypyrrole by changing its conductivity.^[50,75] This has been used for “edge-card” materials in low observable aircraft.^[60]

The stability of PPy coated PET and PVA fibres for use as microwave and millimeterwave obscurants have been studied for environmental concerns.^[169]

2.7.4.3 Conducting Polymer Latex

Conducting polymer latex falls into two categories, pure latex and core-shell latex where a conducting polymer shell is coated onto an existing non-conducting latex core. Another area that falls into this general subject heading is that of conducting polymer nanocomposites which have been reviewed.^[170]

Methylcellulose has been used to stabilise chemically formed polypyrrole, resulting in small particles dispersed in a methylcellulose matrix.^[171] Similarly, PPy-Polystyrene sulfonate particles have been made by oxidizing pyrrole in presence of Fe³⁺.^[172] The size of particles is controlled by the Fe:py ratio. Pure conducting polypyrrole lattices have been formed by the polymerization of the monomer in the presence of a steric stabilizer such as poly(vinylpyrrolidone), PVP, or poly (vinyl alcohol-co-acetate, PVA,^[173,174] poly (2-vinyl pyridine-co-butyl methacrylate,^[175] and a comprehensive study of a number of stabilizers.^[176] Poly(ethylene oxide), PEO, polyacrylic acid and various block copolymers based on PEO, failed to provide steric stabilization. PANI latex has also been made and forms needle shaped particles.^[177,178] Polypyrrole and polyaniline lattices and composite beads (PPy-PMMA) have been synthesized and cast into conducting films by mixing with a dispersion of a 1:1 copolymer of polymethylmethacrylate-polybutylacrylate.^[179] The PPy lattices were spherical and PANI lattices needle-like, giving percolation thresholds of about 20 and 5 wt% respectively. The surface energy of conducting polymers (PPy and PANI) is high, capable of strong interactions either via London dispersion or Lewis acid-base forces.^[180] For PPy, the surface energy decreases within a few days, which is not seen

for PANI. PMMA adsorbs to the PPy particles, forming a uniform coating when 1,4-dioxane is used as the solvent and a patchy coating when chloroform is used.

Conducting polymer-coated latex particles (core-shell) have been reviewed.^[181] Conducting polymers based on pyrrole, aniline and EDOT, polymerized with ferric chloride, APS and ferric tosylate. Core lattices discussed are PS and PU^[182,183]. Potential applications are found in anti-corrosion and anti-static coatings. High performance electrochromatography and novel marker particles for immunodiagnostic assays.^[184] PS/PANI core/shell lattices have been made in the presence of PVP,^[180,185] and SDS (sodium dodecyl sulfate).^[186] PPy deposits onto submicron poly (ethylene glycol) stabilized PS latex as nanoparticles, bridging the PS particles and causing flocculation.^[187] Other PANI/PS-co-PSS lattices have been made.^[188]

Nanocomposites of conducting polymers (PPy and PANI) and iron oxide magnetic particles have properties different from pure magnetic particles.^[189] Electrophoretic mobilities of glass beads coated with PPy in the presence of a nonionic surfactant Rhodasurf TB970, have been measured.^[190] 20 nm Silica colloidal particles have been coated with PPy,^[185] and PANI^[191,192]. Both of these produced agglomerates of silica and conducting polymer giving a raspberry like structure. Carboxylic acid derivatized polypyrrole-silica composites showed improved colloidal stability.^[193]

A reverse core-shell PPy/polyacrolein latex has been synthesized and studied by atomic force microscopy, AFM.^[194] The surface of the PPy particle was not completely covered by the polyacrolein.

2.7.5 Polyaniline

Polyaniline, PANI, is another inexpensive, simple to make, readily available conducting polymer that has suitable properties for the fabrication of an absorber. Polyaniline is slightly soluble and there are many derivatives of its monomer. Thus there is a large potential for tuning absorber properties with this material.

2.7.5.1 Polyaniline Fibres

Polyaniline has been used to coat glass fibre textiles^[58,59] and PET textiles.^[59]

2.7.6 Other Conducting Polymers

One of the first calculations showing that conducting polymers could be used for Salisbury Screens and Jaumann layers used the permittivities at 9.89 GHz of poly-p-phenylene-benzobis-thiazole and polyacetylene.^[111,112]

Bithiophene has been electropolymerised into a latex matrix deposited onto a conducting plate. It was also noted that the latex could contain magnetic particles and other polymers such as pyrrole would be effective.^[195]

2.7.7 Tubules and Filaments

Polypyrrole tubules have been synthesized chemically and electrochemically by growth within a pore or by using surfactant mediation. Pore templated growth of PPy tubes has been accomplished by polymerisation within the pores of porous alumina^[196] and polycarbonate^[197-200] membranes. Selective dissolution of the membrane results in PPy tubules. A two probe method for measuring the tubule resistance (conductivity) is given with conductivity decreasing for thicker tubes. The centres of the tubules tend to be filled with less well-ordered polymer.

A number of surfactant systems have been used to template the growth of polypyrrole tubules. A reverse microemulsion system using sodium bis(2-ethylhexyl) sulfosuccinate (AOT) was found to form nanotubes about 95 nm wide and up to 5 μm long.^[201] Naphthalene-2-sulphonic acid also acts as template for polypyrrole growth (chemical or electrochemical) with a range of morphologies dependent on the surfactant concentration.^[202,203] Diacetylenic phospholipid tubules template polypyrrole growth, however, it tends to be at the seams or edges of the lipid tubules, rather than coating the walls.^[204] Polymer fibrils have also been detected in electrochemical deposits with *p*-Toluene sulfonic acid as the dopant.^[205]

Radar absorbing materials can be formed by loading an insulating polymer matrix with conducting filaments or tubules. The length of the filaments should be less than $\frac{1}{2} \lambda$ of the median frequency to be absorbed. For these materials, ϵ' reaches a maximum as the loading increases and starts to fall off at the percolation threshold, where the composite becomes macroscopically conducting. ϵ'' increases with loading around the percolation threshold and continues to increase to a saturation value at high loading. This is due to the dependence of ϵ'' on the conductivity. For spherical particles the percolation threshold is about 33 volume percent according to an effective-mean field theory^[206]. For elongated particles, tubules or filaments, the percent conductive material required for percolation is considerably reduced. Some of these materials have been made from lipid derived tubules that were coated by electroless deposition of copper or nickel.^[207,208] Other tubule formation has been noted for polyaniline and polypyrrole where surfactant drives tubule formation^[209] and through templating reactions in ion etched polycarbonate microchannels.^[200]

2.7.8 Chiral Materials

A reasonable amount of work has been conducted on chiral inclusions in a matrix as a radar absorbing material. Dallenbach layers have been formulated with metal inclusions such as right or left handed metal wire helices.^[33,115,210] A helix is said to be chiral (ie it is not superimposable with its mirror image). Materials made with these chiral inclusions have been shown to be effective microwave absorbers and have been patented.^[33] The propagation constant for these materials is modified from isotropic materials due to the optical activity and circular dichroism of the material. A term is added for the chirality admittance similar to the permeability and permittivity,^[33]

which gives another method of fine tuning the reflectivity. Chiral materials have the effect of rotating linearly polarized electromagnetic radiation to the right or left as it passes through the media and this has been noted for microwaves.^[115,210] The chirality of the material has been thought to lead to enhanced loss and greater design capability due to the chirality parameter β . This parameter is complex similar to the permittivity, ϵ^* , and permeability, μ^* , and results in a variation of the Maxwell equations (Drude-Born-Fedorov equations)

$$\mathbf{D} = \epsilon\mathbf{E} + \beta\epsilon\nabla \times \mathbf{E} \quad \text{and} \quad \mathbf{B} = \mu\mathbf{H} + \beta\mu\nabla \times \mathbf{H} \quad 2.31$$

The left and right fields propagate with different complex propagation constants which are expressed as

$$k_L = \frac{k}{1 - k\beta} \quad \text{and} \quad k_R = \frac{k}{1 + k\beta} \quad 2.32$$

k is the commonly expected propagation constant, which for $\mu_r = 1$, is

$$k = \omega\sqrt{\epsilon\mu} \quad 2.33$$

Spherical objects coated with absorber material including chiral inclusions have been studied theoretically with the conclusion that the radar cross section is lower than without the chiral material.^[211,212]

Theoretical^[213] and experimental^[115] studies of chiral materials concluded that chiral inclusions are not necessary in the formulation of RAM. The chiral and racemic mixtures both showed rotation and ellipticity, possibly from improper mixing of the racemic mixture. The decrease in reflectivity was slightly greater for the chiral medium, on the order of a few dB at the resonance point. Chiral materials will not produce thinner RAM than achiral materials.^[213] It was noted that the absorption properties of the chiral inclusion comes partly from the interaction of the electric field with the metal helices, producing a magnetic field through induction and hence a complex permeability. These materials could be classified as circuit analog.

More recently it is acknowledged that chiral inclusions are not necessary, however, helical inclusions can be useful in the design of microwave absorbers. Modelling and measurement of real absorbers are presented.^[214]

2.8 Shielding

Many of the materials discussed above can be used for shielding. For instance PET and PE fabrics coated with PPy or metal show utility as electromagnetic interference (EMI) shielding, giving between 20 and 80 dB depending on thickness and conductivity.^[68]

2.9 Conclusion

Many of the absorber structures considered here would be useful for military applications. Coatings in the form of Dallenbach layers, although not broadband, would be useful for reducing the RCS from intricate shapes. Jaumann layers would be appropriate for broadband lightweight absorbers or structural materials and a genetic algorithm should be used for design optimisation. If the military is to move to composite materials for ships or super structures then frequency selective surfaces and circuit analog absorbers should be embedded into the composite. Dynamic absorbers should be studied in order to counter frequency agile radars. Combined electric-magnetic materials offer the best potential for thin broadband absorption. Magnetic materials are limited to carbonyl iron and ferrites, raising a question of corrosion resistance. Conducting polymers are attractive electrical materials due to the potential for controlling their permittivity and permeability through synthetic means.

2.10 References

- (1) Severin, H. *IRE Trans. Antennas & Propagat.* **1956**, AP-4, 385.
- (2) Emerson, W. H. *IEEE Trans. Antennas Propag.* **1973**, AP-21, 484.
- (3) Vinoy, K. J.; Jha, R. M. *Sadhana* **1995**, 20, 815.
- (4) Petrov, V. M., Gagulin, V.V. *Inorganic Materials* **2001**, 37, 93.
- (5) Lederer, P. G. "An Introduction to Radar Absorbent Materials (RAM)," Royal Signals and Radar Establishment, Malvern, **1986**.
- (6) Gaylor, K. "Radar Absorbing Materials - Mechanisms and Materials," DSTO Materials Research Laboratory, **1989**.
- (7) Ruck, G. T. *Radar Cross Section Handbook*; Plenum Press: New York, **1970**; Vol. II.
- (8) Vinoy, K. J.; Jha, R. M. *Radar Absorbing Materials: From theory to Design and Characterization*; Kluwer Academic Publishers: Boston, **1996**.
- (9) Knott, E. F., Shaeffer, J.F., Tuley, M.T. *Radar Cross Section*, 2Rev. ed ed.; Artech House: Norwood, **1993**.
- (10) Machinerieen, N. V., FR Patent 802728. **1936**.
- (11) Halpern, O., US Patent 2923934. **1960**.
- (12) Halpern, O.; Johnson, M. H. J.; Wright, R. W., US Patent 2951247. **1960**.

- (13) Salisbury, W. W., US Patent 2599944. **1952**.
- (14) Neher, L. K., US Patent 2656535. **1953**.
- (15) Tiley, J. W., US Patent 2464006. **1944**.
- (16) Salati, O. M., CA Patent 507981. **1954**.
- (17) Tanner, H. A., US Patent 2977591. **1961**.
- (18) McMillan, E. B., US Patent 2822539. **1958**.
- (19) Pratt, B. C., US Patent 2992425. **1961**.
- (20) Meyer, E., Severin, H., Umlauf, G. *Zeitschrift fur Physik* **1954**, 138, 465.
- (21) Meyer, E., Severin, H. *Zeitschrift fur angewandte Physik* **1956**, 8, 105.
- (22) Munk, B. A. *Frequency Selective Surfaces: Theory and Design*; John Wiley & Sons Inc.: New York, **2000**.
- (23) Suetake, K., US Patent 3623099. **1971**.
- (24) Connolly, T. M.; Luoma, E. J., US Patent 4038660. **1977**.
- (25) Stubbs, H. V. G.; Wickenden, B. V. A.; Howell, W. G.; Perry, E. D., UK Patent GB 2058469A. **1981**.
- (26) Nahmias, M. E., US Patent 4030098. **1977**.
- (27) Fante, R. L.; McCormack, M. *IEEE Transactions on Antennas and Propagation* **1988**, 36, 1443.
- (28) du Toit, L. J.; Cloete, J. H. *Antennas & Propagation Society International Symposium, 1989. AP-S. Digest* **1989**, 3, 1558.
- (29) du Toit, L. J.; Cloete, J. H. *Antennas & Propagation Society International Symposium, 1990. AP-S. Merging technologies for the 90's. Digest* **1990**, 3, 1212.
- (30) Nortier, J. R., Van der Neut, C.A., Baker, D.E. *Microwave Journal* **1987**, 219.
- (31) Kasevich, R. S.; Broderick, F., US Patent 5223849. **1993**.
- (32) Van Der Plas, G., Barel, A., Schweicher, E. *Antennas and Propagation, IEEE Transactions on*, **1989**, 37, 1327.
- (33) Jaggard, D. L., Engheta, N. *Elect. Lett.* **1989**, 25, 173.

- (34) Chakravarty, S.; Mittra, R.; Williams, N. R. *Microwave Theory and Techniques, IEEE Transactions on* **2001**, *49*, 1050
- (35) Chakravarty, S.; Mittra, R.; Williams, N. R. *Antennas and Propagation, IEEE Transactions on* **2002**, *50*, 284
- (36) Cheldavi, A.; Kamarei, M. *Microwave Symposium Digest, 1997., IEEE MTT-S International* **1997**, *3*, 1555.
- (37) Foroozesh, A. R.; Cheldavi, A.; Hodjat, F. *Antennas, Propagation and EM Theory, 2000. Proceedings. ISAPE 2000. 5th International Symposium on* **2000**, 227.
- (38) Johnson, J. M.; Rahmat-Samii, Y. *Antennas and Propagation Magazine, IEEE* **1997**, *39*, 7.
- (39) Mosallaei, H.; Rahmat-Samii, Y. *IEEE Trans. Antennas Propag.* **2000**, *48*, 1594.
- (40) Weile, D. S.; Michielssen, E.? ?
- (41) Bornemann, J. *IEEE Trans. Antennas Propag.* **1993**, *41*, 1588.
- (42) Bristow, H. M.; Buckingham, J., GB Patent 665747. **1952**.
- (43) Broderick, J. F.; Tessier, N. J.; Heafey, M. S.; Kocsik, M. T., US Patent 5576710. **1996**.
- (44) Diaz, R. E.; McKinzie III, W. E., US Patent 6512494 B1. **2003**.
- (45) Simovski, C. R., Kondratiev, M., He, S. *Microwave And Optical Technology Letters* **2000**, *25*, 302.
- (46) Terracher, F.; Berginc, G. *Antennas and Propagation Society International Symposium, 2000. IEEE* **2000**, *2*, 846.
- (47) Topsakal, E., Volakis, J.L., Ross, D.C. *Antennas & Propagation Society International Symposium, 1999. IEEE* **1999**, *3*, 1832.
- (48) Kasevich, R. S.; Kocsik, M.; Heafey, M., US Patent 5214432. **1993**.
- (49) Wright, R. W.; Wright, J. W., US Patent 3887920. **1975**.
- (50) Adams, L. W.; Gilpatrick, M. W.; Cuddihee, M. E., US Patent 5292573. **1994**.
- (51) Barry Jr., C. N., U.S. Patent 5,176,851. **1993**.
- (52) Bjorklund, R. B.; Lundstroem, I. *J. Electron. Mat.* **1984**, *13*, 211.

- (53) Child, A. D., Patent 5,833,884. **1998**.
- (54) Child, A. D.; DeAngelis, A. R., US Patent 6001749. **1999**.
- (55) Collins, G. E.; Buckley, L. J. *Synth. Met.* **1996**, 78, 93.
- (56) DeAngelis, A. R.; Childs, A. D.; Green, D. E., Patent 5,624,736. **1997**.
- (57) DeAngelis, A. R.; Childs, A. D.; Green, D. E., US Patent 5,720,892. **1998**.
- (58) Genies, E. M.; Petrescu, C.; Olmedo, L. *Synth. Met.* **1991**, 41-43, 665.
- (59) Gregory, R. V.; Kimbrell, W. C.; Kuhn, H. H. *Synth. Met.* **1989**, 28, C823.
- (60) Gregory, R. V.; Kimbrell, W. C.; Cuddihee, M. E., US Patent 5162135. **1992**.
- (61) Kim, S. H.; Seong, J. H.; Oh, K. W. *J. Appl. Poly. Sci.* **2002**, 83, 2245.
- (62) Kim, M. S.; Kim, H. K.; Byun, S. W.; Jeong, S. H.; Hong, Y. K.; Joo, J. S.; Song, K. T.; Kim, J. K.; Lee, C. J.; Lee, J. Y. *Synthetic Metals* **2002**, 126, 233.
- (63) Kuhn, H. H.; Kimbrell, W. C., US Patent 4,803,096. **1989**.
- (64) Kuhn, H. H.; Kimbrell, W. C.; Worrell, G.; Chen, C. S. *Tech. Pap. Soc. Plast. Eng.* **1991**, 37, 760.
- (65) Kuhn, H. H.; Kimbrell, W. C., US Patent 4,981,718. **1991**.
- (66) Kuhn, H. H., US Patent 5,108,829. **1992**.
- (67) Kuhn, H. H.; Child, A. D.; Kimbrell, W. C. *Synth. Met.* **1995**, 2139
- (68) Lee, C. Y.; Lee, D. E.; Joo, J.; Kim, M. S.; Lee, J. Y.; Jeong, S. H.; Byun, S. W. *Synth. Met.* **2001**, 119, 429
- (69) Liu, H., Clark, R., Yang, S. C. *Mat. Res. Soc. Symp. Proc.* **1998**, 488, 747.
- (70) Machell, G., Thomas, M.A., Patent 3,909,195. **1975**.
- (71) Marchant, S.; Jones, F. R.; Wong, T. P. C.; Wright, P. V. *Synth. Met.* **1998**, 96, 35.
- (72) Newman, P.; Warren, L.; Witucki, E., US Patent 4617228. **1986**.
- (73) Oh, K. W., Hong, K.H., Kim, S.H. *J. Appl. Poly. Sci.* **1999**, 74, 2094.
- (74) Olmedo, L., Hourquebie, P., Jousse, F. *Synth. Met.* **1995**, 69, 205
- (75) Pitman, E. H., Kuhn, H.H., US Patent 5102727. **1992**.

- (76) Rhode, W., Sparks Jr., H.F., US Patent 6,253,581 B1. **2001**.
- (77) Rowe, P. E., Kocsik, M.T., U.S. Patent 6,043,769. **2000**.
- (78) Thieblemont, J. C.; Planche, M. F.; Petrescu, C.; Bouvier, J. M.; Bidan, G. *Synthetic Metals* **1993**, 59, 81.
- (79) Thieblemont, J. C.; Planche, M. F.; Petrescu, C.; Bouvier, J. M.; Bidan, G. *Polymer Degradation and Stability* **1994**, 43, 293.
- (80) Truong, V.-T., Ternan, J.G. *Polymer* **1995**, 36, 905
- (81) Truong, V.-T.; Riddell, S. Z.; Muscat, R. F. *J. Mat. Sci. Lett.* **1998**, 33, 4971.
- (82) Warren, L. F., Klivans, D.S., Maus, L., Patent 4,582,575. **1986**.
- (83) Wettermark, U. G., Worrell, G.H., US Patent 5,523,119. **1996**.
- (84) Woldanski, G. L., US Patent 6,231,794 B1. **2001**.
- (85) Tennant, A.; Chambers, B. *Smart Mater. Struct.* **2003**, 13, 122.
- (86) Chambers, B. Electromagnetic Structures Conference, **1995**, Nottingham, UK.
- (87) Chambers, B. *Electr. Lett.* **1996**, 32, 1711.
- (88) Chambers, B.; Tennant, A. IEE Proc. - Radar, Sonar Navig., **1996**.
- (89) Chambers, B. *Elect. Lett.* **1997**, 33, 529.
- (90) Gau, J.-R. J.; Burnside, W. D.; Gilreath, M. *Antennas and Propagation , IEEE Transactions on* **1997**, 45, 1286.
- (91) Jiang, Y., Martin, A.Q. *Antennas & Propagation Society International Symposium* **1999**, 4, 2622.
- (92) Jones, A. K., Wooding, E.R. *IEEE Trans. Antennas and Propagation* **1964**, AP-12, 508.
- (93) Dallenbach, W.; Kleinstuber, W. *Hochfreq. u Elektroak* **1938**, 51, 152.
- (94) Marouby, E., Gouy, J.P., Levrel, J.R. *Antennas & Propagation Society International Symposium* **1992**, 280
- (95) Wallace, J. L. *IEEE Transactions on Magnetics* **1993**, 29, 4209.
- (96) Mayer, F., US Patent 5872534. **1999**.

- (97) Perini, J., Cohen, L.S. *IEEE Transactions on Electromagnetic Compatibility* **1993**, 35, 223.
- (98) Timmerman, A. T., CA Patent 2026535. **2000**.
- (99) Hatkeyama, K.; Inui, T. *IEEE Trans. Magnetics* **1984**, MAG-20, 1261.
- (100) Musal, J. H. M.; Hahn, H. T. *IEEE Trans. Magnetics* **1989**, MAG-25, 3851.
- (101) Amin, M. B.; James, J. R. *Radio and Electron Engineering* **1981**, 51, 209.
- (102) Fernandez, A.; Valenzuela, A. *Electronics Letters* **1985**, 21, 20.
- (103) Hahn, H. T. *J. Appl. Phys* **1991**, 69, 6195.
- (104) Rozanov, K. N. *Antennas and Propagation*, *IEEE Transactions on* **2000**, 48, 1230.
- (105) Chambers, B.; Wong, T. C. P.; Anderson, A. P.; Wright, P. V. Proc. 15th Annual meeting of the antenna meas. Tech. Ass., **1993**, Dallas, US.
- (106) Wong, T. C. P.; Chambers, B.; Anderson, A. P.; Wright, P. V. *Elect. Lett.* **1992**, 28, 1651.
- (107) Wong, T. C. P.; Chambers, B.; Anderson, A. P.; Wright, P. V. Proc. 8th International Conference on antennas and propagation, **1993**, Edinburgh, UK.
- (108) Wong, T. C. P.; Chambers, B.; Anderson, A. P.; Wright, P. V. *Proc. 3rd Int Conf. on Electromagnetics in Aerospace Applications, 14-17 Sept 1993, Turin, Italy.* **1993**.
- (109) Wong, T. C. P.; Chambers, B.; Anderson, A. P.; Wright, P. V. Ninth International Conference on Antennas and Propagation, **1995**.
- (110) Chen, C. *Southeastcon '92, Proceedings., IEEE* **1992**, 1, 71.
- (111) Naishadham, K., Kadaba, P.K. *IEEE Transactions on Microwave Theory and Techniques* **1991**, 39, 1158.
- (112) Liao, W.-P. C., F.-L. *Microwave Theory and Techniques, IEEE Transactions on* **1996**, 44, 1188.
- (113) Sengupta, L. C.; Spurgeon, W. A. 6th Int. SAMPE Electronics Conference, **1992**.
- (114) Wright, P. V.; Wong, T. C. P.; Chambers, B.; Anderson, A. P. *Adv. Mat. Optics & Electronics* **1994**, 4, 253.

- (115) Kuehl, S. A., Grove, S.S., Kuehl, E., Bingle, M., Cloete, J.H. Manufacture of Microwave Chiral Materials and Their Electromagnetic Properties. In *Advances in Complex Electromagnetic Materials*; Kluwer Academic Publishers: Netherlands, **1997**.
- (116) Jacobs, I. *Bell System Technical Journal* **1958**, *37*, 913.
- (117) Chen, C.-C. *IEEE Transactions on Microwave Theory and Techniques* **1970**, *MTT-18*, 627.
- (118) Hall, R. C.; Mittra, R. *IEEE Trans. Antennas and Propagation* **1985**, *AP-33*, 1009.
- (119) Gross, F. B.; Kuster, E. J. *IEEE Trans. Antennas Propag.* **1987**, *AP-35*, 1492.
- (120) Tsao, C.-H., Mittra, R. *IEEE Trans. Antennas and Propagation* **1982**, *AP-30*, 303.
- (121) Tsao, C.-H., Mittra, R. *IEEE Trans. Antennas and Propagation* **1984**, *AP-32*, 478.
- (122) Kuhnhold, R., US Patent 2771602. **1956**.
- (123) Narang, S. C., Nigam, A., Yokoi, S.-I., Schmitt, R.C., Harker, K.J., McHenry, M.A., US Patent 5976666. **1999**.
- (124) Morris, S. B. *IEE Colloquium on low profile absorbers* **1992**.
- (125) Smith, F. C. *IEE Proc. Microwave Antennas Propagation* **1999**, *146*, 55.
- (126) Yu, W., Werner, D.H., Mittra, R. *IEEE Trans. Magnetics* **2001**, *37*, 3798.
- (127) Sha, Y.; Jose, K. A.; Neo, C. P.; Varadan, V. K. *Microwave and Optical Technology Letters* **2002**, *32*, 245.
- (128) Vinoy, K. J.; Jose, K. A.; Varadan, V. K.; Varadan, V. V. *Proceedings of the SPIE - The International Society for Optical Engineering* **2001**, *4334*, 176.
- (129) Sugimoto, S., Kondo, S., Okayama, K., Nakamura, H., Book, D., Kagotani, T., Homma, M., Ota, H., Kimura, M., Sato, R. *IEEE Transactions on Magnetics* **1999**, *35*, 3154.
- (130) Cho, H.-S.; Kim, S.-S. *IEEE Transactions on Magnetics* **1999**, *35*, 3131.
- (131) Pitman, K. C.; Lindley, m. W.; Simkin, D.; Cooper, J. F. *IEE Proc.-F* **1991**, *138*, 223.
- (132) Smith, F. C. *Electronic Letters* **2002**, *38*, 1052.

- (133) Chambers, B. *Elect. Lett.* **1994**, 30, 1626.
- (134) Chambers, B. *SPIE* **1997**, 3041, 590.
- (135) Chambers, B. *Smart Mater. Struct.* **1997**, 6, 521.
- (136) Chambers, B. *Electr. Lett.* **1997**, 33, 2073.
- (137) Chambers, B. *Smart Mat. Struct.* **1999**, 8, 1.
- (138) Chambers, B.; Tennant, A. *Electromagnetic Compatibility, IEEE Transactions on* **2002**, 44, 434
- (139) Weile, D. S.; Michielssen, E.; Goldberg, D. E. *IEEE Transactions on Electromagnetic Compatibility* **1996**, 38, 518
- (140) Liu, J.-C.; Ho, S.-S.; Bor, S.-S.; Lu, P.-C. *IEE Proc.-H* **1993**, 140, 414.
- (141) Lederer, P. G. IEE Colloquim on Low Profile Absorbers, **1992**.
- (142) Chambers, B. *Electr. Lett.* **1994**, 30, 1353.
- (143) Presque, J. J.; Bouche, D. P.; Mittra, R. *Microwave Theory and Techniques, IEEE Transactions on* **1992**, 40, 1789.
- (144) Michielssen, E.; Ranjithan, S.; Mittra, R. *Optoelectronics, IEE Proc.-J* **1992**, 139, 413.
- (145) Michielssen, E.; Sajer, J.-M.; Mittra, R. *IEEE* **1993**, 1167.
- (146) Michielssen, E.; Sajer, J.-M.; Ranjithan, S.; Mittra, R. *IEEE Transactions on Microwave Theory and Techniques* **1993**, 41, 1024.
- (147) Chambers, B.; Anderson, A. P.; Mitchell, R. J. Genetic Algorithm in Engineering Systems: Inovations and Applications, **1995**.
- (148) Chambers, B.; Tennant, A. Antennas and Propagation, **1995**.
- (149) Chambers, B.; Tennant, A. Proceedings of the 16th Annual Meeting on Antenna Measurement Techniques Association, **1994**.
- (150) Chambers, B.; Tennant, A. *Electr. Lett.* **1994**, 30, 1530.
- (151) Cheldavi, A. *IEICE Transactions on Fundamentals of Electronics, Communications and Computer Sciences* **1999**, E82-A, 704.
- (152) Cheldavi, A.; Kamarei, M. *IEEE Antennas and Propagation Society. International Symposium (1997: Montreal)* **1997**, 3, 1708.

- (153) Qian, J.; Wang, X.; Wu, R.; Pei, M.
- (154) Weile, D. S.; Michielssen, E. *Antennas and Propagation*, *IEEE Transactions on* **1997**, *45*, 343.
- (155) Kern, D. J.; Werner, D. H. *Microwave and Optical Technology Letters* **2003**, *38*, 61.
- (156) Kern, D. J.; Werner, D. H. *Antennas & Propagation Society International Symposium, 2003*. **2003**, *2*, 1119.
- (157) Kern, D. J.; Werner, D. H.; Wilhelm, M. J.; Church, K. H. *Microwave and Optical Technology Letters* **2003**, *38*, 400.
- (158) Charles, A.; Towers, M. S.; McCowen, A. *Computation in Electromagnetics, Third International conference on (Conf. Publ. No 420)* **1996**, 117.
- (159) Chambers, B. Nat. Conf. Antennas Propagation Conference Publication No. 461, **1999**.
- (160) Charles, A.; Towers, M. S.; McCowen, A. *Microwaves, Antennas & Propagation, IEEE Proceedings* **1999**, *146*, 257.
- (161) Stoyanov, A. J., Howell, B.F., Fischer, E.C. *J. Appl. Phys.* **1999**, *86*, 3110
- (162) Janos, W. A., US Patent 5298903. **1994**.
- (163) Capaccioli, S.; Lucchesi, M.; Rolla, P. A.; Ruggeri, G. *Journal of Physics: Condensed Matter* **1998**, *10*, 5595.
- (164) Mohamed, A. B. H.; Miane, J. L.; Zangar, H. *Polymer International* **2001**, *50*, 773.
- (165) Olmedo, L.; Hourquebie, P.; Jousse, F. *Adv. Mat.* **1993**, *5*, 373.
- (166) Truong, V.-T.; Turner, B. D.; Muscat, R. F.; Russo, M. S. *SPIE* **1997**, *3241*, 98.
- (167) Ruffoni, J. M., US Patent 5151222. **1992**.
- (168) Roberts, W. P., Scholz, L.A., US Patent 4,604,427. **1986**.
- (169) Buckley, L. J.; Eashoo, M. *Synthetic Metals* **1996**, *78*, 1.
- (170) Gangopadhyay, R.; De, A. *Chem. Mater.* **2000**, *12*, 608
- (171) Bjorklund, R. B.; Liedberg, B. *J. Chem. Soc., Chem. Commun.* **1986**, 1293.
- (172) Qi, Z.; Pickup, P. G. *Chem. Mater.* **1997**, *9*, 2934

- (173) Armes, S. P., Vincent, B. J. *Chem. Soc., Chem. Commun.* **1987**, 288
- (174) Armes, S. P.; Miller, J. F.; Vincent, B. J. *Colloid Interface Sci.* **1987**, *118*, 410
- (175) Armes, S. P., Aldissi, M. *Polymer* **1990**, *31*, 569
- (176) Simmons, M. R.; Chaloner, P. A.; Armes, S. P.; Greaves, S. J.; Watts, J. F. *Langmuir* **1998**, *14*, 611
- (177) Barry Jr., C. N.; Kuhn, H. H., US Patent 5,240,644. **1993**.
- (178) Armes, S. P., Aldissi, M. *J. Chem. Soc., Chem. Commun.* **1989**, 88
- (179) Cooper, E. C.; Vincent, B. J. *Phys. D.: Appl. Phys.* **1989**, *22*, 1580.
- (180) Chehimi, M. M.; Abel, M. L.; Sahraoui, Z.; Fraoua, K.; Lascelles, S. F.; Armes, S. P. *Int. J. Adhesion and Adhesives* **1997**, *17*, 1.
- (181) Khan, M. A.; Armes, S. P. *Adv. Mater.* **2000**, *12*, 671
- (182) Wiersma, A. E., European Patent App Patent 0 589 529 A1. **1994**.
- (183) Wiersma, A. E.; vd Steeg, L. M. A.; Jongeling, T. J. M. *Synthetic Metals* **1995**, *71*, 2269.
- (184) Lascelles, S. F.; Armes, S. P. *Adv. Mater.* **1995**, *7*, 864
- (185) Barthet, C.; Armes, S. P.; Lascelles, S. F.; Luk, S. Y.; Stanley, H. M. E. *Langmuir* **1998**, *14*, 2032
- (186) Li, X. G.; Huang, M. R.; Wang, L. X.; Zhu, M. F.; Menner, A.; Springer, J. *Synth. Met* **2001**, *123*, 435.
- (187) Cairns, D. B.; Armes, S. P.; Bremer, L. G. B. *Langmuir* **1999**, *15*, 8052
- (188) Kim, B. J.; Oh, S. G.; Han, M. G.; Im, S. S. *Polymer* **2002**, *43*, 111
- (189) Kryszewski, M.; Jeszka, J. K. *Synth. Met.* **1998**, *94*, 99
- (190) Zelenev, A.; Sonnenberg, W.; Matijevic, E. *Colloid Polym. Sci.* **1998**, *276*, 838
- (191) Gill, M.; Mykytiuk, J.; Armes, S. P.; Edwards, J. L.; Yeates, T.; Moreland, P. J.; Mollett, C. J. *Chem. Soc., Chem. Commun.* **1992**, 108.
- (192) Terrill, N. J.; Crowley, T.; Gill, M.; Armes, S. P. *Langmuir* **1993**, *9*, 2093

- (193) McCarthy, G. P.; Armes, S. P.; Greaves, S. J.; Watts, J. F. *Langmuir* **1997**, *13*, 3686
- (194) Miksa, B.; Slomkowski, S.; Marsault, J.-P. *Colloid Polym. Sci.* **1998**, *276*, 34
- (195) Henry, F.; Broussoux, D.; Dubois, J.-C., US Patent 5104580. **1992**.
- (196) Rajesh, B.; Thampi, K. R.; Bonard, J.-M.; Mathieu, H. J.; Xanthopoulos, N.; Viswanathan, B. *Chem. Comm.* **2003**, 2022.
- (197) Menon, V. P.; Lei, J.; Martin, C. R. *Chem. Mater.* **1996**, *8*, 2382
- (198) De Vito, S.; Martin, C. R. *Chem. Mater.* **1998**, *10*, 1738
- (199) Demoustier-Champagne, S.; Stavaux, P. *Chem. Mater.* **1999**, *11*, 829
- (200) Martin, C. R. *Adv. Mater.* **1991**, *3*, 457
- (201) Jang, J.; Yoon, H. *Chem Commun* **2003**, 720.
- (202) Liu, J.; Wan, M. *Synth. Met* **2001**, *124*, 317.
- (203) Yang, Y.; Wan, M. *J. Mater. Chem.* **2001**, *11*, 2022.
- (204) Goren, M.; Qi, Z.; Lennox, R. B. *Chem. Mater.* **2000**, *12*, 1222.
- (205) Kaynak, A. *Materials Research Bulletin* **1997**, *32*, 271.
- (206) Celzard, A.; McRae, E.; Deleuze, C.; Dufort, M.; Furdin, G.; Mareche, J. F. *Phys. Rev. B.* **1996**, *53*, 6209.
- (207) Schoen, P. E., US Patent Navy Case No. 79423. **2001**.
- (208) Price, R. R., Schnur, J.M., Schoen, P.E., Zabetakis, D., Spector, M., US Patent 6013206. **2000**.
- (209) Wan, M., Li, J., Li, S. *Polymers for Advanced Technologies* **2001**, *12*, 651.
- (210) Varadan, V. V., Ro, R., Varadan, V.K. *Radio Science* **1994**, *29*, 9.
- (211) Bahattacharyya, A. K. *Elect. Lett.* **1990**, *26*, 1066.
- (212) Sharma, R.; Balakrishnan, N. *Smart Mat. Struct.* **1998**, *7*, 851.
- (213) Bohren, C. F.; Luebbers, R.; Langdon, H. S.; Hunsberger, F. *Applied Optics* **1992**, *31*, 6403.
- (214) Reinert, J., Psilopoulos, J., Grubert, J., Jacob, A.F. *Microwave and Optical Technology Letters* **2001**, *30*, 254.

3. Reflectivity from Materials

The aim of this section is to set out the theory behind the interaction of electromagnetic radiation with matter so that the materials scientist can understand the physical optics^[1-5] behind microwave absorbing materials^[6-8] and its design. Emphasis will be placed on the properties of materials with examples of the different features. An attempt will be made to bring the literature from the different fields into a common description.

3.1 Interaction of Electromagnetic Radiation with Matter

Electromagnetic radiation is comprised of oscillating orthogonal electric and magnetic fields that are perpendicular to the direction of propagation. Both of these fields interact with matter^[2,4] and apply force to charged species. The total force is comprised of components due to the electric and magnetic fields, $\mathbf{F}=\mathbf{F}_E+\mathbf{F}_M$. The electric field causes distortions in the internal charge distribution by applying a force of

$$\mathbf{F}_E = q\mathbf{E} \quad 3.1$$

where q is charge. \mathbf{F}_E is oscillatory and has a time average of zero. The magnetic field applies a force

$$\mathbf{F}_M = q\mathbf{v} \times \mathbf{B} \quad 3.2$$

where \mathbf{v} is the velocity of the charge carrier and \mathbf{B} is the magnetic induction.

Charged species are typically found in polar molecules with permanent dipoles, molecules where dipoles are induced and in the electrons surrounding the nuclei of atoms. The interaction of these charged species with electromagnetic radiation give rise to processes termed Atomic (or Distortion), Orientation, and Electronic polarisation.

Orientation polarisation occurs when an electric field acts on molecules with a permanent dipole moment, the force applies a torque that causes the molecules to rotate with the field. Due to the relatively large mass of a molecule it can only follow the electric field at low frequencies.

Atomic polarisation occurs at the inter-atomic level, where the electric field distorts the arrangement of atoms in a molecule or lattice by bending or stretching them. The result is an induced dipole moment. The time for a molecule to bend is on the order of the time it takes to vibrate so at frequencies higher than the infrared, distortion polarisation decreases. This occurs in steps corresponding to vibration absorption bands, an effect that is exploited in IR spectroscopy.

Electronic polarisation occurs at the subatomic level, where the electric field causes a displacement of electrons with respect to the nucleus. Due to the small mass of the electron, electronic polarisation extends to very high frequencies. Electronic and atomic polarisation processes give rise to induced dipole moments. All the polarisation processes result in an electric polarisation \mathbf{P} defined as the electric dipole moment per unit volume.

Most dielectric material and diamagnetic, paramagnetic and antiferromagnetic material have permeabilities about 1, ie there is little influence of the magnetic field on the material. Only ferromagnetic and ferrimagnetic materials have permeabilities above that of free space and are magnetically lossy. In these materials the magnetic field interacts with the electron spin, contributing to the magnetization \mathbf{M} , which is defined as the magnetic dipole moment per unit volume. Ferromagnetic materials have very high permeabilities and good conductivity so radiation does not penetrate. Ferrimagnetic materials, known as ferrites, have strong magnetic effects at microwave frequencies that result in anisotropic properties and have low conductivity.

These processes are the basis for interaction of electromagnetic radiation with matter. To be able to quantify these interactions with respect to the electric and magnetic field strengths it is necessary to resort to Maxwell's Equations.

3.1.1 Maxwell's Equations

Maxwell's equations describe the relationships between electric and magnetic fields and their interaction with the properties of matter.^[1-4] The Gauss, Faraday and Ampere laws are other names for three of Maxwell's equations.

Gauss' law is a restatement of Coulomb's law, which relates the charge density ρ to the field strength \mathbf{E} , by

$$\nabla \cdot \mathbf{E} = \frac{\rho}{\epsilon} \quad 3.3$$

This relationship indicates that the electric field lines originate on the electric charge and that the integral of the electric field over a closed surface is proportional to the enclosed charge. For most materials there is no net space charge so $\nabla \cdot \mathbf{E} = 0$.

Faraday's law shows that the amount of voltage induced around a closed loop is proportional to the time rate of change of enclosed magnetic flux.

$$\nabla \times \mathbf{E} = -\frac{\partial \mathbf{B}}{\partial t} \quad 3.4$$

Ampere's law shows that magnetic field \mathbf{H} , is caused by an electric current density \mathbf{J} , and the time-changing displacement current $\frac{\partial}{\partial t}$.

$$\nabla \times \mathbf{H} = \mathbf{J} + \frac{\partial \mathbf{D}}{\partial t} \quad 3.5$$

Note, sometimes the Faraday and Ampere laws are expressed as

$$\nabla \times \mathbf{E} = -\frac{1}{c} \frac{\partial \mathbf{B}}{\partial t} \quad \text{and} \quad \nabla \times \mathbf{H} = \frac{4\pi}{c} \mathbf{J} + \frac{1}{c} \frac{\partial \mathbf{D}}{\partial t}$$

The final Maxwell equation is not named and relates to the magnetic induction. The magnetic induction field lines, \mathbf{B} , always close back on themselves and do not begin or end on any form of charge density. This expression is

$$\nabla \cdot \mathbf{B} = 0 \quad 3.6$$

Matter, through the polarisation processes described above, can store electric and magnetic energy which modifies the free space electric \mathbf{E} and magnetic \mathbf{H} field intensities. Thus the displacement flux \mathbf{D} (in units of coulombs/m²), is

$$\mathbf{D} = \epsilon_0 \mathbf{E} + \mathbf{P} \quad 3.7$$

where ϵ_0 is the permittivity of free space and \mathbf{P} the polarisation. In a homogeneous, linear, isotropic material, \mathbf{P} and \mathbf{E} are in the same direction and proportional ($\mathbf{P}=\chi_e \mathbf{E}$ where χ_e is the electric susceptibility). This also makes \mathbf{D} proportional to \mathbf{E} so that

$$\mathbf{D} = \left(1 + \frac{\chi}{\epsilon_0}\right) \epsilon_0 \mathbf{E} = \epsilon_r \epsilon_0 \mathbf{E} \quad 3.8$$

In a similar way, the magnetic induction \mathbf{B} (in units webers/m²), is related to the Magnetic field strength \mathbf{H} , and the magnetization \mathbf{M} , through

$$\frac{1}{\mu_0} \mathbf{B} = \mathbf{H} + \mathbf{M} \quad 3.9$$

where μ_0 is the permeability of free space. Magnetization is generally a nonlinear function of the magnetic field or magnetic induction (cf hysteresis in B-H and M-H curves). For many materials which are linear and isotropic \mathbf{M} and \mathbf{H} can be related through the magnetic susceptibility χ_m , through $\mathbf{M}=\chi \mathbf{H}$, so

$$\mathbf{B} = (1 + \chi_m) \mu_0 \mathbf{H} = \mu_r \mu_0 \mathbf{H} \quad 3.10$$

The third constitutive equation is Ohm's law, which relates the electric field to the current density,

$$\mathbf{J} = \sigma \mathbf{E} \quad 3.11$$

where σ is the conductivity (in units Siemens/m). Equations 3.8, 3.10 and 3.11 are called the constitutive equations.^[7]

3.1.2 The Wave Equation

Maxwell's equations can be reformulated into the differential wave equation that can be used to describe the reflection and refraction processes when electromagnetic waves interact with matter. Ampere's law (equation 3.5) is expanded using equations 3.8 and 3.11.

$$\nabla \times \mathbf{H} = \mathbf{J} + \frac{\partial \mathbf{D}}{\partial t} = \sigma \mathbf{E} + \varepsilon \frac{\partial \mathbf{E}}{\partial t} \quad 3.12$$

Faraday's law is used with $\mathbf{B} = \mu \mathbf{H}$ to give

$$\nabla \times \mathbf{E} = -\mu \frac{\partial \mathbf{H}}{\partial t} \quad 3.13$$

The vector identity

$$\nabla \times (\nabla \times \mathbf{E}) = \nabla(\nabla \cdot \mathbf{E}) - \nabla^2 \mathbf{E} \quad 3.14$$

and the fact that $\nabla \cdot \mathbf{E} = 0$ if there is no space charge, are used to give the differential wave equation

$$\nabla^2 \mathbf{E} - \mu \varepsilon \frac{\partial^2 \mathbf{E}}{\partial t^2} - \mu \sigma \frac{\partial \mathbf{E}}{\partial t} = 0 \quad 3.15$$

Assume a solution to the above equation is of the form of a plane wave

$$\mathbf{E} = E_0 e^{i(kr - \omega t)} \quad 3.16$$

Note here that in the field of physics, the exponential term is usually $i(kr - \omega t)$ rather than $j(\omega t - kr)$ used in engineering. Also note that any reasonable expression can be used for a plane wave, (eg $i\omega(t - x/v)$ or $i\frac{2\pi}{\lambda}(x - vt)$). Differentiating equation

3.16 and substituting into equation 15 gives an expression, which is a solution to the differential wave equation

$$(ik)^2 \mathbf{E} - \mu \varepsilon (-i\omega)^2 \mathbf{E} - \mu \sigma (-i\omega) \mathbf{E} = 0 \quad 3.17$$

Solving for k gives

$$(ik)^2 - \mu\epsilon(-i\omega)^2 - \mu\sigma(-i\omega) = 0 \quad 3.18$$

or

$$k^2 = \mu\epsilon\omega^2 \left(1 - \frac{i\sigma}{\epsilon\omega} \right) \quad 3.19$$

The value k is called the propagation number and can also be expressed as

$$k = \frac{2\pi}{\lambda} = k_o N = \frac{2\pi}{\lambda_o} N = \frac{2\pi f}{c} N = \frac{\omega N}{c} \quad 3.20$$

where N is the refractive index, c is the speed of light in a vacuum, f is the frequency, and λ and λ_o are the wavelengths in matter and free space, respectively. The expression for k is related to a similar expression called the propagation number^[1] through

$$\gamma = ik = \sqrt{(\sigma + i\omega\epsilon)(i\omega\mu)} = \alpha + i\beta \quad 3.21$$

where α is the attenuation constant and β the phase constant. α and β can be solved for such that

$$\alpha = \omega\sqrt{\mu\epsilon} \left\{ \frac{1}{2} \left[\sqrt{1 + \left(\frac{\sigma}{\omega\epsilon} \right)^2} - 1 \right] \right\}^{1/2} \text{ in Np/m} \quad 3.22$$

$$\beta = \omega\sqrt{\mu\epsilon} \left\{ \frac{1}{2} \left[\sqrt{1 + \left(\frac{\sigma}{\omega\epsilon} \right)^2} + 1 \right] \right\}^{1/2} \text{ in rad/m} \quad 3.23$$

The refractive index, N, is defined as the ratio of the speed of light in free space, c, to the speed of the electromagnetic radiation in matter, v, and can be a complex number.

Using the expression $k = \frac{N\omega}{c}$, and the fact that $c = \frac{1}{\sqrt{\epsilon_o\mu_o}}$ it is possible to show

that the refractive index can be expressed in terms of the permeability and permittivity,

$$N = \frac{c}{v} = n' - in'' = \frac{\sqrt{\epsilon\mu \left(1 - \frac{i\sigma}{\epsilon\omega} \right)}}{\sqrt{\epsilon_o\mu_o}} \quad 3.24$$

where n' is the real component of the refractive index and n'' the imaginary.

3.2 Reflection from an Interface

Radiation incident on an interface between two media will be reflected and refracted to an extent that depends on the refractive index of the media (Figure 3.1) the angle of incidence θ_i (θ_i is the angle between the propagation vector \hat{k} and the surface normal) and the orientation of the electric field to the surface (ie the polarisation not to be confused with \mathbf{P}). The polarisation or orientation of the electric field with respect to the plane of incidence is described in the literature by a number of terms. When the electric field is polarised perpendicularly to the plane of incidence, it is called transverse electric or H-polarised with the notations E_{\perp}, E_{TE}, E_s . The electric field parallel to the plane of incidence is termed transverse magnetic or E polarised, with notations $E_{\parallel}, E_{TM}, E_p$. Here E_{\perp}, E_{\parallel} will be used.

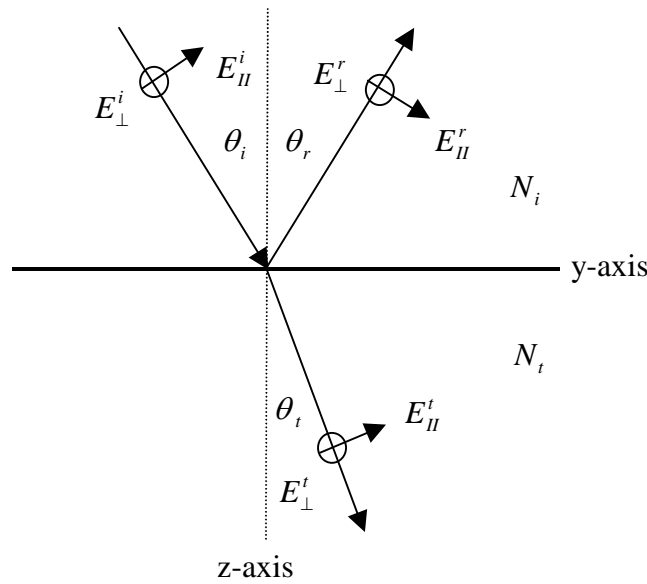


Figure 3.1. Reflection and refraction at an interface between two media with refractive indices N_i and N_t . The x -axis points into the page as does E_{\perp} , which is represented by the X in the circles. E_{\parallel} is in the plane of incidence.

Define the incident plane along the y - z plane, the surface normal in the $+z$ direction and the interface between the two media along the y - x plane. The incident, reflected and transmitted waves have the propagation vectors $\hat{k}_i, \hat{k}_r, \hat{k}_t$. These can be expressed in terms of the \hat{y} and \hat{z} unit vectors as,

$$\hat{k}_i = k_i (\hat{y} \sin \theta_i + \hat{z} \cos \theta_i)$$

$$\hat{k}_r = k_r (\hat{y} \sin \theta_r - \hat{z} \cos \theta_r) \quad 3.25$$

$$\hat{k}_t = k_t (\hat{y} \sin \theta_t + \hat{z} \cos \theta_t)$$

The electric field vectors can then be described as

$$\begin{aligned} \mathbf{E}_i &= \left[E_{||}^i (\hat{y} \cos \theta_i - \hat{z} \sin \theta_i) + \hat{x} E_{\perp}^i \right] e^{i[k_i (y \sin \theta_i + z \cos \theta_i) - \omega t]} \\ \mathbf{E}_r &= \left[E_{||}^r (\hat{y} \cos \theta_r + \hat{z} \sin \theta_r) + \hat{x} E_{\perp}^r \right] e^{i[k_r (y \sin \theta_r - z \cos \theta_r) - \omega t]} \\ \mathbf{E}_t &= \left[E_{||}^t (\hat{y} \cos \theta_t - \hat{z} \sin \theta_t) + \hat{x} E_{\perp}^t \right] e^{i[k_t (y \sin \theta_t + z \cos \theta_t) - \omega t]} \end{aligned} \quad 3.26$$

where the $||$ and \perp subscripts indicate the electric field parallel and perpendicular to the plane of incidence. A boundary condition can be applied at the interface, which is, that the tangential component of \mathbf{E} (parallel to the surface) must be identical on either side (ie the parallel components of the combined incident and reflected fields must equal the parallel components of the transmitted field). So

$$\begin{aligned} &\left[E_{||}^i (\hat{y} \cos \theta_i) + \hat{x} E_{\perp}^i \right] e^{i[k_i (y \sin \theta_i) - \omega t]} + \left[E_{||}^r (\hat{y} \cos \theta_r) + \hat{x} E_{\perp}^r \right] e^{i[k_r (y \sin \theta_r) - \omega t]} \\ &= \left[E_{||}^t (\hat{y} \cos \theta_t) + \hat{x} E_{\perp}^t \right] e^{i[k_t (y \sin \theta_t) - \omega t]} \end{aligned} \quad 3.27$$

This expression must hold for all values of y and t , so the exponential terms must be equal. This gives then means that

$$\omega_i = \omega_r = \omega_t \equiv \omega$$

and

$$k_i \sin \theta_i = k_r \sin \theta_r = k_t \sin \theta_t$$

Using $k_i = k_r = N_i \frac{\omega}{c}$ (which gives the law of reflection $\theta_i = \theta_r$), $k_t = N_t \frac{\omega}{c}$ and

Snell's law ($N_1 \sin \theta_i = N_2 \sin \theta_t$) the above equation simplifies to

$$E_{\perp}^i + E_{\perp}^r = E_{\perp}^t \quad 3.28$$

and

$$\left(E_{||}^i + E_{||}^r \right) \cos \theta_i = E_{||}^t \cos \theta_t \quad 3.29$$

Similar equations can be derived for \mathbf{B} and using Faraday's Law (equation 3.4) it can be expressed in terms of the electric field

$$\mathbf{B} = \frac{\hat{k} \times \mathbf{E}}{\omega} = \frac{N}{c} \mathbf{u} \times \mathbf{E} \quad 3.30$$

where $\mathbf{u} = \hat{k} / k$ is the unit vector in the direction \hat{k} .

$$\mathbf{B}_i = \frac{N_i}{c} \left[-\mathbf{x}E_{||}^i + E_{\perp}^i (-\mathbf{z} \sin \theta_i + \mathbf{y} \cos \theta_i) \right] e^{i[k_i(y \sin \theta_i + z \cos \theta_i) - \omega_i t]}$$

$$\mathbf{B}_r = \frac{N_r}{c} \left[\mathbf{x}E_{||}^r + E_{\perp}^r (-\mathbf{z} \sin \theta_r - \mathbf{y} \cos \theta_r) \right] e^{i[k_r(y \sin \theta_r - z \cos \theta_r) - \omega_r t]} \quad 3.31$$

$$\mathbf{B}_t = \frac{N_t}{c} \left[-\mathbf{x}E_{||}^t + E_{\perp}^t (-\mathbf{z} \sin \theta_t + \mathbf{y} \cos \theta_t) \right] e^{i[k_t(y \sin \theta_t + z \cos \theta_t) - \omega_t t]}$$

These equations can be reformulated in terms of the magnetic field, \mathbf{H} , which introduces a $1/\mu$, term into the right hand side. Setting the boundary condition that parallel components have to be equal on either side of the $z=0$ plane, gives

$$\frac{N_i}{\mu_i c} \left[-\mathbf{x}E_{||}^i + \mathbf{y}E_{\perp}^i \cos \theta_i \right] + \frac{N_r}{\mu_r c} \left[\mathbf{x}E_{||}^r - \mathbf{y}E_{\perp}^r \cos \theta_r \right]$$

$$= \frac{N_t}{\mu_t c} \left[-\mathbf{x}E_{||}^t + \mathbf{y}E_{\perp}^t \cos \theta_t \right] \quad 3.32$$

which reduces to two simple expressions

$$\frac{N_i}{\mu_i c} (E_{||}^i - E_{||}^r) = \frac{N_t}{\mu_t c} E_{||}^t \quad 3.33$$

and

$$\frac{N_i}{\mu_i c} (E_{\perp}^i - E_{\perp}^r) \cos \theta_i = \frac{N_t}{\mu_t c} E_{\perp}^t \cos \theta_t \quad 3.34$$

Equations 3.26, 3.27, 3.31 and 3.32 describe the fields on either side of the interface. The reflection and transmission coefficients can be extracted from these equations. The reflection coefficient is the ratio of the reflected to the incident electric field and the transmission coefficient is the ratio of the transmitted to the incident electric field. This gives the equations

$$r_{\perp} = \left(\frac{E_{\perp}^r}{E_{\perp}^i} \right) = \frac{\frac{N_i}{\mu_i c} \cos \theta_i - \frac{N_t}{\mu_t c} \cos \theta_t}{\frac{N_i}{\mu_i c} \cos \theta_i + \frac{N_t}{\mu_t c} \cos \theta_t} \quad 3.35$$

$$t_{\perp} = \left(\frac{E_{\perp}^t}{E_{\perp}^i} \right) = \frac{2 \frac{N_i}{\mu_i c} \cos \theta_i}{\frac{N_i}{\mu_i c} \cos \theta_i + \frac{N_t}{\mu_t c} \cos \theta_t} \quad 3.36$$

$$r_{\parallel} = \left(\frac{E_{\parallel}^r}{E_{\parallel}^i} \right) = \frac{\frac{N_t}{\mu_t c} \cos \theta_i - \frac{N_i}{\mu_i c} \cos \theta_t}{\frac{N_i}{\mu_i c} \cos \theta_t + \frac{N_t}{\mu_t c} \cos \theta_i} \quad 3.37$$

$$t_{\parallel} = \left(\frac{E_{\parallel}^t}{E_{\parallel}^i} \right) = \frac{2 \frac{N_i}{\mu_i c} \cos \theta_i}{\frac{N_i}{\mu_i c} \cos \theta_t + \frac{N_t}{\mu_t c} \cos \theta_i} \quad 3.38$$

The terms $(N/\mu c)$ can also be obtained from the ratio of H/E . This can be seen from the combination of equations 3.12 and 3.26. This ratio is often called the optical admittance Y and its reciprocal is the impedance Z . Another form for the admittance is

$$Y = \frac{k}{\mu \omega} = \frac{N}{\mu c} = \sqrt{\frac{\sigma + i \varepsilon \omega}{i \mu \omega}} \quad 3.39$$

The reflection and transmission coefficients in equations 3.35-3.38 can be represented in terms of the admittance (or impedance). These equations simplify in the case of normal incidence to

$$r_{\perp} = r_{\parallel} = \frac{Y_i - Y_t}{Y_i + Y_t} \quad 3.40$$

$$t_{\perp} = t_{\parallel} = \frac{2Y_i}{Y_i + Y_t} \quad 3.41$$

For oblique incidence the tilted admittance, η , can be used to simplify the reflection and transmission coefficients. For transverse electric fields, E_{\perp} , the tilted admittance is

$$\eta_{\perp}^i = Y_i \cos \theta_i \quad 3.42$$

and for the transverse magnetic field, E_{\parallel} , the tilted admittance is

$$\eta_{\parallel}^i = \frac{Y_i}{\cos \theta_i} \quad 3.43$$

The reflection and transmission coefficients then can be expressed as,

$$r = \frac{\eta_i - \eta_t}{\eta_i + \eta_t} \quad 3.44$$

and

$$t = \frac{2\eta_i}{\eta_i + \eta_t} \quad 3.45$$

where appropriate attention has to be paid to the polarisation of the electromagnetic wave. The admittance used in these equations could be replaced by the impedance, Z , which is often done by electrical engineers and is commonly found in the literature of radar absorbing materials. The reflectance, R , is defined as the ratio of the reflected over the incident flux (or power) and transmittance, T , as the ratio of the transmitted over the incident flux. These can be expressed as

$$R = \left(\frac{E^r}{E^i} \right)^2 = r^2 = \left| \frac{\eta_i - \eta_t}{\eta_i + \eta_t} \right|^2 \quad 3.46$$

and, using the relationship $1=R+T$,

$$T = \frac{4\eta_i\eta_t}{(\eta_i + \eta_t)^2} \quad 3.47$$

For normal incidence, $R = R_{\parallel} = R_{\perp}$, and $T = T_{\parallel} = T_{\perp}$.

3.3 Practical Details: Reflection from an Interface

Now that we have equations for expressing the reflectance and transmittance in terms of the refractive index, or permeability and permittivity, it is useful to make some

observations on the physics, which will be helpful in the formulation of radar absorbing materials. (The algorithm for calculating reflectivity is given in Appendix 1. The code was tested and reproduces other reflectivity calculations, eg Figures 2, 5 and 14 are partially or complete reproductions of figures found in Stratton,^[9] Born and Wolf,^[2] and Knott, Shaeffer and Tuley^[6]). The first point to note is from equation 3.46, the larger the step in the admittance across the interface, the larger the reflectance (from the engineering point the larger the impedance mismatch the larger the reflected signal). If the incident medium is air then from equation 39 the admittance is

$$Y = \sqrt{\frac{\sigma + i\omega\epsilon}{i\omega\mu}} = \sqrt{\frac{\epsilon_o}{\mu_o}} = \sqrt{\frac{8.85 \times 10^{-12}}{4\pi \times 10^{-7}}} = \frac{1}{377} \quad 3.48$$

The impedance ($Z=1/Y$) is about 377 ohms. For materials with an impedance of 377 ohms there will be no reflection at the interface.

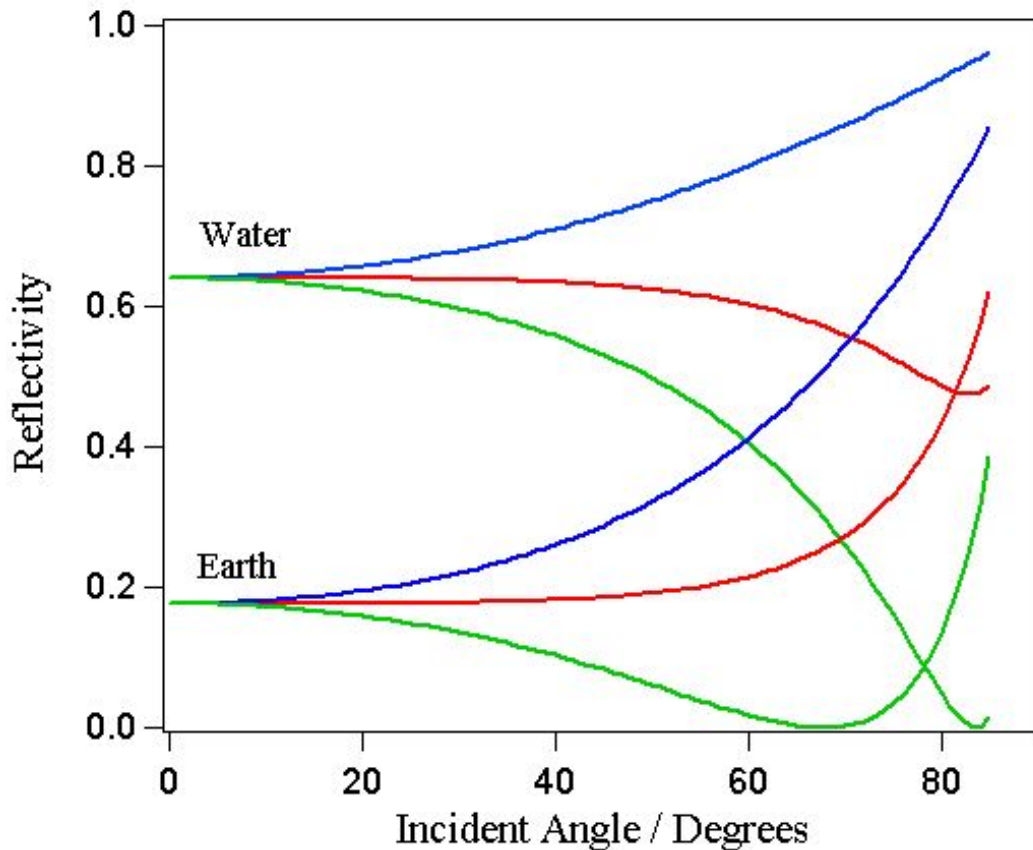


Figure 3.2. Reflectivity of 10 GHz microwaves from water ($\epsilon_r = 81$, $\mu_r = 1$ and $\sigma = 0$) and earth ($\epsilon_r = 6$, $\mu_r = 1$ and $\sigma = 0$, red = R , blue = R_{\perp} , green = R_{\parallel}). As θ_i tends to 90, R tends to 1 so smooth surfaces will appear as perfect reflectors.

Figure 2 shows the reflectivity from water and earth as a function of incident angles. The perpendicular and parallel polarisations produce very different reflectivity profiles. The interesting point to note here is that a radar looking down on an object on water with a reflectivity of 0.64 will not be able to distinguish the object unless the radar's resolution is better than the vertical dimensions of the object. The reflectivity resulting from the parallel polarised electric field, for both water and earth is seen to reach a minimum reflectivity. This is known as the polarization angle where r_{\parallel} passes through zero.

3.3.1 Reflectivity from a Single Layer

Reflectivity from a single layer can be treated in the same way as reflectivity from an interface. In this case there are multiple reflections between the two interfaces and the resultant fields from these have been summed into E^r , E^{mi} , E^{mr} , and E^t for the parallel and perpendicular components (and similarly for the magnetic fields). The

boundary condition requires that the tangential components of the electric and magnetic fields are continuous across the interface and the end objective is to be able to relate the E_i , E_r and E_t in terms of the optical properties of the layer.

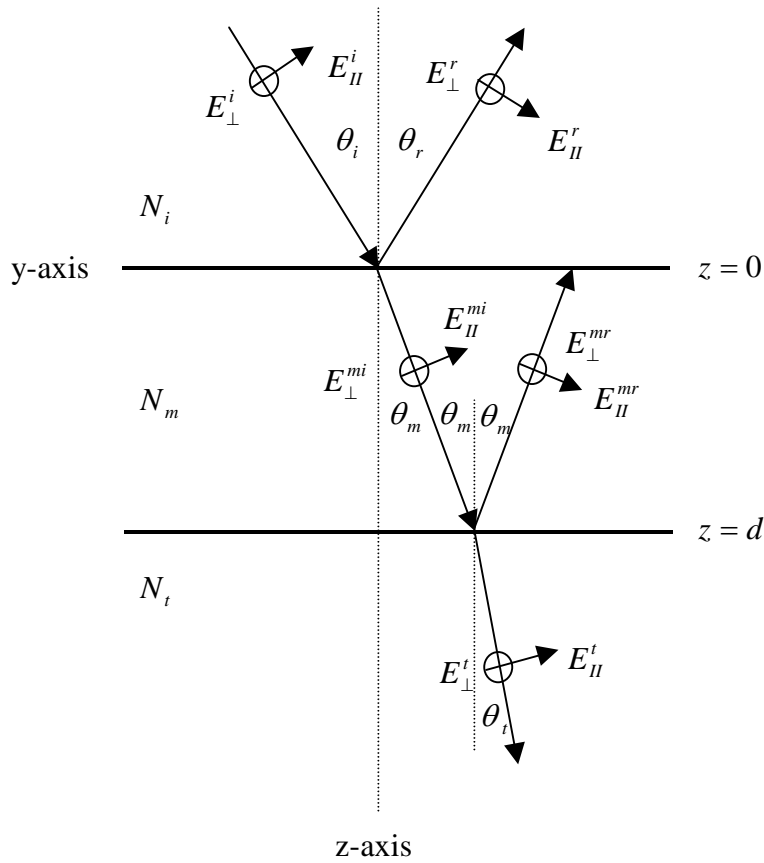


Figure 3.3. Reflection and refraction from a single layer. The E^r and E^t fields in the incident and transmitting media (N_i and N_i) are defined as being the sum of all waves arising from multiple reflections in the middle media (N_m).

At the first interface between media N_i and N_m , the equations for the electric and magnetic fields are

$$E_{\perp 1} = E_{\perp}^i + E_{\perp}^r = E_{\perp 1}^{mi} + E_{\perp 1}^{mr} \quad 3.49$$

$$H_{\perp 1} = \frac{N_i}{c\mu_i} (E_{\perp}^i - E_{\perp}^r) \cos \theta_i = \frac{N_m}{c\mu_m} (E_{\perp 1}^{mi} - E_{\perp 1}^{mr}) \cos \theta_m \quad 3.50$$

$$E_{\parallel 1} = \cos \theta_i (E_{\parallel}^i + E_{\parallel}^r) = \cos \theta_m (E_{\parallel 1}^{mi} + E_{\parallel 1}^{mr}) \quad 3.51$$

$$H_{\parallel 1} = \frac{N_i}{c\mu_i} (E_{\parallel}^i - E_{\parallel}^r) = \frac{N_m}{c\mu_m} (E_{\parallel 1}^{mi} - E_{\parallel 1}^{mr}) \quad 3.52$$

At the second interface, between the media with N_m and N_t , the equations for the electric and magnetic fields are

$$E_{\perp 2} = E_{\perp 2}^{mi} + E_{\perp 2}^{mr} = E_{\perp}^t \quad 3.53$$

$$H_{\perp 2} = \frac{N_m}{c\mu_m} (E_{\perp 2}^{mi} - E_{\perp 2}^{mr}) \cos \theta_m = \frac{N_t}{c\mu_t} E_{\perp}^t \cos \theta_t \quad 3.54$$

$$E_{\parallel 2} = (E_{\parallel 2}^{mi} + E_{\parallel 2}^{mr}) \cos \theta_m = E_{\parallel 2}^t \cos \theta_t \quad 3.55$$

$$H_{\parallel 2} = \frac{N_m}{c\mu_m} (E_{\parallel 2}^{mi} - E_{\parallel 2}^{mr}) = \frac{N_t}{c\mu_t} E_{\parallel 2}^t \quad 3.56$$

The subscripts 1 and 2 indicate the first and second interface. The electric field in the layer undergoes a phase shift of $\delta = k_m d \cos \theta_m$ by traversing the layer. The complex propagation constant k_m also takes into account the absorption in the layer. The electric fields in the layer can be related to their values at the interfaces by

$$E_2^{mi} = E_1^{mi} e^{-ik_m d \cos \theta_m} \quad 3.57$$

$$E_2^{mr} = E_1^{mr} e^{ik_m d \cos \theta_m} \quad 3.58$$

These expressions for the electric field can be substituted into equations 3.53-3.56 in order to relate them to the first interface, equations 3.49-3.52. At this point consider the Transverse Electric (E_{\perp}) case, equations 3.53 and 3.54 become

$$E_{\perp 2} = E_{\perp 1}^{mi} e^{-ik_m d \cos \theta_m} + E_{\perp 1}^{mr} e^{ik_m d \cos \theta_m} \quad 3.59$$

$$H_{\perp 2} = \frac{N_m}{c\mu_m} (E_{\perp 1}^{mi} e^{-ik_m d \cos \theta_m} - E_{\perp 1}^{mr} e^{ik_m d \cos \theta_m}) \cos \theta_m \quad 3.60$$

Using equations 3.59 and 3.60 to solve for $E_{\perp 1}^{mi}$ and $E_{\perp 1}^{mr}$, and then substituting these values into equations 3.49 and 3.50, expressions for the electric and magnetic fields are obtained (using the relationships $\cos \theta = \frac{e^{i\theta} + e^{-i\theta}}{2}$ and $i \sin \theta = \frac{e^{i\theta} - e^{-i\theta}}{2}$),

$$E_{\perp 1} = E_{\perp 2} \cos(k_m d \cos \theta_m) + H_{\perp 2} \frac{c\mu_m}{N_m \cos \theta_m} i \sin(k_m d \cos \theta_m) \quad 3.61$$

$$H_{\perp 1} = E_{\perp 2} \frac{N_m}{c\mu_m} i \cos \theta_m \sin(k_m d \cos \theta_m) + H_{\perp 2} \cos(k_m d \cos \theta_m) \quad 3.62$$

Equations 3.61 and 3.62 can be simplified, using the tilted admittance (for E_{\perp} , $\eta_m = \frac{N_m}{c\mu_m} \cos \theta_m$, and for E_{\parallel} , $\eta_m = \frac{N_m}{c\mu_m} \frac{1}{\cos \theta_m}$), and $\delta = k_m d \cos \theta_m$. The resulting equations are identical except for the tilted admittances. Thus

$$E_{\perp 1} = E_{\perp 2} \cos(\delta) + H_{\perp 2} \frac{i \sin(\delta)}{\eta_m} \quad 3.63$$

$$H_{\perp 1} = E_{\perp 2} \eta_m i \sin(\delta) + H_{\perp 2} \cos(\delta) \quad 3.64$$

These can be expressed in matrix notation as

$$\begin{bmatrix} E_{\perp 1} \\ H_{\perp 1} \end{bmatrix} = \begin{bmatrix} \cos \delta & \frac{i \sin \delta}{\eta_m} \\ \eta_m i \sin \delta & \cos \delta \end{bmatrix} \begin{bmatrix} E_{\perp 2} \\ H_{\perp 2} \end{bmatrix} \quad 3.65$$

or

$$\begin{bmatrix} (E_{\perp}^i + E_{\perp}^r) \\ (E_{\perp}^i - E_{\perp}^r) \eta_{\perp}^i \end{bmatrix} = \begin{bmatrix} \cos \delta & \frac{i \sin \delta}{\eta_m} \\ \eta_m i \sin \delta & \cos \delta \end{bmatrix} \begin{bmatrix} E_{\perp}^t \\ \eta_{\perp}^t E_{\perp}^t \end{bmatrix} \quad 3.66$$

The matrix $\begin{bmatrix} \cos \delta & \frac{i \sin \delta}{\eta_m} \\ \eta_m i \sin \delta & \cos \delta \end{bmatrix}$ identified as $M = \begin{bmatrix} m_{11} & m_{12} \\ m_{21} & m_{22} \end{bmatrix}$, will be used more

in the section, which considers multilayer reflectivity. Here the two equations represented by equation 66 are

$$1 + r = m_{11} t + m_{12} t \eta_{\perp}^t \quad 3.67$$

$$(1 - r) \eta_{\perp}^i = m_{21} t + m_{22} t \eta_{\perp}^t \quad 3.68$$

where use has been made of the relations $r = \frac{E^r}{E^i}$ and $t = \frac{E^t}{E^i}$ and m_{11} , m_{12} , m_{21} and m_{22} are the elements of the matrix. These equations can be solved for r and t (the reflectivity and transmission coefficients),

$$r_{\perp} = \frac{\eta_{\perp}^i m_{11} + \eta_{\perp}^i \eta_{\perp}^t m_{12} - m_{21} - \eta_{\perp}^t m_{22}}{\eta_{\perp}^i m_{11} + \eta_{\perp}^i \eta_{\perp}^t m_{12} + m_{21} + \eta_{\perp}^t m_{22}} \quad 3.69$$

$$t_{\perp} = \frac{2\eta_{\perp}^i}{\eta_{\perp}^i m_{11} + \eta_{\perp}^i \eta_{\perp}^t m_{12} + m_{21} + \eta_{\perp}^t m_{22}} \quad 3.70$$

For E_{\parallel} , η_{\perp} is replaced by η_{\parallel} in equations 3.69 and 3.70. The intensity of the reflected, (R = reflectance), and transmitted, (T = transmittance), are then

$$R = rr^* \quad 3.71$$

$$T = \text{Re}\left(\frac{\eta^t}{\eta^i}\right) tt^* \quad 3.72$$

where the asterisk represents the complex conjugate. The intensity (irradiance) of the electric fields has units of watts per unit area. The process of refraction changes the illuminated area by a factor involving the ratio of the admittance terms. The absorption from a layer can be calculated from the expression $1 = A + R + T$ and equations 71 and 72. This gives

$$A = \frac{4\eta^i \left\{ \text{Re}\left[(m_{11} + m_{12}\eta^t)(m_{21} + m_{22}\eta^t)^* \right] - \eta^t \right\}}{\left[\eta^i (m_{11} + m_{12}\eta^t) + (m_{21} + m_{22}\eta^t) \right] \left[\eta^i (m_{11} + m_{12}\eta^t) + (m_{21} + m_{22}\eta^t) \right]^*} \quad 3.73$$

If the film is mounted on a perfect electrical conductor (PEC) then the reflectivity coefficient is

$$r = \frac{\eta_{\perp}^i m_{12} - m_{11}}{\eta_{\perp}^i m_{12} + m_{11}} \quad 3.74$$

$$t = 0 \quad 3.75$$

and

$$A = \frac{4\eta_{\perp}^i \text{Re}\{m_{12}m_{11}^*\}}{(\eta_{\perp}^i m_{12} + m_{11})(\eta_{\perp}^i m_{12} + m_{11})^*} \quad 3.76$$

3.3.2 Practical Details: Reflection from a Layer

The equations above have been developed for layered materials that show resonance (destructive interference) effects, ie Dallenbach layers and Jaumann stacks. Impedance matching absorbers can be modelled by the above equations if they are represented as layered materials.

The optical path difference, Λ , between a wave reflected from the first interface and a wave reflected from the second interface (Figure 3.4) is

$$\Lambda = 2N_m d_m \cos \theta_m$$

3.77

When Λ is $\frac{m}{2} \lambda_o$ ($m=1, 2, 3 \dots$) the waves are out of phase by 180 degrees (the phase difference is $\delta = k_o \Lambda = 2k_m d \cos \theta_m$ or twice the phase shift in traversing the film once) and a minimum results as seen in Figure 3.5. As the incident angle increases (and hence the transmitted angle), the opd decreases. The result of the decrease in the opd means that higher frequency, shorter wavelength, will satisfy the requirement for a minimum. This is seen in Figure 3.6 as a curve to higher frequency.

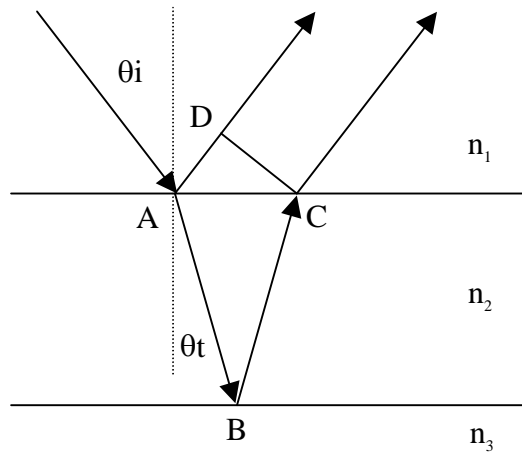


Figure 3.4. The optical path difference between the two reflected waves is $\Lambda = AB + BC - AD$. When this is equal to $1/2 \lambda$ the waves are 180° out of phase and destructive interference results in a minimum.

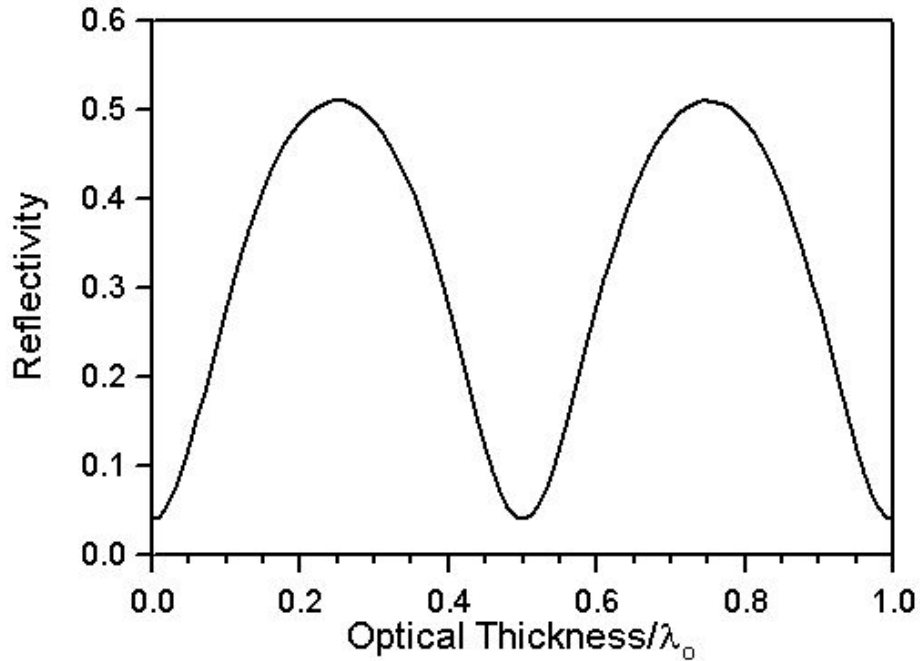


Figure 3.5. Total reflectivity from a non-absorbing layer (Incident medium is air, Layer $\epsilon_r = 9$, $\mu_r = 1$ and $\sigma = 0$, and substrate $\epsilon_r = 2.25$, $\mu_r = 1$ and $\sigma = 0$, normal incidence) as a function of the ratio of the optical path length difference to wavelength. The reflectivity has a finite value at the minima due to the difference in dielectric constants of the air and substrate layers.^[2]

On a perfect electrical conductor the layer in Figure 3.5 results in a reflectivity near 1, even where interference results in a minimum. (Note these simulations are assuming a constant value of the permittivity and permeability across the frequency range. Another approximation is made by only accounting for the first reflection from a layer. At this point it is instructive to get the details behind the physical optics, to see where devices can be made and then to explore the more realistic cases).

The reflectivity generally increases with incident angle as it approaches 90 degrees.

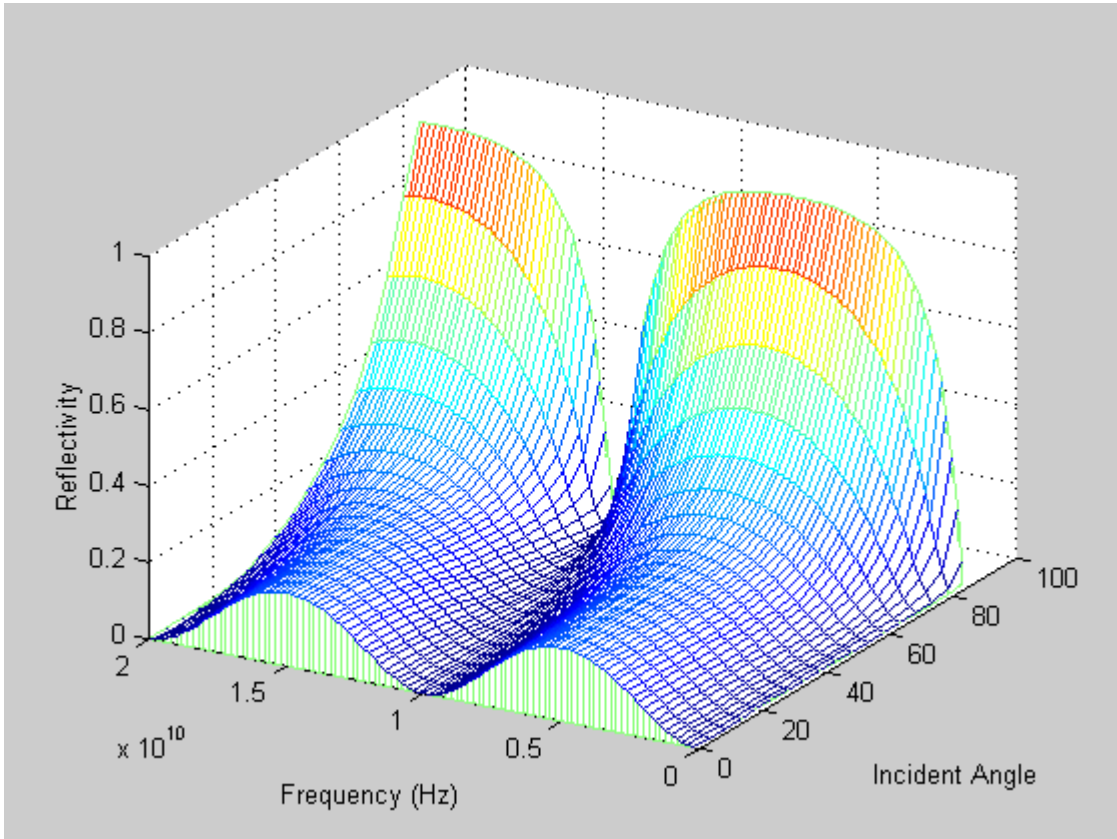


Figure 3.6. Total reflectivity as a function of frequency and Incident angle for a single 0.9375 cm thick non lossy layer with $\epsilon_r = 2.56$, $\mu_r = 1.0$ and $\sigma = 0$, surrounded by air. The minimum in reflectivity shifts to higher frequency due to a decrease in optical path length difference as the incident angle increases.

When $N_m > N_t$ the optical path difference will put the waves 180 out of phase when the layer thickness is $\lambda_m/2$. This is due to the wave undergoing a phase shift of π on reflection at the first interface and no phase shift on reflection at the second interface. For the material shown in Figure 3.6 the 10 GHz reflectivity is at a minimum when the layer thickness is $d = \lambda_0/2N_m = 0.9375$ cm.

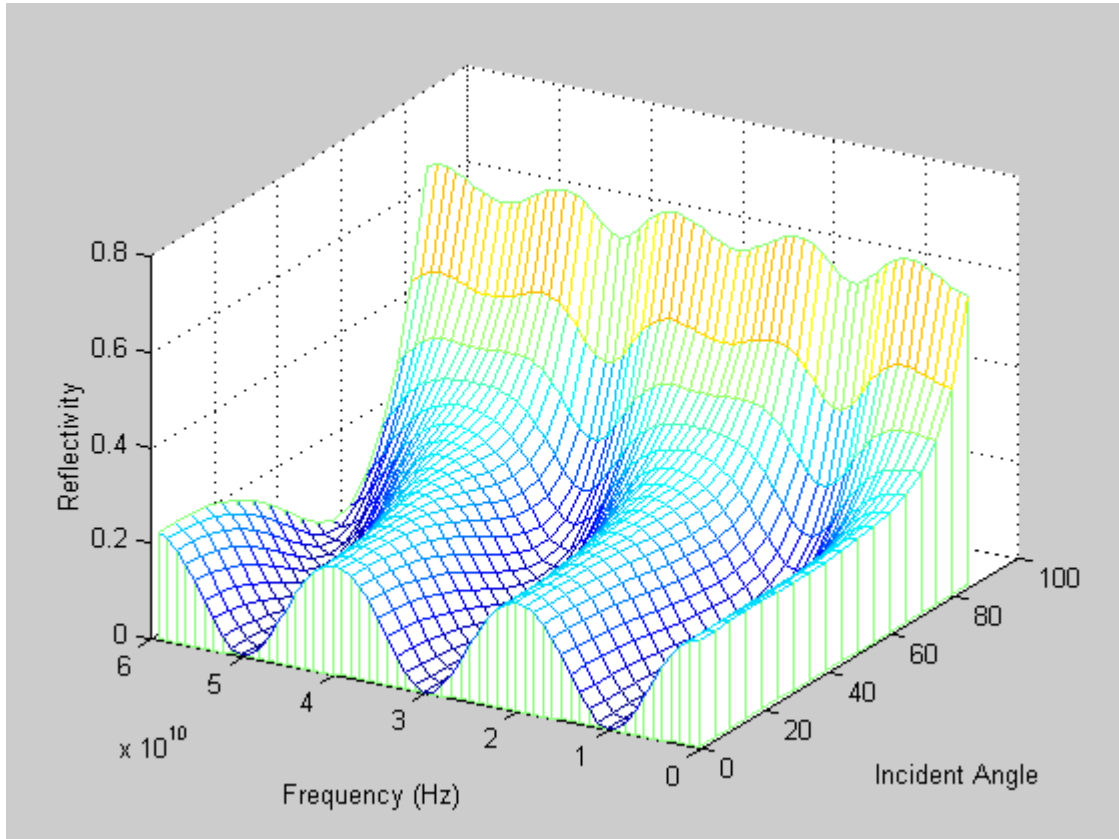


Figure 3.7. Total reflectivity as a function of frequency and incident angle for a single 0.4688 cm thick non lossy layer with $\epsilon_r = 2.56$, $\mu_r = 1.0$ and $\sigma = 0$, incident medium of air and transmitted medium with $\epsilon_r = 8$, $\mu_r = 1.0$ and $\sigma = 0$. The minimum in reflectivity again shifts to higher frequency due to a decrease in optical path length difference as the incident angle increases. Reflectivity also approaches 1 as incident angle increases. The transmittance = $1-R$.

If $N_m < N_t$ then the wave undergoes π phase shifts at the first and second interfaces so the thickness required to produce a minimum is reduced to $d = \lambda_o/4N_m = 0.4688$ cm. This is seen in Figure 3.7 where the layer has a lower refractive index than the substrate.

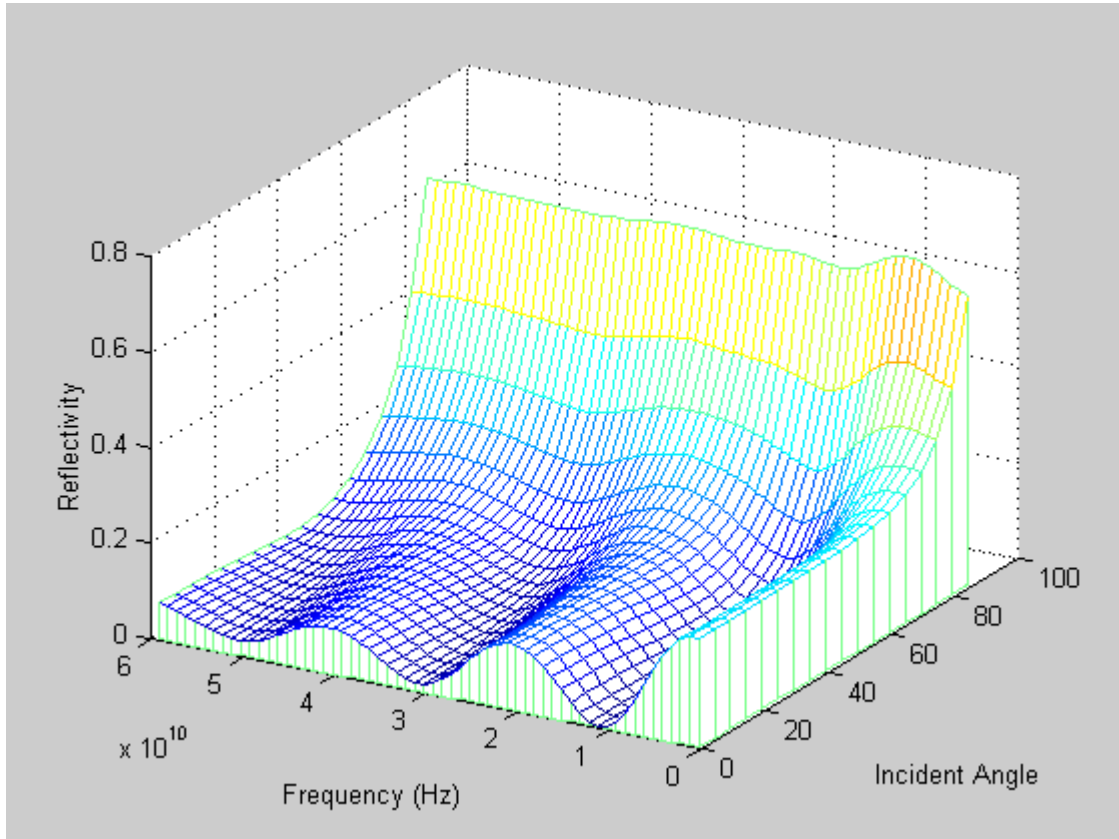


Figure 3.8. Total reflectivity of a lossy layer as a function of frequency and incident angle. System has the same parameters as modelled in Figure 3.7, however, the permittivity of the layer is now $\epsilon_r = 2.56 - 0.5i$. The effect of the absorption is to damp the reflectivity at higher frequency, due to the longer optical pathlength. As the frequency tends to infinity, the reflectivity tends to that from the first interface assuming an infinite medium (ie $R=0.0576$).

If the layer is lossy, the reflectivity decays with increasing frequency to a limiting value equal to the reflectivity from first interface (ie $R=0.0576$). The reflectivity at low frequency (long wavelength) is near that of the non-lossy material due to the layer thickness being small in comparison to the wavelength.

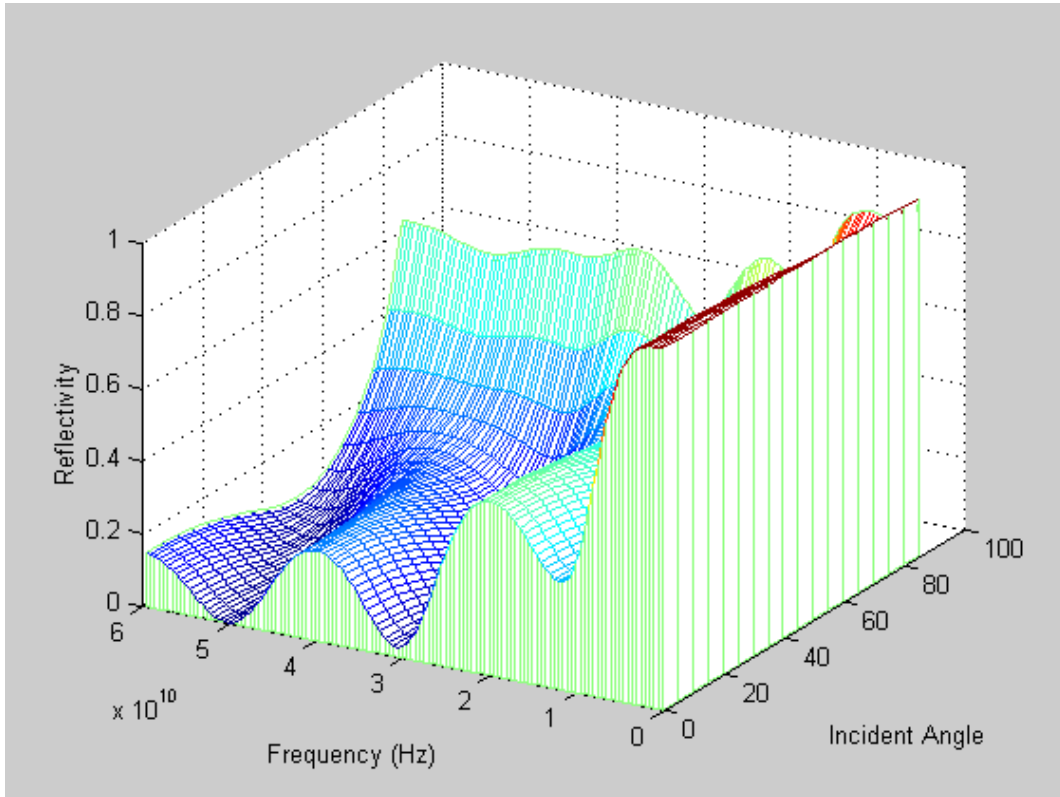


Figure 3.9. Total reflectivity from the film of Figure 3.8 mounted on a perfect electrical conductor (PEC). The overall reflectivity is much higher than seen in Figure 3.8, especially at low frequencies where the layer thickness is small in comparison to the wavelength. Again reflectivity approaches the infinite medium reflectivity (reflectivity from an interface).

When the substrate is a perfect electrical conductor (PEC), the reflectivity profile changes considerably. At low frequency, the wavelength is long and most of the radiation penetrates to and is reflected from the PEC. At high frequency (in this example 50 GHz) the reflectivity hits a minimum and then tapers off to the reflectivity from an infinite-medium interface.

The distance that a wave must travel through a lossy medium before it is attenuated to $1/e$, or 36.8%, of its original intensity is defined as the skin depth, or $1/\alpha$, where α is the attenuation given in equation 21. At 1 GHz, for the layer shown in Figure 3.9, this depth is 3 cm, at 10 GHz it has dropped to about 1 cm and it is down to about 0.4 cm at 50 GHz, which is on the order of the thickness of the layer. It is for this reason that the minima in the reflectivity are not constant as a function of frequency.

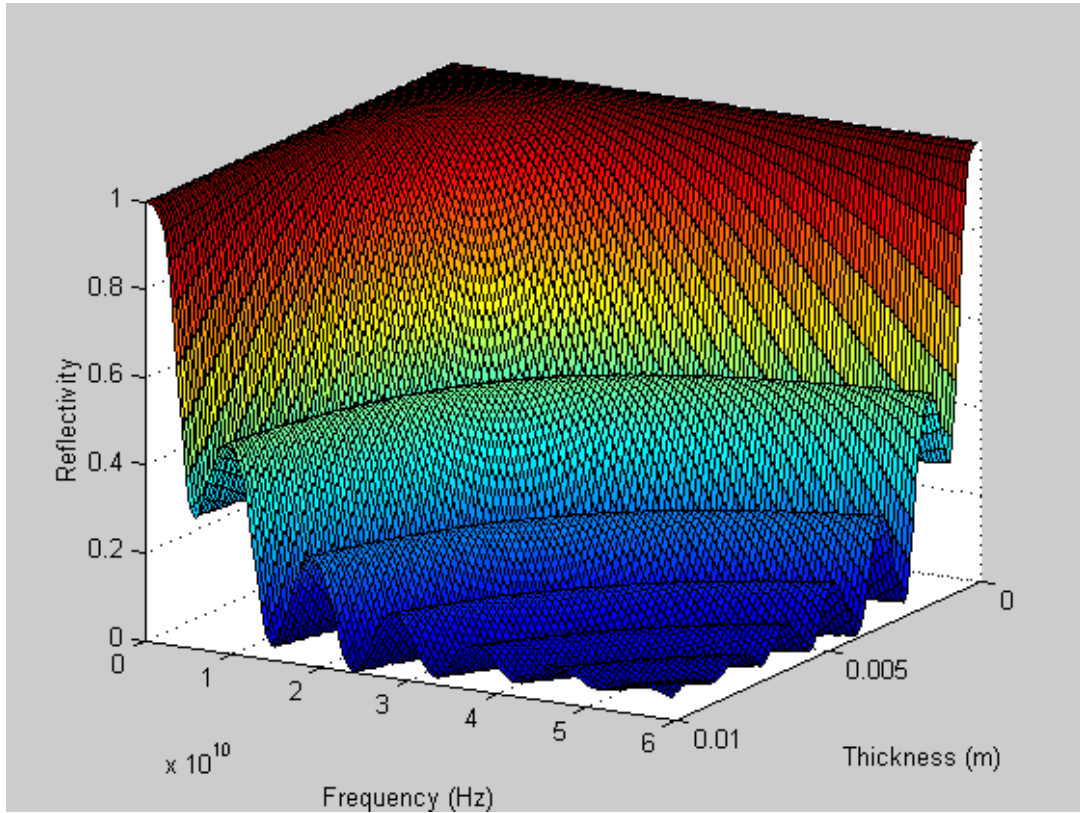


Figure 3.10. Total reflectivity from the material in Figure 3.9 mounted on a PEC as a function of film thickness. Notice the relationship between frequency and thickness.

The reflectivity of an absorbing layer is a function of the layer thickness and frequency, as shown in Figure 3.10, and these parameters are related to each other by the number of quarter-wavelengths each represents. This figure indicates that a similar reflectivity can be achieved for a thin layer at high frequency as for a thick layer at low frequency.

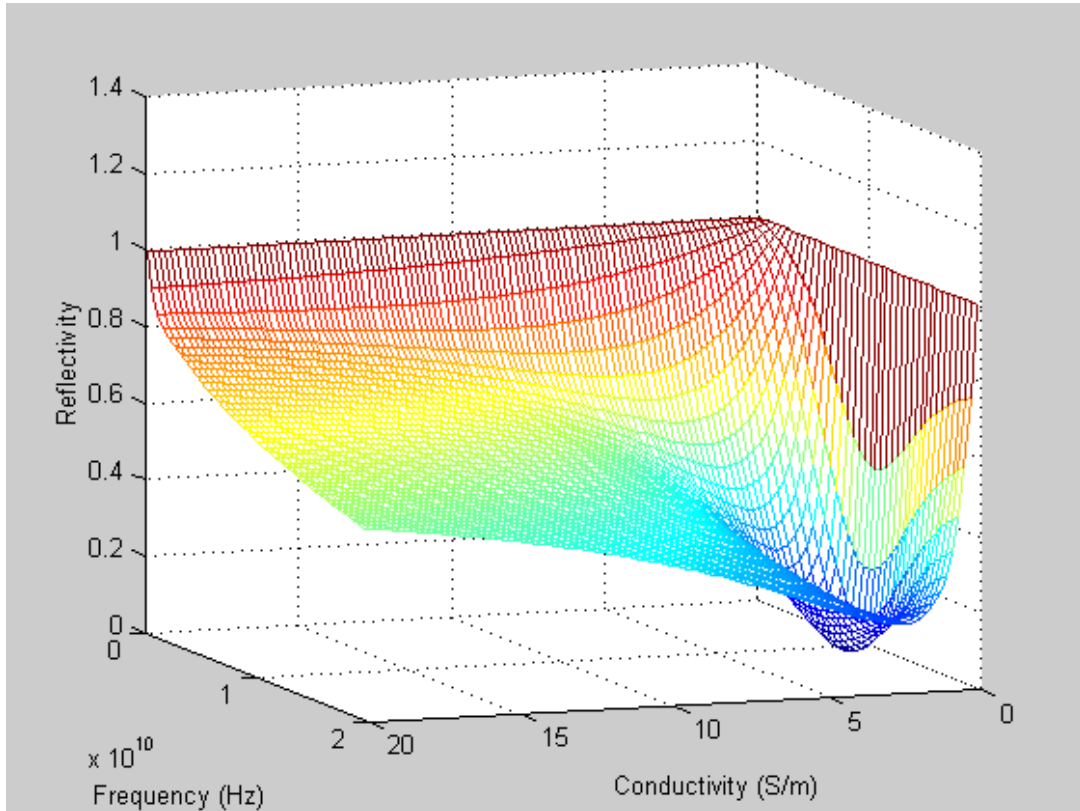


Figure 3.11. Total reflectivity of the film in Figure 3.7 as a function of film conductivity with $\epsilon_r' = 2.56$ on a PEC. Notice that the minimum reflectivity for this case results from a conductivity of about 1.1 S/m. For larger values of ϵ_r' , the minimum occurs at higher.

For the optimum design of a single layer absorber (a Dallenbach layer), equation 3.48 comes into play. The trick is to match the impedance of the layer to the impedance of air (377 ohms) by adjusting the layer's conductivity. The optimum conductivity required to achieved a minimum reflectivity at the desired frequency can be calculated from

$$\sigma_{optimum} = \frac{2}{377 \cdot d} \text{ in units of S/m}$$

where d is the actual film thickness. A requirement for a specific thickness and center frequency dictates the required permittivity necessary to achieve this. For example a 0.25 cm thick film with absorption centered at 10 GHz is the requirement. The quarter wavelength (destructive interference requirement) for 10 GHz, ($\lambda = 3$ cm) requires a 0.75 cm thick layer. However the optical thickness of the layer is approximately

$\sqrt{\epsilon_r'}$ times larger than the physical thickness (if the material is nonmagnetic, equation 3.24), so thinner films can be achieved by increasing the permittivity. In this case the thickness factor is 3, and hence the real permittivity must be about 9. The imaginary portion of the permittivity and the conductivity also influence the optical

thickness so a real permittivity of 9.5 and a conductivity of 2.2 S/m result in the optimum single layer absorber centered at 10 GHz.

Examples of two other hypothetical materials to be used for absorption at 10 GHz include a 0.1 mm thick layer with ϵ_r' of about 5700 and a conductivity of 53 S/m, and a layer of water ($\epsilon_r'=81$) with enough salt to bring the conductivity to 6.4 S/m would need to be 0.833 mm thick. The former of these two materials could possibly be crafted as a composite of isolated metal particles. The reflectivity curves for these three examples are shown in Figure 3.12. Notice how the bandwidth of the absorption decreases as the permittivity is increased. It is apparent that the optimum absorber, in terms of bandwidth, will have a permittivity as close to 1 as possible, at the expense of being a thicker film.

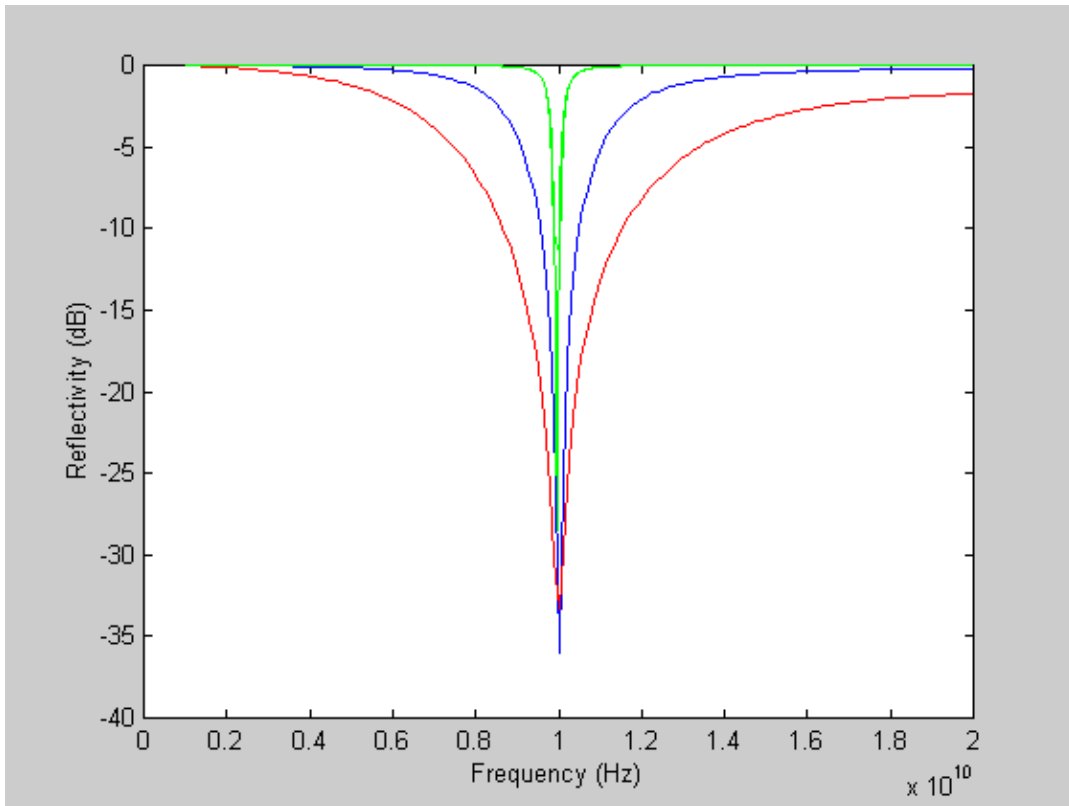


Figure 3.12. Total reflectivity from three hypothetical absorbing materials. Red, $d = 0.25$ cm, $\epsilon_r' = 9.5$ and $\sigma = 2.2$ S/m, Blue $d = 0.083$ cm, $\epsilon_r' = 81$ and $\sigma = 6.4$ S/m and Green $d = 0.01$ cm, $\epsilon_r' = 5700$ and $\sigma = 53$ S/m. Incident medium is air, and supporting medium is a PEC.

The conductivity needed to create a minimum in the reflectivity from a Dallenbach layer is quite small and achievable from a number of materials. The bandwidth of a Dallenbach layer limits the utility of this type of material.

It will be noticed that the reflectivity in Figure 3.12 is reported in units of decibels (dB). The number for the decibel scale is achieved from $R_{dB} = 10\log(R)$.

Sometimes the reflectivity coefficient is used to determine the decibel parameter and the equation is then $r_{dB} = 20 \log(r)$.

3.3.3 Magnetic Material

Magnetic materials that have been used for RAM include carbonyl iron and ferrites. The iron particles are conducting so they need to be kept isolated in a matrix. This results in a lower packing density than the ferrites, which are not conductors. Particle size is an important factor affecting the material's permeability.

A material with its permeability equal to the permittivity, in both real and imaginary

parts, results in an impedance of the layer of Z_o ($Z = Z_o \sqrt{\frac{\mu_r}{\epsilon_r}}$). When this case

arises, the material is impedance matched to air and no reflection occurs at the air/material interface. The wave propagating through the material is attenuated (equation 3.22). This is seen (Figure 3.13), at normal incidence, as the linear decrease in reflectivity as a function of frequency. This state is hard to achieve though as both the real and imaginary components of the permittivity and permeability have to be matched.

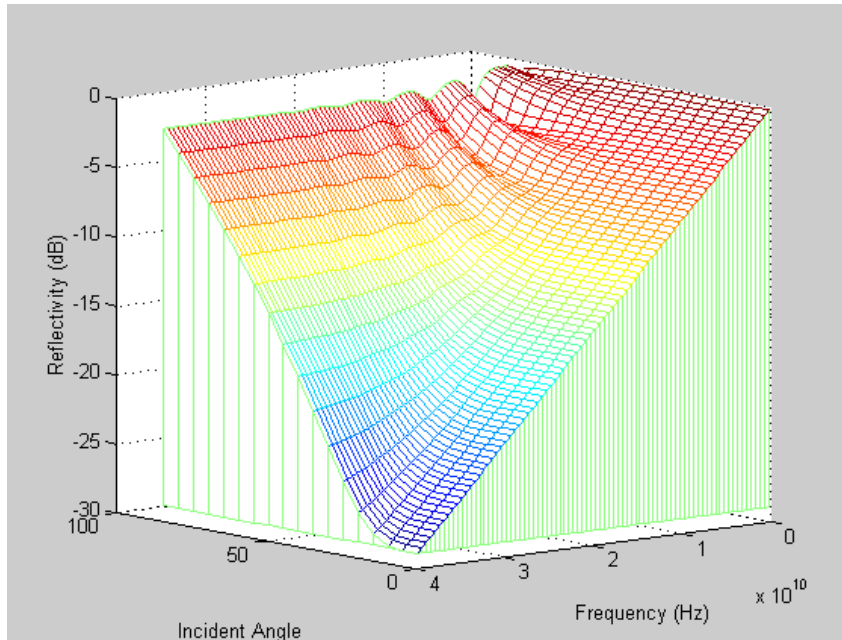


Figure 3.13. A special case arises for a material with equal permittivity and permeability. The impedance of material and air are matched and the reflectivity at zero incident angle is a linear function of the film thickness. ($air/d=0.004$ m, $\epsilon_r= 3.9-0.5j$, $\mu_r=3.9-0.5j$ /PEC).

Currently existing magnetic materials tend to have appreciable permittivity. Hybrid materials containing lossy electric and magnetic components can improve absorber properties as seen in Figure 3.14. The reflectivity and bandwidth are greatly improved, though the trade off with using magnetic materials is of course their density. The material simulated in Figure 3.14 does not account for the frequency dependence of the permittivity and permeability and therefore presents a better absorber than may be achieved in practice.

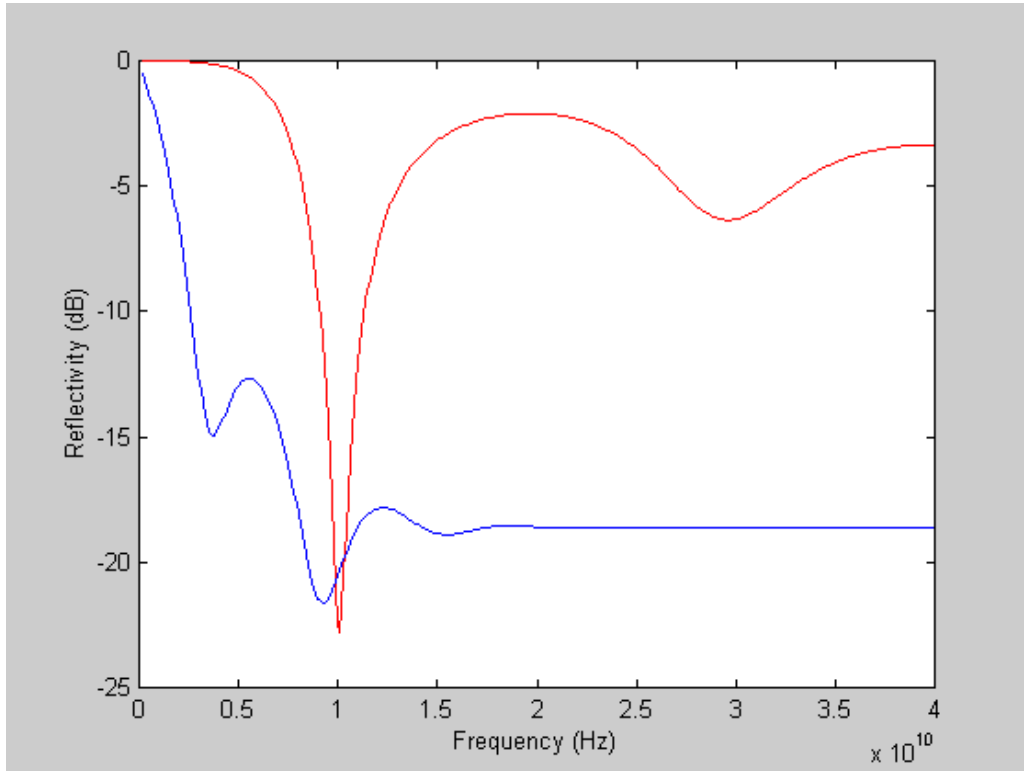


Figure 3.14. Comparison of the total reflectivity from an electric (red) and a hybrid, electric-magnetic (blue) absorber. The reflectivity is lower over most of the frequency range for the hybrid material (Red air/d=0.001875 m, $\epsilon_r = 16 - 5.8i$, $\mu_r = 1$ /PEC, Blue air/d=0.001875 m, $\epsilon_r = 16 - 5.8i$, $\mu_r = 10 - 3.6i$ /PEC).

3.4 Reflection from Multiple Layers

Reflection from a multilayer^[1,3] can be treated in the same manner as reflection from a single layer. For a multilayer there is a specific matrix M_i (as in equation 3.66) for each layer, excluding air and the final substrate. A resultant matrix is obtained from the product of all the layer matrices and this can then be used as the matrix in equation 66 to calculate the reflection, transmission and absorption.

$$M_{total} = \begin{bmatrix} m_{11} & m_{12} \\ m_{21} & m_{22} \end{bmatrix} = \prod_{i=2}^{L-1} M_i \quad 3.78$$

This approach is often called the cascading matrix method or the optical matrix method.

Bandwidth and reduced reflectivity can be improved by increasing the number of absorbing layers in a material. One useful technique that has been employed is to use a material with a refractive index (impedance) gradient. Small steps in wave impedance from air to absorber, allow waves to penetrate into the absorbing body with minimal reflection at the air-absorber interface. This class of absorber is referred to as impedance matching. One of the most effective absorbers consists of a pyramidal surface structure: presenting an impedance gradient. The pyramidal structure can be approximated by a series of slabs with increasing impedance into the absorber, however, diffraction or off specular effects need to be taken into consideration when the wavelength is on the order of the size of the surface features.

Resonant absorbers, of which the “quarter wavelength” Dallenbach layer is the simplest, can be improved on by the addition of more layers and using impedance matching techniques. These types of absorbers tend to be thinner than the purely impedance matching absorbers which are typically on the order of several wavelengths thick. A variation on the Dallenbach layer is the Salisbury Screen also a quarter wavelength absorber, where a thin resistive sheet is spaced a quarter wavelength in front of a PEC. The reflectivity of a Dallenbach layer and a Salisbury Screen are compared in Figure 3.15. The bandwidth of the Salisbury screen is larger than that of the Dallenbach layer. Remember that high permittivity results in a narrow bandwidth for a Dallenbach layer (Figure 3.12) and most of the Salisbury screen has low permittivity foam as the spacer.

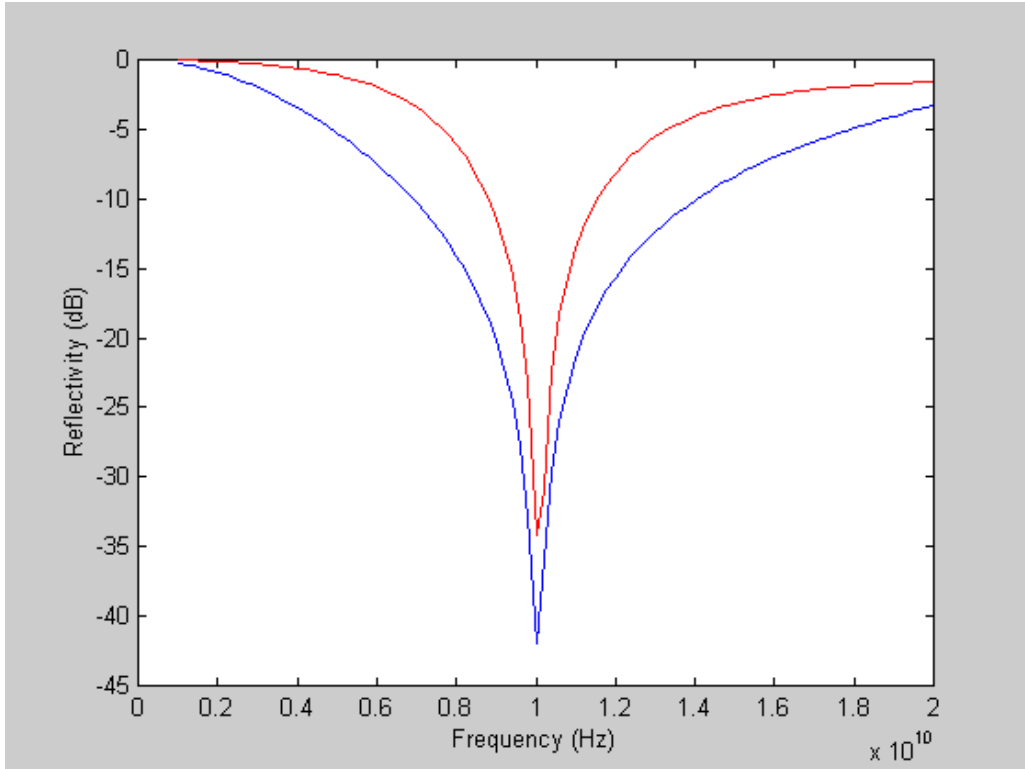


Figure 3.15. Reflectivity from a Salisbury Screen (blue) and a Dallenbach layer (red), optimised for a minimum at 10 GHz. The bandwidth of the Salisbury screen is seen to be larger than that of the Dallenbach layer. (parameters Dallenbach Layer air/ absorber $d=0.0024$ m, $\epsilon_r=10$, $s=2.2$ S/m./ PEC. Salisbury Screen, air/ absorber $d=0.0001$ m, $\epsilon_r=20$, $s=27$ S/m, spacer $d= 0.0055$ m, $\epsilon_r=1.05$ / PEC). The bandwidth is 2.2 GHz for the Salisbury Screen and 0.8 GHz for the Dallenbach layer at a reflectivity of -20 dB.

The optimum conductivity for the Salisbury screen is determined from

$$\sigma_{optimum} = \frac{1}{(377 * d)},$$

where d is the thickness of the resistive screen. The screen is

then spaced a distance from the PEC substrate that is dependent on the permittivity of the spacer. A high permittivity for the spacer results in a thinner absorber, at the cost of bandwidth. The optimum bandwidth is obtained with the smallest permittivity as seen for the Dallenbach layer (Figure 3.12). When the conductivity is not at the optimum value, the reflectivity of the layer increases, (Figure 3.16).

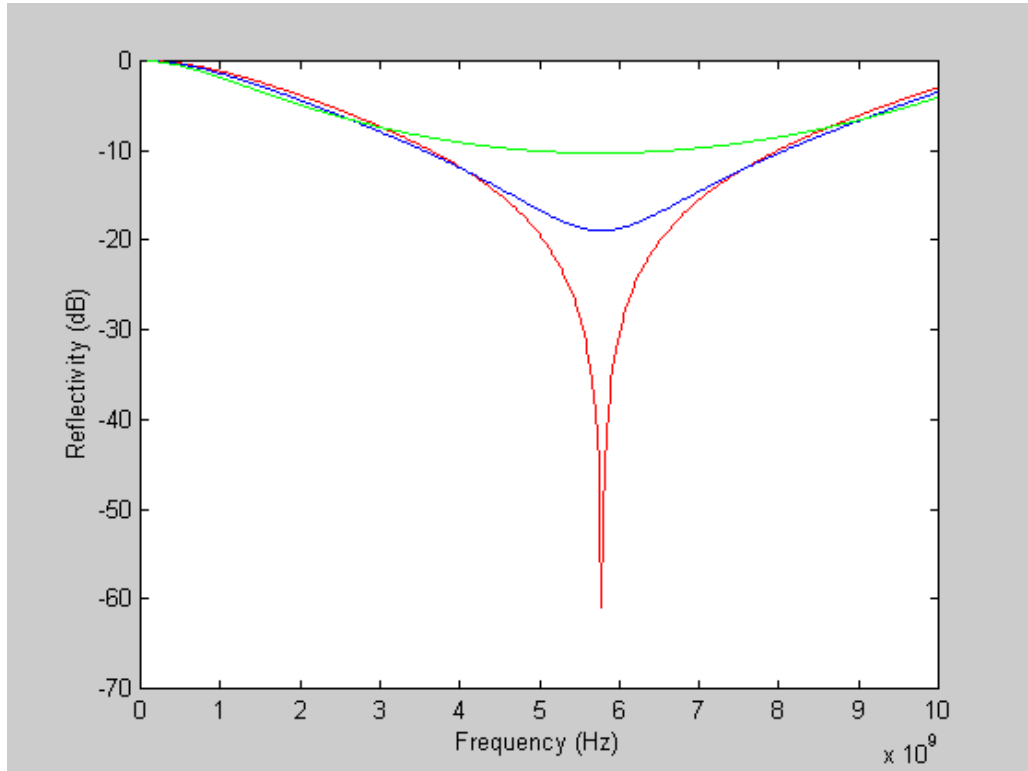


Figure 3.16. Reflectivity from a Salisbury Screen as a function of the layer impedance. Red = 377 ohms, Blue = 300 ohms, green = 200 ohms. This repeats figure 8.9 of reference^[6].

Some methods used for modelling the reflectivity from a multilayer stack (such as the Salisbury) assume that the resistive sheets are very thin and can be neglected. The method used here assumes that the resistive sheets have a thickness.

The bandwidth of the Salisbury Screen can be improved by adding more quarter wavelength-spaced layers. This structure is called a Jaumann device, and is analogous to the anti-reflective coatings found in visible optics, which is comprised of stacks of high and low refractive index material to reduce reflections. Figure 3.17 shows the affect of increased layers on the bandwidth with the parameters listed in Table 3.1. Beyond two layers the problem cannot be analytically optimised and iterative optimisation routines are required to maximize bandwidth while minimizing reflectivity and thickness. The optimization of a 4 resistive sheet stack by trail-and-error simulation becomes very difficult due to the number of variables. For these structures the material has been optimized for maximum bandwidth with the reflectivity below -20 dB without attention to the overall thickness, which has increased from 6.65 mm for the Salisbury screen to 19.95 mm for the 3 resistive-sheet Jaumann structure. The bandwidth as a function of frequency and incident angle can be seen in Figure 3.18.

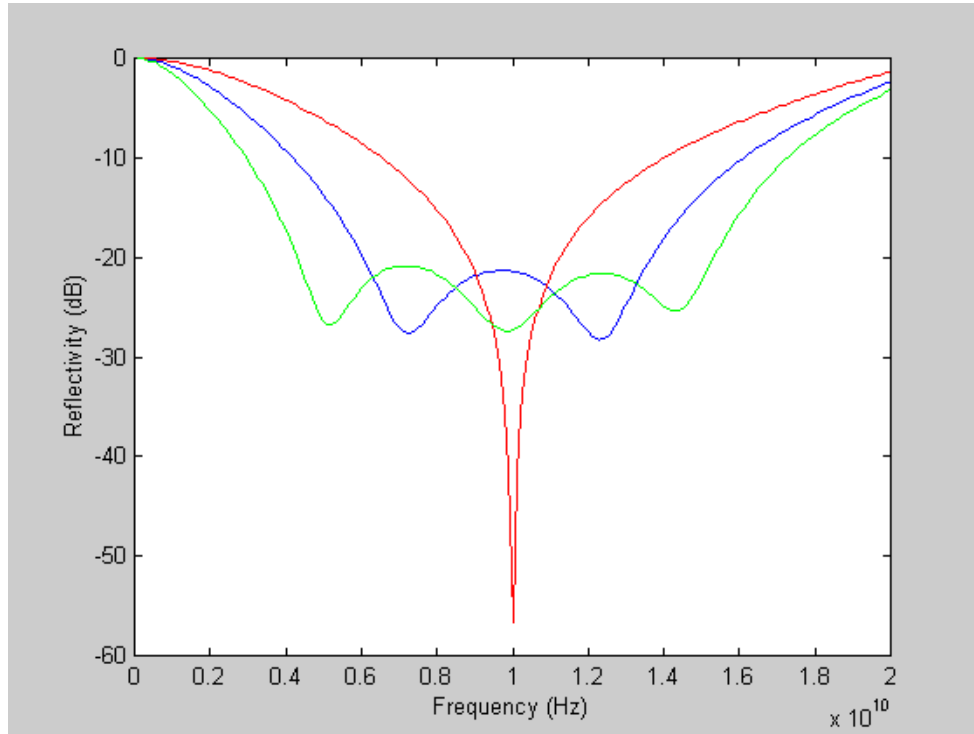


Figure 3.17. Reflectivity from Jaumann structures with 1(red), 2(blue) and 3(green) resistive sheets. The spacers are 0.00655 m thick and the resistive sheets are 0.1 mm thick with ϵ_r of 9.

To optimise the design of Jaumann layers several methods have been tried:

1. Binomial Design (Maximally Flat), where the reflectivity decreases from both sides of the bandwidth towards the centre frequency.^[1]
2. Tschebyscheff Design (Equal-Ripple), where the reflectivity is below the required reflectivity minimum and follows a ripple pattern, as per Figure 3.17.^[1]
3. Genetic Algorithm a stochastic method based on the principles of genetics and evolution that uses available material properties to design the optimum absorber based on requirements such as minimum reflectivity and thickness with maximum bandwidth.^[10,11]

The genetic algorithm is very flexible and can optimize absorber design based on a catalogue of available materials and their optical properties.

Current efforts in the literature are focused on absorbing devices based on circuit analog materials (frequency selective surfaces) and their optimization through the use of micro-genetic algorithms.^[12,13] Capacitive and inductive elements, in the frequency selective surface, provide more loss pathways and hence greater potential for creating wide bandwidth materials.

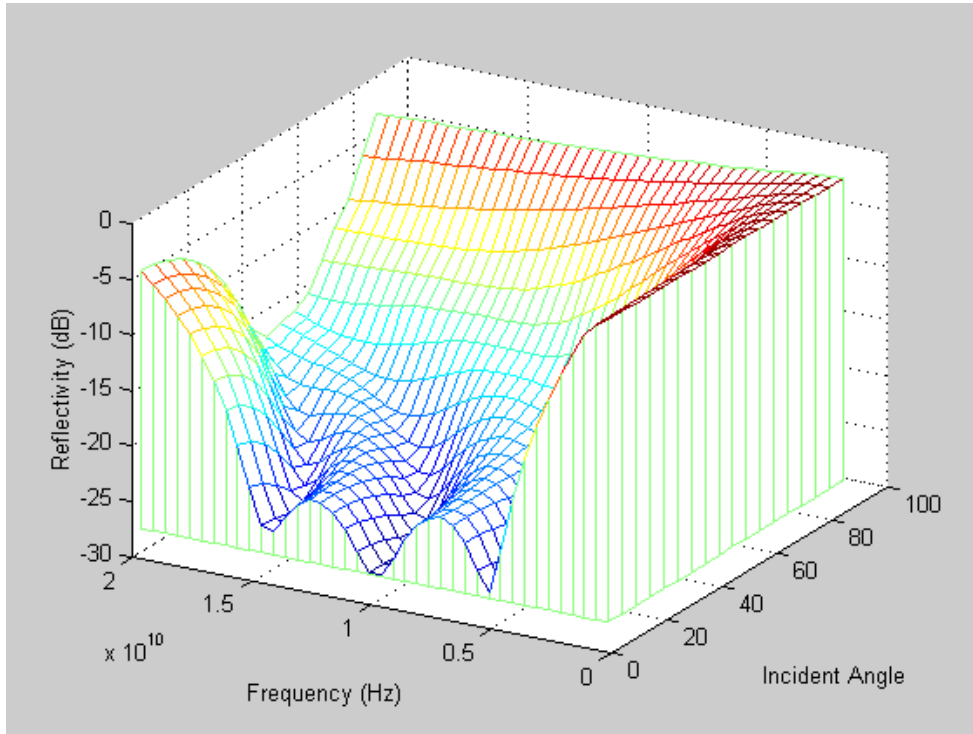


Figure 3.18. Reflectivity from three layer Jaumann centered at 10 GHz with reflectivity below -20 dB. Parameters as per Table 3.1.

Table 3.1. Material Thickness and Properties for Jaumann Layers

Media / d (m)	ϵ_r'	μ_r'	σ (S/m)
Salisbury Screen			
Air	1	1	0
0.0001	9	1	26.5
0.00655	1.03	1	0
PEC			
Jaumann 2 Layer			
Air	1	1	0
0.0001	9	1	8.5
0.00655	1.03	1	0
0.0001	9	1	33.5
0.00655	1.03	1	0
PEC			
Jaumann 3 Layer			
Air	1	1	0
0.0001	9	1	5.5
0.00655	1.03	1	0
0.0001	9	1	12.5
0.00655	1.03	1	0
0.0001	9	1	37.0
0.00655	1.03	1	0
PEC			

3.5 Conclusions

Development of radar absorbing material requires knowledge of the interaction of electromagnetic radiation with matter. From the material side, having the ability to make materials with specific complex permittivity and permeability over a suitable frequency range is essential. The optical properties can be modelled with the theory given here to determine the reflectivity of an absorber as a function of frequency, incident angle, conductivity and thickness. The wavelength of the microwave radiation, physical optics for resonance absorption and the nature of absorbing materials are at odds with military requirements of low reflectivity, thin materials and wide absorption bandwidth: optimization of one feature often comes at the expense of another.

Matching the impedance of the absorber with that of air helps minimize the reflectivity. Impedance matching can be accomplished by graded interfaces or by matching the permittivity to the permeability of the absorbing layer.

A single (Dallenbach) layer of lossy material acts as an amplitude splitting device, which results in a resonance, or destructive interference. The resonance occurs at frequencies, which are half wavelength multiples of the layer's optical thickness if the layer is mounted on a transmitting medium, and quarter wavelength multiples when mounted on a PEC. The reflectivity reaches a minimum when the optical thickness of the film is on the order of the skin depth for the material, and a resonance condition occurs. For thick absorbing layers or high frequency, the reflectivity levels off at the reflectivity calculated from the first interface alone. The conductivity required to match the impedance of a material with air depends on the thickness and permittivity of the layer. The frequency bandwidth of the absorption depends on the permittivity with low values favouring larger bandwidths. Hybrid absorbers containing electric and magnetic materials would provide the best single layer absorber. The minimum reflectivity shifts to higher frequency as the incident angle increases. The conductivity required to produce an optimum absorbing material is small and easily achieved with materials such as conducting polymers, and carbon and metal powders.

Multilayer absorbers include stacked Dallenbach layers, Salisbury screens and Jaumann layers. These multilayer devices can be designed to improve on the bandwidth obtained with the Dallenbach layer. Impedance matching / graded impedance techniques are used to minimize the reflectivity from these resonant absorbers. The penalty is the increase in absorber thickness. Optimization techniques are needed for multilayer materials.

3.6 Future Work

Improvements to the code used for the simulations in this report can be made in the following areas

1. Currently the theory and code only accounts for single reflections from an interface. Even for a single layer, the ray that is reflected from the medium /

substrate interface will be partially reflected from the air/medium interface and so on. The return is diminishing and so the inclusion of 2 or 3 reflection terms will provide an accurate answer.

2. The complex permittivity and permeability of real materials have a frequency dependence. This is very evident for magnetic materials where the frequency dependence is a function of the particle size. For predicting accurate absorber characteristics the frequency dependent permittivity and permeability need to be used in reflectivity simulations.

The design process of multilayer absorbers also needs to be optimized. Approximate solutions to optimized multilayer structures have been presented in the literature, and these need to be considered for inclusion in a modelling package.

It is the goal of this project to be able to make materials with specific optical properties, model the reflectivity from absorbing devices created with these materials and to optimize the characteristics of absorbers for various applications.

3.7 References

- (1) Balanis, C. A., *Advanced Engineering Electromagnetics*; John Wiley and Sons, **1989**.
- (2) Born, M., Wolf, E., *Principles of Optics: Electromagnetic Theory of Propagation, Interference, and Diffraction of Light.*; Pergamon Press: New York, **1975**.
- (3) Hecht, E., Zajac, A., *Optics*; Addison-Wesley: London, **1979**.
- (4) Wooten, F., *Optical Properties of Solids*; Academic Press: New York, **1972**.
- (5) Macleod, H. A., *Thin-Film Optical Filters*; Adam Hilger: London, **1981**.
- (6) Knott, E. F., Shaeffer, J.F., Tuley, M.T., *Radar Cross Section*; 2Rev. ed ed.; Artech House: Norwood, **1993**.
- (7) Vinoy, K. J., Jha, R.M., *Radar Absorbing Materials: From Theory to Design and Characterization*; Kluwer Academic Publishers: Boston, **1996**.
- (8) Pascoe, K. J., "Reflectivity and Transmissivity through Layered, Lossy Media: A User-Friendly Approach," Graduate School of engineering and Management Air Force Institute of Technology Wright-Patterson Air Force Base, **2001**, AFIT/EN-TR-01-07.
- (9) Stratton, J. A., *Electromagnetic Theory*; McGraw-Hill, **1941**.
- (10) Weile, D. S., Michielssen, E., Goldberg, D.E., *Genetic Algorithm Design of Pareto Optimal Broadband Microwave Absorbers, IEEE Transactions on Electromagnetic Compatibility* **1996**, 38, 518 - 525.
- (11) Johnson, J. M., Rahmat-Samii, Y., *Genetic Algorithms in Engineering Electromagnetics, Antennas and Propagation Magazine, IEEE* **1997**, 39, 7-21.
- (12) Chakravarty, S., Mittra, R., Williams, N.R., *Application of a Microgenetic Algorithm (Mga) to the Design of Broadband Microwave Absorbers Using Multiple Frequency Selective Surface Screens Buried in Dielectrics, Antennas and Propagation, IEEE Transactions on* **2002**, 50, 284 - 296.
- (13) Chakravarty, S., Mittra, R., Williams, N.R., *On the Application of the Microgenetic Algorithm to the Design of Broad-Band Microwave Absorbers Comprising Frequency-Selective Surfaces Embedded in Multilayered Dielectric Media, Microwave Theory and Techniques, IEEE Transactions on* **2001**, 49, 1050 - 1059.

4. Organic Radar Absorbing Materials

Conducting polymers have the potential to be used as RAM, providing a lightweight alternative to other materials. Moreover, the conductivity of these polymers can be tailored, enabling more scope in absorber design.

In order to absorb radar (high frequency electromagnetic radiation), materials must interact with either the electric field of the radiation. Conducting polymers are electrically conductive and therefore interact with the electric component of EM radiation. The dielectric constant, or permittivity, ϵ , describes how a material interacts with EM radiation. The permittivity is a complex number, $\epsilon = \epsilon' - j\epsilon''$, in which the imaginary component, ϵ'' , represents the loss as a result of the interaction. When EM radiation impinges on a lossy material, the electric field induces oscillation of the conducting electrons. The current flow is proportional to the electric field strength by the resistance of the material. Electrical energy is converted to thermal energy as a consequence of the current flowing through a resistor. The loss tangent, $\tan \delta_e$, is a function of the conductivity and permittivity of the material, as well as the angular frequency of radiation. It is used to differentiate between a good conductor and a good insulator. If the loss tangent is greater than 1, the material is a good conductor. The material is an insulator if the loss tangent is less than one.

$$\tan \delta_e = \frac{\sigma + \omega\epsilon''}{\omega\epsilon'} \approx \frac{\epsilon''}{\epsilon'} \quad (4.1)$$

Effort needs to be extended to determine the conductivity and permittivity of conducting polymers. Effort also needs to be made for determining the synthetic conditions that can be used to control the polymers conductivity in a reproducible manner. Conductive polymers do not have very useful material properties in terms of processing them directly into shaped objects or coatings. For this reason they must be formulated into coatings or fabricated into composite materials. Processing steps add more research requirements into reproducibly fabricating the same conductor-matrix distribution, and control of the permittivity-conductivity of that material. Finally material property stability is important. Conducting polymers can thermally and chemically decompose. These processes reduce the conductivity and permittivity. An absorber's performance is dependent on these properties and therefore its stability must be assessed and improved on.

The objective of the section is to present results achieved in the synthetic control of conducting polymers, and their processing into usable materials. Also the stability of new conducting polymers is explored, as is the stability of existing material.

4.1 Conducting Polymers

Conducting polymers possess a conjugated π system and exhibit a dramatic increase in electrical conductivity upon doping (generally oxidation of π electrons from the

conjugated π system). The three most common conducting polymers are polyaniline (PAni), polypyrrole (PPy), and polythiophene (PTh) (see Figure 4.1). The structure of polyaniline differs from both polypyrrole and polythiophene, in that the heteroatom is not part of the ring system, and takes part in the π -conjugation. Doping of these conducting polymers usually results in a positively charged backbone and counteranions in close proximity. Doping of polypyrrole and polythiophene occurs by the removal of electrons (oxidation) from the conjugated pi system. This is accomplished either chemically or electrochemically. Polyaniline is most commonly prepared by chemical oxidative polymerization of aniline in acidic solution. The positively charged backbone, and thus the formation of charge carriers is achieved by the protonation of nitrogen atoms (specifically the imine sites), known as acid doping.

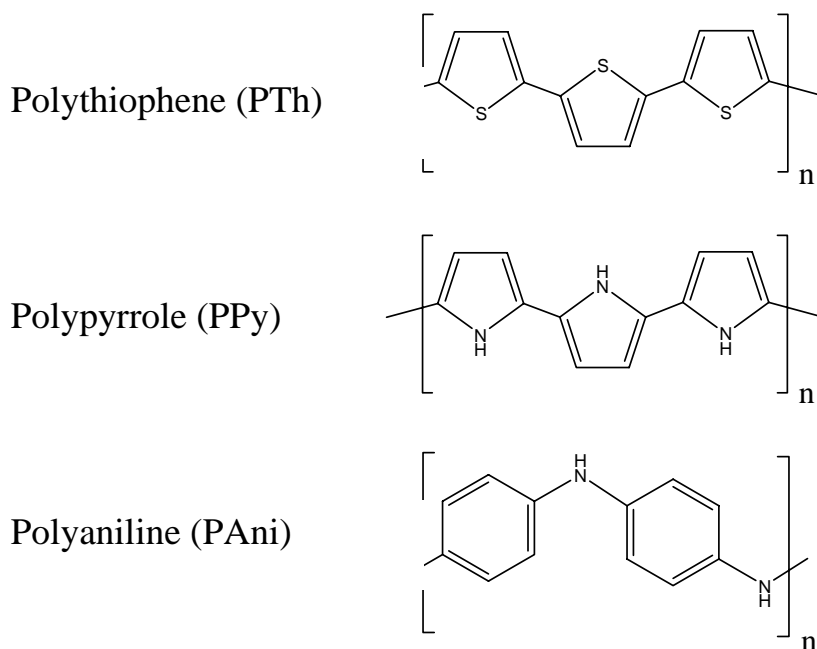


Figure 4.1. Common conducting polymers, (top-bottom) polythiophene, polypyrrole and polyaniline.

4.2 Polyaniline

Polyaniline can exist in a range of oxidation states from leucoemeraldine (most reduced) through emeraldine (half oxidized) to pernigraniline (most oxidized). Oxidation of the backbone chain results in the oxidation of amine nitrogen atoms to imine nitrogen atoms, as well as the conversion of benzenoid phenyl rings to quinoid rings. The varying oxidation states are illustrated in Figure 4.2 using octamers of aniline.

The most common method of doping polyaniline involves the protonation of the imine sites, yielding a positively charged backbone and counteranions in close proximity (see Figure 4.3). The resulting structure quickly relaxes, ultimately yielding the polaron, the most common charge carrier in polyaniline.

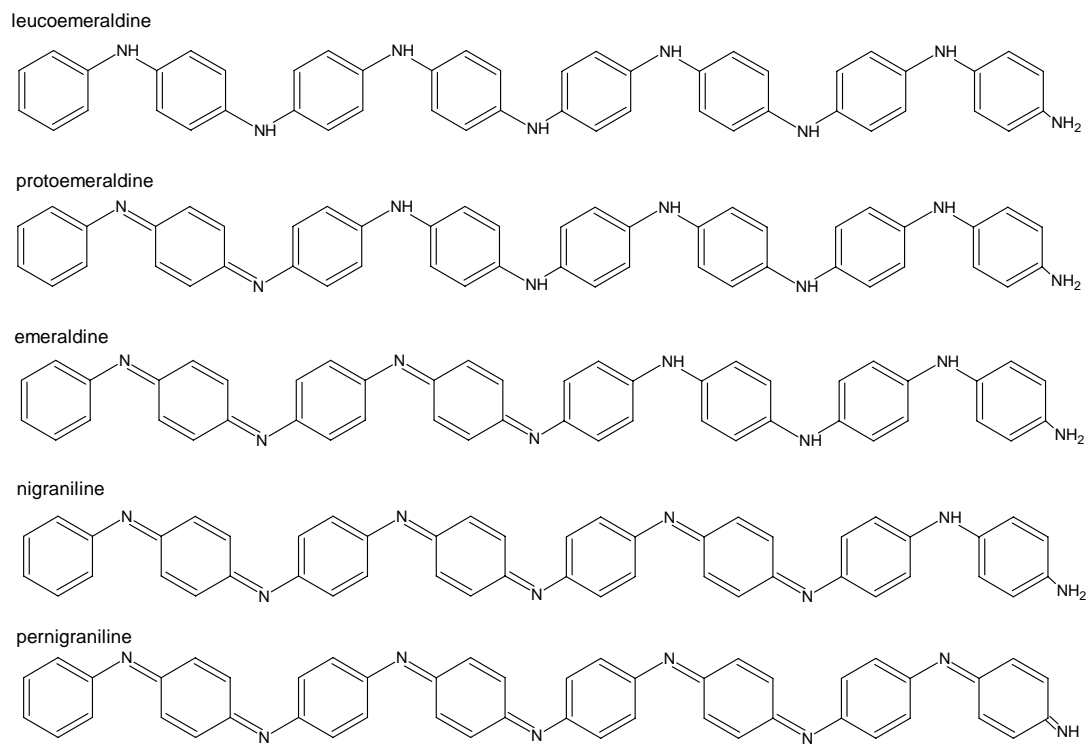


Figure 4.2. Variable Oxidation State Octamers of Aniline

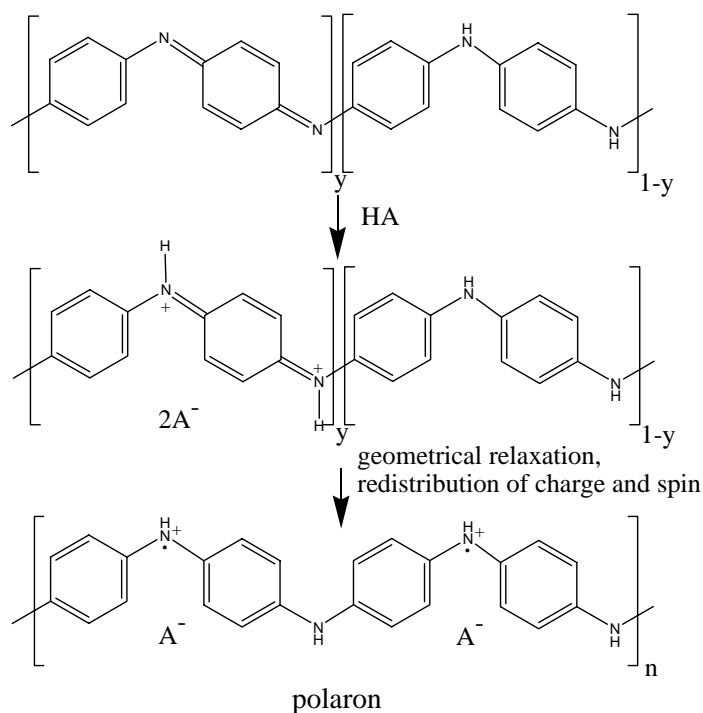


Figure 4.3. Acid Doping of Polyaniline: The Formation of Charge Carriers

There are a number of factors that affect the morphology, and thus the electrical conductivity of conducting polymers. The morphology is largely influenced by the synthetic conditions, hence one of the goals of the TIF project was to systematically assess the effect of various synthetic parameters on electrical conductivity, as measured by the dc conductivity. The conductivity depends directly on the number of charge carriers, n , the charge on the carriers, q , and the mobility of the charge carriers, η (see Equation 4.2).

$$\sigma = nq\eta \quad 4.2$$

Furthermore, there are two contributors to electrical conductivity for conducting polymers, the intrachain conductivity, in which charge transport occurs along the chain, and the interchain conductivity, in which charge hopping between neighbouring chains occurs.

$$\sigma_{\text{total}} = \sigma_{\text{intrachain}} + \sigma_{\text{interchain}} \quad 4.3$$

The intrachain conductivity depends largely on the conjugation length (CL), which is a measure of the extent of conjugation along the chain, whereas the interchain conductivity is primarily dependent on the polymer morphology. In the case of polyaniline, the interchain contribution is predominant. Synthetic parameters that influence the proximity of neighbouring chains will affect the interchain conductivity, whereas those that influence the conjugation length will affect the intrachain conductivity.

Much of the TIF work on polyanilines involved experiments in which a number of different synthetic parameters were varied and the products were characterized in order to assess their effect on the polymer product. In addition to varying reaction conditions, copolymers were prepared and aniline derivatives were introduced. The use of substituted aniline monomers is expected to result in polyanilines that exhibit lower conductivity, but are much more soluble in common solvents, resulting in more processible products. Characterization of the samples involved measurement of the dc conductivity, as well as the measurement of the permittivity of composites or fabric-coated samples.

Additional research focussed on the preparation and characterization of polyaniline-coated carbon nanotubes and nanofibres. There is precedent in the literature for the existence of electronic interaction between conducting polymers and carbon nanotubes. Such an interaction has been found to result in enhanced capacitance values relative to the parent components, thus these composites are of interest for a number of potential applications including RAM.

4.2.1 Effect of Synthetic Parameters on Conductivity: Polyaniline

Polyaniline was synthesized under a wide range of synthetic conditions, in order to assess their effect on dc conductivity, and in some cases the permittivity. Based on dc conductivity measurements, it was found that the nature of the dopant, the oxidant/monomer ratio, and the pH (thus degree of protonation) exhibited the greatest influence on the electrical conductivity. Also investigated were the effects of temperature and time, although these parameters appeared to have much less influence on the electrical conductivity.

These results may be understood by considering the contributing factors to electrical conductivity. Given the predominance of the interchain contribution, the influence of the dopant, which strongly affects the distance between neighbouring chains, is readily explained. Table 4.1 gives the structure of each dopant, and Figure 4.4 presents the conductivity as a function of dopant. An inverse relationship between the dopant size and polymer conductivity is readily apparent; the larger the dopant the farther apart the neighbouring chains, thus the lower the interchain conductivity.

The oxidant/monomer ratio affects the average oxidation state of the polyaniline chain; given that the emeraldine oxidation state (half-oxidized) yields the most conductive polymer when doped (due to having the largest number of charge carriers), it stands to reason that both high and low oxidant/monomer ratios should yield less conductive polymers. Oxidant/monomer ratios that are low or high should yield polyaniline in the leucoemeraldine, or pernigraniline oxidation states, respectively. These oxidation states are not particularly conductive as the number of charge carriers is fairly low. This is precisely what was observed experimentally, (see Figure 4.5). It was also observed that the yield increased with increasing oxidant/monomer ratio, which is explainable from a kinetics standpoint. The higher the oxidant concentration, the faster the reaction, thus more product is formed.

Table 4.1: Dopant Structure

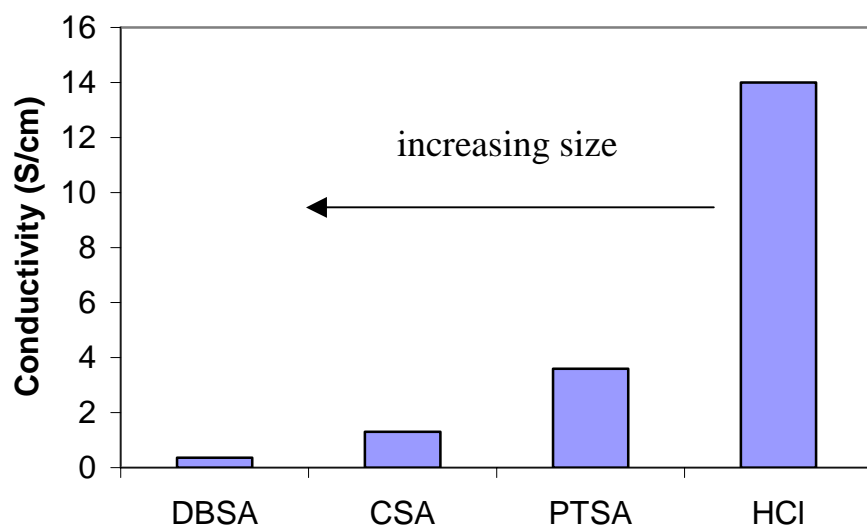
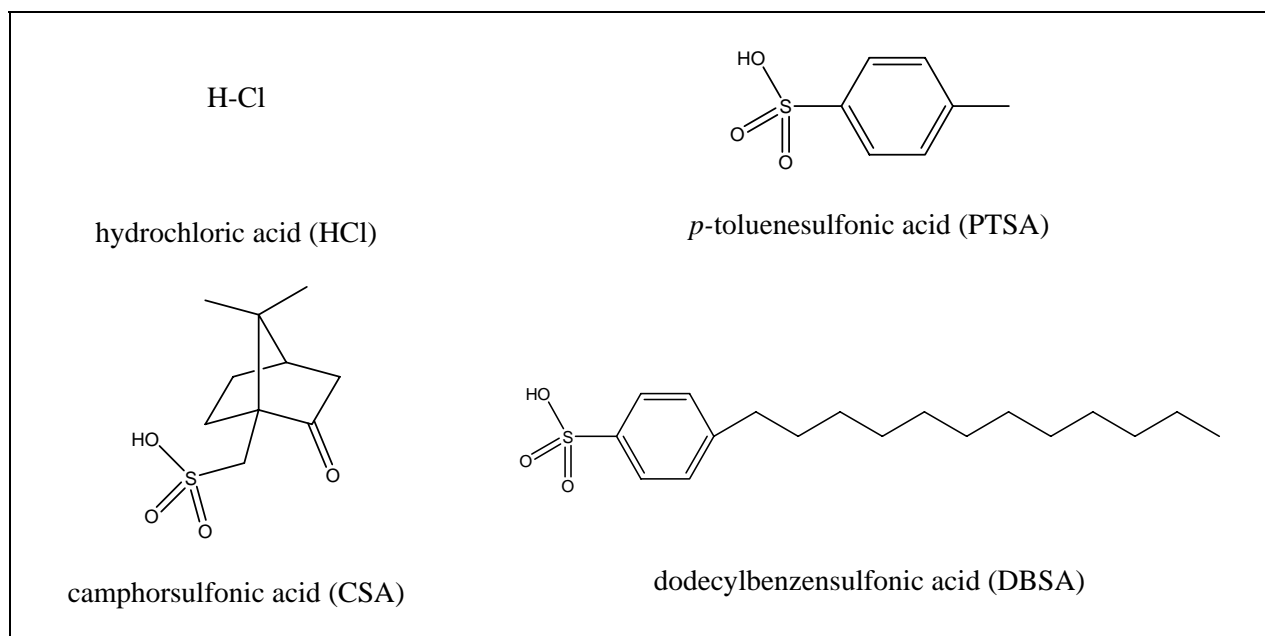


Figure 4.4. Conductivity as a Function of Dopant Structure

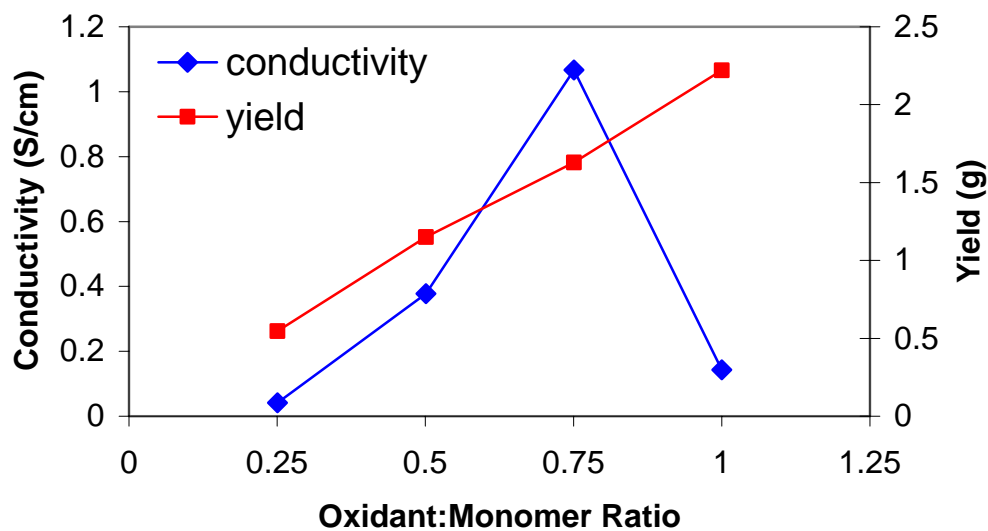


Figure 4.5. Conductivity and Yield as a Function of Oxidant: Monomer Ratio

The conductivity's dependence on the acid concentration, and thus the pH, can also be attributed to the number of charge carriers, with a higher acid concentration (lower pH), resulting in a higher degree of protonation of imine sites, hence a greater number of charge carriers (see Figure 4.6).

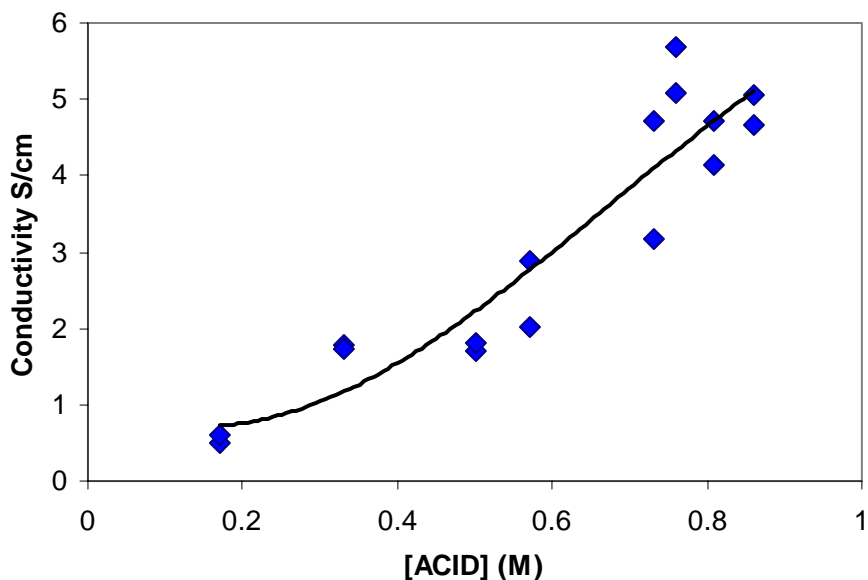


Figure 4.6. Conductivity as a Function of Acid Concentration

4.2.2 Effect of Substituents on Conductivity: Polyaniline

It is well known that polymerizing aniline derivatives (aniline containing a non-hydrogen substituent), results in less conductive polymers, however, with the reduction in conductivity comes improvement in solubility, and therefore processibility. In order to assess whether the trade-off is worthwhile, a number of copolymers and polyaniline derivatives were prepared and characterized. The reduction in conductivity may be attributed to two factors: twisting of the polymer backbone to accommodate the steric requirements of the non-hydrogen substituent, which results in poorer orbital overlap in the conjugated pi system, and an increase in interchain distance due to the larger size of the substituent relative to hydrogen. In addition, the nature of the substituent, electron withdrawing or donating, is also expected to have an effect on the copolymer conductivity. Figure 4.7 illustrates the effect on the polymer conductivity by varying the ratio of aniline/aniline-2-sulfonic acid. Further studies are currently underway.

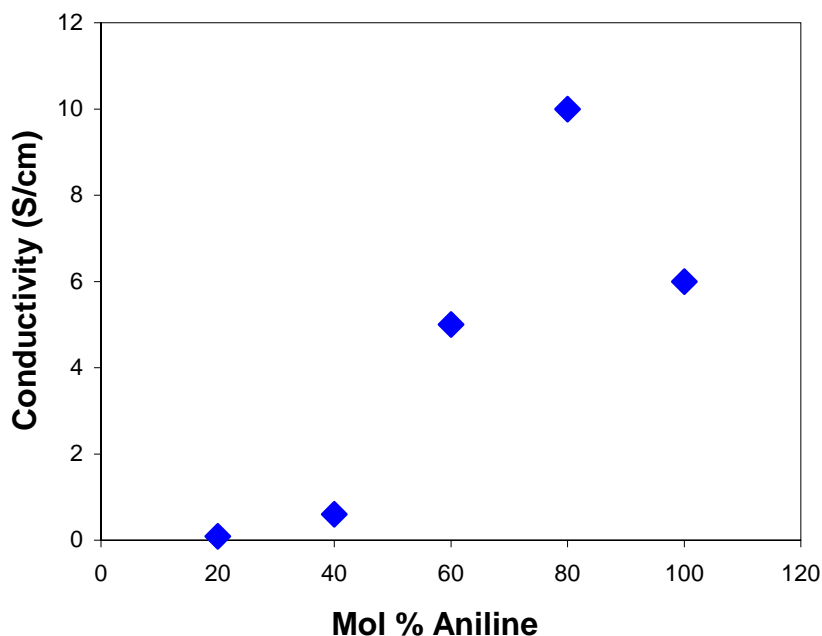


Figure 4.7. Conductivity as a Function of Mole % Aniline in Feed Stock

4.2.3 Effect of Processing Parameters on Permittivity: Polyaniline

As mentioned previously, there is a requirement for either incorporation of the conducting polymers into a polymeric matrix, or deposition onto fabric. In the case of polyaniline, deposition onto fabric was much less feasible than incorporation into a polymeric matrix. Thus the processing method of choice was incorporation of the polyaniline in a polymethyl methacrylate, (PMMA), matrix. This particular matrix was chosen as it is easily milled precisely to fit into the waveguide for permittivity measurement, is readily available as a powder (for ease of mixing) in a number of molecular weight distributions, and it has a glass transition temperature, T_g , easily exceeded with a compression molder. After mixing together the polyaniline, plasticizer, and PMMA powder, the mixture was placed in a compression molder, and heated beyond the T_g , followed by cooling. The result is a small hard composite disk, or plaque (1.25" in diameter), which is then milled, and its permittivity measured.

The permittivity of each sample is critically dependent on the distribution of the polyaniline within the PMMA. Interaction of electromagnetic radiation with a sample will vary dramatically depending on whether the sample possesses a conductive network (or percolation network) of polyaniline throughout the matrix, or not. The permittivity will also depend on the amount of polyaniline, thus the overall conductivity of the composite. The dispersion of an electrically conducting species in an insulating matrix yields a composite of varying electrical properties depending on

the loading and dispersion of the conductive species. At very low loadings, well-dispersed conducting species do not impart any electrical conductivity to the composite. However, as the loading of the conductive species increases, assuming a reasonably homogeneous dispersion within the matrix, there will be a point at which the conductive species will form a conductive network. This point is known as the percolation threshold, and is generally expressed as volume % conductive species. At the percolation threshold, the conductivity increases dramatically (usually several orders of magnitude). At loadings beyond the percolation threshold, the composite becomes more conductive. Theory indicates that the maximum attenuation of EM radiation occurs with samples close to the percolation threshold. In addition, higher loadings, which result in higher composite conductivity, are more likely to reflect EM radiation as a consequence of greater impedance mismatch with air. Ideally, for the condition of zero-reflectance, the impedance of the composite should match that of air; this is known as impedance matching.

There are a number of parameters that affect the dispersion of the conducting polymer in a polymeric matrix, such as amount and type of plasticizer, heating temperature, heating time, cooling rate, average molecular weight of PMMA, and the degree of mixing. Several of these parameters were varied systematically in order to assess their effect on the composite, as measured by the permittivity. The effect of the degree of loading on the permittivity was also investigated, once processing conditions were reasonably optimized.

Permittivity is dependent on frequency, as illustrated in Figure 4.8, which shows a typical result for polyaniline in PMMA. The pink line represents the imaginary (or lossy) component, ϵ'' , and the blue line represents the real component, ϵ' . The red line indicates the theoretical ϵ'' , calculate from the measured dc conductivity of the sample. Mismatch between the theoretical and measured ϵ'' may be attributed to an inaccurate dc conductivity measurement, possibly from inhomogeneous dispersion of polyaniline. A second reason occurs for very conductive species, where the fitting algorithm does not accurately converge. A third option, the best case scenario, the sample possesses an additional high frequency loss mechanism that is ac in nature, thus not detectable by dc measurement.

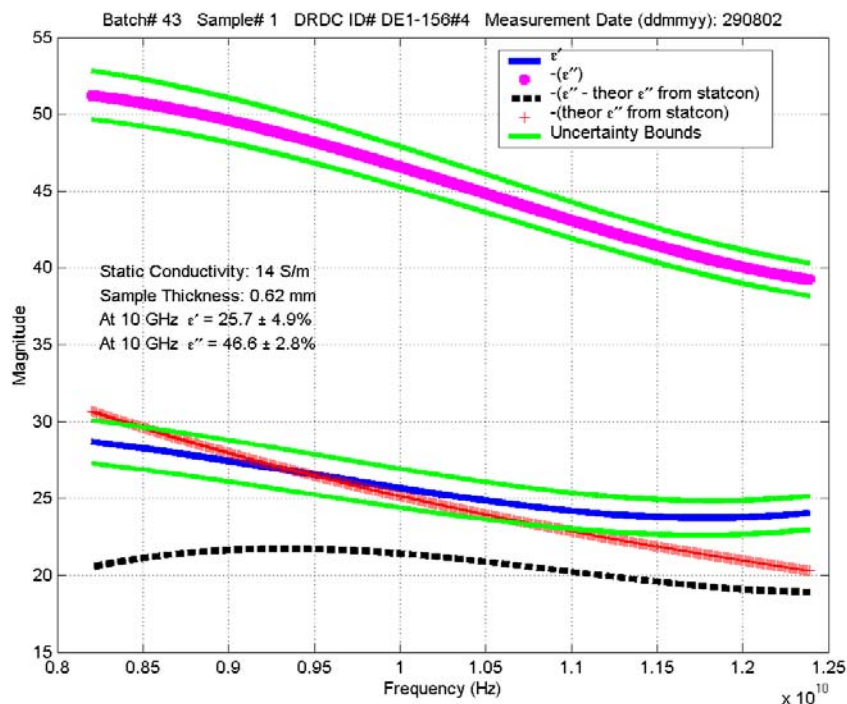


Figure 4.8. A Typical Plot of Permittivity as a Function of Frequency

It was found that most of the parameters investigated had some effect on the polyaniline dispersion in the PMMA, and some will be highlighted here. Most notably, the plasticizer content exhibited a large influence on the dispersion, and therefore the permittivity (see Figure 4.9). The plasticizer improves the compatibility of the polyaniline and PMMA, and enables the polyaniline to move more freely under molten conditions. Without any plasticizer, the polyaniline and the PMMA are not very compatible, and have a tendency to phase separate, or segregate. As a result, the polyaniline is inhomogeneously dispersed, without a conductive network, hence the very low conductivity and imaginary component (thus loss tangent). The effect of the plasticizer appears to be optimized at around 5 wt %, based on the maximum ϵ'' and loss tangent observed at this point. The reduction in ϵ'' and loss tangent at higher plasticizer content is attributed to the polyaniline being too mobile and phase separating.

These findings are consistent with the experimental data in which the heating time is varied (see Figure 4.10). The permittivity and the conductivity were found to decrease with heating time, which likely indicates increased phase separation.

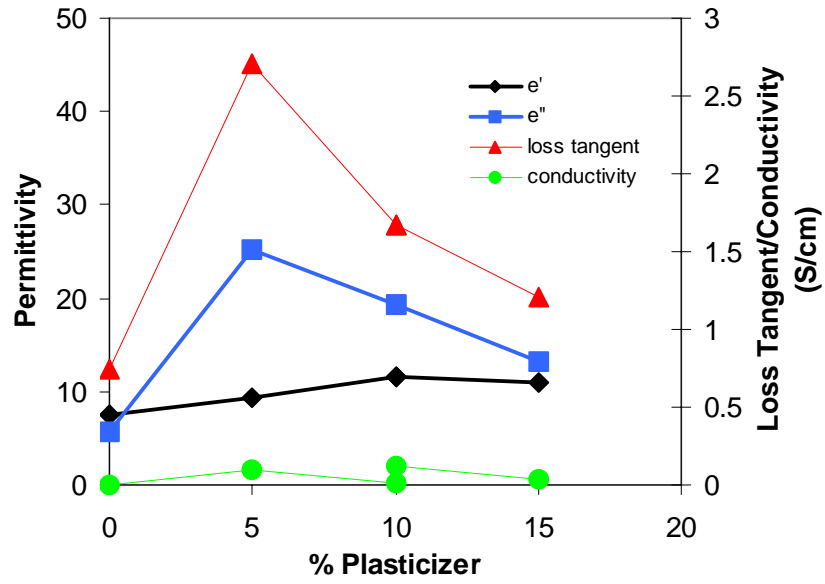


Figure 4.9. Permittivity, Loss Tangent, and Conductivity as a Function of Plasticizer Content

A series of plaques were prepared in which the loading of polyaniline was increased from 5 – 50 weight %. The permittivity and dc conductivity of the plaques were measured (see Figure 4.11); initially all parameters (including loss tangent) increased with increasing loading, however at ~ 25 wt %, the real component levelled off, and the imaginary component (and thus loss tangent) and conductivity continued to increase. The loading of the polyaniline has a large effect on the permittivity, as one would expect.

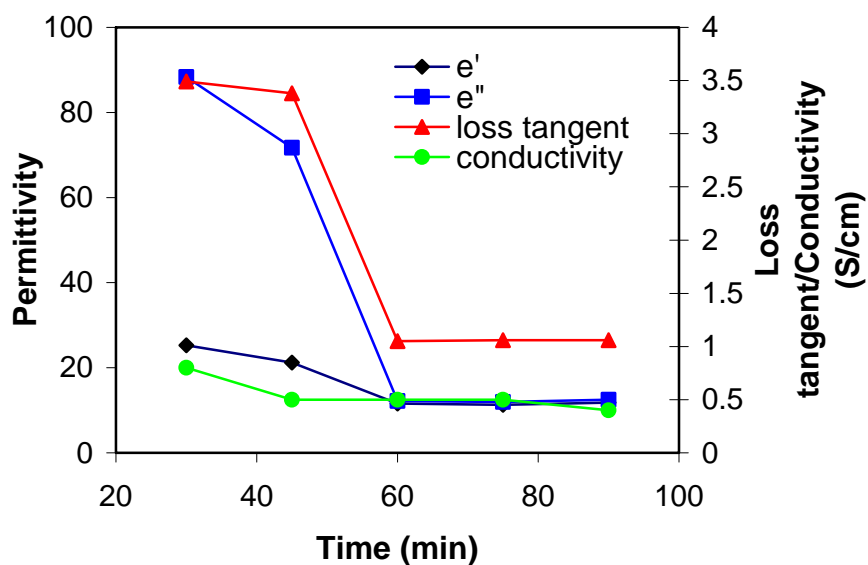


Figure 4.10. Permittivity, Loss Tangent, and Conductivity as a Function of Heating Time

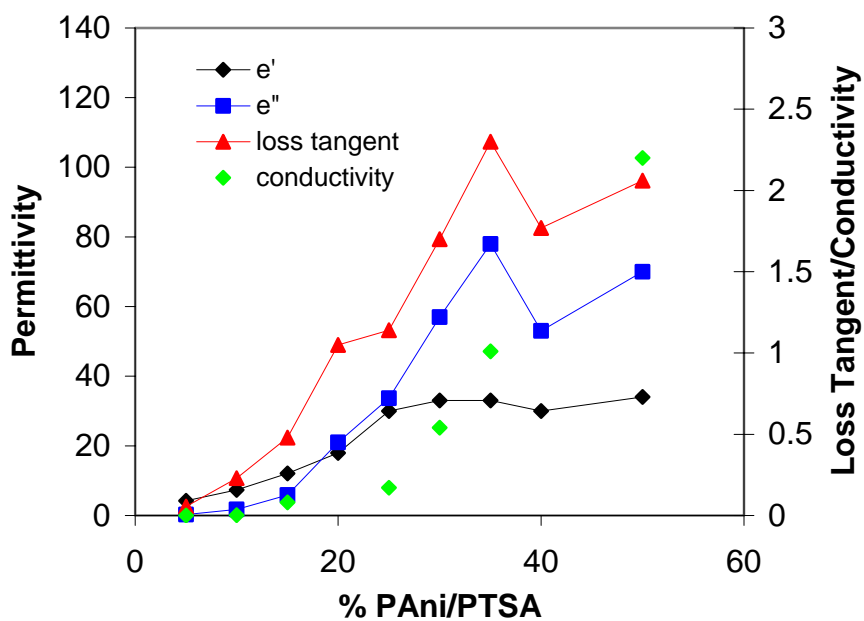


Figure 4.11. Permittivity, Loss Tangent, and Conductivity as a Function of Polyaniline Loading

4.2.4 Polyaniline-Carbon Nanostructure Composites

A variety of methods were employed to prepare polyaniline - carbon nanotube and polyaniline – carbon nanofibre composites. The composites were characterized by scanning electron microscopy (SEM) and transmission electron microscopy (TEM), as well as conductivity of the bulk composites and permittivity composites dispersed in an acrylic matrix. Imaging indicates that the polyaniline does indeed coat the tubes (see Figures 4.12 and 4.13), under optimal synthetic conditions, and the composite conductivity appears to be enhanced relative to the parent compounds (see Figure 4.14) (although increased density also plays a role in the conductivity increase). This work is continuing, and full results will be presented at a later date.

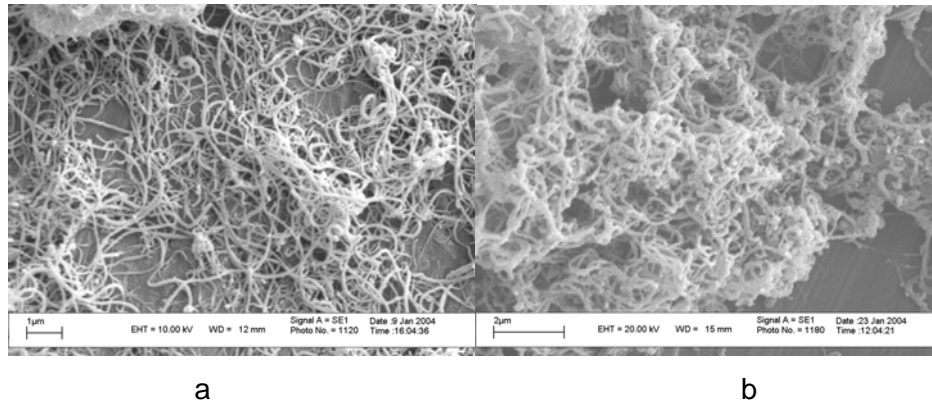


Figure 4.12. SEM Images of a) as received MWNT, and b) Polyaniline – MWNT Composite

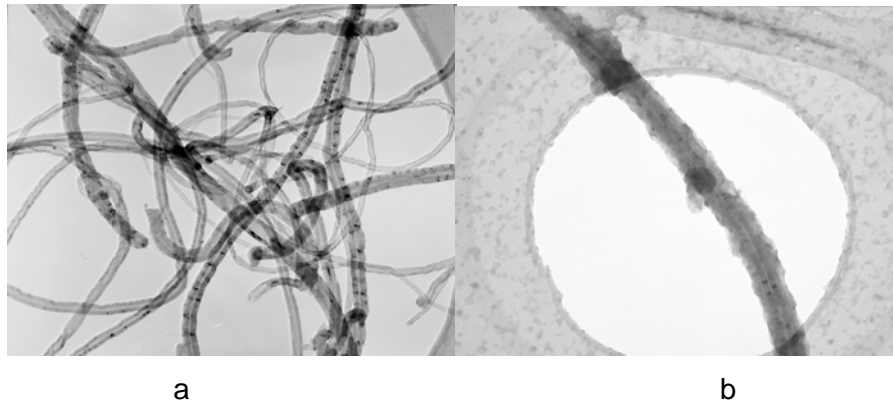


Figure 4.13. TEM Images of a) as received MWNT, and b) Polyaniline – MWNT Composite

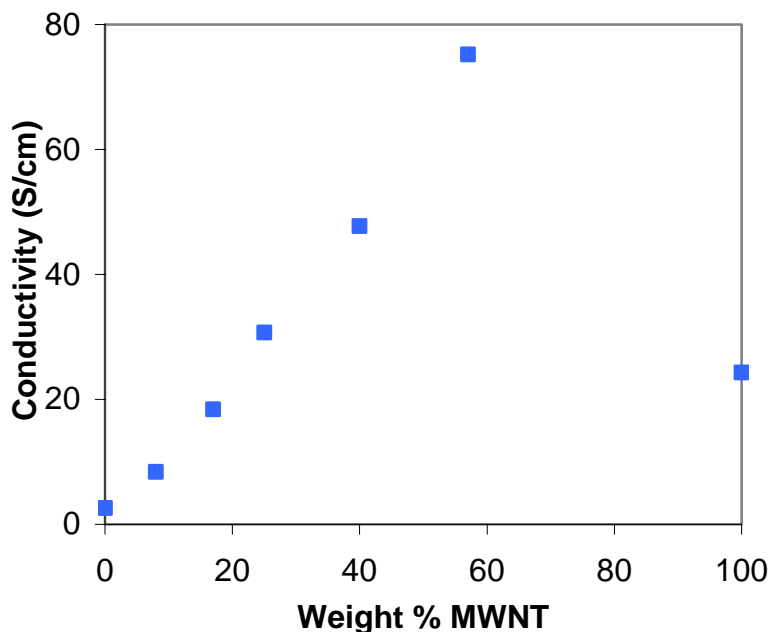


Figure 4.14. Conductivity as a Function of MWNT Content

4.2.5 Polyaniline Summary

This work has resulted in the development of expertise and capability in the area of polyaniline and carbon nanotubes. The knowledge base in conducting polymers and carbon nanotubes is extremely useful, not only as applied to RAM, but also provides a strong foundation for further development in many areas, including sensors, actuators, energy storage, and electrochromic displays.

Through experimentation, we have developed the capability of producing conducting polymers, and conducting polymer composites (coated fabrics, coatings, and polymeric composites) exhibiting a wide range of electrical and optical properties, with improved processibility. This capability enables us to tailor and fine-tune conducting polymers for a wide range of applications.

Some of the work has already been published (in the form of technical memoranda) and presented at various conferences (see Appendix A).

4.2.6 Future Work: Polyaniline

The conductivity and permittivity of polyaniline and polyaniline-based materials can be adjusted over a wide range. Reproducibility however is an issue, both for the

conductivity of the polyaniline and for the properties of the composites. The properties of composites (and polyaniline) will require strict control of synthetic and processing conditions.

Stability is another issue that needs to be address for polyaniline. The effects of aging time and temperature need to be studied.

4.2.7 References

1. Huber, T.; Saville, P.; Edwards, D. *Investigations into the Polyaniline and Polypyrrole Families of Conducting Polymers for Application as Radar Absorbing Materials*, DRDC Atlantic TM 2003-005.
2. Huber, T.A. *A Literature Survey of Polyaniline, Part 1, Polyaniline as a Radar Absorbing Material*, DRDC Atlantic TM 2003-014.
3. Huber, T.A.; Edwards, D. *Polyaniline as a Potential Radar Absorbing Material. Preliminary Experiments*, DRDC Atlantic TM 2003-153.
4. Huber, T.A.; Diep, M.N. *Synthesis and Characterization of Polyaniline – Carbon Nanostructure Composites. Preliminary Experiments*, DRDC Atlantic TM 2003-206.
5. Huber, T.A., *Polymer – Carbon Nanotube Composites, A Literature Review*, DRDC Atlantic TM 2004-091.
6. Makeiff, D.A.; Huber, T., *Permittivity of Polyaniline/Carbon Nanotube and Polyaniline/Carbon Nanofiber Nanocomposites in X-band*, DRDC Atlantic TM 2004-124
7. Makeiff, D. *The Effect of Processing Parameters on the Microwave Absorption by Polyaniline/PMMA Composites*, DRDC Atlantic TM 2004-301.
8. Makeiff, D. *Microwave Absorption by Polyaniline-coated Polyester Fabrics*. DRDC Atlantic TM 2005-023.

4.3 Polypyrrole

Polypyrrole is a conducting polymer that has attractive characteristics for use as a radar absorbing material.^[1] Usually it is formed as a powder and needs to be processed into a usable form. Such forms might include conducting powder dispersed in a coating, applied to a fabric or dispersed in a polymeric matrix. In the next section polypyrrole is reviewed with attention to suitable applications for microwave

absorbing materials. Then results are presented for polypyrrole powders, textiles, and coatings.

4.3.1 Review of Polypyrrole: Synthesis

Polypyrrole (PPy) can be formed chemically or electrochemically through oxidative polymerization of pyrrole monomer, Figure 4.15.

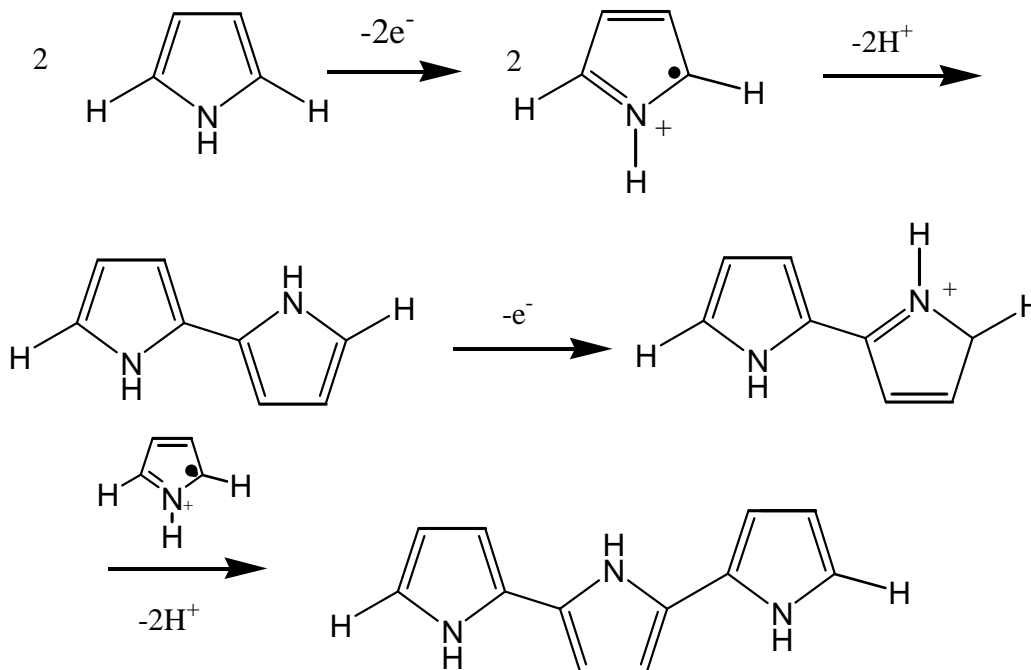
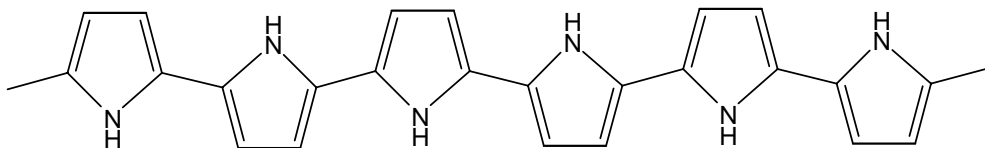
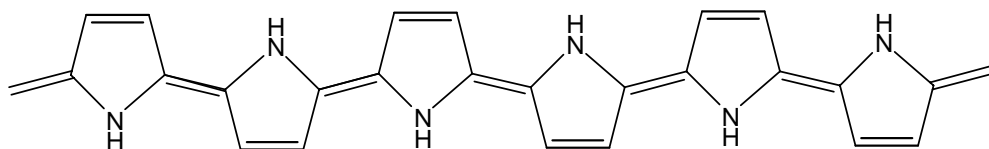


Figure 4.15. Oxidative polymerisation of pyrrole to polypyrrole proceeds via a one electron oxidation of pyrrole to a radical cation, which subsequently couples with another radical cation to form the 2,2'-bipyrrrole. This process is then repeated to form longer chains.

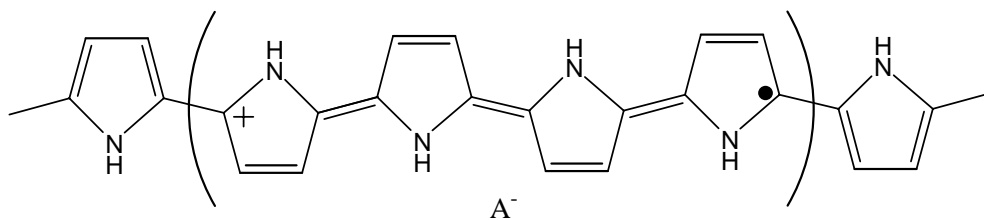
The final form of polypyrrole is that of a long conjugated backbone as seen in Figure 4.16. The polymer has resonance structures that resemble the aromatic or quinoid forms. In this neutral state the polymer is not conducting and only becomes conducting when it is oxidized. The charge associated with the oxidized state is typically delocalised over several pyrrole units and can form a radical cation (polaron) or a dication (bipolaron).



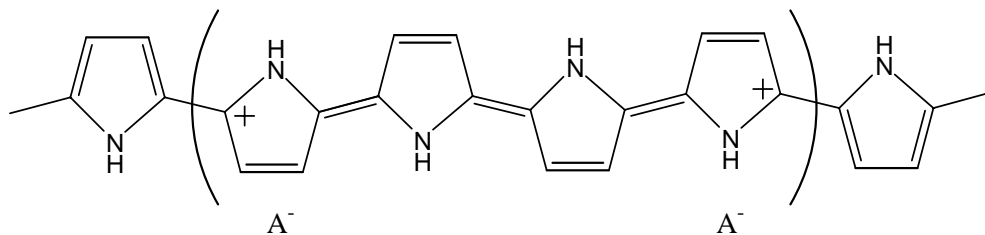
Aromatic



Quinoid



Polaron



Bipolaron

Figure 4.16. Chemical structures of polypyrrole in neutral aromatic and quinoid forms and in oxidized polaron and bipolaron forms.

The physical form of polypyrrole is usually an intractable powder resulting from chemical polymerization and an insoluble film resulting from electropolymerization.

4.3.1.1 Electropolymerisation of Pyrrole

Electrochemical oxidation of pyrrole forms a film of conducting polymer at the electrode surface. The electropolymerisation of pyrrole to polypyrrole precedes as follows, (Figure 4.15):

Initiation. Formation of monomer radical cation by electrochemical oxidation, +0.8 V vs SCE.

Propagation. Combination of two radical cation monomers (or oligomers) followed by loss of two hydrogen ions. The linkage formed is at the 2 position of the pyrrole ring, forming 2,2'-bipyrrole. 2,5-disubstituted pyrroles do not polymerize and 2-monosubstituted pyrroles only form dimers. Propagation continues by re-oxidation of the bipyrrole and further combination of radicals.

Termination. Occurs when no further monomer is present for oxidative polymerization or side reactions terminate the PPy chain. An example of a termination reaction is the reaction with water to form the amide group.

The success of electropolymerisation of pyrrole is due to the stability of the radical through charge delocalization, and the ease of electro-oxidation. The loss of the hydrogen ions makes the dimer (oligomer) formation irreversible so proton acceptors, such as water, pyridine and bases, enhance electropolymerisation. Good solvents for electropolymerisation^[2] include water, acetonitrile, butanone, propylene carbonate, dimethylformamide (DMF) and ethanol though the presence of a bit of water (1 v/v%) enhances the polymer formation. Water can also result in chain termination.

Potentiostatic, potential cycling, and galvanostatic methods can be used to electropolymerise pyrrole. Potentiostatic methods (constant potential) and cycling the potential yield the most consistent films of about the same quality. Galvanostatic deposition (constant current), does not produce as good a quality film as the other methods, but is useful for controlling film thickness.

Electrochemical oxidation of a 5-member pyrrole oligomer^[3] shows two reversible one-electron oxidation processes at $E^{\circ} = -0.28$ and -0.08 V vs Ag/Ag⁺. These correspond to the formation of the radical cation and dication, respectively, which are stable and do not polymerize. Another oxidation peak at $E_p = 0.75$ V marks the start of polymerization. Extrapolation of the E° value to infinite chain length for the first one electron oxidation gives a value of -0.59 V, compared to the measured value of -0.57 V for polypyrrole from the pentamer.^[3]

AFM studies of polypyrrole production indicate that time and substrate influence the final film morphology.^[4,5] Supporting electrolyte was found to affect deposition kinetics.^[5] Cyclic voltametry and NIR-Vis spectroscopy have also been used to show the affect of pH and counter ion.^[6] Neutral polypyrrole is noted to be very unstable in water or air. In basic solutions the polymer was doped with hydroxide ions and other anions in acidic solutions. Incorporation of polymeric counter ions has been investigated for imbuing other properties such as thermoresponsiveness.^[7]

4.3.1.2 Chemical Polymerisation of Pyrrole

Chemical synthesis of polypyrrole proceeds via the oxidation of pyrrole with an oxidant such as ferric chloride. The mechanism is similar to that for electropolymerisation of pyrrole and conductivities are comparable. The resulting polymer in its oxidized form is conducting with charge compensation afforded by FeCl_4^- . The conductivity of polypyrroles formed from different ferric salts (effect of dopant ion) has been related to the $\text{Fe}^{2+}/\text{Fe}^{3+}$ redox potential with strong acid anions providing the most oxidizing ferric species. Weaker acid anions typically coordinate Fe^{3+} ions more strongly, reducing its oxidizing potential.^[2] An investigation into the ferric ion equilibria in aqueous solutions showed that above a concentration of 0.5 M HClO_4 there was no change in the amount of available $\text{Fe}(\text{H}_2\text{O})_6^{3+}$.^[8]

The solvent the reaction occurs in also changes the redox potential. For example the $\text{Fe}^{2+}/\text{Fe}^{3+}$ redox potential is lower in water than acetonitrile. If the redox potential is too high, an irreversible dissolution of polypyrrole can occur, as for ferric perchlorate in acetonitrile.^[9] Methanol has been found to produce the best conducting polymer based on conductivity and morphology.^[10,11] The conductivity was related to the redox potential of the $\text{Fe}^{2+}/\text{Fe}^{3+}$ system and could be varied by adding FeCl_2 . The optimum redox potential in methanol was +0.5 V vs SCE. The solvent also has an influence on the dopant ion that remains in the Polypyrrole, PPy, film. In ether using FeCl_3 as oxidant leaves FeCl_4^- as the dopant ion, while in methanol, the dopant is mainly Cl^- with some FeCl_4^- .^[2] Water was found to be trapped in the PPy with formation of pyrrolidinone rings at chain terminations similar to electrochemically produced films.^[2]

Other counter ions to the ferric ion will also be incorporated into the PPy film^[2] as will ions present in solution. Dopants whose bonds are labile such as Cl-O, B-F, P-F, should be avoided for sake of polymer stability.^[12] Polymerisation of pyrrole in the presence of surfactants such as dodecylbenzyl sulphonic acid or a salt like sodium dodecyl sulphate, leads to an increase in mass yield due to incorporation of the salt/surfactant into the polymer.^[13] Cationic surfactants were found to inhibit the polymerization of pyrrole. Polymerisation of pyrrole in the presence of polystyrene sulphonate (PSS) produced particles (non-colloidal) with the size being inversely proportional to the concentration of ferric chloride oxidant.^[14] The size effect is due to the affinity of pyrrole and the ferric ion to PSS. Acid concentration affects the polymerisation process.

The conductivity of polypyrrole increases as the synthesis temperature is reduced. This is thought to be due to a reduction in the number of side reactions. Polypyrrole's conductivity as a function of temperature is studied as well as reflectivity, and classified into metallic, critical and insulating regions.^[15]

The density of polypyrrole has been determined to be 1.48 g cm^{-3} and $1.44 \pm 0.05 \text{ g cm}^{-3}$.^[14,16]

Polypyrrole derivatives have been prepared and their properties studied. By blocking the 3,4- positions on the pyrrole ring, unwanted side reactions at these sites are eliminated. This has been noted to yield higher conductivity in the case of poly 3,4-dimethoxypyrrole.^[17,18] Various alkylendoxypyrroles have been synthesised and studied including a series of soluble species.^[17,19,20] N-substituted pyrroles tend to induce twisting relative to adjacent pyrrole rings, thus limiting the conjugation length and conductivity. Solid state NMR has been used to elucidate some of the conducting mechanisms and structures.^[21] Bipolarons appear to be the charge carriers and conductivity is linked to the loss or decomposition of the dopant ions. Elevated temperatures in air reduce the quinoid content and oxidise the 3,4-positions. Dodecyl sulphate is less stable than *p*-toluene sulphonate at elevated temperatures. Under argon the dodecyl sulphate doped film become brittle indicating cross linking at elevated temperatures.^[21]

The polymer produced by electrochemical or chemical synthesis of PPy is generally an intractable solid or powder. The next section presents some of the strategies that have been investigated for the purpose of producing useable material.

4.3.2 Processability

Researchers have been looking at a number of methods for making conducting polymers practical.^[22] The trade off is often lower conductivities, though sometimes there is the serendipitous gain of stability. Some of these methods include direct polymerisation onto polymers sheets, glass, polymer and inorganic particles, clays, zeolites, porous membranes, fibres and textiles and soluble matrices. The methods used to coat these materials are reviewed below to highlight potential avenues for the development of radar absorbing materials.

4.3.2.1 Solutions

The solubility of polypyrrole is limited due to its rigid structure and cross-linking. Attempts at increasing the solubility have been made by derivatizing the pyrrole ring at the 3- and 4- positions with alkyl groups, or substituents on the pyrrole's nitrogen. Another techniques that has been proven successful for some conducting polymers is to use long chain surfactant dopants like sodium dodecyl benzene sulfonate,^[23-25] di(2-ethylhexyl) sulfosuccinate sodium salt,^[26] or polystyrene sulfonate.^[14] These polymers are then soluble in *m*-cresol, NMP, DMSO, DMF and THF.

4.3.2.2 Composites-Chemical Preparation

Since polypyrrole is generally intractable, attempts have been made to polymerize pyrrole onto or into the material where it is desired. In one strategy, the oxidant is mixed with the substrate and then exposed to pyrrole.^[27] For instance, ferric chloride has been mixed with polyvinyl alcohol,^[28] polyvinyl acetate,^[29] polyethylene oxide,^[30] poly(styrene-butyl acrylate-hydroxethyl acrylate),^[31] poly(methyl acrylate-co-acrylic acid),^[31] or rubber^[32] and exposed to pyrrole vapours. The variation of this method is

to soak the substrate with the pyrrole monomer and then immerse it in an oxidant solution.^[27,33]

Polypyrrole can be deposited directly onto a substrate surface, by placing the object in a solution containing pyrrole and oxidant. This coating strategy has been applied to fabrics^[34] and is discussed in greater detail below.

Surfaces have been derivatised with dopant groups to facilitate polypyrrole-substrate adhesion and deposition. Low density polyethylene has been sulphonated and used as a template for the polymerisation of pyrrole yielding PPy layers up to 80 nm thick and conductivity up to 150 S/cm.^[35,36] A similar system was investigated using a sulphonic acid derivative of polystyrene grafted polyethylene,^[37] and compression molded sulphonated polystyrene objects.^[38] Other researchers have attempted to improve deposition and adhesion of the polypyrrole by graft polymerisation of other polymers to the polyethylene.^[39] Polypyrrole has been deposited onto acrylic, polystyrene, polyimide and polyurethane foam.^[22] Composites have been made by dispersing polypyrrole powder in melted LDPE, HDPE and PS,^[40] or by dispersing polypyrrole powder or flakes in silicone rubber or vinyl ester and curing the material.^[41] Colloidal PPy has been made by stabilisation with methylcellulose.^[42]

4.3.2.3 Copolymers and Graft Copolymers

Processable or soluble polypyrrole has been formed by graft copolymerisation of pyrrole. This has been accomplished by (i) coupling pyrrole to a reactive monomer, polymerizing the monomer and then polymerizing the pyrrole as was done for methyl-methacrylate,^[43-45] or (ii) derivitization of a preformed polymer with pyrrole and then polymerizing the pyrrole as has been done for polystyrene-co-poly (chlorostyrene).^[46] These materials were initially soluble with a tendency to become insoluble at high pyrrole content.

Direct copolymerization of pyrrole with other monomers has produced soluble conducting product. Examples include the polymerisation of pyrrole with various aniline derivatives,^[47-49] and methyl ethyl ketone formaldehyde resin.^[50] The conductivity and solubility depends on the feed ratio of pyrrole.

4.3.2.4 Composites-electrochemical

Pyrrole has been electrochemically copolymerised with a liquid crystal derivatised thiophene forming an insoluble film.^[51]

4.3.2.5 Composite Blends

Simple blending of the polypyrrole powders with matrix materials such as epoxy, rubber or paint, have been investigated for producing conducting composites.^[52,53] The process of dispersing the powder in a matrix can degrade the conductivity,^[52] as do

chemical reactions used for matrix materials. Several other techniques have been investigated in order to make the polymer more processable. These include solubilization,^[23,24] graft polymerization,^[43,44,46] and in-situ polymerization such as composites,^[33,37,46,54-56] latex formation,^[42,57-63] Langmuir-Blodgett films^[64] and textile and fibre coatings.^[65-73] It is this latter material, polypyrrole coated textiles, that will be investigated here as a function of textile type.

4.3.2.6 Textiles

Conductive textiles^[74] can be produced by weaving thin metallic or carbon wires, impregnating fibre materials with conducting powders, metallizing material, or by blending filament-sized fibres of stainless steel or carbon fibre. Conducting fibres have also been made from conducting polymers by solution spinning, however, they are typically brittle, expensive to produce and hard to manufacture on a large scale.^[75] Conducting powder (carbon) incorporation is most cost effective, though the high content required to yield percolation reduces the mechanical properties of the fibres. Core/shell strategies, where normal textile fibres are coated with a conducting material, maintain the original mechanical strength. Conducting polymers have been used for this application, and yield conductivities that fall between metallized fabrics and carbon-based blends.

4.3.2.7 Conducting Polymer-Textile Formation

One of the earliest reports of the deposition of polypyrrole onto fibres involved a two-step process, whereby paper was soaked in a ferric chloride solution before immersion in a pyrrole solution.^[33] Variations on this method include exposing the ferric chloride to pyrrole monomer in the vapour phase^[76,77] and soaking the substrate in monomer before polymerization in an oxidizing solution.^[78] The process is also applicable to the use of various solvents.^[79]

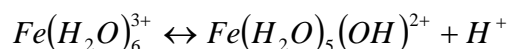
The easiest method of applying conductive polymer to a textile is from a solution of the conducting polymer. The solubility of highly conducting polymers (PPy, PANI and PTh) is limited to solvents that are not generally compatible with the textiles.^[25] Water-based systems have been used for coating textiles such as the PANI-PSSA system and emulsion polymerized monomers to form latex.^[58,80]

In-situ polymerization is another method for producing conductive coatings on textile substrates.^[69,71,81] The mechanism for conducting polymer deposition proceeds through the adsorption of oligomeric species onto the textile surface, nucleation, from which subsequent polymerization occurs, growth, forming a smooth continuous film. Neither the monomer nor the oxidant is adsorbed to produce nucleation sites. In the presence of a fibrous surface, little or no polymer is found in solution. The coatings made by this method do not form significant fibre-to-fibre bonds, unlike solution and emulsion methods.

Polymer deposition is independent of surface material yielding films less than 1 μm thick and very uniform for coverages of 1-5%. Substrate material does not have a

significant effect on the polymerization of pyrrole, yielding essentially the same conductivity for the same mass of textile. Clean glass fabric is reported to not coat well with polypyrrole,^[74] though its adhesion can be improved by the use of aminosilane or pyrrole-silane molecules that chemically bond to the glass surface.^[82-84] Factors important to determining the conductivity include surface area, hydrophobicity, surface polarity and porosity. Porous fibres (nylon and polyacrylonitrile) and materials with polar groups tend to increase adhesion and polymer deposition while non-polar fibres such as polyethylene and polytetrafluoroethylene and dense crystalline fibres such as polyester yield poorer adhesion. The conductivity is not a linear function of the mass of polypyrrole deposited.^[74] Fabrics prepared from continuous filament yarns produce better conducting films than those prepared from spun fiber yarns.^[67] The conductivity of PPy-Textiles does not vary greatly as a function of humidity.

Kinetics of the polypyrrole deposition on textiles has been studied.^[69] The rate of polymerization is dependent on the concentration of monomer and type of oxidizing agent. Ammonium persulfate, APS, is much faster than FeCl₃. Acidic FeCl₃ is much faster than more basic FeCl₃ as the acid drives the equilibrium to the left.



The hydrated species is smaller and not as tightly coordinated, so the reaction is more facile. Highly coordinating ligands or high pH slows the reaction rate. Comparing reactions with and without the presence of fibres in the reaction vessel, the reaction rate is faster with fibres present and second order, though first order reaction rates can be achieved if the Fe³⁺ concentration is significantly increased. Without fabric, the reaction rate is second order and slower. Pure solvents such as methanol, methylene chloride or acetonitrile permit polymerization to occur in the solution phase, so no PPy is deposited on the fabric.

Pure solvents have already been noted to inhibit the deposition of PPy on the textile, whereas mixed solvents give mixed results. For instance, 20 g/L acetone in water inhibits PPy deposition, whereas the same concentration of methanol does not interfere. Textiles may be scoured with surfactants before sale and these may have an effect on PPy formation. Surfactants that are cationic or nonionic do not promote adsorption while dodecylbenzene sulfonic acid, DBSA, marginally decreases adsorption. Hydrophobic surfactants such as alkyl naphthylsulfonate promote film formation. Other additives, such as 1,4-dihydroxybenzene, reduce adsorption while p-nitrophenol does not interfere. PPy – Fabric (Polyethyleneterephthalate and Polyethylene) samples have been chemically polymerized, using Poly (vinyl alcohol) as a surfactant to improve PPy coating on non-woven materials and NSA as a dopant with APS as oxidant.^[15] The dc conductivity(T) indicates 3-d variable range hopping. Electrochemically treated PPy-fabrics in AQSA follow a power law where σ_{dc} is proportional to T^β indicating that the electrochemical treatment has induced charge delocalization.

Conducting fibres have been fabricated by electropolymerising pyrrole with a cotton, silk or wool fibre wrapped around the electrode.^[85]

A considerable body of work exists for polyaniline, PANI, coated textiles.^[86] Polyaniline on glass fibres has been studied.^[71] The glass was cleaned in sulphuric acid to remove impurities before polymerization in HCl, aniline and PTSA. Conductivities up to 1.79 S/cm were realized based on the thickness of the film rather than the thickness of the fabric. It is pointed out here that in the rinsing stages of the PANI/HCl or PANI/PTSA fabrics, a solution containing the counterion must be used as rinsing with pure water leaches out the dopant.^[87]

4.3.2.8 Stability of Conducting Polymer Coated Textiles

Conducting polymers have a high reactivity to oxygen, which disrupts the percolative networks and reduces conductivity.^[88] Exclusion of oxygen with nitrogen, or by encapsulating the polymer in a protective coating, decreases conductivity loss. Examples of potentially useful oxygen barriers include poly (vinyl chloride), paraffin, poly (vinylidene chloride)-poly(acrylic acid) copolymer, poly (vinylidene chloride, polyester and polyolefin.^[89,90] Epoxy resin has also been used to encapsulate PPy coated textiles.^[53] In the absence of oxygen, the rate of conductivity decrease is greatly reduced and seems to be dependent on Cl⁻ ion content in the films. PPy prepared from Fe(PTSA)₃ does not lose conductivity at elevated temperatures, whereas codoped Cl⁻ and PTSA films do, though at a lower rate than in the presence of oxygen.

Kinetics of PPy-textile degradation has been studied as a function of dopant ion (Cl⁻, PTSA, NDSA, N2SA, AQSA).^[68] The degradation process was found to be diffusion controlled and first order. For polypyrrole this is thought to be due to the polymer having a high concentration of polarons (free radical sites) and since oxygen adsorption is assumed faster than reaction with the polymer backbone, so first order kinetics are observed. Other studies have shown an increase in carbonyl functionality during degradation though with no accompanying mass increase. This would follow the suggestion that hydroxyl groups are incorporated in the structure during chemical polymerization.^[91] Subsequent stability studies have indicated that the conductivity degradation is controlled by the diffusion of the oxidizing species into the film.^[92-95] Diffusion control is applicable at short times with the reaction rate becoming first order at long times.^[68]

Polypyrrole morphology and stability is dependent on its composition. Conducting films made with ferric chloride have chloride counterions (dopant), which has a higher mobility than other counterions. Chloride ion doped films tend to dedope at elevated temperatures in contrast to other less mobile ions. Adding other suitable salts (eg sodium salts of aryl sulfonates) results in films containing mixed dopants. Elimination of chloride ions from the film can be achieved by using other ferric salts of the arylsulfonates.^[2] These hydrophobic dopants tend to form more compact, stable and conducting films which is due in part to their planar structure, though it is surmised that the hydrophobic nature may favour their thermodynamic incorporation in the film.^[68] In the case of anthraquinone-2-sulfonic acid salts, AQSA, it may be more a question of working near the solubility limit of the AQSA in water that favours its incorporation in the film.^[67] Studies of the atomic ratios of Cl/N for films made with FeCl₃, PTSA and AQSA show a decreasing trend in the amount of chlorine in the films, while the S/N ratio shows an increasing trend in the sulfur content. The total

(S+Cl)/N increases to 0.34 for AQSA which is effectively the doping limit of one counterion per three monomer units. Another ratio that has been looked at is the O/N ratio, which is smallest for the AQSA films. Some of the oxygen will come from included water^[2], and some from chain termination reactions forming pyrrolidinone. Another possible source has been identified as nucleophilic hydroxyl substitution of the pyrrole rings.^[91]

Scanning TGA measurements made of PPy coated PET show mass loss at 400° C, which is the same as pure PET. Isothermal TGA at 300° C show greater mass decreases for PPy Coated PET than pure PET.^[96]

4.3.2.9 Microwave Properties of Conducting Polymer Coated Textiles

There are some literature reports of the microwave properties of conducting polymer composites.^[73,97-100] Composites made from powdered carbon or metals do not have an appreciable effect on the lossy component to the complex permittivity, until the particles are nearly forming a percolative network. The tunnelling currents between adjacent particles render the material lossy. At the percolation threshold the particles are in contact and the material becomes conductive. The real part of the permittivity (the capacitance) increases as this type of composite is loaded with powder, whereas the imaginary component (loss) is small until the percolation threshold.

In contrast, for conducting polymer coated textiles, it is reported that the imaginary component of the permittivity can be varied over a large range without a great increase in the real component.^[73] Looking at the data, the conductivity varies from 0-0.5 S/cm. A plot of σ vs ϵ' is nonlinear for PPy coated polyesters encapsulated in polyester resins over the frequency range of 26-40 GHz, whereas the same plot is linear for PPy coated S-glass. Plots of ϵ'' vs ϵ' are linear with slopes of about 2.2 and 1.7 for PET and S-glass substrates respectively.

The use of paper and textiles coated with polypyrrole, have been studied for use as Salisbury screens and Jaumann layers.^[98-102] High levels of polypyrrole loading on the textile or paper result in relatively frequency independent reflectivity, whereas light loadings are frequency dependent. These materials are modelled as a parallel RC circuit, where at high loading the sheets are mainly resistive and at light loadings sheet capacitance becomes the dominant term. Physically at light loadings, polypyrrole forms a uniform coating around the fibres of the textile and the capacitance is high. Heavy loadings result in the formation of particles on the textile surface, causing short circuits between fibre strands. These shorts reduce the capacitance and increase the conductivity. Formation of glass fibre and resin composites incorporating the PPy-textile sheets shows only small changes to the reflectivity.

4.3.2.10 Polypyrrole - Latex

Conducting polymer latex falls into two categories, pure latex and core-shell latex where a conducting polymer shell is coated onto an existing non-conducting latex

core. Another area that falls into this general subject heading is that of conducting polymer nanocomposites which have been reviewed.^[103]

Methylcellulose has been used to stabilise chemically formed polypyrrole, resulting in small particles dispersed in a methylcellulose matrix.^[42] Similarly, PPy-Polystyrene sulfonate particles have been made by oxidizing pyrrole in presence of Fe³⁺.^[14] The size of particles is controlled by the Fe:Py ratio. Pure conducting polypyrrole lattices have been formed by the polymerization of the monomer in the presence of a steric stabilizer such as poly(vinylpyrrolidone), PVP, or poly (vinyl alcohol-co-acetate), PVA,^[59,60] poly (2-vinyl pyridine-co-butyl methacrylate),^[62] and a comprehensive study of a number of stabilizers.^[104] Poly(ethylene oxide), PEO, polyacrylic acid and various block copolymers based on PEO, failed to provide steric stabilization. PANI latex has also been made and forms needle shaped particles.^[61,86] Polypyrrole and polyaniline lattices and composite beads (PPy-PMMA) have been synthesized and cast into conducting films by mixing with a dispersion of a 1:1 copolymer of polymethylmethacrylate-polybutylacrylate.^[105] The PPy lattices were spherical and PANI lattices needle-like, giving percolation thresholds of about 20 and 5 wt% respectively. The surface energy of conducting polymers (PPy and PANI) is high, capable of strong interactions either via London dispersion or Lewis acid-base forces.^[106] For PPy, the surface energy decreases within a few days, which is not seen for PANI. PMMA adsorbs to the PPy particles, forming a uniform coating when 1,4-dioxane is used as the solvent and a patchy coating when chloroform is used.

Conducting polymer-coated latex particles (core-shell) have been reviewed.^[107] Conducting polymers based on pyrrole, aniline and EDOT, have been polymerized with ferric chloride, APS and ferric tosylate. Core lattices discussed are polystyrene and polyurethane^[58,80]. Potential applications are found in anti-corrosion and anti-static coatings. High performance electrochromatography and novel marker particles for immunodiagnostic assays.^[108] PS/PANI core/shell lattices have been made in the presence of Polyvinylpyrrolidone,^[106,109] and SDS (sodium dodecyl sulfate).^[47] PPy deposits onto submicron poly (ethylene glycol) stabilized PS latex as nanoparticles, bridging the PS particles and causing flocculation.^[110] Other PANI/PS-co-PSS lattices have been made.^[111]

Nanocomposites of conducting polymers (PPy and PANI) and iron oxide magnetic particles have properties different from pure magnetic particles.^[112] Electrophoretic mobilities of glass beads coated with PPy in the presence of a nonionic surfactant Rhodasurf TB970, have been measured.^[113] 20 nm Silica colloidal particles have been coated with PPy,^[109] and PANI^[114,115]. Both of these produced agglomerates of silica and conducting polymer giving a raspberry like structure. Carboxylic acid derivatized polypyrrole-silica composites showed improved colloidal stability.^[116]

A reverse core-shell PPy/polyacrolein latex has been synthesized and studied by atomic force microscopy, AFM.^[117] The surface of the PPy particle was not completely covered by the polyacrolein.

4.3.2.11 Improved Adhesion to Inorganic Substrates

The adhesion of polypyrrole to the substrate has been discussed above in reference to using anionic surface groups to act as templating and dopant sites. When it comes to the fabrication of structural materials, it is important that all the layers in the composite are well bonded in order to avoid delamination. For this reason the promotion of adhesion to glass fibres and other inorganic materials has been investigated.^[82,84,118] These papers present pyrrole-siloxane molecules for the promotion of adhesion to glass surfaces through coupling of the siloxane to hydroxyl groups on the glass. The pyrrole monomers are then polymerised with extra pyrrole from solution to form a conducting layer. Layer thickness vs conductivity results^[118] indicate increasing conductivity to a particular thickness, while other results indicate the siloxane coupling agent promotes higher conductivities than other adhesion promoting agents.^[82] Pullout failure of pyrrole coated glass fibres, with siloxane adhesion promoters, embedded in a polymer matrix showed similar failure loads to uncoated glass fibres and no failure at the glass-polypyrrole interface.^[82] This surface treatment has also been used for coating silica gel for chromatography purposes.^[119]

4.3.2.12 Tubules/Fibres

Polypyrrole tubules have been synthesized chemically and electrochemically by growth within a pore or by using surfactant mediation. Pore templated growth of PPy tubes has been accomplished by polymerisation within the pores of porous alumina^[120] and polycarbonate^[121-124] membranes. Selective dissolution of the membrane results in PPy tubules. A two-probe method for measuring the tubule resistance (conductivity) is given with conductivity decreasing for thicker tubes. The centres of the tubules tend to be filled with less well-ordered polymer.

A number of surfactant systems have been used to template the growth of polypyrrole tubules. A reverse microemulsion system using sodium bis(2-ethylhexyl) sulfosuccinate (AOT) was found to form nanotubes about 95 nm wide and up to 5 μm long.^[125] Naphthalene-2-sulphonic acid also acts as template for polypyrrole growth (chemical or electrochemical) with a range of morphologies dependent on the surfactant concentration.^[126,127] Diacetylenic phospholipid tubules template polypyrrole growth, however, it tends to be at the seams or edges of the lipid tubules, rather than coating the walls.^[128] Polymer fibrils have also been detected in electrochemical deposits with *p*-toluene sulfonic acid as the dopant.^[129]

4.3.3 Polypyrrole Stability

The conductivity of polypyrrole is not as stable, with respect to time and temperature, as one would like. A variety of analytical and spectroscopic techniques have been used to try to elucidate mechanisms that result in decreased conductivity and attempts have been made to improve the polymer's useful life.

UV/Visible spectroscopy has been used to study the charge carrier species of freshly electro-polymerised polypyrrole. Over the first 90 minutes while the film was still

drying, an increase in the sum of polarons, transverse bipolarons and bipolarons was observed. The spectra also showed a decrease in the amount of polarons or transverse bipolarons though the overall change is small, at most 6%.^[131] These samples were then heated above the glass transition temperature, T_g , for PPy at 80° C for 35 hours, allowing the polypyrrole to form more structurally favourable conformations. In this case more polarons and neutral polypyrrole is observed along with a decrease in the amount of the transverse bipolarons. Polypyrrole doped with dodecyl sulphate initially behaved differently on heating than polymer doped with *p*-toluene sulphonate. The polymer and material were observed to undergo a phase change, increasing crystallinity, before the high temperature resulted in a collapse of the structure.^[131] Cooling the samples showed a reversal of the changes in carrier population effected upon heating. This study does not consider the degradation of the polypyrrole, or its conductivity, however, it does elucidate changes in charge carriers that might be more susceptible to oxidation. The rest of the review on thermal degradation will consider specific systems.

The temperature and dopant ion have large roles to play in the stability of polypyrrole. Solid state NMR^[21] of polypyrrole films at 150 °C indicates the loss of dopant ion accompanies the loss of conductivity. Dodecyl sulphate,^[21,93] decomposes on heating, possibly leaving a sulphate ion and tends to cross-link the polypyrrole in an inert atmosphere. This dopant ion was observed to be less stable than *p*-toluene sulphonic acid. Infrared and mass-spectral data taken during the thermal degradation of electrochemically grown polypyrrole doped with *p*-toluene sulphonic acid, indicate a high concentration of oxygen defects. In the initial stages H₂O, CO, CO₂ and CH₃C₆H₄ are evolved, though SO₃⁻ could not be resolved and no evidence of pyrrole was seen.^[153] At higher temperatures evolution of HCN and SO₂ was evident.^[93,153]

DSC measurements have been made of *p*-toluene sulphonate and dodecyl sulphate doped polypyrroles.^[148] The *p*-toluene sulphonate doped polymer appears to undergo a water-plasticized endotherm at that is dependent on the method of film preparation. Above 100° C there is evidence of water loss. For dodecyl sulphate films a similar endotherm may be due to a surfactant induced phase change as noted by crystallography.^[131]

Mechanical and electrical properties of aged polypyrrole have been made.^[151] Aged samples quickly became stiff and brittle probably due to egress of plasticizing solvent from the film. Highly doped polypyrrole had a lower breaking stress than lightly doped material due to the crack propagating along granular boundaries found in the highly doped film. Lightly doped films were noted to be smooth.^[151]

At room temperature chemically formed polypyrrole is less stable than that formed by electrochemical methods due to a larger surface area.^[40] When the polypyrrole powder is dispersed in polymer matrices, such as LDPE, HDPE or polystyrene, the conductivity behaviour depends on the glass transition temperature of the polymer. For LDPE and HDPE, annealed at 55 or 80° C (higher than T_g), the conductivity steeply decreased before reaching a steady state. It is surmised that the thermo-expansion and mobility of the matrix allows it to encapsulate the conducting particles.

Polypyrrole dispersed in polystyrene and annealed at these temperatures had a very stable conductivity.

Conducting polymers have a high reactivity to oxygen, which disrupts the percolative networks and reduces conductivity.^[88] Exclusion of oxygen with nitrogen, or by encapsulating the polymer in a protective coating, decreases conductivity loss. Examples of potentially useful oxygen barriers include poly (vinyl chloride), paraffin, poly (vinylidene chloride)-poly(acrylic acid) copolymer, poly (vinylidene chloride), polyester and polyolefin.^[89,154] Epoxy resin has also been used to encapsulate PPy coated textiles.^[53] In the absence of oxygen, the rate of conductivity decrease is greatly reduced and seems to be dependent on Cl⁻ ion content in the films. PPy prepared from Fe(PTSA)₃ does not lose conductivity at elevated temperatures, whereas codoped Cl⁻ and PTSA films do, though at a lower rate than in the presence of oxygen.

Kinetics of PPy-textile degradation has been studied as a function of dopant ion (Cl⁻, PTSA, NDSA, N2SA, AQSA).^[68] The degradation process was found to be diffusion controlled and first order. For polypyrrole this is thought to be due to the polymer having a high concentration of polarons (free radical sites)^[131] and since oxygen adsorption is assumed faster than reaction with the polymer backbone, so first order kinetics are observed. Other studies have shown an increase in carbonyl functionality during degradation though with no accompanying mass increase. This would follow the suggestion that hydroxyl groups are incorporated in the structure during chemical polymerization.^[91] Subsequent stability studies have indicated that the conductivity degradation is controlled by the diffusion of the oxidizing species into the film.^[92-95] Diffusion control is applicable at short times with the reaction rate becoming first order at long times.^[68]

Polypyrrole morphology and stability is dependent on its composition.^[147] Conducting films made with ferric chloride have chloride counterions (dopant), which has a higher mobility than other counterions. Chloride ion doped films tend to dedope at elevated temperatures in contrast to other less mobile ions. Adding other suitable salts (eg sodium salts of aryl sulfonates) results in films containing mixed dopants. Elimination of chloride ions from the film can be achieved by using other ferric salts of the arylsulfonates.^[2] These hydrophobic dopants tend to form more compact, stable and conducting films which is due in part to their planar structure, though it is surmised that the hydrophobic nature may favour their thermodynamic incorporation in the film.^[68] In the case of anthraquinone-2-sulfonic acid salts, AQSA, it may be more a question of working near the solubility limit of the AQSA in water that favours its incorporation in the film.^[67] Studies of the atomic ratios of Cl/N for films made with FeCl₃, PTSA and AQSA show a decreasing trend in the amount of chlorine in the films, while the S/N ratio shows an increasing trend in the sulfur content. The total (S+Cl)/N increases to 0.34 for AQSA which is effectively the doping limit of one counterion per three monomer units. Another ratio that has been looked at is the O/N ratio which is smallest for the AQSA films. Some of the oxygen will come from included water^[2], and some from chain termination reactions forming pyrrolidinone. Another possible source has been identified as nucleophilic hydroxyl substitution of the pyrrole rings.^[91]

Scanning TGA measurements made of PPy coated PET show mass loss at 400° C, which is the same as pure PET. Isothermal TGA at 300° C show greater mass decreases for PPy Coated PET than pure PET.^[96]

4.3.4 Material Characterisation

4.3.4.1 Spectroscopy of Polypyrrole

UV/Vis spectroscopy of oxidized polypyrrole (conducting) shows two absorbance maxima at about 430 and 900 nm. These two peaks have been attributed to transitions of the valence to polaron and bipolaron/polaron states. Extrapolation of λ_{\max} for the first one-electron oxidation peak of oligomers, to infinite chain length, gives the optical transition E_g of 2.81 eV or 435 nm and polymerised product yielded 435 nm.^[3] The ratio of the two absorbance maxima mirrors the doping level of the polymer which in itself is dependent on the degree of oxidation and the length of conjugation. An electrochemically grown tosylate doped polypyrrole film was reported to have a ratio of 1.6.^[130] This ratio decreases if the polymer is reduced or over oxidized. Reduced polypyrrole has an absorption band at about 410 nm which is assigned as the $\pi \rightarrow \pi^*$ interband or valence to conduction band transition.

More recent UV/Vis measurements of electrochemically grown polypyrrole^[131] and theory indicate four possible states for polypyrrole existing all at the same time. These states are the neutral polymer, polaron (radical cation), bipolaron (dication) and transverse bipolaron. This latter class describes polarons on adjacent chains that couple to form “transverse bipolarons”. The bands at 1.4 and 1.8 eV are assigned to the sum of the polarons and transverse polarons. The band at 2.44-2.5 eV is assigned to the sum of the polarons, bipolarons and transverse bipolarons, and the band at 3.2 to 3.6 eV is due to the bandgap of polypyrrole.

4.3.4.2 IR-Raman spectroscopy of polypyrrole

If PPy is considered as a chain of coplanar pyrrole units in the anti conformation, then the one dimensional lattice is of the D_{2h} point group with $16 \times 3 - 4$ normal modes.^[132] These are as follows

In-plane modes: 8 A_g (Raman polarised) + 8 B_{1g} (Raman dep) + 7 B_{2u} (IR) + 7 B_{3u} (IR)

Out-of-plane modes: 3 A_u (inactive) + 4 B_{1u} (IR) + 3 B_{2g} (Raman dep) + 4 B_{3g} (Raman-dep).

There is a vibration, termed the R vibration, which corresponds to the expansion / shrinking of the bonds representing the HOMO “aromatic” structure and LUMO “quinoid” structure of PPy, and this leads to modes that are apparent in the Raman. Of the Raman modes, only those that are symmetric tend to produce a noticeable absorption. For PPy calculations have predicted that only three of the totally symmetric modes will be Raman active.^[132]

The effective conjugation lengths of pyrrole oligomers and pyrrole were measured.^[3,91,132-135] The main bands are listed in Table 4.2. What is interesting is the presence of bands, which can be assigned to the oligomer chain-ends and these are still apparent for polypyrrole.^[132] The work with oligomers shows an increasing delocalisation of the π -electrons with increasing conjugation length. This indicates a 0° conformational angle between the inter-ring carbon bonds. The effective delocalisation length appears to reach a limit at 7-9 pyrrole rings. Protecting groups on the pyrrole cause a distortion to the planarity of the rings (inter-ring angle of 70°) though there is indication of delocalisation.^[3]

Table 4.2. IR and Raman absorption frequencies.		
IR FREQUENCY OF ABSORPTION CM⁻¹	RAMAN FREQUENCY OF ABSORPTION CM⁻¹	ASSIGNMENT
3558		O-H stretching covalently bound due to lack of O-H bending at 1620 cm ⁻¹ in undoped PPy ^[91]
3400		N-H stretching
3110		Aromatic C-H stretching
	1557 (S)	Ag R vibration
1547		C=C stretching
1497		
1440		C-C, C-N stretching
	1312	Ag
1310		Mixed bending and stretching vibrations associated with C_N links
1223		
1180		C=N stretching
1115		C-O vibration for undoped PPy ^[91]
	1037	Ag
1035 (1043)		N-H wagging
759		N-H wagging

4.3.4.3 Characterisation of Polypyrrole's Permittivity and Conductivity at Microwave Frequencies

The permittivity of a material is a function of frequency, and it depends on the conduction and polarisation processes within the material. In the case of conducting

polymers the observed loss characteristics are due to conduction processes,^[1] which depend on inter- and intra-chain charge transport. Decreasing polymer defects and increasing chain length increase intra-chain transport, while decreasing dopant and polymer substituent size and increasing pressure increases inter-chain transport. These effects have a direct bearing on the real and imaginary components of the permittivity. ϵ' and ϵ'' both increase with increasing polymer chain length and decreasing defect number. Increasing the chain separation by dopant, substituent or lower pressure, lowers the values of ϵ' and ϵ'' .^[1]

Permittivity results have been presented for polypyrrole powder and electrochemically prepared polypyrrole flakes dispersed in silicone rubber and vinyl ester as a function of volume percent polypyrrole.^[41] The composites were found to be conductive if the powder aggregated in the silicone rubber before setting. The pyrrole flakes do not form a percolating network even at high loadings. Increased conductivity of the polypyrrole used in the composite resulted in higher values of ϵ' . This higher permittivity was assigned to the increase in interfacial polarisation between dispersed particles and insulating matrix.^[41] When the conducting medium is isolated from other particles the conductivity of that material has little overall effect on ϵ'' , compared to composites where a percolation path is established. Surface tension of the conducting and insulating matrix phases will facilitate aggregation if there is a large mismatch, and will facilitate dispersion if they are similar. Silicone rubber has a very low surface tension. Particle size will also favour aggregation if the particles are small, due to the interfacial energy gained upon dispersing small particles.

4.3.4.4 Conducting Nature of Polypyrrole

Charge carriers in polypyrrole result when the neutral, non-conducting polymer is oxidized, leading to polaron or bipolaron states.^[136]

A conducting polymer is generally thought of as a disordered material, though exceptions exist.^[137,138] In the undoped state there are no conduction paths ($\sigma_{dc} = 0$). As the polymer becomes partially doped, islands of conducting material develop which are oxidized sites on the polymer chains. These sites are generally fixed by structural disorder and dopant and generally isolated from each other. A small percentage of the sites will form a network across the material, yielding a small, finite dc (static) conductivity. Tunneling or hopping of charge carriers between sites (islands) in the polymer (variable range hopping model, VRH) accounts for the ac conductivity or intra/interchain conduction noted at higher frequencies. The total conductivity is thus a combination of the frequency dependent and dc conductivities. Higher doping levels increase the network density through the polymer and at the same time eliminating the number of isolated sites that give rise to the ac conductivity. At the limit of very high doping levels the number of isolated sites is at a minimum and the dc conductivity dominates the total conductivity.

For conducting polymers the conductivity is both temperature and frequency dependent.

4.3.4.5 Temperature Dependence of Conductivity

The temperature dependence of the dc conductivity^[137,138] of conducting polymers tends to follow the Variable Range Hopping model's prediction of

$$\sigma = \sigma_o \exp\left[-\left(\frac{T_o}{T}\right)^{1/4}\right] \quad 4.3$$

where

$$\begin{aligned} \sigma_o &= e^2 R^2 v_{ph} N(E_F) \\ T_o &= \frac{\lambda \alpha^3}{kN(E_F)} \end{aligned} \quad 4.4$$

and T_o is the characteristic temperature, e is the electronic charge (1.602×10^{-19} C), k is Boltzmann's constant (8.616×10^{-5} eV/K), R is the average hopping distance (cm) v_{ph} is the phonon frequency ($\sim 10^{13}$ Hz), $N(E_F)$ is the density of localized states at the fermi level ($\text{cm}^{-3} \text{eV}^{-1}$), λ is the dimensional constant (~ 18.1) and α is the coefficient of exponential decay of the localized states (cm^{-1}).

A plot of $\ln(\sigma)$ vs $(T)^{-1/4}$ is a straight line for a number of conducting polymers. For lightly doped polypyrrole, the average hopping distance, R , was calculated to decrease from 1.6 to 0.44 nm at 300 K and 3.7 to 1.0 nm at 10 K for increasing dopant levels. These numbers equate to 5 - 1.5 and 12 - 3 monomer units at each temperature.^[139]

4.3.4.6 Frequency Dependence

Low frequency methods ($10^{-2} - 10^7$ Hz) of measuring electrical relaxations in a material yield the equivalent parallel conductance, G , and capacitance, C . These terms then define the complex permittivity, ϵ^* , conductivity, σ^* , resistivity, ρ^* , and complex modulus, M^* .

$$\epsilon^* = \epsilon' - i\epsilon'' = \frac{1}{M^*} = \frac{\sigma^*}{i\omega\epsilon_o} = C - \frac{iG}{\omega\epsilon_o} \quad 4.5$$

$$\sigma^* = \frac{1}{\rho^*} = G + i\omega\epsilon_o C \quad 4.6$$

$$\rho^* = \rho' - i\rho'' = \frac{G}{G^2 + \omega^2 \epsilon_o^2 C^2} - i \frac{\omega\epsilon_o C}{G^2 + \omega^2 \epsilon_o^2 C^2} \quad 4.7$$

$$M^* = \frac{\omega^2 \epsilon_o^2 C}{G^2 + \omega^2 \epsilon_o^2 C^2} + i \frac{\omega\epsilon_o G}{G^2 + \omega^2 \epsilon_o^2 C^2} \quad 4.8$$

From studies of dielectric relaxation on mobile charge carriers, a contribution to the permittivity is assumed to arise from the mobile charge carriers that is frequency dependent

$$\varepsilon''_{\sigma} = \frac{\sigma_{DC}}{\omega \varepsilon_o} \quad 4.9$$

where σ_{DC} is the static or low frequency conductivity of the material and accounts for long-range charge transport. This expression is often subtracted from the imaginary component of the permittivity to account for dielectric relaxation processes not involved in long-range charge transport. The resultant expression for the complex permittivity is

$$\varepsilon^* = \varepsilon' - i \left(\varepsilon'' - \frac{\sigma_{DC}}{\omega \varepsilon_o} \right) \quad 4.10$$

This equation makes the assumption that the transport mechanism, leading to long-range DC conductivity, has no influence on the complex permittivity other than the contribution from equation 4.9. This in turn implies that the conductance process can be defined by one relaxation time, τ_{σ} ,

$$\tau_{\sigma} = \frac{\varepsilon_o \varepsilon_s}{\sigma_{DC}} \quad 4.11$$

For a disordered system such as a conducting polymer, or conducting composite, a distribution of relaxation times, $\langle \tau \rangle$, is more appropriate.

$$\sigma_{DC} = \frac{\varepsilon_o \varepsilon_s}{\langle \tau \rangle} = \frac{\varepsilon_o}{M_s \langle \tau \rangle} \quad 4.12$$

where M_s is the static modulus or the reciprocal of the static permittivity.

From the above discussion of the conduction mechanisms it is clear that the conductivity of polypyrrole is also dependent on the level of doping (oxidation) and the frequency. The total conductivity of a material is the sum of the ac and dc components

$$\sigma_{Total} = \sigma_{ac} + \sigma_{dc} \quad 4.13$$

For lightly doped polypyrrole films, the ac conductivity is larger than the dc when the frequency is high due to conduction by hopping transitions. At low frequencies the dc conductivity is larger and dominates charge transport due to the charge carriers having time to cross the sample following the percolation network. At high dopant levels the dc conductivity dominates and the total conductivity is frequency independent.^[139]

The imaginary component of the permittivity is related to the ac and dc conductivity by the equation

$$\varepsilon'' = \frac{\sigma_{ac} + \sigma_{dc}}{\omega \varepsilon_0} \quad 4.14$$

4.3.4.7 Conductivity of Composites

For a polypyrrole poly(methyl methacrylate) composite above the percolation threshold, the conductivity shows different behaviour in three frequency regions. At low frequency, the conductivity is frequency independent and follows the scaling law

$$\sigma = A(p - p_c)^t \quad 4.15$$

where p and p_c are the weight fractions PPy in the composite and at the percolation threshold, respectively, t is the percolation exponent (t has a theoretical value of 2 for percolation) and A is a constant related to the bulk conductivity of the PPy, (ie at $p = 1$, $\sigma = \sigma_{PPy}$). Experiment gave an exponent t of 1.95.^[140]

At intermediate frequencies, MHz-GHz, a relaxation transition has been observed and attributed to space-charge relaxation. Above the percolation threshold an infinite cluster exists as well as finite and isolated clusters of all sizes. The mean size of finite clusters, L , is governed by percolation theory and varies as

$$L \propto (p - p_c)^{-\nu} \quad \text{at } p < p_c. \quad 4.16$$

Charge transport in this region is diffusive and the imaginary permittivity peaks at a frequency of

$$f_{\max} = \frac{D}{2\pi L^2} \quad 4.17$$

where D is the diffusion coefficient of the charge carrier. From this equation it is seen that the maximum frequency is dependent on the length of the clusters, L . This is why ε'' peaks at the percolation threshold, where L is at a maximum. It can be shown that

$$f_{\max} \propto (p - p_c)^{2\nu} \quad 4.18$$

where the theoretical value of ν is 1 for percolation theory and experiment give $\nu = 1.2$.^[140]

At high frequencies, >1 GHz, the ac contribution to the conductivity results from the hopping process and is given by

$$\sigma_{ac} \propto \omega^x \quad \text{where } x > 0 \quad 4.19$$

$$\epsilon'_{ac} \propto \omega^y \quad \text{where } y < 0 \text{ and } x-y = 1. \quad 4.20$$

Composites of PPy-PMMA follow this behaviour.^[140]

Pelster and Simon study and review dispersions of nano conducting particles in a matrix.^[141] The conductivity is related to the penetration depth, δ , of electromagnetic radiation into a material by the equation

$$\delta = \sqrt{\frac{2}{\omega\sigma\mu}} \quad 4.21$$

where ω is the angular frequency, $2\pi f$, and μ is the permeability of free space.^[142]

4.3.5 Polypyrrole use in Radar Absorbing Materials

A big issue with the preparation of radar absorbing materials from polypyrrole is the process by which the material is made. Polypyrrole dispersed in a matrix yields very different permittivity characteristics than does *in situ* composite formation.^[1]

4.3.5.1 Dallenbach Layers / Polypyrrole Composites

One of the few references that presents permittivity, conductivity and reflectivity data for polypyrrole, shows that processing has a great effect on the final product.^[143] Polypyrrole/PVC composite was compression moulded and melt injected into sheets.

The compressed material was macroscopically conductive with $\epsilon'' \propto K\omega^{-s} = \frac{\sigma(\omega)}{\omega\epsilon_0}$,

where K is a constant and the conductivity is frequency dependent. The melt-injected material was macroscopically insulating with Maxwell-Wagner type relaxation. The

relaxation frequency is given by $f_r = \frac{\sigma_2}{2\pi\epsilon_0(2\epsilon'_1 + \epsilon'_2)}$, where the subscript 1 denotes

the properties of the matrix and 2 the conducting phase. The compressed material is difficult to make into a tuned absorber, while the melt injected material readily forms a resonant Dallenbach layer.^[143] This material shows a very narrow absorption with more than -40 dB reflectivity.

Dallenbach layers have also been made from polypyrrole doped with *p*-toluene sulphonic acid sodium salt, or 5-sulfosalicylic acid dehydrate.^[52,144] The chemically prepared powder was dispersed in a commercial paint, or milled with natural rubber and moulded into flat sheets and both were applied to an aluminum backing panel. These materials show resonance absorption if the content of the conductive powder is not below the percolation threshold. The rubber composites, and inclusion of conducting fibres that did not produce a macroscopically conductive material, still had

a reasonable high value of ϵ'' and were therefore useful in making Dallenbach layers. A hybrid dielectric/magnetic material was also made using carbonyl iron, however, extra bandwidth was not realised for this material.^[52,144] Powder processing was noted to have an influence on the final material properties.

Materials with conductive gradients have been made.^[144] Phenolic foam, with a pore size on the order of 1 μm , was soaked in aqueous ferric chloride and then exposed to pyrrole vapour from one side. The gradient was obtained by controlling the exposure time. Uniformly coated foam was prepared by immersing the oxidant doped foam in an aqueous pyrrole solution and flowing the pyrrole solution through the foam. The permittivity of the foam was measured and showed very low values of ϵ_r' in the range of 1-2 and good values of ϵ_r'' in the range of 0.5-10. Two problems are associated with vapour polymerization, a thick coating on one surface of the foam and poorly conducting polymer doped with chloride from the ferric chloride. The wet method produced a material with better properties and a gradient could be induced into the material. It was noted that a 15 mm thick foam prepared in this manner^[144] performed better than other published gradient absorbers.^[145,146]

Paper, cotton and polyester fabrics have been coated with polypyrrole as discussed above.^[98,99,101,102] Modelling the reflectivity from the material alone with a resistance-capacitance model, shows some interesting properties.^[100] The capacitance of the material increases with increasing loading of polypyrrole on the fabric, until granular deposits form which are thought to short circuit the fibres. The conductivity still increases with increased loading, however, the capacitance was observed to decrease.^[98,100,101] These materials have been made into Salisbury screens and Jaumann layers. The presence of capacitance in the material allows for additional design control with the production of thinner absorbers. Asymmetric weave has a polarisation effect.^[100] The effect of incident angle and polarization were measured and presented.^[102]

Polypyrrole coated textile fibres have been considered as replacements for metallised fibreglass chaff. With the correct chemical composition the impact on the environmental and accelerated degradation could be limited.^[147]

4.3.5.2 Stability

The conductivity of polypyrrole is not stable and decreases with time. The degradation rate is influenced by: temperature, oxygen level and dopant species. Thermal stability experiments, have shown that the rate of conductivity degradation increases with increasing temperature.^[40,94] The process follows kinetics characterized by a diffusion-controlled mechanism at high temperatures and first-order kinetics at lower temperature^[148]. It is thought that the conductivity loss is due to the diffusion of oxygen into the polymer^[94] where it can react to form functional groups such as carbonyls that disrupt the conjugated π -network. It has also been proposed^[95] that the conductivity loss is due to a process in which oxygen exchanges with the dopant species, and subsequently oxidises the polymer backbone. The aging of polypyrrole

samples at elevated temperatures under inert atmospheres such as argon and nitrogen^[40,93] does not affect conductivity even when the temperature is raised to 200°C. Dopants also affect the rate of conductivity decrease. Aryl sulfonates have been shown to slow this loss compared to mineral anions. It is thought that the aryl sulfonates are less susceptible to volatilization, decomposition and chemical reaction^[95].

4.3.6 Experimental

4.3.6.1 Synthesis of Conducting Polypyrrole Powder

A typical chemical synthesis of polypyrrole is as follows. Ferric chloride hexahydrate (21.6 mmol), FeCl₃, was used as the oxidant. FeCl₃ was added along with a dopant (2.3 mmol) (in the case of these experiments dopants were aryl-sulphonates, Table 4.3) to 750 mL of high purity H₂O, 0.75 mL of conc. HCl and 1 mL of distilled pyrrole (7.2 mmol) were then added. The reaction vessel was then placed in an environmental chamber set at 1°C where it was mechanically stirred and allowed to polymerize for 24 hours. The ratio of oxidant to monomer was set to 3:1. After the 24 hour polymerization period, the reaction vessel was removed and the black opaque liquid was suction filtered leaving black polypyrrole powder. This powder was then dried under vacuum for 12 hours.

Table 4.3. Dopants and Acronym

DOPANT	ACRONYM
Anthraquinone-2-sulfonic acid, sodium salt	AQSA
Anthraquinone-2,6-disulfonic acid, disodium salt	AQDSA
1-Naphthalene sulfonic acid, sodium salt	NSA-1
2-Naphthalene sulfonic acid, sodium salt	NSA-2
1,5-Naphthalenedisulfonic acid, disodium salt	NDSA
Para-toluene sulfonic acid	PTSA

4.3.6.2 Formation of Polypyrrole Coated Fabric

All reactions are based on the recipe of 50 g fabric, 16.7 g ferric chloride, 2 g pyrrole, 1.5 g of 37% HCl, 1.5 L deionized water and 10% Anthraquinone-2 sulfonic acid, sodium salt by mass of fabric. These amounts were scaled in proportion to the mass of

the fabric used. The fabric was used as supplied, cut, weighed, and placed into 100 mL Schott glass bottles with plastic lids. Appropriate amounts of oxidant, ferric chloride, anthraquinone salt, water and HCl were added. The solutions were placed in an environmental chamber on a rotary stage and cooled for approximately 1 hour to 1 degree Celsius. To the solutions were added the appropriate amount of distilled pyrrole and returned to the rotary stage in the environmental chamber. These solutions were allowed to react for 18.5 hours, maintained at 1 degrees Celsius, after which they were removed from the chamber and the reactants were poured out of the bottles. The fabric was then rinsed with deionized water to remove excess reagents, until no residual colour could be detected leaching from the sample. The material was allowed to air-dry at room temperature overnight and then weighed.

The fabrics used in this study included cotton, polyester (PET), polyamide and glass fibre. The properties of the fabrics are summarized in Table 4.4.

Table 4.4. Fabric description.

Fabric	Density Fabric (g m ⁻²)	Thickness cm	Weave type	Fabric Count (Warps x Fills /25 mm)	Filament type	Filaments per Strand	Filament Diameter/ Fibril Diameter (mm) ^c
Cotton #1	132	0.024	Satin ^a	100 x 57	Spun	-	0.22 / 0.02
Cotton #2	70.4	0.017	Plain	105 x 84	Spun	-	0.10 / 0.02
Polyester #1	87.2	0.013	Plain	150 x 90	Rovings	35-37	0.02 /
Polyester #2 ^b	90.8	0.014	Plain	103 x 75	Rovings	34	0.022 /
Polyester #3	37.6	0.013	Plain	72 x 55	Spun	-	0.10 / 0.02
Polyamide	34.0	0.025	Tissue		Single	1	0.06 /
Glass Fibre	36.7	0.020	Tissue		Single	1	0.02 /

^a 5-Harness Satin, 5 ends base of 3

^b Polyester fabric corona treated.

^c The Spun filaments are comprised of fibrils.

4.3.6.3 Polypyrrole Pellet Formation

Pellets of polypyrrole/dopant were made by measuring approximately 150 mg of ppy powder into a 13 mm die press compressed to 138 MPa (10 tons/in²) for a period of 2 minutes. The pellets produced were thin black cylinders with a uniform appearance.

4.3.6.4 Coating Formulation

Several commercial coating systems were used for the formulation of polypyrrole coatings. The products used were

- a. Latex: A carboxylated styrene/butadiene latex dispersed in water from Dow Chemical Inc (DI 238Na), the latex was found to contain 43.5% volatiles.
- b. Alkyd#1: A Sico epoxyflex modified alkyd. With the epoxyflex systems varsol had to be added to achieve paints over 15% ppy to allow application by conventional means. This coating has a low pigment content so higher loadings of PPy could be achieved.
- c. Alkyd#2: A marine enamel alkyd paint containing 30% volatiles from Cloverdale Paint.
- d. Alkyd#3: A urethane modified alkyd marine trim enamel with 15.1% volatiles.
- e. Polyurethane (GP-200): A two part urethane/talc non-slip coating. The GP-200 is a very viscous paint to begin with so in most cases above 7% ppy had to be applied with a troweling technique. The curing times between the two systems varied as epoxyflex > GP-200.
- f. Epoxy: A two-part epoxy paint system from International Paints Ltd., consisting of base coat and curing agent. The parts were mixed in a 4:1 ratio by volume of base coat to curing agent. The base coat was a low molecular weight epoxy resin dispersed in xylene and n-butanol. The curing agent contained polyamino amide and propylene glycol methyl ether with a xylene continuous phase. The base coat and curing agent were found to be 44.2 and 58.9 % volatiles.

Initial attempts to incorporate polypyrrole into paint systems yielded very rough films even after grinding through implementation of a mortar and pestle. Ball milling helped but measurable conductivities were illusive with these preps. The bulk powders were sifted through a 590 micron screen before subsequent paint mixtures were formulated. This achieved a smoother finish as well as bulk to the paint without a loss of measurable conductivity. A speed mixer (Flactec) was used to mix polypyrrole into the GP-200 base (1.5 minutes @ 2400 rpm).

4.3.6.5 Conductivity Measurements

The conductivity of the 13mm diameter polypyrrole pellets, fabric and paints were determined using a Jandel multi-height four-point probe apparatus. D.C conductivity measurements for paint samples were also made using small polyacrylic plaques, which had a conducting silver paint covering the ends of one face. Thin wires were embedded into the epoxy and the sample would be painted onto the plaque covering one side. A voltmeter attached to the wires was used to measure resistance. IR measurements on pellets were made using a Nicolet Nexus 670 FT-IR spectrometer with a Thunderdome attachment. Pyrolysis data was gathered with the Nexus 670

equipped with a Pyroprobe 2000 attachment. Thermal measurements were made using a TGA 51 and a DSC 910. Both the thermogravimetric analyzer and the differential scanning calorimeter were made by TA instruments. For DSC and TGA runs a heating rate of 10°C/min. was used unless otherwise stated.

4.3.6.6 Permittivity Measurements

Samples were machined to fit closely into an X-band waveguide and the S-parameters measured with either a HP 8720C or an Agilent 8364B vector network analyser. The permittivity was fit to the experimental S-parameters by calculating S-parameters based on the material structure and permittivity. The permittivity was varied by a nonlinear least squares optimisation routine that minimised the difference between the experimental and calculated S-parameters.

4.3.6.7 Weathering

Weathering of paint samples was done using ASTM method D 5894. Ultra-violet / Condensation exposure was done using an Atlas screening device. Fog exposure was done using a Prohesion fog cabinet.

4.3.7 Results

4.3.7.1 Galvanostatic Polymerisation of Pyrrole and Control of Film Thickness

A linear relationship between film thickness and reaction time was observed for a series of PTSA doped films, which also appeared to hold regardless of dopant. Electrodeposited film thickness is well controlled through galvanostatic deposition of polypyrrole from an aqueous PTSA electrolyte solution. The results presented in Figure 4.17 cover a range of pH reaction conditions, which do not appear to affect the film thickness.

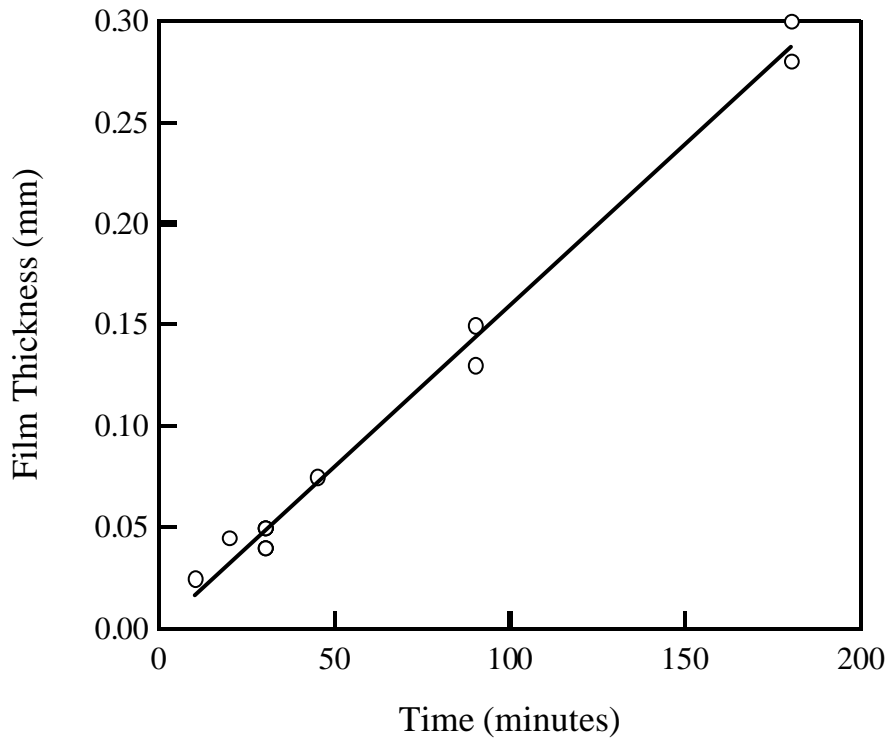


Figure 4.17. Polypyrrole/PTSA film thickness as a function of polymerisation time at constant current. Polymerisation temperature 1°C, current density $\sim 3 \text{ mA/cm}^2$, $0.4 < \text{pH} < 11.4$.

4.3.7.2 Effect of pH on the Conductivity of Electrodeposited Polypyrrole

Conductivity is shown as a function of pH, Figure 4.18, and appears to be inversely proportional to the electrolyte pH. Some deviation from linearity was observed, but it was generally consistent with differences in surface morphology (such as tubular or nodular structures protruding from the surfaces of the films) rather than true film thickness.

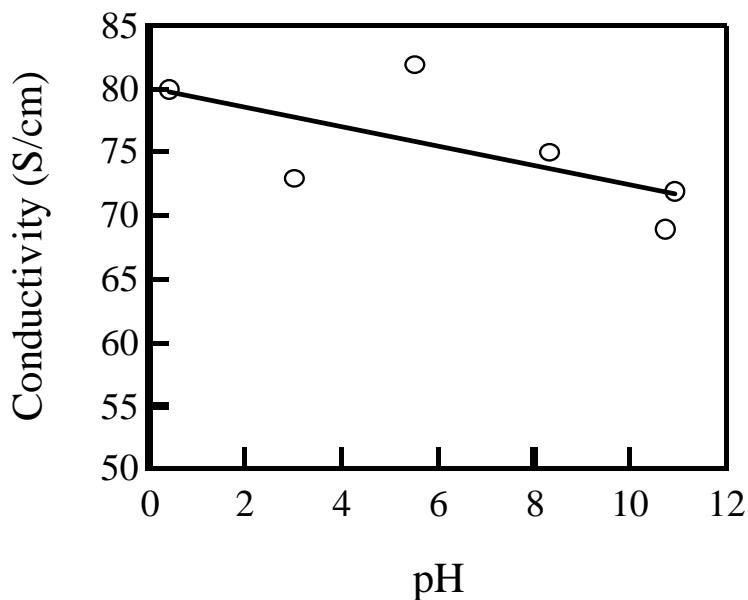
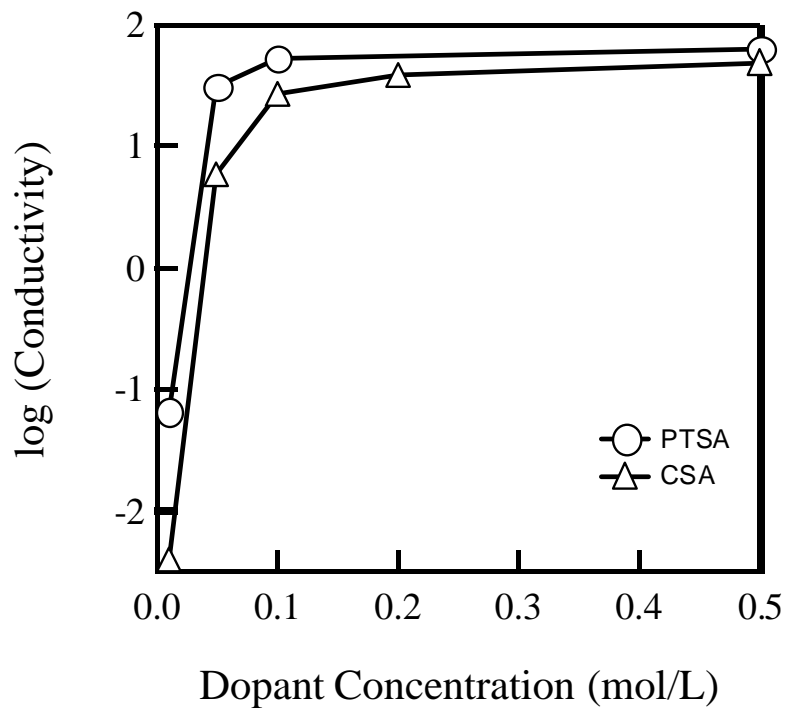


Figure 4.18. Polypyrrole/PTSA film conductivity as a function of initial electrolyte pH.

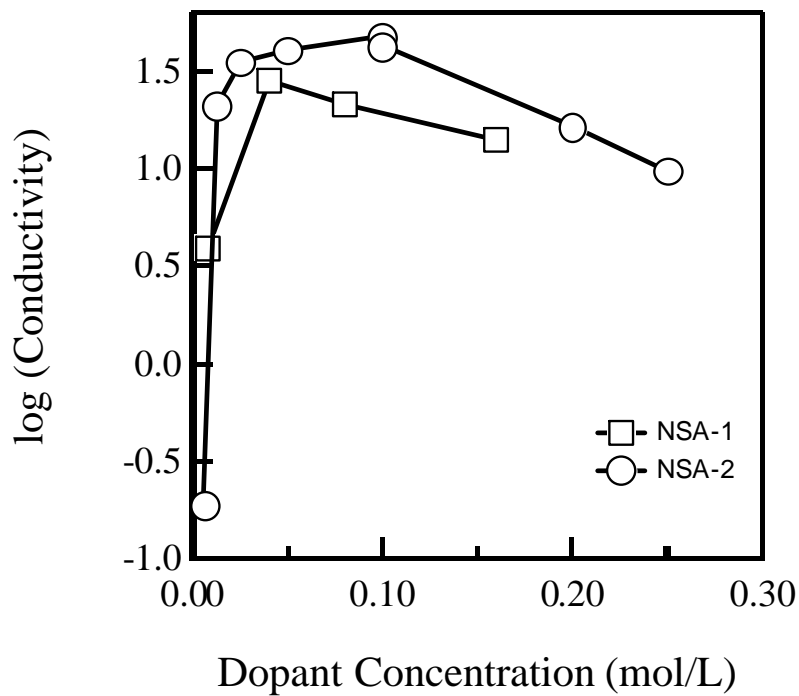
4.3.7.3 Effect of Electrolyte Type on Conductivity

The effect of dopant type and concentration on the conductivities of polypyrrole films was extensively investigated. All dopants investigated showed a similar relationship between concentration and conductivity – this relationship is illustrated for two dopants in Figure 4.19. High conductivities were observed for high dopant concentrations and approached a limiting value above 0.1 M. The electrolytes made with NSA dopants were observed to form gels at higher concentrations, coinciding with a decrease in the overall conductivity of the films.

The mechanical properties of the electropolymerised films improved with the doping level/conductivity. Although all films could fairly easily be removed from the electrodes, lightly doped films were very brittle and tended to crack and chip, whereas the highly doped films were flexible, pliable, and quite resilient. Most of the films produced were highly conductive, so much so in fact that their dielectric behaviour was essentially metallic, with reflection rather than absorption or transmission dominating over the frequency range investigated.



a



b

Figure 4.19. Conductivity as a Function of Dopant Concentration for Electrochemically Synthesized Polypyrrole Films. The conductivity of NSA-1 and NSA-2 doped films decreases at higher concentrations due to the a gellation of the electrolyte (b).

4.3.7.4 Electrodeposition onto Pyrrole Coated Fabric

Initially, an attempt was made to electropolymerise pyrrole onto fabric connected to the electrode. No polypyrrole appeared to be deposited onto the fabric, however, a series of polypyrrole tubules were observed to have grown from the electrode through the weave of the fabric.

Electrochemical deposition/graft polymerization onto fabric chemically coated with polypyrrole was successful, however not reproducible, given difficulties in obtaining consistent current densities through the fabric electrodes.

4.3.7.5 Undoping of Polypyrrole Films

Cycling of the films was also attempted, however the result of the oxidative portion of the cycle was typically degradation of the film, with a loss of both mechanical properties and of electrical conductivity. This may be consistent with the changes in free volume associated with doping (increase in free volume) and dedoping (decrease in free volume). This free volume change is believed to arise from Coulombic repulsions between chains as they are oxidized to their cationic form^[149], and the reverse process taking place on reduction. This expansion and contraction of the films on cycling may well account for their mechanical failure.

4.3.7.6 Polypyrrole Powders

Polypyrrole powder was compressed into pellets for use in studying various properties. Several factors were noted to have an effect on pellet conductivity and these are considered below.

4.3.7.7 Effect of Pellet Density

A variation was noted in the conductivity of pellets pressed from the same batch of polypyrrole. To understand this observation the density of the pellets were determined, and the conductivity plotted as a function of the density, Figure 4.20. Essentially this plot is a straight line up to a density of about 1.16 g/cm³, after which the conductivity appears to plateau.

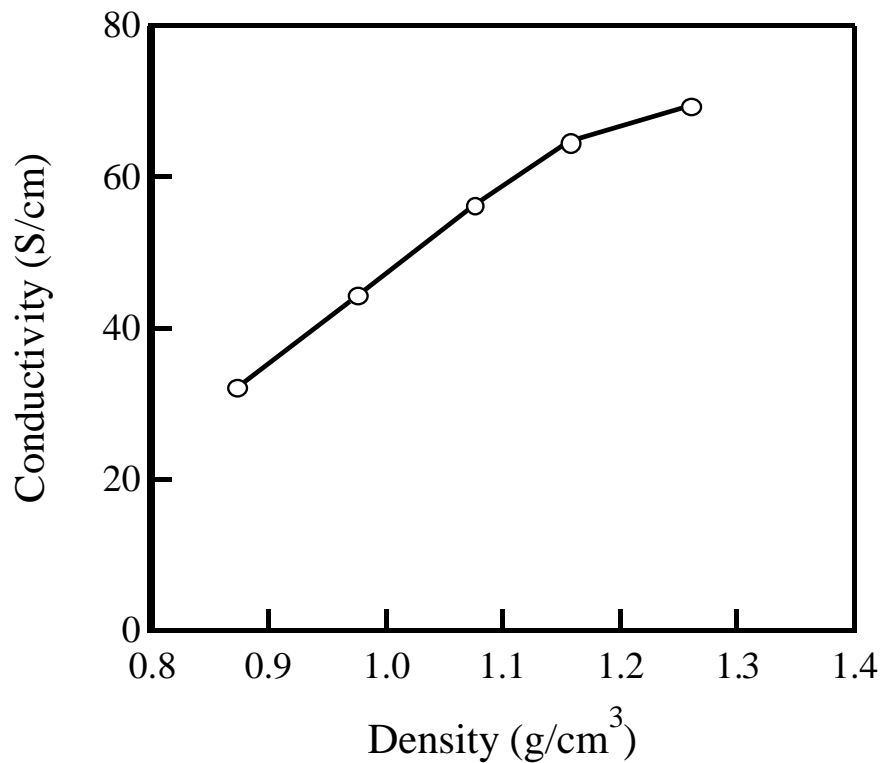


Figure 4.20. Conductivity of pressed polypyrrole pellets as a function of pellet density. Dopant is NSA-1.

4.3.7.8 Effect of Powder Milling

Two different milling techniques were used to make a fine powder of an AQDSA doped PPY. Some of the powder was ground with a mortar and pestle for 10 minutes, some was ground in a ball-mill for 30 minutes and some was un-milled as a control. Pellets were pressed from these powders and the measured conductivities plotted in Figure 4.21. At first appearance the order of increasing conductivity is ball-milled < un-milled < mortar and pestle (Top Figure 4.21). Examination under a microscope at 50.69X magnification showed a difference between the powders. Ball milling produced the smallest particle size followed by the mortar and pestle then the non-processed.

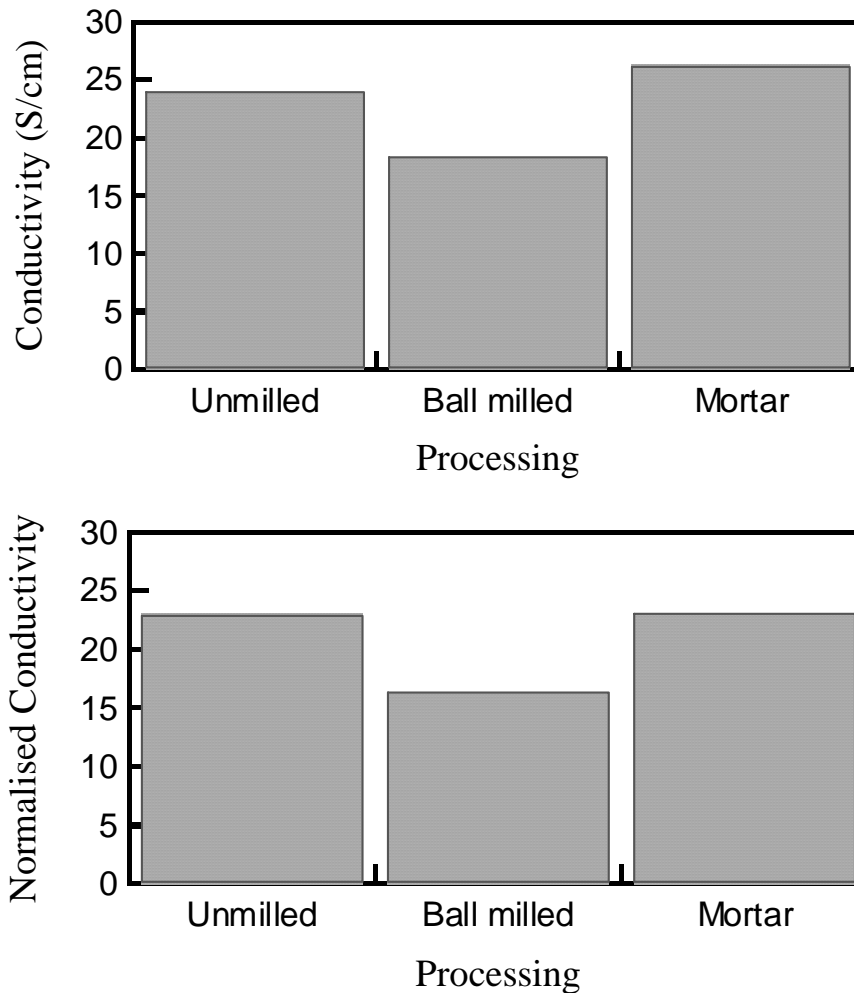


Figure 4.21. Top, conductivity of polypyrrole pellets pressed from powders milled in different ways. Bottom, same plots with the conductivity normalised by the density. Dopant used AQDSA.

In light of the effect of density on the conductivity, the conductivity of these three pellets were normalised by dividing by the pellet density. The result is that the normalised conductivities of the un-milled and mortared pellets are the same, while the ball milled powder produced the pellet with the lowest conductivity. These results indicate that excessive grinding or ball milling degrades the polypyrrole conductivity.

4.3.7.9 Effect of Dopant on Pellet Conductivity

PPy powders were prepared with the dopants listed in Table 4.3. Each polymer was prepared in the same manner and resulted in indistinguishable fine black particles regardless of the dopant. Pellets were pressed for the different powders and the conductivity measured (Figure 4.22).

Measured conductivities ranged from about 10 to 40 S/cm, with the disulfonic acid salts yielding the highest conductivity and AQSA the lowest. This trend partially agrees with other findings,^[94] however, the density of the pellets were not taken into account. Pellets made with AQSA, PTSA and FeCl₃ doped polypyrrole had the lowest densities while AQDSA, NDSA and NSA typically had high densities. At this time is not known if this density trend is inherent in the chemical nature of the material or the way in which the powders were compressed into pellets. AQDSA and NDSA doped polypyrrole pellets have similar normalised conductivities, as do PTSA, NSA and FeCl₃. AQSA has a lower normalised conductivity. Note the comparison of normalised conductivity may not be valid for differently doped polypyrroles.

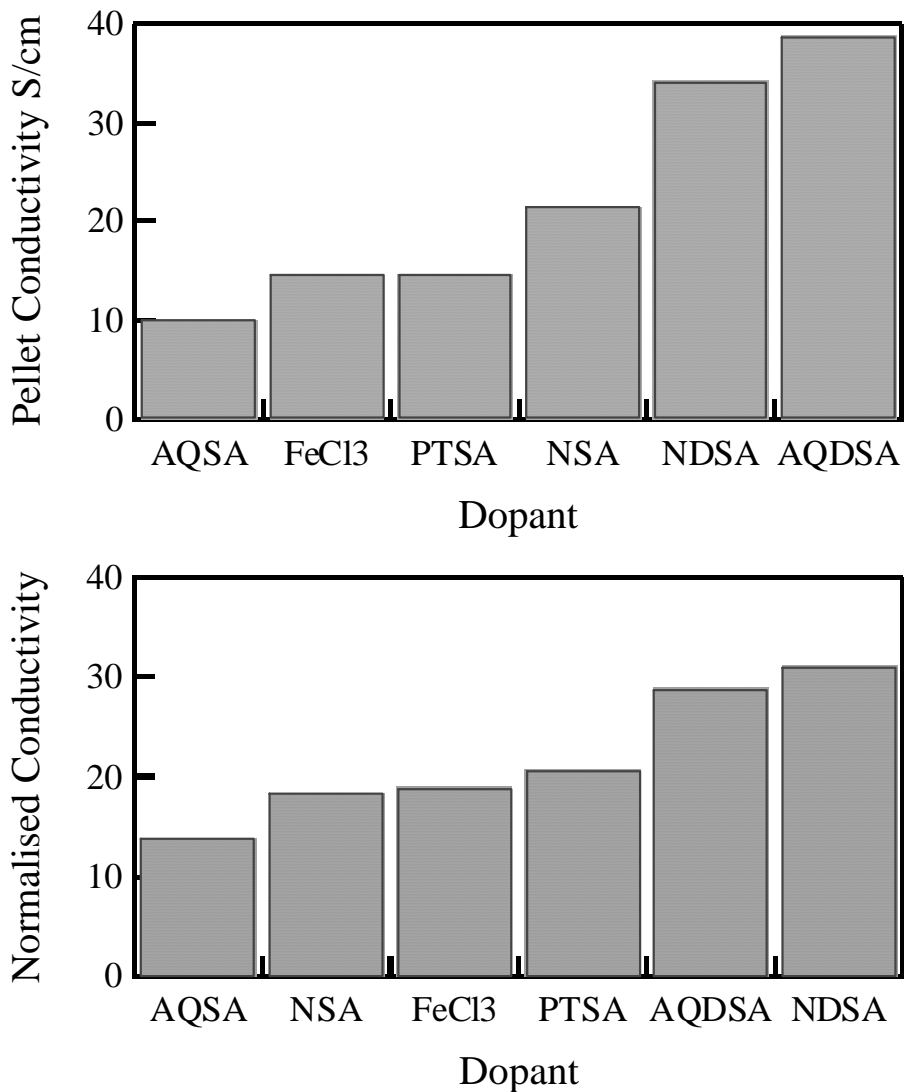


Figure 4.22. Top, conductivity of pressed polypyrrole pellets as a function of dopant. Bottom, normalised conductivity (conductivity/density) of the same pellets.

4.3.7.10 Effect of Dopant to Monomer Concentration Ratio

The data shown in Figure 23 indicate that the conductivity approaches a maximum as the ratio of dopant to monomer approaches 1:3. This ratio is typical for the number of dopant ions to pyrrole rings in oxidised polypyrrole. The scatter in data at this ratio likely arises from concentration variations in the actual reaction mixture.

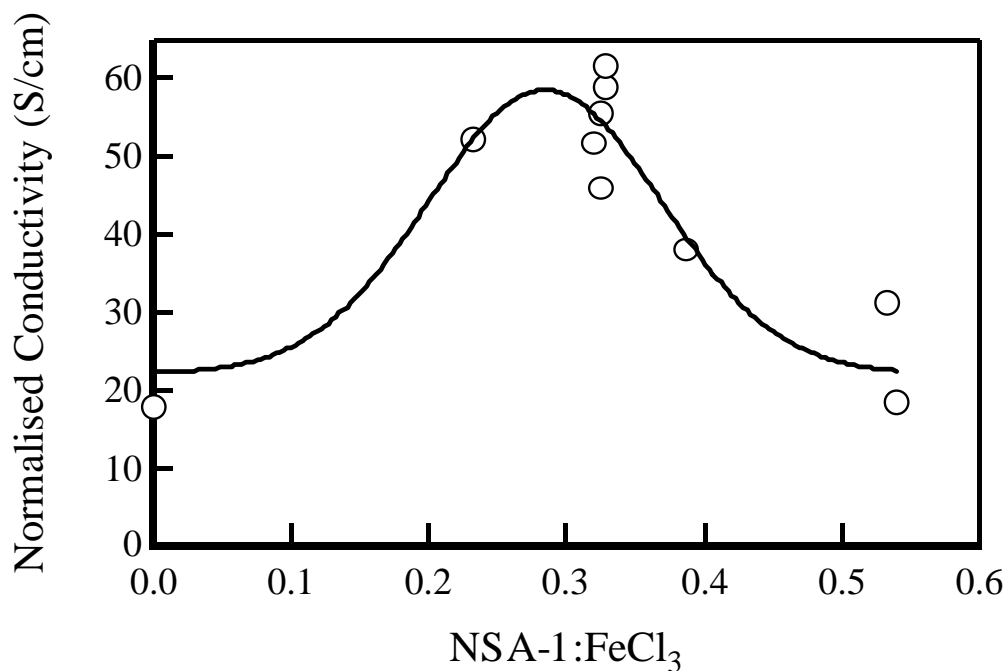


Figure 4.23. Effect of dopant to monomer ratio on the conductivity (normalised for density) of pressed polypyrrole pellets. Dopant ion NSA-1.

4.3.7.11 Effect of Fabric Type

Polypyrrole synthesized in most solvents tends to form particles due to a lack of solubility. These particles usually precipitate as a powder. Adsorption sites that are energetically favourable to the oligomeric pyrrole result in the nucleation and growth of uniform polypyrrole coatings and this is found for the fabric samples, whose fibres become coated with polypyrrole. The resulting material is bluish black to dark green in colour, depending on the reaction conditions and thickness of coverage. Low loadings of polypyrrole produce low conductivities and the material is still highly flexible. At higher loadings the conductivity improves and the material becomes stiffer.

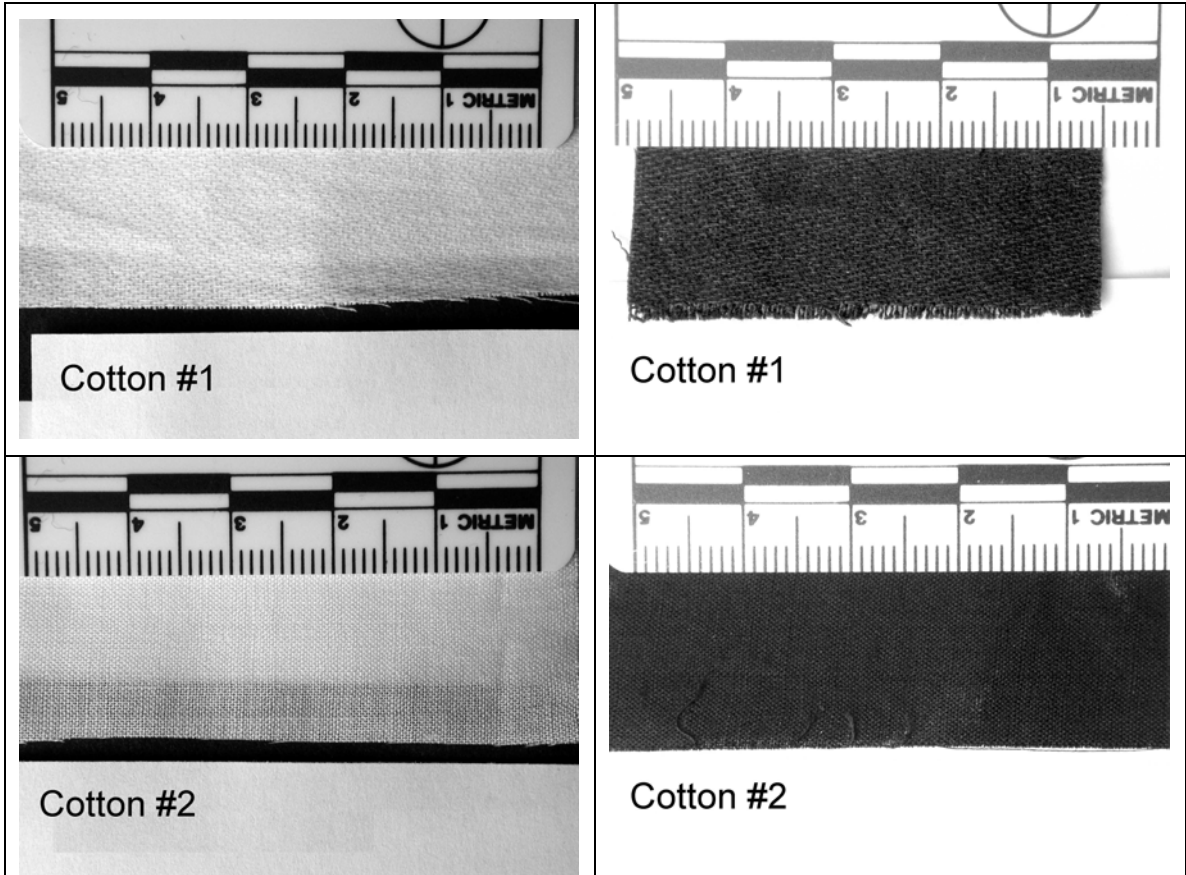


Figure 4.24. Cotton Fabric Samples before and after coating with polypyrrole. The cotton textiles have different weaves and densities and are made from spun fibres.

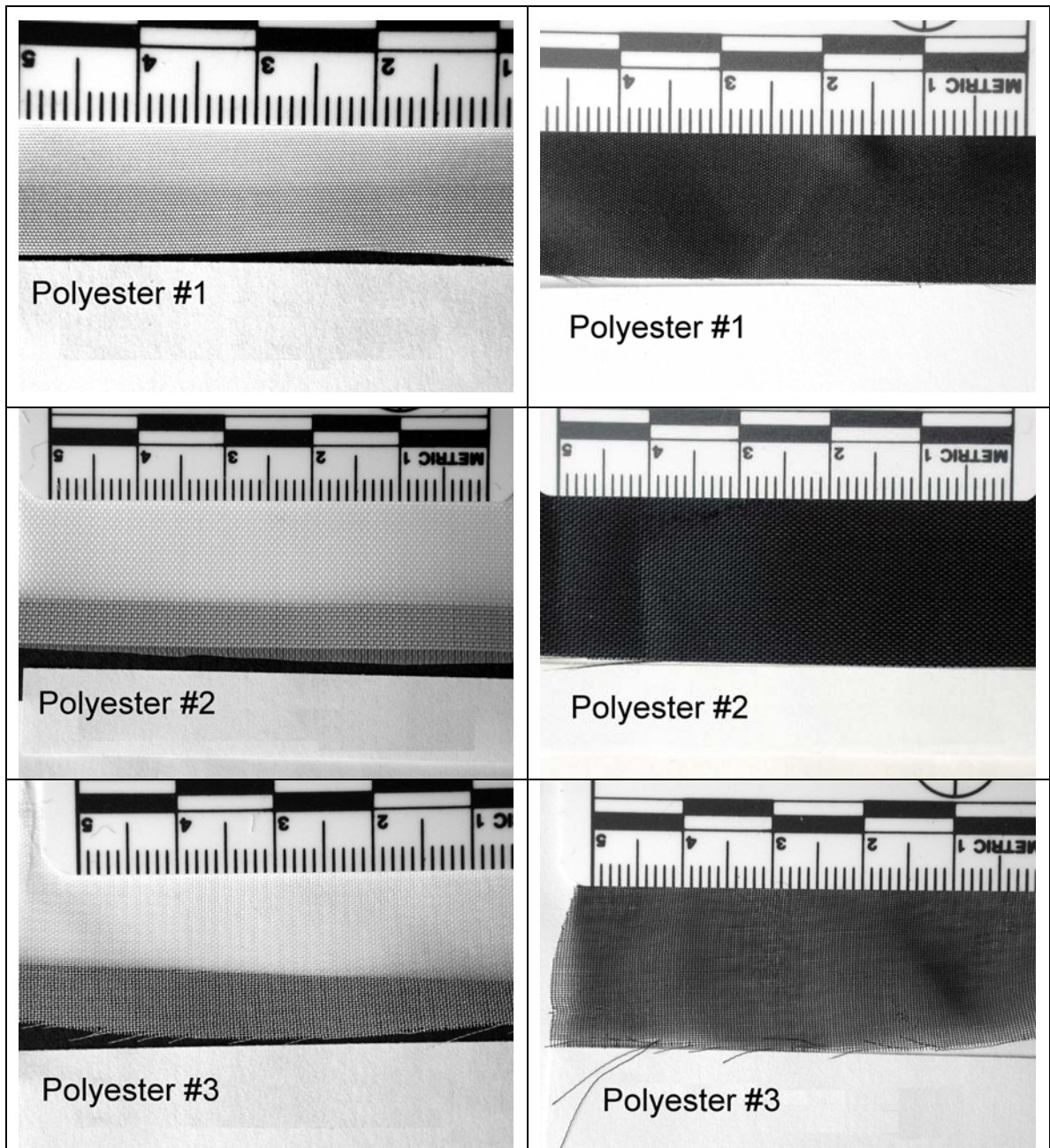


Figure 4.25. Polyester fabric samples before and after coating with polypyrrole. Polyester #1 and #2 have similar densities and are woven from rovings (a loosely associated bundle of untwisted filaments) of about 35 filaments. Polyester #2 had been previously treated in a corona. Polyester #3 has a density more than 50% less than the other polyesters and is woven from spun fibres.

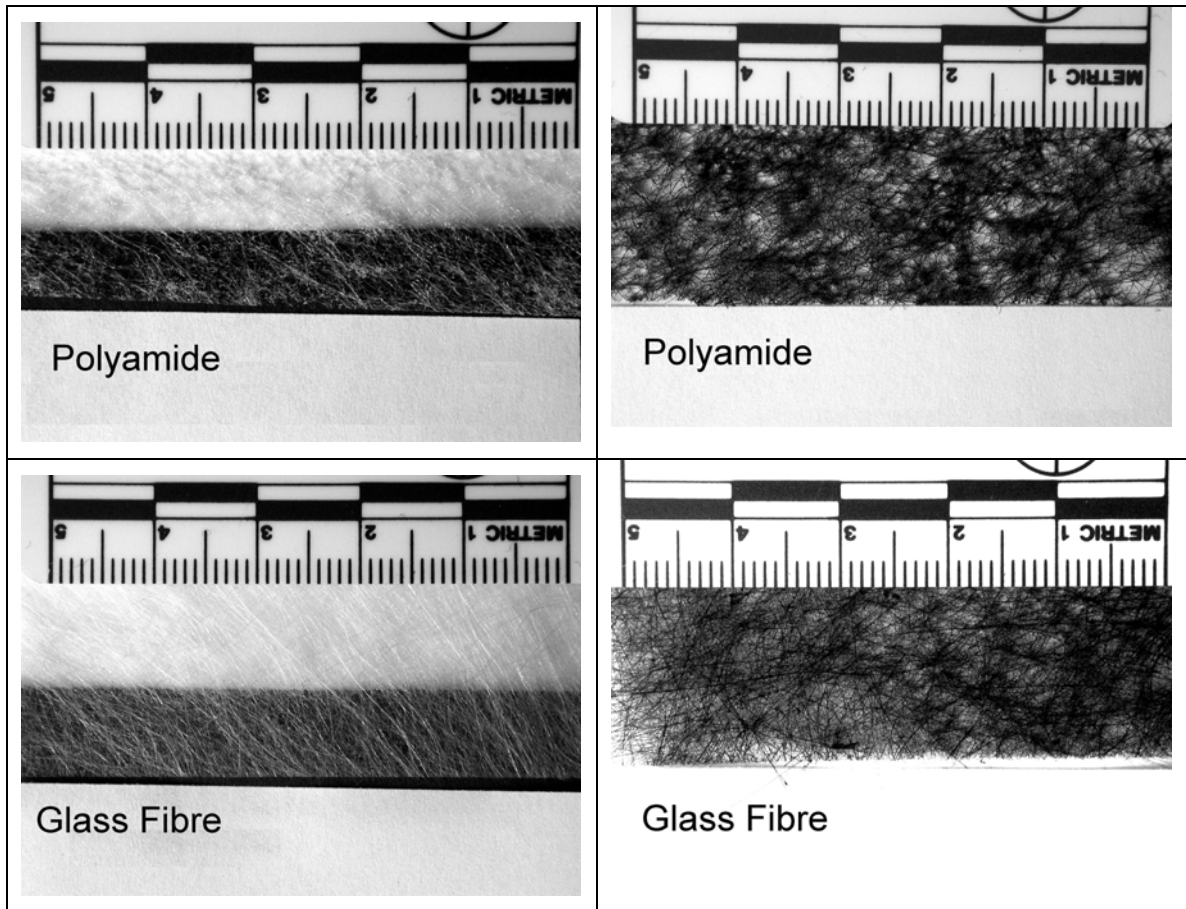


Figure 4.26. Polyamide and Glass tissues before and after coating with polypyrrole. These textiles are made from randomly oriented single filament fibres. The glass fibres are sized while the polyamide fibres appear to be fused.

The polypyrrole coated and uncoated textiles used in this study are shown in Figures 4.24-4.26. The coating is usually black with greenish-blue tinges. These textiles represent a small range of natural and synthetic materials with different weaves, filaments and densities, Table 4.4. The properties of the composite materials are summarized in Table 4.5. The thickness of the polypyrrole coating is roughly estimated by taking the gross surface area of the fabric (length x width x 2) and using the deposited PPy mass and assuming its density to be 1 g/cm^3 . A thickness on the order of $1 \text{ }\mu\text{m}$ is obtained.

Table 4.5. Polypyrrole coated textile properties.

Fabric	Thickness (cm)	wt% PPy	Density PPy (kg/m ³)	% Theoretical Yield	σ (S/cm)	ϵ'_r	ϵ''_r
Cotton #1	0.024	8.68	52.2	98	0.129	10.3	26.4
Cotton #2	0.017	9.08	41.4	103	0.080	7.2	14.8
Polyester #1	0.013	6.03	43.0	86	1.42	95	250.5
Polyester #2	0.014	4.11	27.8	55	1.08	69	170
Polyester #3	0.013	6.35	19.6	39	0.480	17	87
Polyamide	0.025	5.91	8.54	67	0.152	6.2	28.5
Glass Fibre	0.020	5.77	11.24	63	0.283	13	42

The percent theoretical yield of polypyrrole was calculated based on the mass increase of the fabric and does not account for the polymer that was deposited on the sides of the reaction flask or poorly adhering and so lost during washing. An assumption is made that there is one anthraquinone-2 sulfonate group for every 3 pyrrole groups making up the conducting polymer. Very high yields are observed for the natural fibres (~100%) indicating high absorption of reactants from solution. This is attributed partly to the high surface area of these spun fibres and potentially to larger chemical or physical adsorption energies. Polyester #3 is also woven from spun fibres though the percent theoretical yield of polypyrrole is the lowest of all the textiles.

Figure 4.27 shows the conductivity of the PPy-coated fabrics as a function of the polypyrrole density. The density of the polypyrrole is calculated by dividing the mass of polypyrrole on the fabric by the volume of the textile. There is a linear relationship between the conductivity and polypyrrole density for the synthetic fibres. The cotton fibres do not fall onto this line. This may be due to the large surface area of these materials, giving a large number of nucleation sites for polymer growth, however, due to the large surface area, the growing polypyrrole islands are not connecting to give the continuous films that yield high conductivity. This is in agreement with literature observations for spun filaments compared to continuous filament yarns.^[67] Another explanation for the inconsistency in the trend is that the natural fibres absorb other species from solution, thus yielding a higher apparent mass.

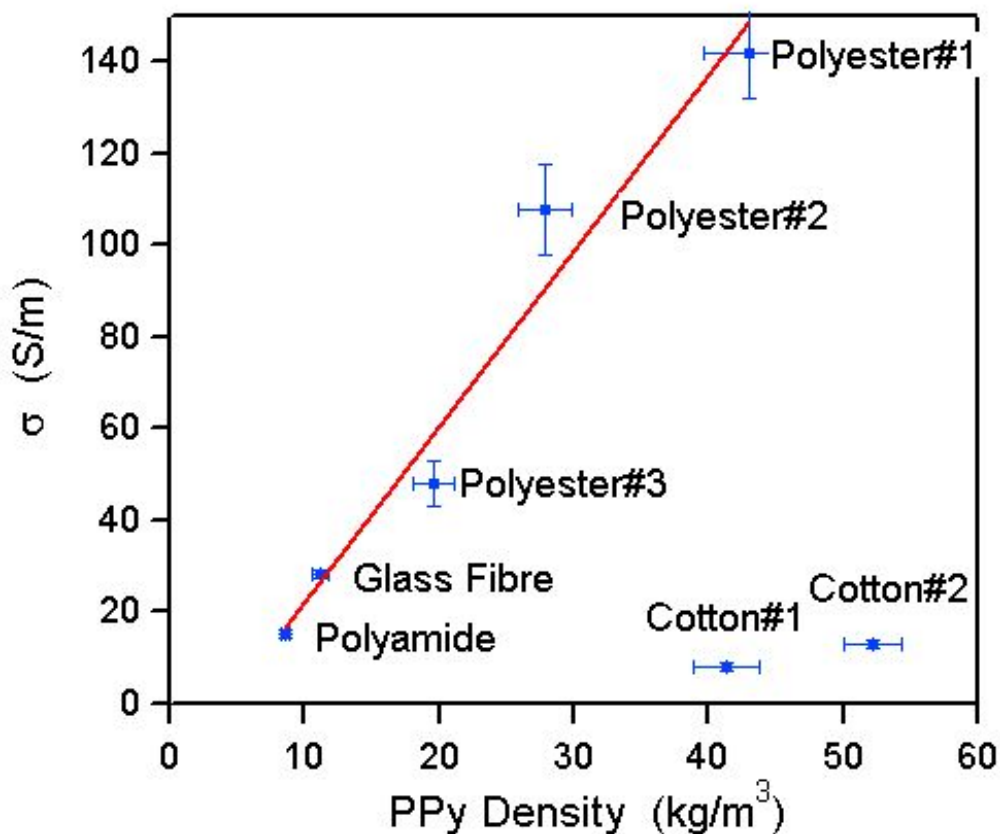


Figure 4.27. For synthetic fibres the conductivity is proportional to the density of polypyrrole in the composite fabric (ie mass of polypyrrole per unit volume of fabric). Data from Table 4.5. Natural cotton fibres present a higher surface area and absorb more reactants from solution.

In preparation for waveguide measurement, the fabric samples were laminated to acrylic blocks by using either tape or glue, Table 4.6. The weight percent polypyrrole is recorded as the same for the tape and glue entries as they were both cut from the same fabric that was used to derive the weight percent. The conductivity from the same sample varies due to the inhomogeneous coating of the fabric by the polypyrrole. This inhomogeneity arises from the limited size of the reaction flask and volumes of reactants used.

The imaginary component of the permittivity, ϵ''_r , determined from the waveguide measurements, is plotted against the theoretical value of the imaginary permittivity calculated from the static conductivity (Equation 4.9), Figure 4.28. Most points fall on the theoretical line indicating that at 10 GHz the loss component is due to the static conductivity.

One set of points, those for Polyester #2, do not fall on the theoretical line, and it is noted that the wt% of PPy on this fabric is lower than found for the other fabrics. These results point to two possible processes: first, the surface chemistry of the corona treated fabric is such that the growth and adhesion of polypyrrole on the fabric

is slower leading to a lower coverage for the given polymerization time. Slower growth rates tend to produce higher conductivities due to fewer side reactions degrading conductivity.^[150] Second, the resultant polypyrrole film coating the PET fibres will be thin and therefore more susceptible to oxidative degradation. As well, the surface chemistry of corona treated polyester is likely to contain reactive groups that can attack the polypyrrole. It has been noted that the conductivity of polypyrrole degrades with time due to oxidation.^[92,93] Since permittivity measurements were made about 10 days after the samples were prepared, it is possible that the conductivity had decreased and so the points no longer fall on the theoretical line in Figure 4.28.

Table 4.6. Measured parameters for various fabrics as a function of whether they were glued or taped to the acrylic block for microwave measurements.

Sample	Adhesive	wt% PPy	σ (S/cm)	ϵ'_r	ϵ''_r
Cotton #1	Glue	9.50	0.09 ± 0.03	11	27
Cotton #1	Glue	9.50	0.136 ± 0.004	7.8	17.7
Cotton #2	Glue	9.99	0.031 ± 0.001	6.5	11.5
Polyester #1	Glue	6.42	1.28 ± 0.09	105	251
Polyester #2	Glue	4.29	1.24 ± 0.08	58	170
Polyester #3	Glue	6.79	0.44 ± 0.03	10	75
Polyamide	Glue	6.28	0.124 ± 0.004	6	33
Glass Fiber	Glue	6.12	0.231 ± 0.006	10	36
Cotton #1	Tape	9.50	0.159 ± 0.005	12	34.5
Cotton #2	Tape	9.99	0.13 ± 0.02	8	18
Polyester #1	Tape	6.42	1.5 ± 0.1	85	250
Polyester #2	Tape	4.29	1.28 ± 0.08	80	170
Polyester #3	Tape	6.79	0.52 ± 0.04	24	99
Polyamide	Tape	6.28	0.181 ± 0.009	6.5	24
Glass Fiber	Tape	6.12	0.34 ± 0.01	16	48

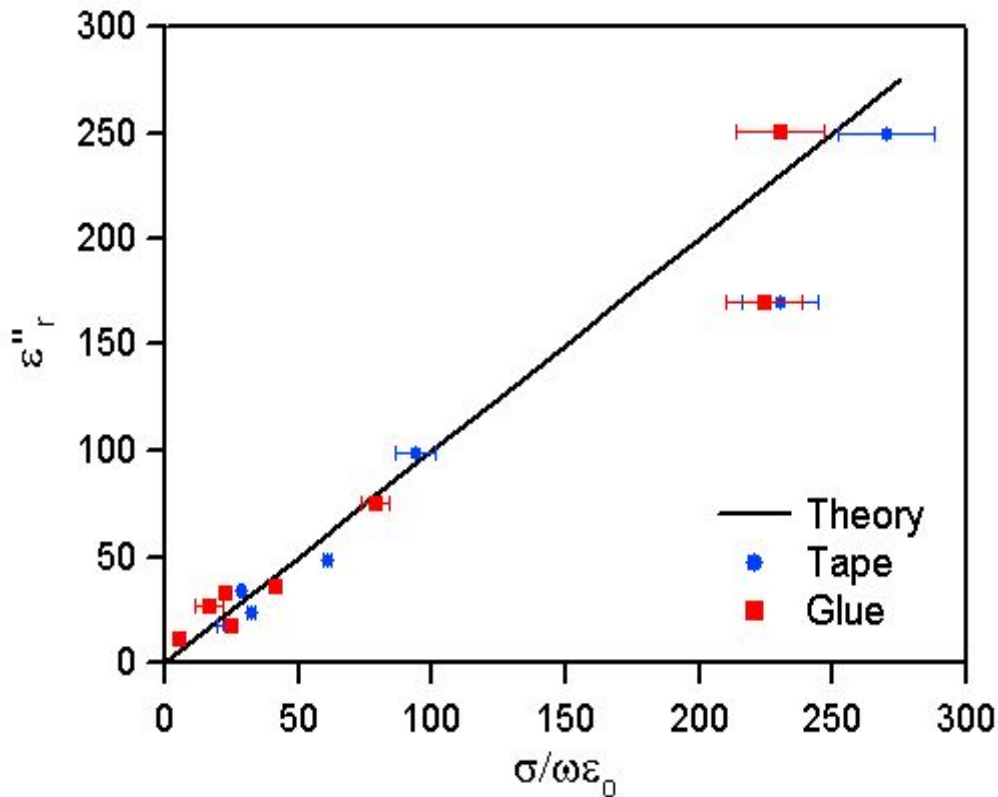
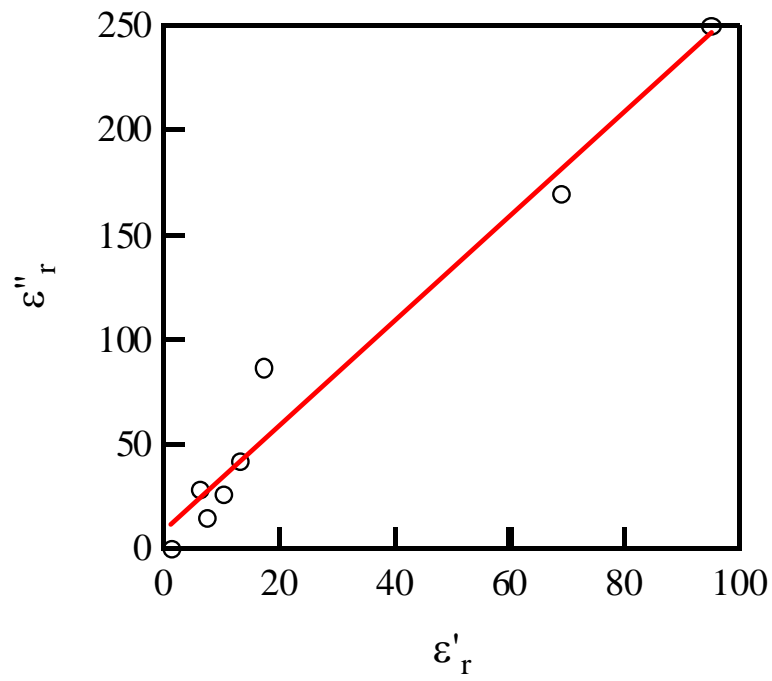
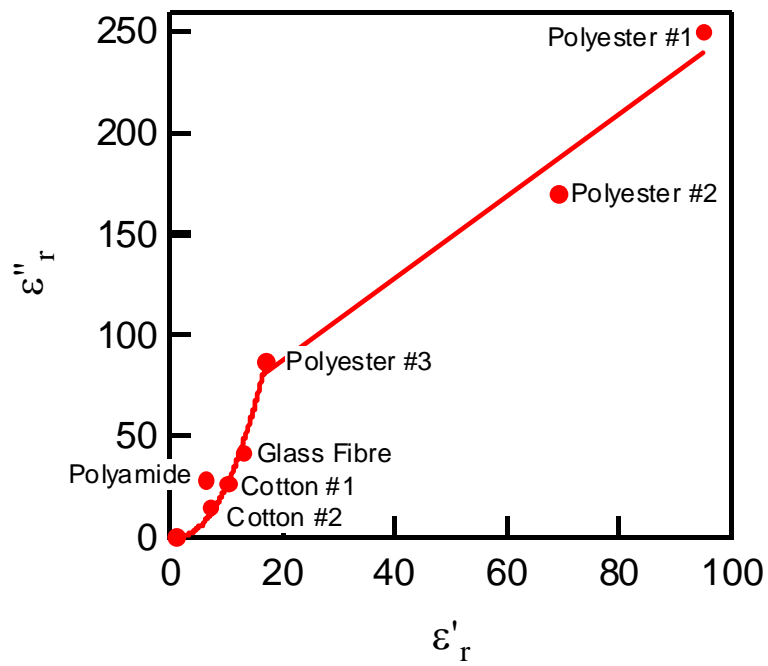


Figure 4.28. Comparison of the measured imaginary component of the permittivity, ϵ''_r , to theoretical value calculated from the static conductivity. Within the uncertainty most points fall on the theoretical line. Uncertainties in the imaginary component are on the order of 5-10%.

The literature shows a nonlinear plot of conductivity vs ϵ'_r , at 35 GHz and for a conductivity range of 0 to 0.5 S/cm^[73] for one type of polypyrrole-polyester textile embedded in resin. The same report shows a linear response in conductivity for PPy-glass fibre, while for both the plot of ϵ''_r vs ϵ'_r are straight lines, even though ϵ''_r was calculated from the conductivity. For the textiles studied here, the imaginary component of the permittivity is essentially equal to the theoretical value calculated from the static conductivity, and as such the two plots follow the same trend. Figure 4.29 plots the imaginary component of the permittivity as a function of the real component. The slope ($\tan \delta$) of a linear fit to the data, Figure 29a, has a value of about 2.5. Figure 29b, shows the same data as 29a, however, displayed with two different regions. The linear section has a slope of 2.0 which is comparable to values found for PPy on PET (2.2) and S-glass fibre (1.7).^[73] At this point it is merely conjecture that there is anything significant in Figure 29b and more work needs to be done on this.



a



b

Figure 4.29. Plot of ϵ'' vs ϵ' for the average values from the glued and taped samples at 10 GHz. Figure 4.31a shows a linear fit to the data with slope, $\tan \delta$, of 2.5. Figure 4.31b shows the data fitted to a nonlinear section at lower values of ϵ'' and a linear section for the higher values.

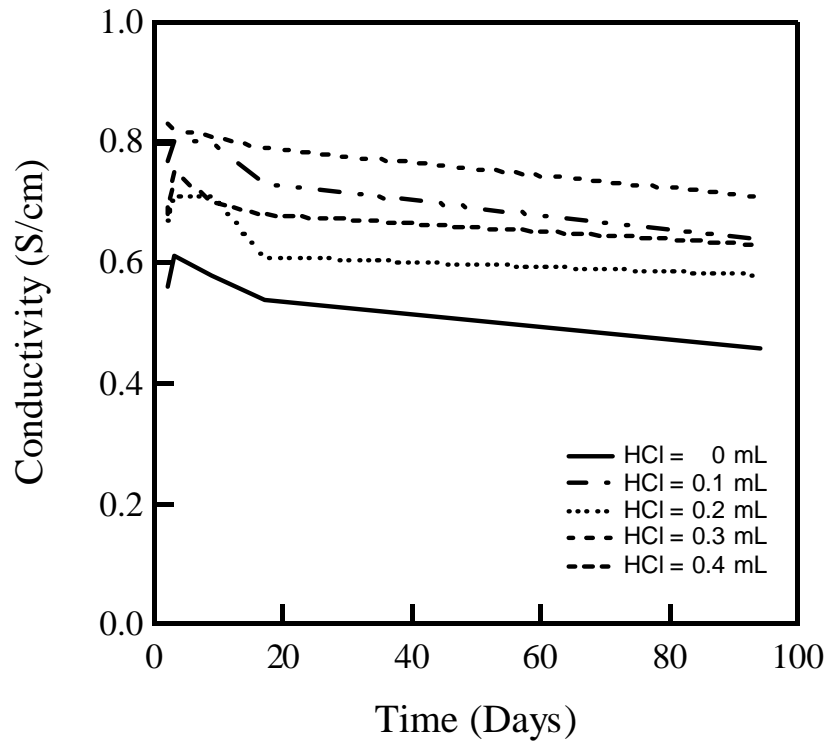
4.3.7.12 The Effect of Aging and Acid on Polypyrrole Coated Fabric

Polypyrrole can be coated onto fabrics by immersing a fabric in a solution containing the reactants for polymerisation of polypyrrole. A uniform coating of polypyrrole is deposited on the fabric with the polymer forming a shell around the individual fibres of the material. The conductivity of the material can be varied over a wide range by controlling deposition time, reagent concentrations, temperature and dopant ions. Here, the amount of HCl included in the synthesis was varied to determine if there was a correlation between the conductivity stability over time and the amount of acid added. Experimental conditions were set with acid volumes varying from 0 to 0.04 mL. All other experimental conditions were kept constant. The experiment is summarized in Table 4.7.

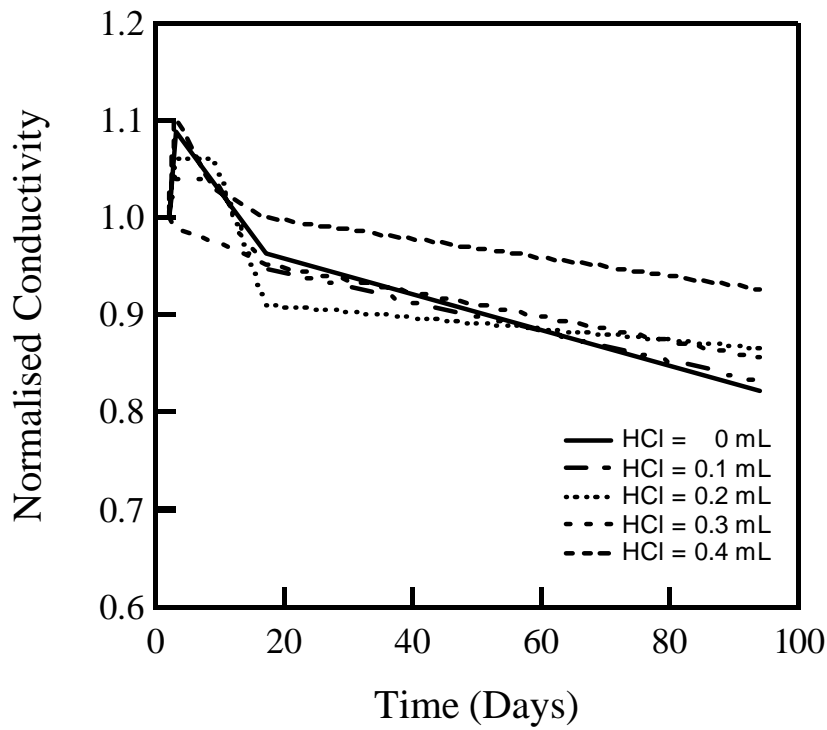
The samples were aged at room temperature in an open atmosphere and the conductivity measured throughout a 2.5 week period. In the plot of normalized conductivity vs. time (Figure 4.30b), each sample showed an initial increase in conductivity over the first 24 hours. After this period the conductivity decreased at a constant rate until the end of the experiment. By the 20th day the conductivities had decreased at least to their initial values for each sample. Over the next 75 day period the loss of conductivity tapered off. The rates of decay are similar for all samples with a value of approximately $-0.005 \text{ Scm}^{-1}/\text{day}$ for the first 20 days and $-0.001 \text{ Scm}^{-1}/\text{day}$ for the last 75 days. From the limited experimental results the most stable material appears to have been made with the 0.02 mL of added acid. Further experimentation needs to be carried out to confirm this observation and to determine if there are any correlations to be drawn.

Table 4.7. Summary of Fabric Aging

AMT. OF ACID ADDED (mL)	INITIAL CONDUCTIVITY (S/cm)	RATE OF CHANGE IN CONDUCTIVITY AFTER INITIAL INCREASE ($\text{Scm}^{-1}/\text{DAY}$)
0	0.566 ± 0.008	-0.0011
0.01	0.775 ± 0.005	-0.0011
0.02	0.678 ± 0.005	-0.0003
0.03	0.837 ± 0.006	-0.0010
0.04	0.68 ± 0.02	-0.0006



a



b

Figure 4.30. Conductivity (a) and normalised conductivity ($\sigma/\sigma_{\text{initial}}$) (b) as a function of aging time.

4.3.7.13 Effect of Aging and Temperature on Pellet Conductivity

Four groups of three ppy pellets were prepared with each group having a different dopant. Dopants used were NDSA, NSA, AQDSA and PTSA. Each of the three pellets from the groups were aged in different temperature environments. These environments were in an oven set to 85 °C, a freezer set to -18 °C and at room temperature. Conductivity measurements were then made on the pellets over the course of a 2.5 week period, Figures 4.31-4.33. Both the low and room temperature pellets showed linear character in the conductivity vs. time plot with the room temperature pellets degrading slightly and the low temperature pellets being essentially stable throughout the test period. The NSA pellets did not follow this linear pattern. These pellets gave an erratic progression, which very roughly followed the same trends as the other PPy/dopant pellets. After the initial 20 day period, the rate of conductivity loss decreased. After the 20 day period the conductivity for PPy/PTSA appears to have increased.

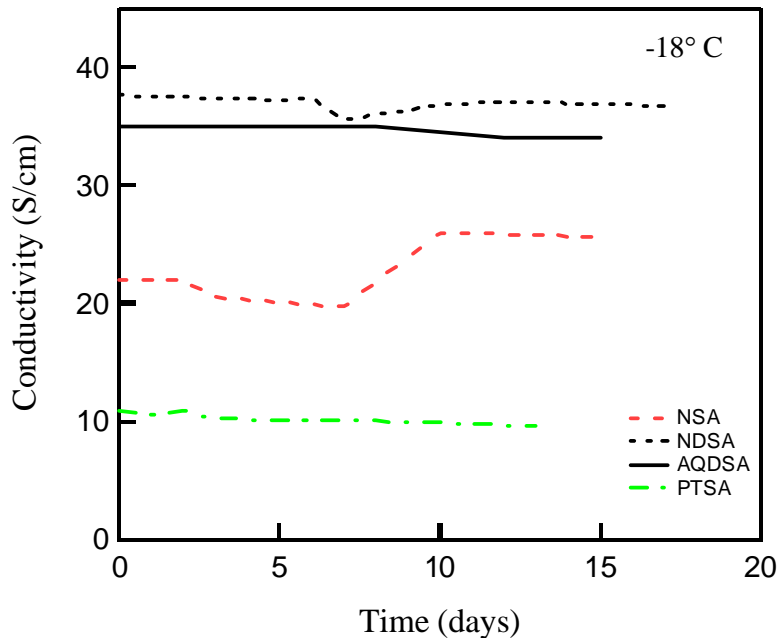


Figure 4.31. Decrease in conductivity for polypyrrole doped with different ions at -18°C.

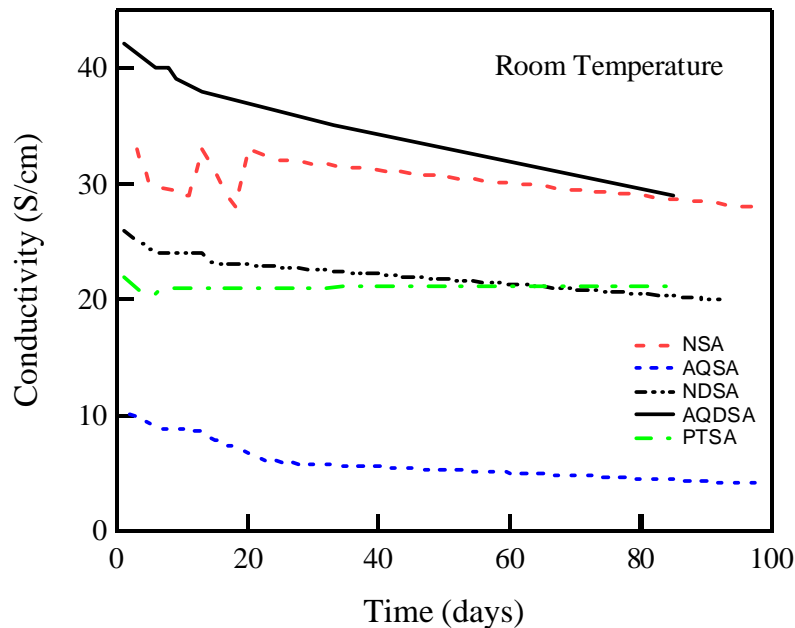


Figure 4.32. Room temperature decrease in conductivity as a function of time for polypyrrole doped with different ions.

The pellets exposed to the higher temperature did not follow a linear relationship with time, Figure 4.33. The normalized conductance vs. time plot showed a rapid decrease in conductivity over the initial six day period and from that point decreased less rapidly. Following the work of Truong^[93], a plot of $\Delta\sigma/\sigma_0$ vs. $t^{1/2}$ (with $\Delta\sigma = \sigma_0 - \sigma_t$) was found to be linear up to $\Delta\sigma/\sigma_0 = 0.5$. Truong compares this plot to the Fickian sorption plot of M_t/M_∞ vs. $t^{1/2}$ where M_t is the absorbed mass at time t and M_∞ is the equilibrium absorbed mass. Assuming that the decrease in conductance is proportional to the amount of absorbed oxygen and that the initial conductance is much greater than the conductance at time t , Truong states that $\Delta\sigma/\sigma_0$ is proportional to M_t/M_∞ meaning that, at least up to $\Delta\sigma/\sigma_0 = 0.5$, the degradation follows Fickian sorption kinetics. Diffusion coefficients were calculated using the following equation: $D=0.04939l^2/t_{0.5}$ with l = thickness of the film and $t_{0.5}$ = time at which $\Delta\sigma/\sigma_0 = 0.5$. Calculated diffusion coefficients are seen in table 2.

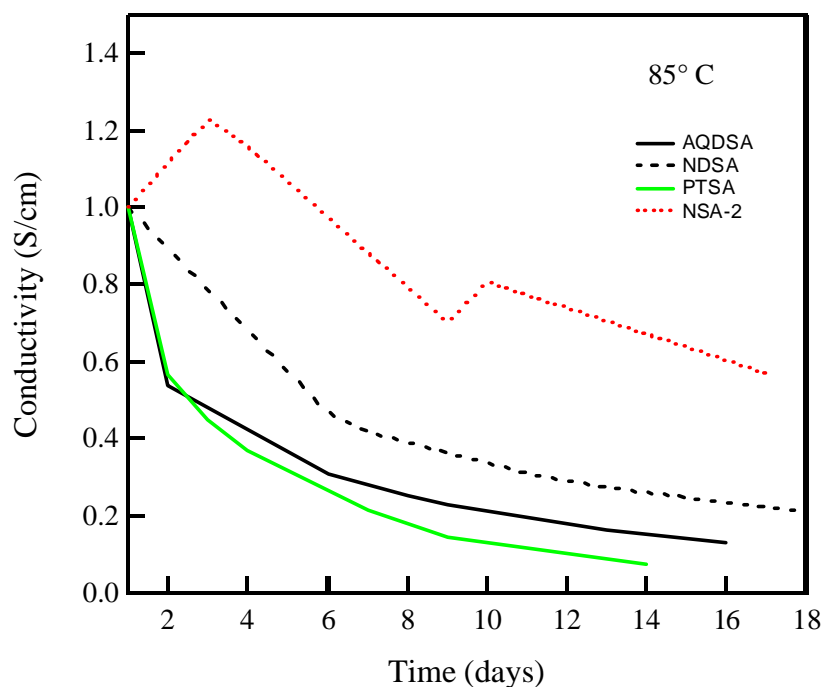


Figure 4.33. Decrease in normalised conductivity as a function of time for polypyrrole doped with different ions at 85° C.

As was the case at low and room temperature, NSA-2 gave erratic conductivity measurements and therefore a diffusion coefficient was not calculated. From the plot of normalized conductance vs. time and the calculated diffusion coefficients the order of increasing rate of loss of conductance at 85° C is: NSA-2 < NDSA < AQDSA < PTSA.

Table 4.8. Diffusion coefficients calculated from loss of conductivity of polypyrrole pellets doped with different ions.

DOPANT	CONDUCTIVITY (S/cm)	DIFFUSION COEFFICIENT (CM ² /s)
AQSA	9.7 ± 0.2	-
NDSA	23 ± 4	5.73 x 10 ⁻¹⁰
NSA-2	33 ± 5	-
PTSA	21 ± 1	1.68 x 10 ⁻⁰⁹
AQDSA	41 ± 6	7.13 x 10 ⁻¹⁰

4.3.7.14 IR Study of Polypyrrole Pellets

Three pellets were made from a single batch of PPy/AQDSA powder and aged at -18°C , room temperature and 85°C for a period of two weeks. After the two week period the IR reflectance spectra for each was collected. From these spectra, the intensity of the peaks at 1500 cm^{-1} were compared to determine if there was correlation between peak intensity at 1500 cm^{-1} and rate of conductance degradation. This experiment follows the work of Kaynak *et al.*^[151] who monitored the peak intensity for samples aged at room temperature. Kaynak observed a slight increase in the intensity of the peak at 1690 cm^{-1} which was attributed to oxidation at the β' position on the pyrrole ring. The spectra collected (Figure 4.34) for this study, however, did not show such a relationship. The expected progression was an increase in absorption from low to high temperature. The peaks at 1590 cm^{-1} increased in absorption in the following order: room temp. $< -18^{\circ}\text{C} < 85^{\circ}\text{C}$, which does not reflect prior findings. This may be due to pellet density which was not accounted for.

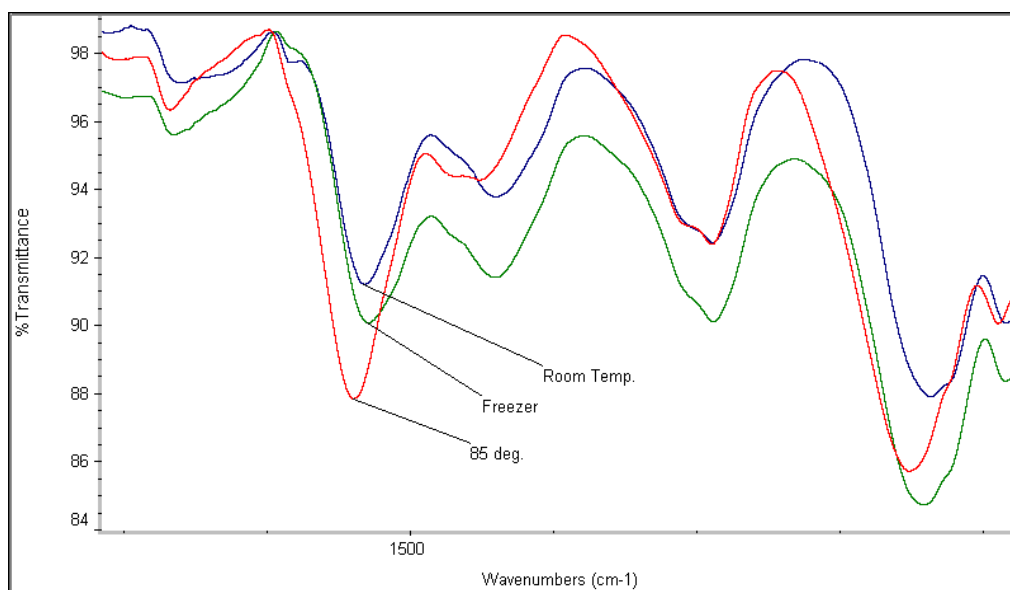


Figure 4.34. Spectra for Three Temperatures

Infrared pyrolysis spectra were collected from a sample of PPy/AQDSA. Six spectra were collected from the same sample in an increasing temperature range of $200, 300, 400, 500, 600$ and 700°C . There were no emissions of note from 200 to 500°C . At 600°C there were peaks characteristic of SO_2 at 1100 cm^{-1} and therefore the breakdown of the dopant. At 700°C there were three groups of peaks: $3200, 2100$ and 1100 cm^{-1} , which are typical of HCN, carbonyl sulphide and SO_2 respectively; breakdown products of the polypyrrole and dopant.

4.3.7.15 Thermal Analysis of Polypyrrole Powders

Thermogravimetric analysis, TGA, and Differential scanning calorimetry, DSC, information was obtained on PPy/AQDSA in epoxy paint at 3 and 5 weight percentage as well as on pure PPy powders with various dopants. These dopants were NSA-2, NDSA, PTSA and AQDSA. The TGA obtained from PPy/AQDSA powder showed three weight losses before 230° C. These weight losses occurred at 127, 160 and 215° C. Pyrolysis spectra were gathered at these temperatures and the 127 °C and 215° C weight losses were attributed to water and NO₂ respectively. TGA data of 3 and 5 weight percent PPy/AQDSA in epoxy showed a mass loss at 400° C. This mass loss at 400° C was also observed for pure epoxy. DSC data of PPy powder with various dopants was obtained. The powder was initially heated at a rate of 20 °C/min. to 110° C to eliminate water. The sample was then cooled to room temperature and then heated at 10° C/min. to 250° C. Each sample showed a dehydration endotherm on the initial run. This endotherm was not observed after cooling and reheating. After the initial run, all dopants showed a single endotherm in the heating range. PPy/NDSA, PPy/PTSA and PPy/AQDSA showed a broad endotherm centered around 130, 130 and 122° C respectively. PPy/NSA-2, however, displayed a narrow endotherm at 105° C.

4.3.7.16 Polypyrrole Coatings

Methods were developed to incorporate PPy powder as a dispersion into paint systems. Variables investigated were: Milling technique and time, painting technique and effects of weathering. The criteria used to judge the suitability of the paints after the addition of PPy were: quality of dispersion /coating and conductance.

4.3.7.17 Polypyrrole Powder Milling and Particle Dispersion

Powders from two different milling techniques (mortar and pestle and ball-milling) were compared to coatings made from un-milled powder (remember Figure 4.23). When these powders were mixed into the latex paint system the milled powders produced superior dispersions compared to the non-milled powder, with no visible discrete PPy particles. No significant differences were observed between the mortar and pestle and ball-mill powder dispersions in terms of coating appearance.

Several methods have been evaluated for dispersing the polypyrrole powder in the coating. These included hand mixing the powder with a stirring rod, a rotating platform, a ball-mill and a speed mixer from Flactec.

Powders ground in a mortar were added to the latex paint. Un-milled powder was used as a control. A suitable dispersion was produced with the ball-mill in approximately 30 seconds, compared to several hours for the rotary platform. The un-milled powder failed to form a suitable suspension by either method, illustrating the need for powder milling.

Addition of 10% (w/w) PPy powder to alkyd#2 produced a spongy material upon mixing. At this loading the critical pigment volume concentration was probably

exceeded. Adding up to 2 % varsol by volume increased the ability of the paint to incorporate the powder. When more than 2% thinner was added the coating was very “watery” and formed beads when applied to a surface surface. Thinner was also needed for the latex mixtures where water was used as the thinner. Thinning was unnecessary for the epoxy, Alkyd#1 and Polyurethane systems.

4.3.7.18 DC Conductivity of Polypyrrole Coatings

The conductivities of coatings, formulated with different weight percentage polypyrrole powder, are shown in Figure 4.35. The powder used for a series of coatings came from the same synthetic batch and were mixed into the alkyd#1 base with a stirring rod. At high loadings all of the formulations have approximately the same conductivity. The series of coatings represented by the black line come from a batch of polypyrrole powder where a pressed pellet of the powder had a conductivity of 31 S/cm. This series required loadings of nearly 20 wt% polypyrrole before high conductivities were obtained. The transition point between low and high conductivities is often referred to as the percolation threshold. The percolation threshold for fine spherical particles has been theoretically calculated to be about 19 %, and the powder used for this series had been sieved through a finer screen than the other series. The other three series represented by the blue, green and red lines in Figure 1 show much the same behaviour, however, the percolation threshold is achieved with loadings of about 8-10 wt%.

The series in Figure 4.35, indicate that particle size and shape are major factors affecting the coating conductivity. Other factors affecting the coating conductivity arise from the degree of mixing. Hand mixing with a stirring rod will produce conductivities that vary from coating to coating.

The latex and other alkyd systems produced similar results. These result are in agreement with Costa *et al.*^[152] who found a percolation threshold of 12% for a PPy/polystyrene composite. No conductivity could be measured from composites made with the epoxy coating.

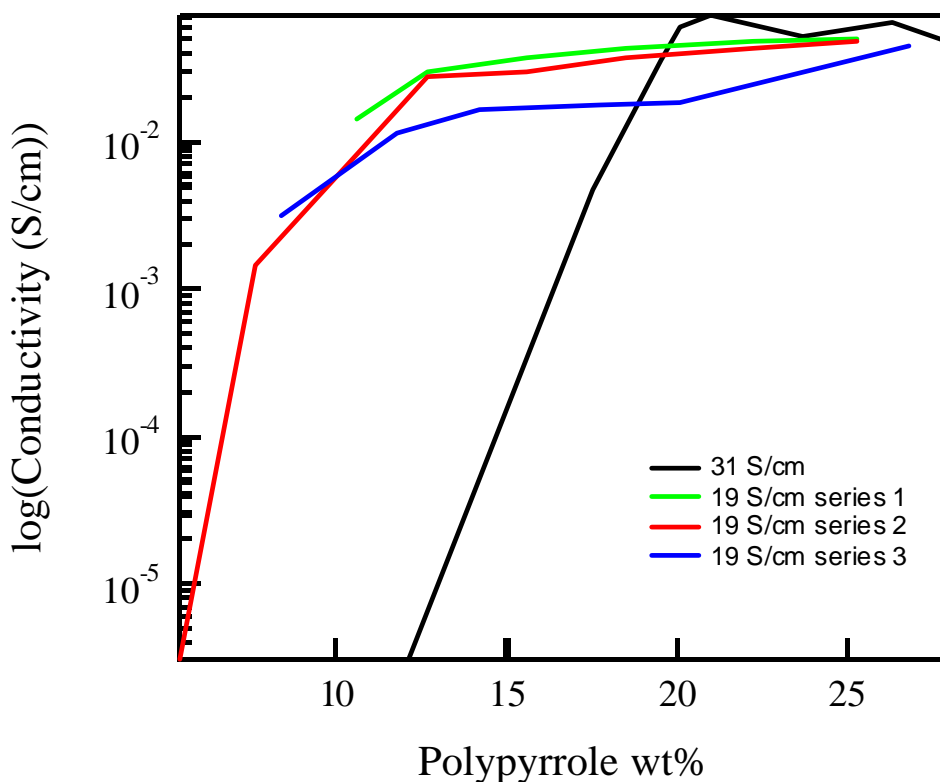


Figure 4.35. Conductivity of some alkyd#1-polypyrrole coatings with the same formulation. Conductivity of pressed pellets of polypyrrole powder was 31 S/cm for black line and 19 S/cm for the other series.

4.3.7.19 Permittivity of Polypyrrole Coatings

The real and imaginary components of the permittivity as a function of the weight percent polypyrrole for a series of polypyrrole coatings are shown in Figure 4.36. The logarithm of the permittivity has been plotted since there is a direct relationship between the imaginary permittivity and dc conductivity (Equation 4.9).

The percolation threshold is apparent in these parameters as well, occurring at about 8 wt% polypyrrole. After the percolation threshold the real and imaginary permittivity continue to slowly increase with higher PPy loadings.

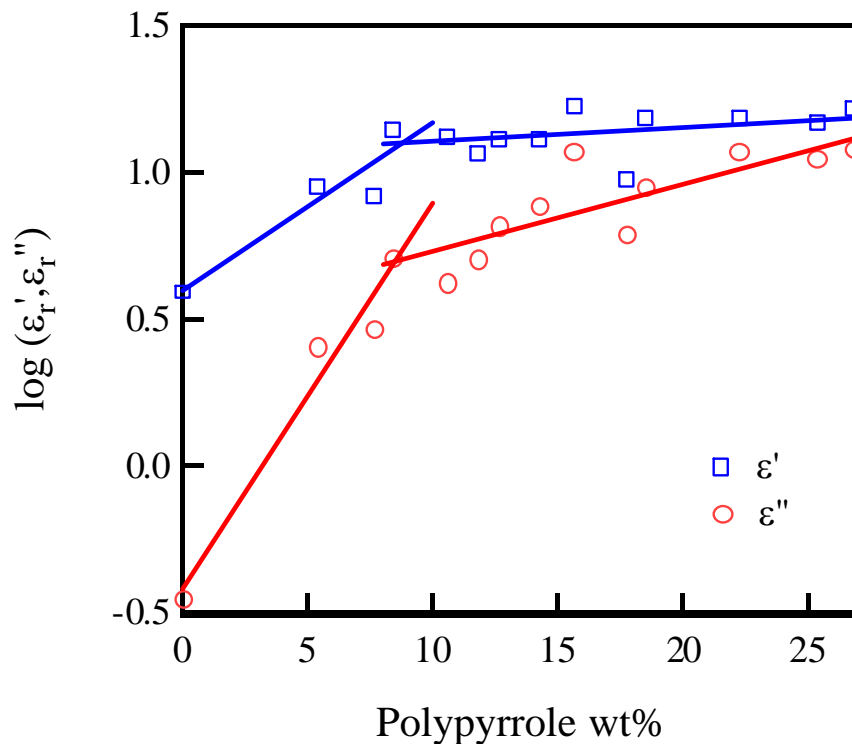


Figure 4.36. Real and Imaginary components of the permittivity as a function of the wt% polypyrrole in alkyd#1 coating. All formulations originate from the same batch of polypyrrole made with NSA-1. ϵ'_r , blue squares, ϵ''_r , red circles.

The polyurethane coating was very thick even before incorporation of polypyrrole. The talc filler for this polyurethane coating was mixed in with the speed mixer and then the polypyrrole was blended in by hand or with the speed mixer. The permittivities of the resultant coatings are shown in Figure 4.37. Hand mixing produced a series of coatings with slightly higher real and imaginary permittivity. This is likely due to the speed mixer producing a more uniform distribution of the conducting particles in the matrix, which are then electrically isolated. The percolation threshold for this coating is low, at about 2.5 wt% PPy. This is likely due to the high viscosity of the coating and/or the talc surface facilitating the formation of conductive paths through the material.

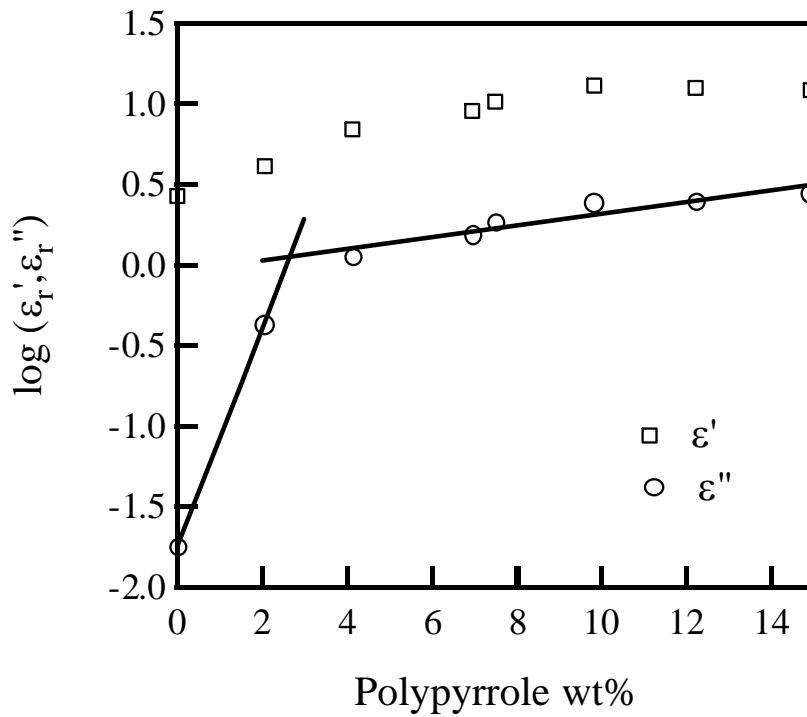
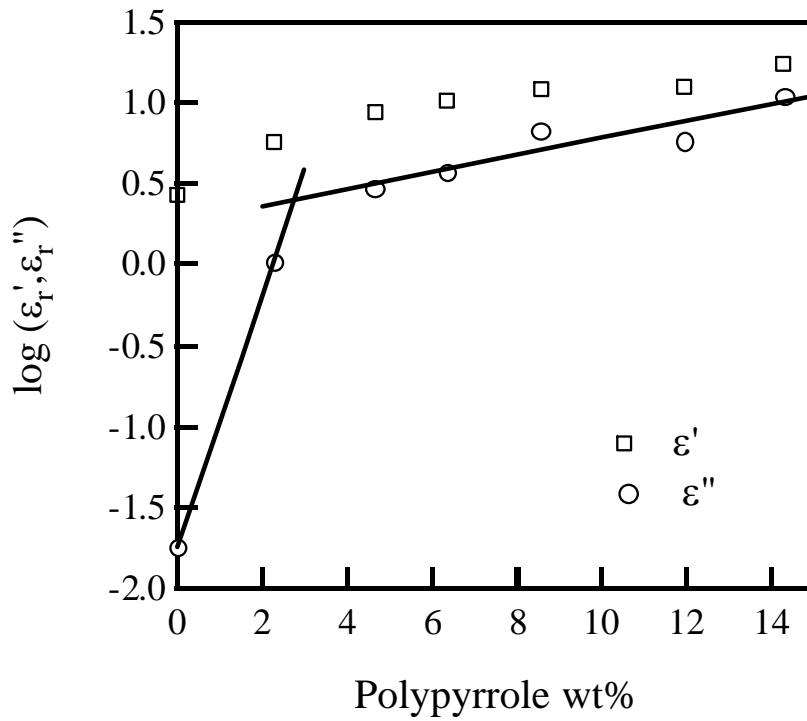


Figure 4.37. Real and Imaginary components of the permittivity as a function of the wt% polypyrrole in the polyurethane non-skid coating. Top graph, hand mixed, bottom graph speed mixed. Dopant NSA-1.

4.3.7.20 Weathering of Polypyrrole Coatings

Limited work has been done on weathering the coating materials. Paint samples were prepared and applied to rectangular polystyrene plaques. The samples consisted of alkyd#2 and epoxy mixtures. The powder used for each sample was PPy/AQDSA. The alkyd coatings were made up with three and five weight percent PPy. The epoxy samples contained one, three and five weight percent. The plaques were placed in the weathering cabinets for the 2 week cycle. Samples were collected from the plaques daily. After the 6th day the epoxies had become too brittle and sampling from these plaques was discontinued. Throughout the entire 2 week cycle the alkyd samples remained unaffected. Permittivity measurements were made on samples collected from the plaques prior to and during the weathering. These showed a relatively stable permittivity, Figure 4.38.

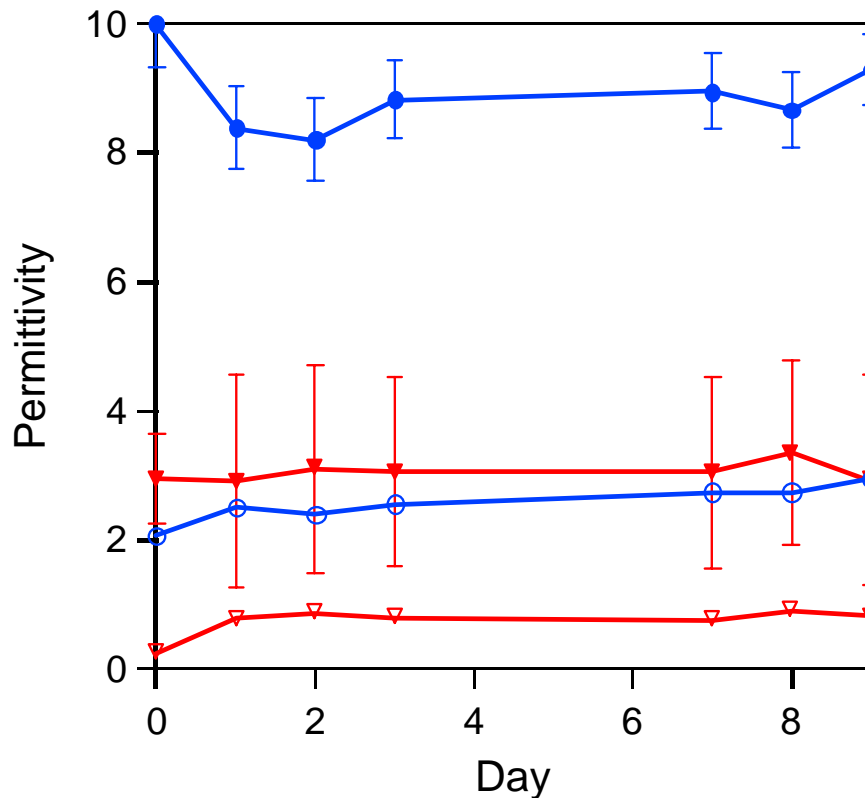


Figure 4.38. Permittivity of PPy/AQDSA-Alkyd#2 coatings as a function of weathering time. Blue markers – 5 wt% red markers 3 wt% polypyrrole. Solid markers the real component of the permittivity and open markers the imaginary component.

4.3.8 Conclusions

Galvanostatically grown polypyrrole films are very conductive and the film thickness is readily controlled by deposition time. The optical properties of these materials could not be accurately determined due to their lack of transmission. Galvanostatic polymerisation has the potential to over oxidise the polymer.

The conductivity of chemically prepared polypyrrole is dependent on the dopant ion, oxidant to monomer ratio, temperature and for pressed pellets of polypyrrole powder the conductivity also depends on the pellet density. Dopant ions based on aryl sulfonates yield powders having large conductivities. Disulfonate species yield higher conductivities than do monosulfonates. Ball milling of polypyrrole powder reduces the conductivity.

Coating fabrics with polypyrrole is a viable method to produce a thin carrier medium suitable for producing microwave absorbing materials. Synthetic non-porous materials appear to be more suitable for the formation of carrier media as the porous natural fibres appear to absorb excess reagents from solution and do not yield high conductivities. The conductivity of PPy-fabric composites is proportional to the density of the polypyrrole on the fabric sample. The conductivity can thus be tuned by using fabrics with different densities and knowledge of fabric density allows the conductivity of different fabrics to be compared.

Polypyrrole is inherently unstable to air oxidation. This was observed through the decrease in conductivity of the coated fabrics and pressed pellets. The oxidation rate is accelerated with increased temperature and decreased by limiting oxygen diffusion through encapsulation in a coating. Dopant ions affect the oxidation rate, possibly by forming different density polypyrrole/dopant particles. The higher density particles may exclude oxygen more effectively.

The amount of HCl present in the reaction does not appear to have a great influence on the oxidation rate of polypyrrole coated fabrics. Other work has shown that the dopant ion does have an effect on the oxidation rate of these materials, probably through the formation of dense polypyrrole layers.

For pellets pressed from polypyrrole powders, the dopant affects the conductivity. The disulfonates have a higher conductivity than do the monosulfonates, with AQSA having the lowest conductivity. This is in contrast to the results for polypyrrole coated fabrics where AQSA was found to form the highest conductivity and most stable material. Temperature experiments with PPy/dopant pellets showed that the electrical stability was inversely proportional to temperature. The data from the high temperature runs show similarities to the Fickian sorption plot up until $\Delta\sigma/\sigma = 0.5$. This suggests that the conductivity loss is due to absorption of oxygen into the polymer. Calculated diffusion coefficients showed that at 85° C electrical stability follows the following order: NSA-2 > NDSA > AQDSA > PTSA. IR spectra of aged PPy pellets were not conclusive possibly due to density effects. TGA data showed that PPy/AQDSA powder was not stable over 160° C. This should be taken into account when considering PPy for elevated temperature use. Further DSC experiments should

be done to determine the nature of the endothermic peak present in each run of PPy/dopant powder.

The conductivity and permittivity of polypyrrole powders dispersed in coating materials depends on the degree of mixing, and the starting material. Percolation thresholds were observed to range from about 2 to 20 wt% polypyrrole in the matrix. This range will severely affect material properties and needs to be more highly controlled. Preliminary weathering tests indicate the stability of the alkyd system.

The utility of polypyrrole (or other conducting particles) coatings as radar absorbing materials requires high stability and reproducible formulation of the material properties. The results here indicate that the stability issue will be satisfied when the polypyrrole is encapsulated in a coating. Reproducible formulation will require tight control of synthetic conditions, milling (particle characteristics), and most importantly powder dispersion in the coating. High viscosity coatings and inclusions that affect the distribution of conducting particles may give better control over the coating properties.

4.3.9 Future Work: Polypyrrole

As was noted with polyaniline reproducible production of conductive polymer and dispersion of the polymer in a matrix will be required in order to produce quality absorbers. Potential improvements may arise by incorporating pre-coated filler materials. To this end polypyrrole coated latex and polypyrrole-coated fibres (fillers) will be dispersed in coating material.

Polypyrrole stability is also an important issue that needs to be addressed. The studies in this report indicate that polypyrrole will not be a suitable material unless it is protected from an oxygen environment. Encapsulating the conductor in an insulating/isolating matrix can be satisfied at the same time as coating formulation and fabrication of composite (eg fibre glass) materials.

Large area materials need to be fabricated in order to measure the through space reflectivity, and in order to start to design actual absorbers.

4.3.10 References

- (1) Olmedo, L., Hourquebie, P., Buvat, P. *Antec* **1997**, 952, 1320.
- (2) Walker, J. A.; Warren, L. F.; Witucki, E. F. *J. Polym. Sci.: Part A: Polym. Chem.* **1988**, 26, 1285
- (3) Martina, S.; Enklemann, V.; Schluter, A.-D.; Wegner, G.; Zotti, G.; Zerbi, G. *Synthetic Metals* **1993**, 55-57, 1096.
- (4) Miles, M. J.; Smith, W. T.; Shapiro, J. S. *Polymer* **2000**, 41, 3349.
- (5) Suarez, M. F.; Compton, R. G. *Journal of Electroanalytical Chemistry* **1999**, 462, 211.

- (6) Li, Y.; Qian, R. *Synth. Met.* **1989**, *28*, C127
- (7) Kim, B. C.; Spinks, G. M.; Too, C. O.; Wallace, G. G.; Bae, Y. H.; Ogata, N. *Reactive & Functional Polymers* **2000**, *44*, 245
- (8) van den Schoor, R. C. G. M.; van de Leur, R. H. M.; de Wit, J. H. W. *Synthetic Metals* **1999**, *102*, 1404.
- (9) Audebert, P.; Bidan, G. *Synthetic Metals* **1986**, *14*, 71.
- (10) Machida, S.; Miyata, S.; Techagumpuch, A. *Synthetic Metals* **1989**, *31*, 311.
- (11) Whang, Y. E.; Han, J. H.; Nalwa, H. S.; Watanabe, T.; Miyata, S. *Synthetic Metals* **1991**, *41-43*, 3043.
- (12) Druy, M. A. *Synth. Met.* **1986**, *15*, 243
- (13) Stejskal, J.; Omastova, M.; Fedorova, S.; Prokes, J.; Trchova, M. *Polymer* **2003**, *44*, 1353.
- (14) Qi, Z.; Pickup, P. G. *Chem. Mater.* **1997**, *9*, 2934
- (15) Mithra, L. M. M.; Cao, Y.; Cho, S.; Sutar, D.; Lee, K.; Menon, R.; Subramanyam, S. V. *Synthetic Metals* **2001**, *119*, 437.
- (16) Lei, J.; Cai, Z.; Martin, C. R. *Synthetic Metals* **1992**, *46*, 53.
- (17) Zotti, G.; Zecchin, S.; Schiavon, G.; Groenendaal, L. B. *Chem. Mater.* **2000**, *12*, 2996
- (18) Gassner, F.; Graf, S.; Merz, A. *Synth. Met.* **1997**, *87*, 75
- (19) Zong, K.; Reynolds, J. R. *J. Org. Chem.* **2001**, *66*, 6873.
- (20) Sonmez, G.; Schottland, P.; Zong, K.; Reynolds, J. R. *J. Mater. Chem.* **2001**, *11*, 289.
- (21) Forsyth, M.; Truong, V.-T.; Smith, M. E. *Synth. Met.* **1993**, *55-57*, 714.
- (22) Malinauskas, A. *Polymer* **2001**, *42*, 3957.
- (23) Kim, C. Y.; Lee, J. Y.; Kim, D. Y., Patent 5,795,953. **1998**.
- (24) Kim, I. W.; Lee, J. Y.; Lee, H. *Synthetic Metals* **1996**, *78*, 117.
- (25) Lee, G. J.; Lee, S. H. *J. Appl. Poly. Sci.* **2002**, *84*, 2583.
- (26) Oh, E. J.; Jang, K. S. *Synth. Met* **2001**, *119*, 109.
- (27) Nicolau, Y. F.; Davied, S.; Genoud, F.; Nechtschein, M.; Travers, J. P. *Synth. Met.* **1991**, *41-43*, 1491.
- (28) Jousse, F.; Olmedo, L. *Synth. Met.* **1991**, *41-43*, 385.
- (29) Chakraborty, M.; Mukherjee, D. C.; Mandal, B. M. *Synthetic Metals* **1999**, *98*, 193.
- (30) Khedkar, S. P.; Radhakrishnan, S. *Thin Solid Films* **1997**, *303*, 167.
- (31) Yin, W.; Liu, H.; Li, J.; Li, Y.; Gu, T. *J. App. Poly. Sci.* **1997**, *64*, 2293.
- (32) Zoppi, R. A.; De Paoli, M.-A. *Polymer* **1996**, *37*, 1999.
- (33) Bjorklund, R. B.; Lundstroem, I. *J. Electron. Mat.* **1984**, *13*, 211.
- (34) Kuhn, H. H. *Textile Chemist and Colorist* **1997**, *29*, 17.
- (35) Onoda, M.; Fujita, D.; Isaki, K.; Nakayama, H. *Electr Eng Jpn* **1999**, *128*, 1.
- (36) Onoda, M.; Tada, K. Proceedings of the 6th International Conference on Properties and Applications of Dielectric Materials June 21-26, 2000., **1999**, Xi'an Jiaotong University, Xi'an, China.
- (37) Zinger, B.; Kijel, D. *Synthetic Metals* **1991**, *41-43*, 1013.
- (38) De Jesus, M. C.; Weiss, R. A.; Chen, Y. *Journal of Polymer Science: Part B: Polymer Physics* **1997**, *35*, 347.
- (39) Neoh, K. G.; Teo, H. W.; Kang, E. T.; Tan, K. L. *Langmuir* **1998**, *14*, 2820.
- (40) Chen, X. B.; Issi, J.-P.; Devaux, J.; Billaud, D. *Journal of Materials Science* **1997**, *32*, 1515.
- (41) Truong, V.-T.; Codd, A. R.; Forsyth, M. *Journal of Materials Science* **1994**, *29*, 4331.
- (42) Bjorklund, R. B.; Liedberg, B. *J. Chem. Soc., Chem. Commum.* **1986**, 1293.
- (43) Stanke, D.; Hallensleben, M. L.; Toppare, L. *Synthetic Metals* **1995**, *72*, 89.

- (44) Stanke, D.; Hallensleben, M. L.; Toppare, L. *Synthetic Metals* **1995**, 72, 95.
- (45) Ng, S.-C.; Chan, H. S. O.; Xia, J.-F.; Yu, W. *J. Mater. Chem.* **1998**, 8, 2347.
- (46) Nazzal, A. I.; Street, G. B. *J. Chem. Soc., Chem. Commun.* **1985**, 375.
- (47) Li, X. G.; Huang, M. R.; Wang, L. X.; Zhu, M. F.; Menner, A.; Springer, J. *Synth. Met* **2001**, 123, 435.
- (48) Li, X. G.; Wang, L. X.; Jin, Y.; Zhu, Z. L.; Yang, Y. L. *J. Appl. Poly. Sci.* **2001**, 82, 510.
- (49) Li, X.-G.; Wang, L.-X.; Huang, M.-R.; Lu, Y.-Q.; Zhu, M.-F.; Menner, A.; Springer, J. *Polymer* **2001**, 42, 6095.
- (50) Ustamehmetoglu, B.; Kizilcan, N.; Sarac, A. S.; Akar, A. *J. Appl. Poly. Sci.* **2001**, 82, 1098.
- (51) Cirpan, A.; Alkan, S.; Toppare, L.; Cianga, I.; Yagci, Y. *Journal of Materials Science* **2002**, 37, 1767.
- (52) Truong, V.-T.; Riddell, S. Z.; Muscat, R. F. *J. Mat. Sci. Lett.* **1998**, 33, 4971.
- (53) Witucki, E. F.; Warren, J., L.F.; Newman, P. R., Patent 4,692,225. **1987**.
- (54) Li, C.; Song, Z. *Synthetic Metals* **1991**, 40, 23.
- (55) Sun, Y., Ruckenstein, E. *Synthetic Metals* **1995**, 72, 261.
- (56) Roberts, W. P., Scholz, L.A., US Patent 4,604,427. **1986**.
- (57) Lafosse, X. *Synth. Met.* **1995**, 68, 227
- (58) Wiersma, A. E.; vd Steeg, L. M. A.; Jongeling, T. J. M. *Synthetic Metals* **1995**, 71, 2269.
- (59) Armes, S. P.; Miller, J. F.; Vincent, B. *J. Colloid Interface Sci.* **1987**, 118, 410
- (60) Armes, S. P., Vincent, B. *J. Chem. Soc., Chem. Commun.* **1987**, 288
- (61) Armes, S. P., Aldissi, M. *J. Chem. Soc., Chem. Commun.* **1989**, 88
- (62) Armes, S. P., Aldissi, M. *Polymer* **1990**, 31, 569
- (63) Dufort, M.; Levassort, C.; Olmedo, L. *Synth. Met.* **1991**, 41-43, 3063.
- (64) Ando, M.; Watanabe, Y.; Iyoda, T.; Honda, K.; Shimidzu, T. *Thin Solid Films* **1989**, 179, 225.
- (65) Kuhn, H. H.; Kimbrell, W. C., US Patent 4,803,096. **1989**.
- (66) Kuhn, H. H.; Kimbrell, W. C., US Patent 4,981,718. **1991**.
- (67) Kuhn, H. H., US Patent 5,108,829. **1992**.
- (68) Kuhn, H. H.; Child, A. D.; Kimbrell, W. C. *Synth. Met.* **1995**, 2139
- (69) Gregory, R. V.; Kimbrell, W. C.; Kuhn, H. H. *Synth. Met.* **1989**, 28, C823.
- (70) Gregory, R. V.; Kimbrell, W. C.; Cuddihee, M. E., US Patent 5162135. **1992**.
- (71) Genies, E. M.; Petrescu, C.; Olmedo, L. *Synth. Met.* **1991**, 41-43, 665.
- (72) Lee, C. Y.; Lee, D. E.; Joo, J.; Kim, M. S.; Lee, J. Y.; Jeong, S. H.; Byun, S. W. *Synth. Met.* **2001**, 119, 429
- (73) Sengupta, L. C.; Spurgeon, W. A. 6th Int. SAMPE Electronics Conference, **1992**.
- (74) Kuhn, H. H.; Child, A. D. Electrically Conducting Textiles. In *Handbook of Conducting Polymers*; Skotheim, T. A., Elsenbaumer, R.L., Reynolds, J.R., Ed.; Marcel Dekker: New York, **1998**; pp 993.
- (75) Gregory, R. V. Solution Processing of Conductive Polymers: Fibres and Gels from Emeraldine Base Polyaniline. In *Handbook of Conducting Polymers*; Skotheim, T. A., Elsenbaumer, R.L., Reynolds, J.R., Ed.; Marcel Dekker: New York, **1998**; pp 437.
- (76) Miyata, S.; Ozio, T., US Patent 4699804. **1987**.
- (77) Maus, L.; Witucki, E. F.; L.F., W., US Patent 4696835. **1987**.
- (78) Newman, P.; Warren, L.; Witucki, E., US Patent 4617228. **1986**.
- (79) Mizuki, T.; Watanabe, K., Japan Patent 01,266,280. **1989**.

- (80) Wiersma, A. E., European Patent App Patent 0 589 529 A1. **1994**.
- (81) Bartholomew, G. W.; Jongchul, K.; Volpe, R. A.; Wenzel, D. J., US Patent 5211810. **1993**.
- (82) Faverolle, F.; Attias, A. J.; Bloch, B.; Audebert, P.; Andrieux, C. P. *Chem. Mater.* **1998**, *10*, 740
- (83) Nagasubramanian, G., US Patent 5066748. **1991**.
- (84) Cho, G.; Jang, J.; Moon, I.; Leeb, J.-S.; Glatzhofer, D. T. *J. Mater. Chem.* **1999**, *9*, 345.
- (85) Bhadani, S. N.; Kumari, M.; Gupta, S. K. S.; Sahu, G. C. *J. App. Poly. Sci.* **1997**, *64*, 1073.
- (86) Barry Jr., C. N., U.S. Patent 5,176,851. **1993**.
- (87) MacDiarmid, A. G.; Chiang, J. C.; Richter, A. F.; Somasiri, N. L. D. Synthesis and Characterization of Emeraldine Oxidation State by Elemental Analysis. In *Conducting Polymers*; Alcaer, L., Ed.; Reidel: Dordrecht, **1987**; pp 105.
- (88) Munstedt, H. *Polymer* **1988**, *29*, 296.
- (89) DeAngelis, A. R.; Childs, A. D.; Green, D. E., US Patent 5,720,892. **1998**.
- (90) Kuhn, H. H.; Kimbrell, W. C.; Fowler, J. E.; Barry, C. N. *Synthetic Metals* **1993**, *55-57*, 3707.
- (91) Lei, J.; Martin, C. R. *Synthetic Metals* **1992**, *48*, 331.
- (92) Truong, V.-T. *Synthetic Metals* **1992**, *52*, 33.
- (93) Truong, V.-T.; Ennis, B. C.; Turner, T. G.; Jenden, C. M. *Polymer International* **1992**, *27*, 187.
- (94) Thieblemont, J. C.; Planche, M. F.; Petrescu, C.; Bouvier, J. M.; Bidan, G. *Polymer Degradation and Stability* **1994**, *43*, 293.
- (95) Thieblemont, J. C.; Planche, M. F.; Petrescu, C.; Bouvier, J. M.; Bidan, G. *Synthetic Metals* **1993**, *59*, 81.
- (96) Collins, G. E.; Buckley, L. J. *Synth. Met.* **1996**, *78*, 93.
- (97) Jousse, F.; Delnaud, L.; Olmedo, L. *40th Int. SAMPE symp. Exhib.* **1995**, 360.
- (98) Wong, T. C. P.; Chambers, B.; Anderson, A. P.; Wright, P. V. *Elect. Lett.* **1992**, *28*, 1651.
- (99) Wong, T. C. P.; Chambers, B.; Anderson, A. P.; Wright, P. V. Proc. 8th International Conference on antennas and propagation, **1993**, Edinburgh, UK.
- (100) Wright, P. V.; Wong, T. C. P.; Chambers, B.; Anderson, A. P. *Adv. Mat. Optics & Electronics* **1994**, *4*, 253.
- (101) Wong, T. C. P.; Chambers, B.; Anderson, A. P.; Wright, P. V. *Proc. 3rd Int Conf. on Electromagnetics in Aerospace Applications, 14-17 Sept 1993, Turin, Italy.* **1993**.
- (102) Wong, T. C. P.; Chambers, B.; Anderson, A. P.; Wright, P. V. Ninth International Conference on Antennas and Propagation, **1995**.
- (103) Gangopadhyay, R.; De, A. *Chem. Mater.* **2000**, *12*, 608
- (104) Simmons, M. R.; Chaloner, P. A.; Armes, S. P.; Greaves, S. J.; Watts, J. F. *Langmuir* **1998**, *14*, 611
- (105) Cooper, E. C.; Vincent, B. *J. Phys. D.: Appl. Phys.* **1989**, *22*, 1580.
- (106) Chehimi, M. M.; Abel, M. L.; Sahraoui, Z.; Fraoua, K.; Lascelles, S. F.; Armes, S. P. *Int. J. Adhesion and Adhesives* **1997**, *17*, 1.
- (107) Khan, M. A.; Armes, S. P. *Adv. Mater.* **2000**, *12*, 671
- (108) Lascelles, S. F.; Armes, S. P. *Adv. Mater.* **1995**, *7*, 864
- (109) Barthet, C.; Armes, S. P.; Lascelles, S. F.; Luk, S. Y.; Stanley, H. M. E. *Langmuir* **1998**, *14*, 2032

- (110) Cairns, D. B.; Armes, S. P.; Bremer, L. G. B. *Langmuir* **1999**, *15*, 8052
- (111) Kim, B. J.; Oh, S. G.; Han, M. G.; Im, S. S. *Polymer* **2002**, *43*, 111
- (112) Kryszewski, M.; Jeszka, J. K. *Synth. Met.* **1998**, *94*, 99
- (113) Zelenev, A.; Sonnenberg, W.; Matijevic, E. *Colloid Polym. Sci.* **1998**, *276*, 838
- (114) Gill, M.; Mykytiuk, J.; Armes, S. P.; Edwards, J. L.; Yeates, T.; Moreland, P. J.; Mollett, C. J. *Chem. Soc., Chem. Commun.* **1992**, 108.
- (115) Terrill, N. J.; Crowley, T.; Gill, M.; Armes, S. P. *Langmuir* **1993**, *9*, 2093
- (116) McCarthy, G. P.; Armes, S. P.; Greaves, S. J.; Watts, J. F. *Langmuir* **1997**, *13*, 3686
- (117) Miksa, B.; Slomkowski, S.; Marsault, J.-P. *Colloid Polym. Sci.* **1998**, *276*, 34
- (118) Wu, C.-G.; Chen, C.-Y. *J. Mater. Chem.* **1997**, *7*, 1409.
- (119) Perruchot, C.; Chehimi, M. M.; Mordenti, D.; Bri, M.; Delamar, M. *J. Mater. Chem.* **1998**, *8*, 2185.
- (120) Rajesh, B.; Thampi, K. R.; Bonard, J.-M.; Mathieu, H. J.; Xanthopoulos, N.; Viswanathan, B. *Chem. Comm.* **2003**, 2022.
- (121) Menon, V. P.; Lei, J.; Martin, C. R. *Chem. Mater.* **1996**, *8*, 2382
- (122) De Vito, S.; Martin, C. R. *Chem. Mater.* **1998**, *10*, 1738
- (123) Demoustier-Champagne, S.; Stavaux, P. *Chem. Mater.* **1999**, *11*, 829
- (124) Martin, C. R. *Adv. Mater.* **1991**, *3*, 457
- (125) Jang, J.; Yoon, H. *Chem Commun* **2003**, 720.
- (126) Liu, J.; Wan, M. *Synth. Met* **2001**, *124*, 317.
- (127) Yang, Y.; Wan, M. *J. Mater. Chem.* **2001**, *11*, 2022.
- (128) Goren, M.; Qi, Z.; Lennox, R. B. *Chem. Mater.* **2000**, *12*, 1222.
- (129) Kaynak, A. *Materials Research Bulletin* **1997**, *32*, 271.
- (130) Aguilar-Hernández, J.; K., P.-K. *Phys. Chem. Chem. Phys.* **1999**, *1*, 1735.
- (131) Cabala, R.; Skarda, J.; Potje-Kamloth, K. *Phys. Chem. Chem. Phys.* **2000**, *2*, 3283.
- (132) Zerbi, G.; Veronelli, M.; Martina, S.; Schluter, A.-D.; Wegner, G. *J. Phys. Chem.* **1994**, *100*, 978.
- (133) Binder, M.; Mammone, R. J.; Schlotter, N. E. *Synth. Met.* **1990**, *39*, 215
- (134) Ahmed, S. M.; Nagaoka, T.; Ogra, K. *Analytical Sciences* **1998**, *14*, 535.
- (135) Sonmez, G.; Sarac, A. S. *Journal of Materials Science* **2002**, *37*, 4609.
- (136) Chandrasekhar, P. *Conducting Polymers, Fundamentals and Applications: A Practical Approach.*; Kluwer Academic Publishers: London, **1999**.
- (137) Kohlman, R. S.; Epstein, A. J. Insulator-Metal Transition and Inhomogeneous Metallic State in Conducting Polymers. In *Handbook of Conducting Polymers*; Skotheim, T. A., Elsenbaumer, R.L., Reynolds, J.R., Ed.; Marcel Dekker: New York, **1998**; pp 85.
- (138) Menon, R.; Yoon, C. O.; Heeger, A. J. Metal-Insulator Transition in Doped Conducting Polymers. In *Handbook of Conducting Polymers*; Skotheim, T. A., Elsenbaumer, R.L., Reynolds, J.R., Ed.; Marcel Dekker: New York, **1998**; pp 27.
- (139) Kaynak, A. *Mater. Res. Bull.* **1998**, *33*, 81
- (140) Mohamed, A. B. H.; Miane, J. L.; Zangar, H. *Polymer International* **2001**, *50*, 773.
- (141) Pelster, R.; Simon, U. *Colloid Polym. Sci.* **1999**, *277*, 2
- (142) Unsworth, J.; Kaynak, A.; Lunn, B. A.; Beard, G. E. *Journal of Materials Science* **1993**, *28*, 3307.
- (143) Olmedo, L.; Hourquebie, P.; Jousse, F. *Adv. Mat.* **1993**, *5*, 373.
- (144) Truong, V.-T.; Turner, B. D.; Muscat, R. F.; Russo, M. S. *SPIE* **1997**, *3241*, 98.
- (145) Stubbs, H. V. G.; Wickenden, B. V. A.; Howell, W. G.; Perry, E. D., UK Patent GB 2058469A. **1981**.
- (146) Ruffoni, J. M., US Patent 5151222. **1992**.

- (147) Buckley, L. J.; Eashoo, M. *Synthetic Metals* **1996**, 78, 1.
- (148) Ennis, B. C.; Truong, V.-T. *Synthetic Metals* **1993**, 59, 387.
- (149) Otero, T. F.; Grande, H. Electromechanical Devices: Artificial Muscles Based on Conducting Polymers. In *Handbook of Conducting Polymers*; 2nd ed ed.; Dekker, M., Ed. New York, **1998**; pp pp. 1015.
- (150) Rapi, S., Bocchi, V., Gardini, G.P. *Synthetic Metals* **1988**, 24, 217.
- (151) Kaynak, A.; Rintoul, L.; George, G. A. *Materials Research Bulletin* **2000**, 35, 813.
- (152) Costa, L. C.; Henry, F.; Valente, M. A.; Mendiratta, S. K.; Sombra, A. S. *Eur. Polym. J.* **2002**, 38, 1495.
- (153) Uyar, T.; Toppare, L.; Hacaloglu, J. *Synth. Met* **2001**, 123, 335.
- (154) Barry Jr., C. N.; Kuhn, H. H., US Patent 5,240,644. **1993**.

4.4 Stable Conducting Polymers

Pi conjugated polymers such as polyacetylene, polythiophene, and polypyrrole can be oxidized, or “doped” to charged states which are often highly conducting. From their discovery in the mid 1970s they have attracted huge worldwide interest. The fundamental physical properties of these materials are extremely unusual and they are also of intense interest for practical applications as plastic-type materials with excellent electrical and optical properties. The 2000 Nobel Prize in Chemistry was awarded to three of the pioneers of this field.

One of the major issues with respect to applications of conjugated polymers is the environmental stability of the polymers in their doped (conducting) states. Most examples are quite stable when they are not doped but become very reactive and difficult to handle when doped. Much research effort over the years has gone into creating conjugated polymers with improved stability in the doped state. One of the original systems, polyaniline, can be thought of as a phenylene based polymer in which the aromatic groups are linked by nitrogen atoms. Another more recent example is poly(3,4-ethylenedioxythiophene), also known as PEDOT, a thiophene derivative with excellent stability properties.

This project focuses on attempts to prepare new kinds of conducting polymers with improved stability properties. The general strategy is to build on the precedents set by polyaniline and PEDOT, i.e. use main group atoms/functional groups to enhance stability of thiophene polymers.

4.4.1 Sulfur-Bridged Thiophenes

In a recent publication (1) it was demonstrated that the introduction of sulfur atoms at the ends of short pieces of thiophene chains inferred great stability to the radical cations and dication of these species. The electron-donating nature of sulfur atoms renders the thiophene chains easier to oxidize and also lends chemical stability of the oxidized forms – some examples are even air stable as radical cations. These small molecular chains can be considered as models for “doped” polymers. We therefore sought to incorporate the electron-donating characteristics of the sulfur atom into polymeric arrays. A series of thiophene and/or EDOT monomers in which the conjugated pi systems are linked by sulfur atoms were synthesized and their polymerization behaviour was investigated.

4.4.1.1 Synthesis of sulfur-bridged thiophenes

Bis(phenylsulfonyl)sulfide proved to be a valuable reagent for the synthesis of bis(thieryl)sulfides **1-5** (Figure 4.39) by reactions with the appropriate lithiated thiophene intermediates.

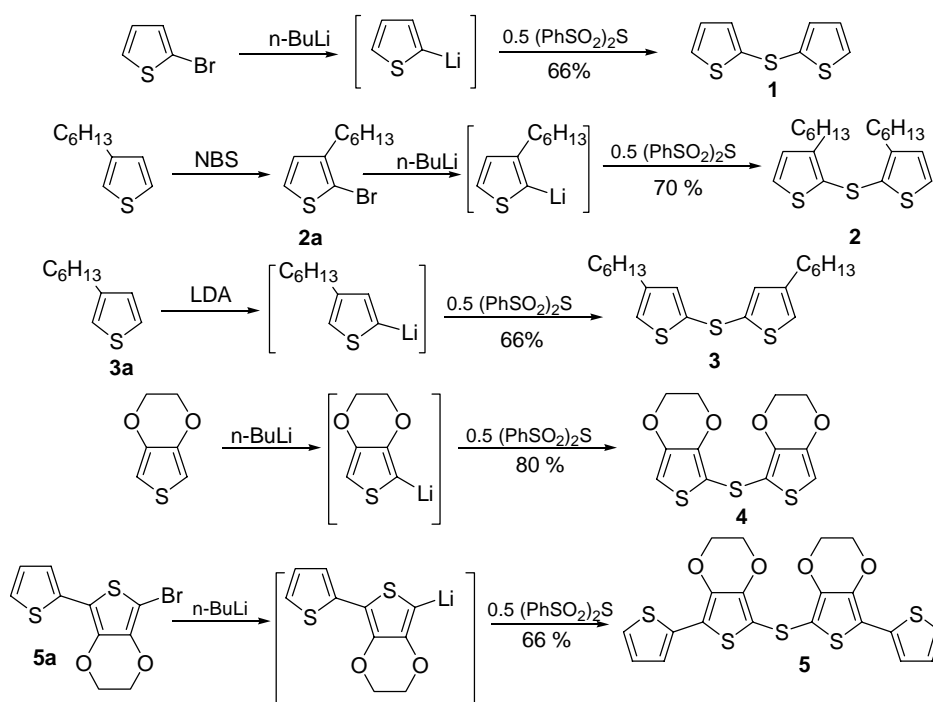


Figure 4.39. Synthesis of 1-5.

The “monomers” **6-8** were prepared using the general reaction of thiophene -2-thiol with the appropriate bromothiophene derivative (Figure 4.40).

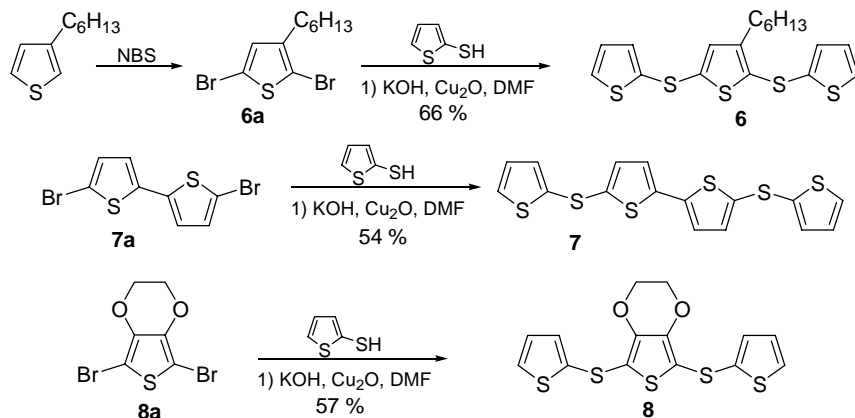


Figure 4.40. Synthesis of **6-8**.

Compounds **9** and **10** were synthesized using Stille cross-coupling reactions of tributylstannyl thiophene derivatives with dibromo derivative **9a** (Figure 4.41).

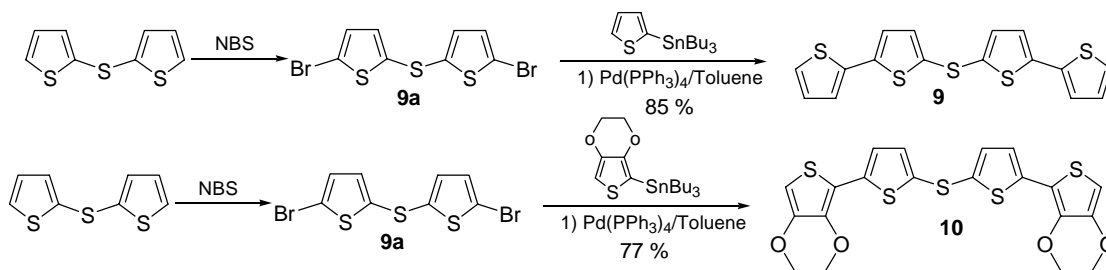


Figure 4.41. Synthesis of **9-10**.

Finally, EDOT-2-thiol was prepared according to established procedures. The thiol actually exists as the “thioquinone” tautomer depicted in Figure 4.42.

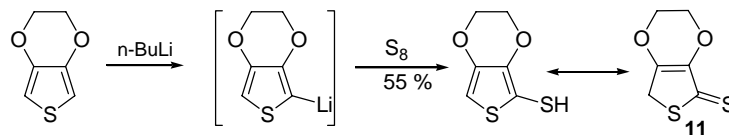


Figure 4.42. Synthesis of **11**.

4.4.1.2 Chemical Polymerizations of sulfur-bridged thiophenes: Synthesis

The FeCl_3 oxidative polymerization method is commonly used to form polythiophenes. We have explored the polymerization of different thiophene monomers (Table). Only the polymers based on **6** and **8** are slightly soluble in dichloromethane and chloroform; their NMR spectra are consistent with their proposed

structures. The others had to be studied by elemental analysis (Table 4.10). The experimental and theoretical ratio of Sulfur/Carbon and Sulfur/Oxygen are very close, which shows the stability of the thiophene-sulfur bonds.

Table 4.9. Results of chemical polymerization of sulfur-bridged thiophenes by FeCl₃.

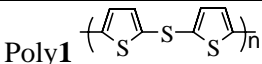
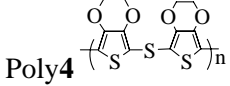
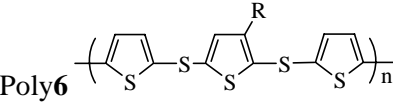
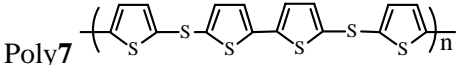
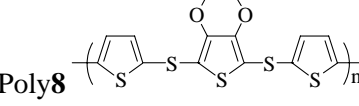
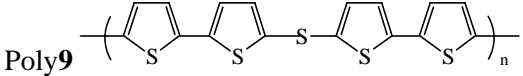
Monomer	Mass (g)	FeCl ₃ (g)	Polymer	Mass (g)	Yield
1	0.202	0.200	Poly1 	0.06	30%
4	0.624	1.011	Poly4 	0.610	97 %
6	0.420	0.235	Poly6 	0.250	60%
7	0.320	0.140	Poly7 	0.200	63%
8	0.864	0.41	Poly8 	0.495	58%
9	0.235	0.110	Poly9 	0.166	71%

Table 4.10. Elemental analyses for FeCl₃ polymerized **1** and **4**.

Element	Poly1			Poly4			or
	Calcd	Found	%S/%C	Calcd	Found	%S/%C %S/%O	
%C	48.98	46.56	0.96 (1)	46.15	43.03	0.67 (0.67)	
%H	2.04	2.99		2.56	2.91		
%S	48.98	44.24		30.77	28.86		
%O	-	-		20.52	21.16	1.36 (1.48)	
%Cl		2.69			3.05		

One concern with the FeCl₃ method is that it may over-oxidize the monomers, and possibly cleave the thiophene-sulfur bonds. To examine this possibility, a model compound based on **1** (which is known to form a stable radical cation on oxidation) was reacted with FeCl₃ as shown in Figure 4.43. It was confirmed that the radical cation of **12** was indeed formed, indicating that the thiophene-sulfur bonds appear to be stable to FeCl₃.

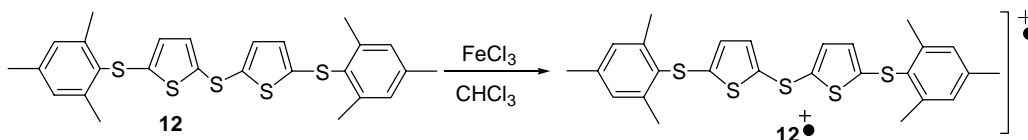


Figure 4.43. Reaction of model compound **12** with FeCl_3 .

4.4.1.3 Conductivity Studies

The four point measurement method was used to estimate the conductivity of the polymers. Only Poly**4** is conducting and its conductivity was found to be $2 \cdot 10^{-4}$ S/cm. The others are not conducting. No conductivity was observed in case of Poly**1** doped with iodine. Poly(**EDOT**) prepared under the same conditions as Poly**4** has a conductivity of $12.5 \cdot 10^{-3}$ S/cm. To increase the conductivity of Poly**4**, polymerization was performed with different ratios of **4** and **EDOT** in CHCl_3 (Figure 4.44).

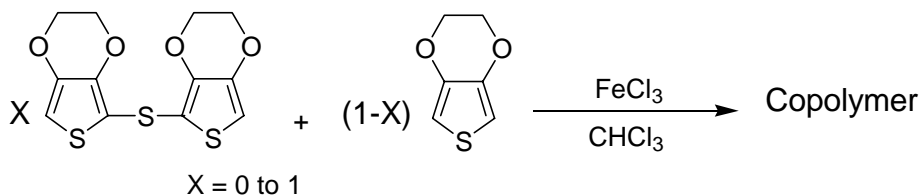


Figure 4.44. Synthesis of EDOT/**4** based copolymers.

The results of the conductivity measurements are summarized in Table 4.11. The copolymer Poly(**4-EDOT**) ($X = 0.5$) has the maximum conductivity, which is close to that of Poly**EDOT** prepared by the FeCl_3 method.

Table 4.11. Conductivity of EDOT/**4** copolymers.

X	10^4 CONDUCTIVITY (S/cm)
1 (ESE)	2
0.8	1.5
0.5	11
0.2	4.8
0 (EDOT)	12.5

4.4.1.4 Optical Properties of de-doped Poly-4

The doped form of Poly4 prepared by FeCl_3 method is insoluble in organic solvents, and is therefore very difficult to characterize using NMR techniques. Treatment with hydrazine reduces the polymer to its neutral state, which is moderately soluble in organic solvents (Figure 4.45).

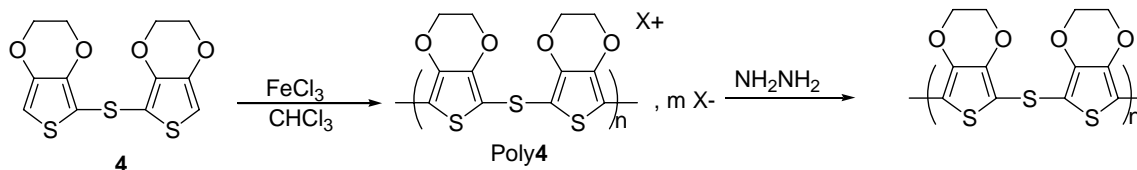


Figure 4.45. Synthesis of doped Poly4 and its reduction to undoped state.

The UV-Vis spectrum of the neutral form of the polymer shows multiple peaks between 400 and 500 nm (Figure 4.46). Poly(EDOT) has a somewhat similar absorption spectrum (see Figure 4.60).

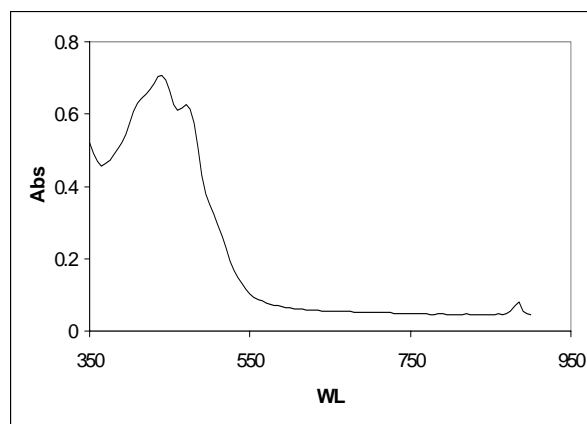


Figure 4.46. UV-Vis of poly4 after reduction with hydrazine.

Poly8 was slightly soluble in CHCl_3 and its UV-Vis spectra shows two sharp peaks at 445 and 475 nm (Figure 4.47). Poly8/ FeCl_3 may not be highly doped, which may explain that the polymers prepared using FeCl_3 methods are not highly conducting.

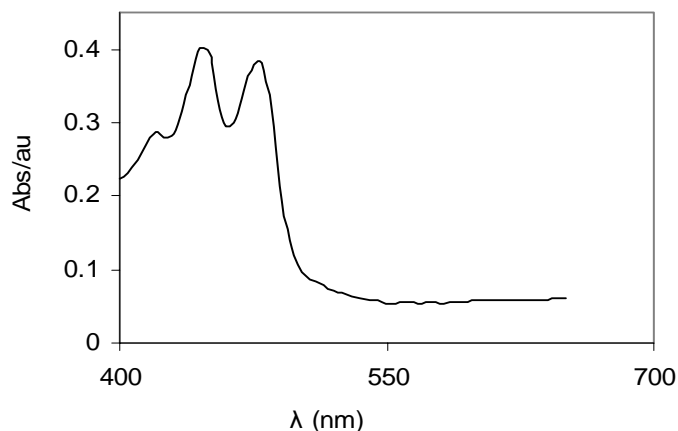


Figure 4.47. UV-Vis of poly**8**/FeCl₃

4.4.1.5 Electrochemistry of sulfur-bridged thiophenes: Oxidation Potentials

Electrochemical measurements were performed on all thiophene monomers using cyclic voltammetry (CV). The electrochemical data for these thiophene monomers are summarized in Table 4.12. Two of the monomers **6** and **8** possessed reversible oxidation processes. The other monomers displayed irreversible oxidation waves as expected for α -unsubstituted thiophenes, which is a desirable feature for electropolymerization reactions. Not surprisingly, attempts to electropolymerize **6** and **8** were not successful; the radical cation formed on oxidation is too stable to react and too soluble to deposit on the electrode surface. Despite the irreversible oxidation waves of **2** and **3**, no deposition of the polymer occurred on the electrode. The hexyl groups render the radical cations too soluble for any further deposition. No electropolymerization of **9** was observed.

Table 4.12. Electrochemical and optical properties of sulfur-bridged thiophenes.

MONOMER	λ (NM) ^A	$10^{-4} \times \epsilon$ (M ⁻¹ • cm ⁻¹) ^B	E ¹ _a (V) vs Ag/Ag/Cl ^C	E ² _a (V) ^D
1	268	0.8	1.550	-
2	250	1.2	1.390	-
3	270	0.9	1.410	-
4	270	1.8	1.180	-
5	345	2.7	0.960	-
6	280	1.3	1.290	1.655
7	335	1.1	1.370	-
8	280	1.7	1.180	-
9	350	2.7	1.170	1.435
10	345	2.6	1.015	1.260
11	345	2	1.360	-
EDOT	260		1.510	-

^Alongest wavelength solution absorption maximum. ^BMolar extinction coefficient for the absorption maxima. ^Cfirst oxidation peak potential. ^Dsecond oxidation peak potential.

4.4.1.6 Electropolymerization of sulfur-bridged monomer 1

After a few cycles beyond the oxidation potential of **1**, deposition of a green film was observed, which was initially interpreted as positive evidence for polymerization of **1** (Figure 4.48). However, no deposition was observed after 20 scans. Poly**1** prepared by electropolymerization seemed to be very sensitive to the oxidation potential and susceptible to degradation of the polymer after formation. The thiophene-sulfur bond can be cleaved yielding thiophene thiols, which can adsorb to the electrode surface and therefore prevent the electropolymerization process.

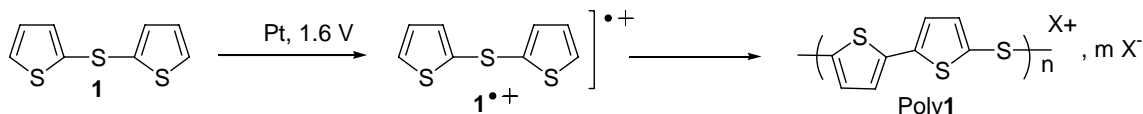


Figure 4.48. Putative electropolymerization of **1**.

4.4.1.7 Electropolymerization of sulfur-bridged monomer 4

Repeated electrochemical cycling between 0 and +1.5V led to new peaks at potentials cathodically shifted relative to monomer **4** and concomitant formation of a dark film.

These observations are indicative of electropolymerization of **4** at the α carbons of each EDOT moiety to give polymer Poly**4** (Figure 4.49).

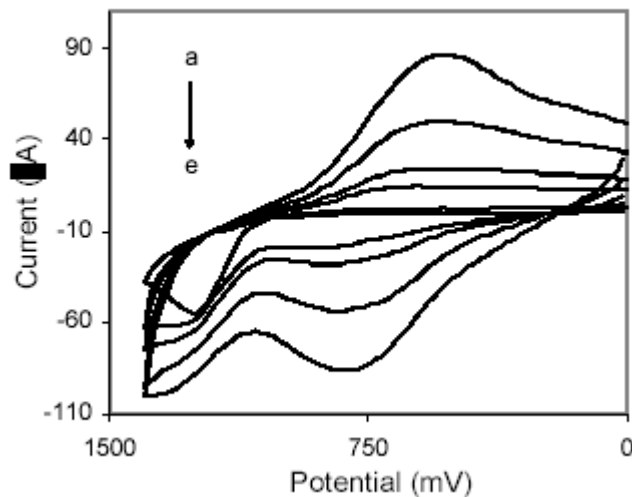
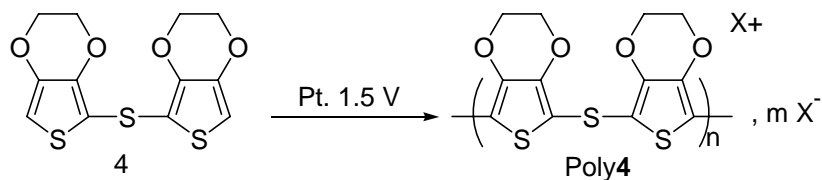


Figure 4.49. Electropolymerization of **4** in CH_2Cl_2 . (a) 1st scan....(e) 40th scan. Y-axis units are in microAmps.

Cyclic voltammograms of as-deposited **4** in fresh (monomer-free) solutions show a broad oxidation process at ca. +600 mV (vs Ag/AgCl). The peak current was found to be linearly dependent on scan rate (Figure 4.50), indicative of a surface-bound species. The doping/de-doping process of Poly**4** is fully reversible: repeated cycling several hundred times did not lead to any detectable change in the electrochemical cyclic behaviour.

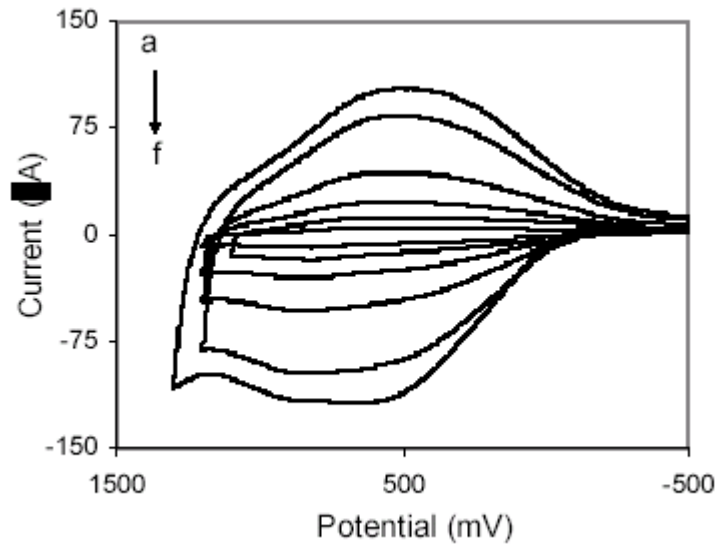


Figure 4.50. CV of Poly4 at different scan rates. (a) 0.05 V/s (b) 0.1 V/s (c) 0.2 V/s (d) 0.4 V/s (e) 0.8 V/s (f) 1 V/s. Y-axis units are in microAmps.

The spectroelectrochemical properties of films of Poly4 were examined on an ITO electrode (Figure 4.51). In the oxidized state the polymer is deep blue with absorption maxima at 605 and 1020 nm. As the potential is lowered, these peaks are gradually replaced by a spectrum with multiple absorptions between 400-500 nm giving a yellow/orange film.

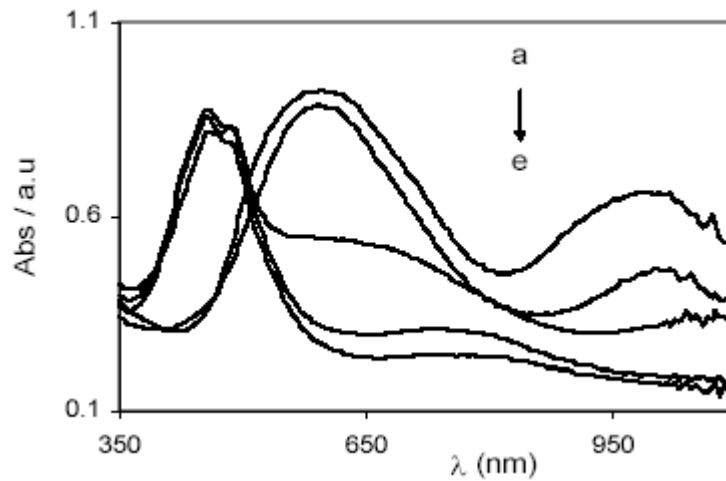


Figure 4.51. Reduction of Poly4 on ITO electrode at different potentials. (a) 1.3 V (b) 0.5 V (c) 0.2 V (d) 0 V (e) -0.2 V

Conductivity studies of films of **Poly4** were carried out *in situ* using the interdigitated electrode method.³ The conductivity rises with increasing potential, reaches a maximum at +0.79V and then decreases (Figure 4.52). This behaviour is consistent with redox-type conductivity, in comparison to the behaviour of conventional conjugated polymers, in which a plateau of high conductivity over a relatively large potential window is seen. The internal maximum conductivity of **Poly4** was determined to be 1.5×10^{-3} S/cm. But the normalized conductivity³ of **Poly4** was found to be 10 S/cm.

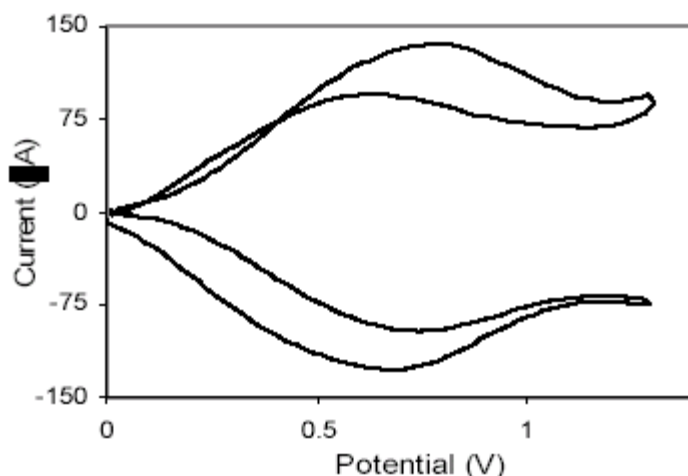


Figure 5.52. Potential-dependent conductivity of **Poly4**. Y-axis units are in microAmps.

4.4.1.8 Electropolymerization of sulfur-bridged monomer 11

Compound **11** has an oxidation peak potential of 1.360 V (vs. Ag/AgCl), which is between the oxidation peak potentials of **EDOT** and **4 (ESE)**. Its electropolymerization via repeated cycling in CH_2Cl_2 (1 M $n\text{-Bu}_4\text{NBF}_4$) on a platinum electrode afforded a dark blue polymer. The polymer modified electrode in a monomer free electrolyte solution showed a broad reversible oxidation wave. The variation of peak current of the modified electrode was found to be linearly dependent on scan rate, which indicates a surface-bound species. No change was observed in the electrochemical properties of the polymer after repeated cycling one hundred times. The oxidation potential of **Poly11** is 0.600 V (vs. Ag/AgCl) which is similar to the oxidation potential of **Poly4**. Moreover, the IR of **Poly11** and **Poly4** are very similar.

Spectroelectrochemical properties of oxidized and reduced films of **Poly11** were examined on an ITO electrode in CH_2Cl_2 (Figure 4.53).

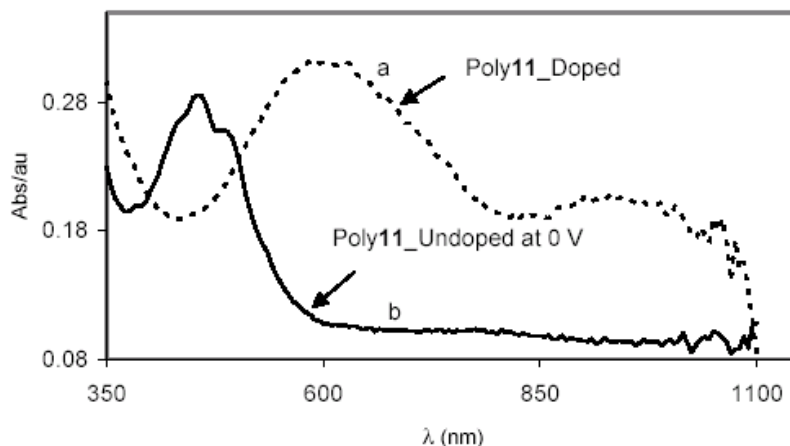


Figure 4.53. Electronic spectrum of poly11 in (a) doped and (b) undoped forms.

Poly11 has two peaks at 600 and 1000 nm in its doped state. When it is reduced at 0 V (vs Ag/AgCl), the neutral form has multiple peaks between 400 and 500 nm. On ITO electrodes, Poly4 and Poly11 have similar optical properties in both states, which indicate that both polymers have identical backbones as shown in Figure 4.54.

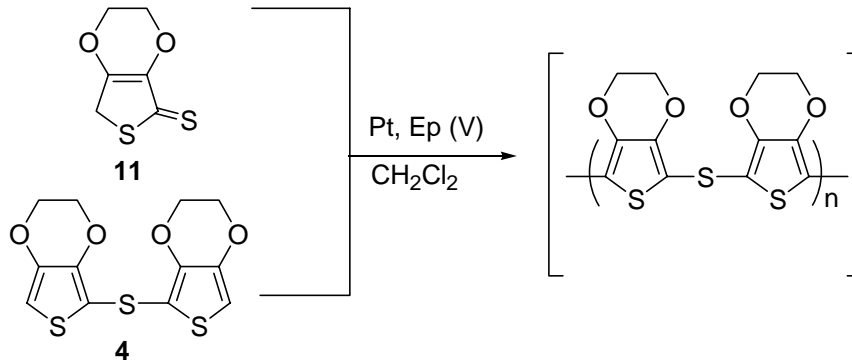


Figure 4.54. Putative electropolymerization of both 4 and 11.

4.4.1.9 Electropolymerization of other sulfur-bridged monomers

Other thiophene monomers were polymerized by CV scans. These polymers present high stability in organic solvents and interesting electro-optical properties. All electrochemical and optical data of the polymers are summarized in Table 4.13.

Table 4.13. Electrochemical and optical properties of sulfur-bridged thiophene polymers.

POLYMER	λ_{doped} (nm)	$\lambda_{\text{de-doped}}$ (nm)	$E_{1/2}$ (V) (vs Ag/AgCl)
Poly1	-	-	1.460
Poly4	600, 1020	435, 450, 480	0.600
Poly5	345, 690	345, 430	0.870
Poly9	620	345, 410	1.310
Poly10	345, 595, 1050	350, 460, 490	0.630
Poly11	600, 1000	430, 450, 480	0.600

4.4.1.10 Conclusions and Future Work

Several new bis(thienyl)sulfides have been prepared and their corresponding (electro)polymerization behaviour have been studied. The polymer resulting from compound **4** exhibits excellent stability in both undoped and doped forms and can be electrochemically switched between the two forms many times without decomposition. The conductivity of the doped polymer is also promising. Future work should focus on this system, for example examination of the stability under harsher conditions (heat, air, humidity). It should also be possible to prepare derivatives of **4** (Figure 4.55) with functional groups that can affect solubility, processibility, and adhesion characteristics while maintaining the favourable electronic properties.

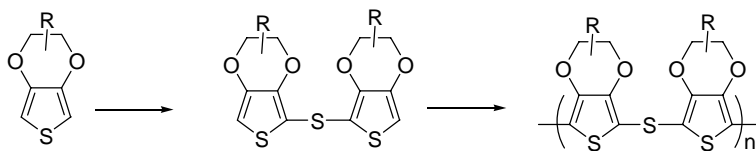


Figure 4.55. Proposed synthesis of Poly4 derivatives with improved processing properties.

4.4.2 Phosphorus-Bridged Thiophenes

The stabilizing effects of the sulfur based substituents described in Chapter 2 prompted studies of other heteroatom-based groups which might also stabilize the electronic properties of conducting polymers. This section describes our efforts to prepare phosphine based thiophene – in particular EDOT – derivatives. It was anticipated that the redox stability of the thiophenes would be facilitated by the lone pair donation from the phosphine. In addition, it was hoped that the presence of phosphines in the polymers would provide a means of further modifying the properties of the polymers through metal ion coordination.

4.4.2.1 Synthesis of phosphorus-bridged thiophenes

A series of thiophene phosphine monomers (**1-5**) were easily synthesized by reaction of appropriate chlorophosphines and lithiated EDOT derivatives (Figure 4.56). The reaction is highly selective and can be controlled to put one, two, or three EDOT groups on a phosphorus atom. All products are air- and moisture stable.

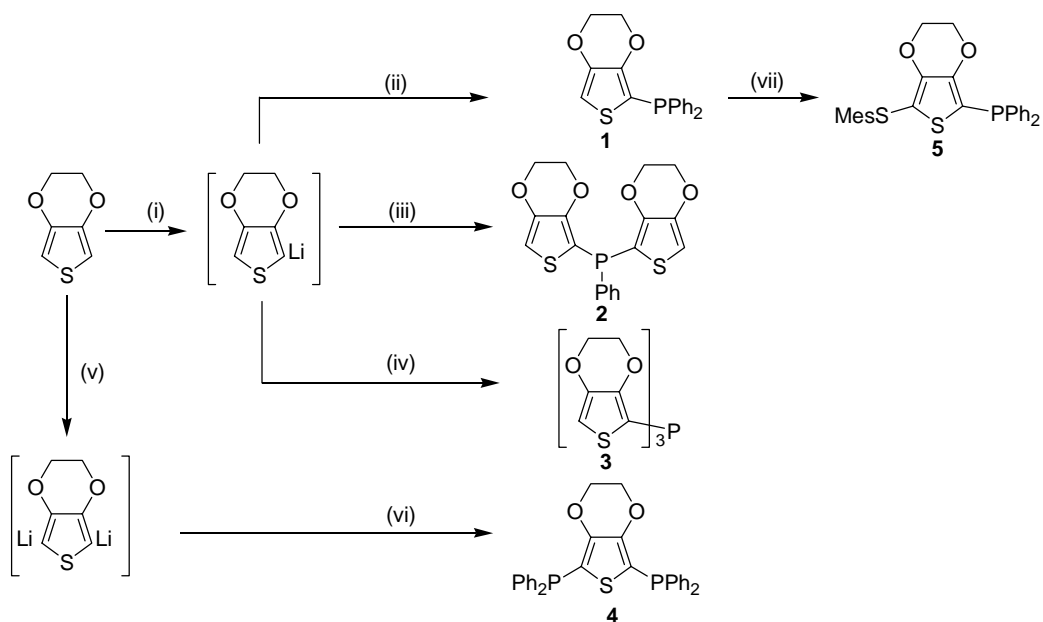


Figure 4.56. Synthesis of EDOT-substituted phosphines **1-5**.

4.4.2.2 Synthesis of metal complexes of P-bridged thiophenes

The EDOT phosphines **1-3** and **5** were reacted with *cis*-Mo(CO)₄(piperidine) to afford two categories of molybdenum complexes as shown in Figure 4.57. In the case of **1** and **5**, disubstituted metal complex products **7** and **8** were obtained; for **2** and **3** monosubstituted products **9** and **10** resulted.

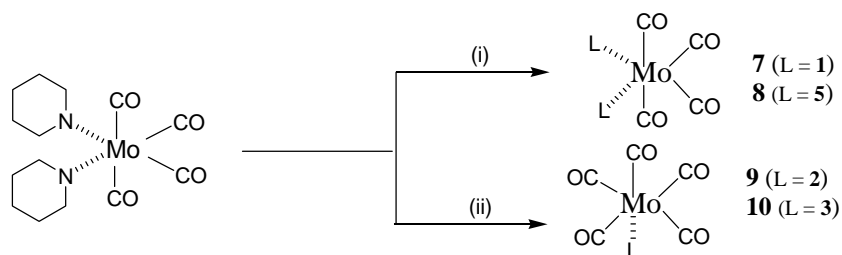


Figure 4.57. Synthesis of Mo complexes of 1-5.

4.4.2.3 Electrochemistry of P-bridged thiophenes and their metal complexes

The redox properties of compounds **1-5** were examined by cyclic voltammetry. All new compounds **1-5** exhibited irreversible oxidation waves at the potentials given in Table 4.14. For compounds **1-3** the irreversible nature of the oxidation was not unexpected because the EDOT groups in these compounds contain unsubstituted positions on the thiophene ring. These unsubstituted positions are known to be highly reactive sites in oxidized thiophenes. However, the bis(phosphine) substituted EDOT **4** also exhibited irreversible behaviour upon oxidation. Thiophenes containing substituents at all the 2 (or 5) positions generally can be electrochemically oxidized to give stable radical cations. The high nucleophilicity of the phosphorus prevented the chain dimerization process of the radical cation, which explains the non electropolymerization of the thiophene phosphines **1-3**. Passivation of the electrode after one scan was observed. The origin of the poor electrochemical properties is believed to be reaction of the radical cations with the phosphine moieties. As a control experiment, the electrochemical polymerization of EDOT itself could not be achieved when attempted in the presence of triphenylphosphine.

Table 4.14. Oxidation peak potentials of EDOT phosphines and their metal complexes.

Product	E_p (V) vs Fc/Fc ⁺ ^A	$E_p - E_{p/2}$ (mV) ^B
EDOT-PPh ₂ 1	0.79 ₈	147
(EDOT) ₂ PPh 2	0.52 ₀	155
(EDOT) ₃ P 3	0.68 ₇	152
Ph ₂ P-EDOT-PPh ₂ 4	0.60 ₇	142
MesS-EDOT-PPh ₂ 5	0.57 ₄	143
<i>cis</i> -Mo(CO) ₄ (EPh ₂) ₂ , 7	0.32 ₄	74
Mo(CO) ₅ (E ₂ PPh), 8	0.67 ₅	89
Mo(CO) ₅ (E ₃ P), 9	0.69 ₆	90
<i>cis</i> -Mo(CO) ₄ (MesEPh ₂) ₂ , 10	0.36 ₆	73
(EDOT)	0.93 ₀	94

^Aoxidation peak potential referenced to the ferrocene/ferrocenium redox couple. ^B difference between peak height and half-peak height potentials.

Cyclic voltammetry studies on complexes **7-10** revealed irreversible oxidations for all compounds. Interestingly, the oxidation peak potential for complexes **8** and **9** are very similar to the peak potentials for the corresponding free ligand, whereas the peak potential for **7** is some 0.4V lower than its free phosphine ligand. This may be related to the fact that **7** has two EDOT phosphine ligands whereas **8** and **9** have one each, although the irreversibility of the oxidations renders direct comparison difficult owing to the scan rate dependence of these processes.

4.4.2.4 Conclusions and Future Work

Clearly the introduction of phosphine substituents has deleterious consequences for the ability to electrochemically polymerize the phosphine functionalized thiophenes. This situation is not remedied upon metal coordination of the phosphine moiety. Future prospects in this area do not appear to be promising.

4.4.3 Silicon-Bridged Thiophenes

Further to the studies described in the previous two chapters, EDOT derivatives linked by silicon were also targeted. Although silanes do not have lone pairs (in contrast to phosphines and sulfides), there are many conducting polymers that incorporate silicon into the polymer backbone.⁽²⁾ It was anticipated that polymers of this sort might have attractive features including low band gaps and processibility.

4.4.3.1 Synthesis of silicon-bridged thiophenes

The lithiated salts of EDOT **1** and biEDOT **2** reacted with $(\text{Me})_2\text{SiCl}_2$ in THF for 24 hours, affording new silicon bridged thiophenes **3** and **4** in high yield (Figure 4.58). Product **3** was purified via column chromatography on silica gel; but product **4** was purified by precipitation using pentane. In the case of **4**, the Si-C bond was cleaved in contact with silica gel and starting material **2** was recovered. Products **3** and **4** are very stable in air and in the presence of organic solvents.

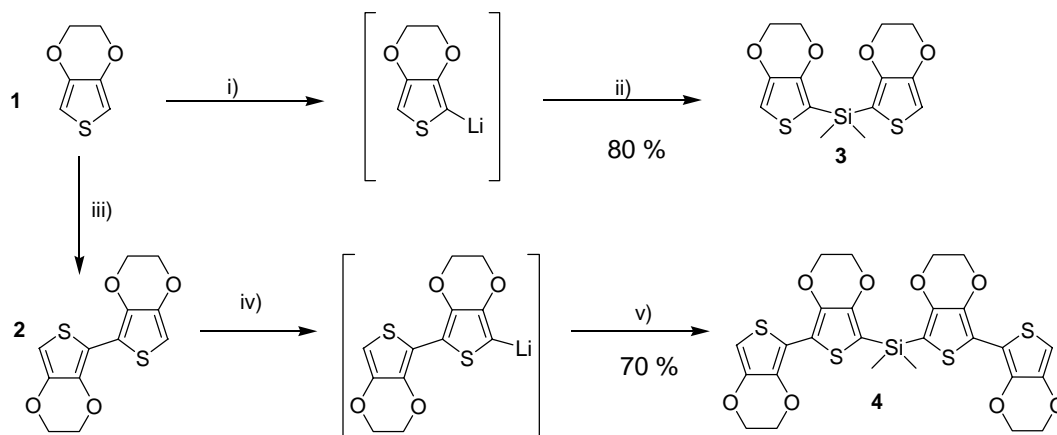


Figure 4.58. Synthesis of EDOT silanes **3** and **4**.

4.4.3.2 Electrochemistry of silicon-bridged thiophenes

In CH_2Cl_2 , compounds **1-4** exhibit one irreversible oxidation wave at potentials of +1.60, 1.04, 1.63 and 1.02 V (vs. Ag/AgCl) respectively. No significant differences in oxidation potentials were observed between **1** and **3**. Similar behavior was observed in the case of **2** and **4**. The presence of silicon therefore does not strongly affect the oxidation peak potential of thiophenes. The oxidation peak potential and visible absorption maxima of the monomers are summarized in Table 4.15.

Table 4.15. Electrochemical and optical properties of EDOT silanes 1-4.

MONOMER	E_{onset} (V) (vs Ag/AgCl) ^A	λ_{max} (nm) ^C
1	1.600	260
2	1.04	330, 350
3	1.630	260
4	1.020	330, 350

The electrochemical oxidations of monomers **1**, **3** and **4** (0.01M) were carried out in CH_2Cl_2 containing 1 M $(n\text{-Bu})_4\text{NBF}_4$ via repeated cyclic voltammetry (CV) cycling to the oxidation potential of the monomers using a scan rate of 0.1 V/s. Supporting electrolyte, $(n\text{-Bu})_4\text{NBF}_4$, of 1 M concentration was used for the electropolymerization process because at this concentration the current of the polymer-modified electrode remained constant after 100 scans, which shows a good adhesion and stability of the polymer on the surface of the electrode.

For all monomers, a dark-blue film formed on the surface of the electrode. The electrochemical properties of the platinum-modified electrodes were studied in a monomer free electrolyte solution. CV's of **Poly1** and "**Poly4**" are shown in Figure 4.59.

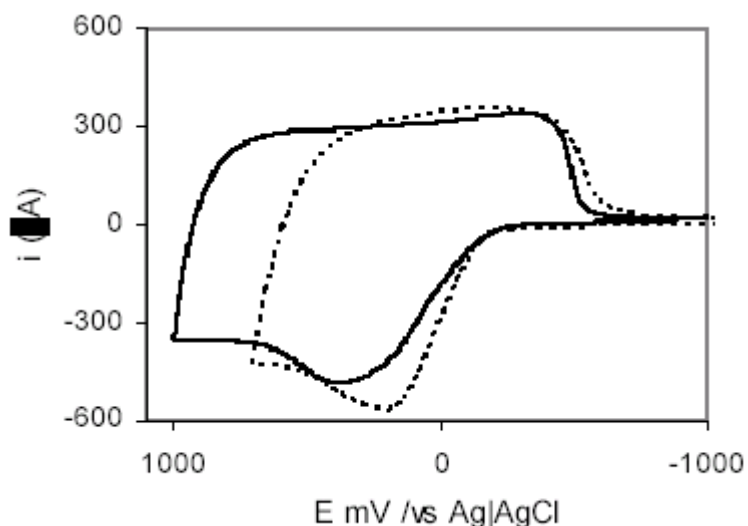


Figure 4.59. CV of **Poly1** (solid line) and **Poly4** (dashed line). Y-axis units are in microAmps.

Poly1, "**Poly3**" and "**Poly4**" modified platinum electrodes exhibit a broad reversible wave. The oxidation potentials ($E_{1/2}$ is the average of peak oxidation and reduction potentials) of **Poly1**, "**Poly3**" and "**Poly4**" were similar and were found to be in the range -0.100 and +0.150 V (vs. Ag/AgCl). The electropolymerization of **3** and **4** yield, via Si-C bond cleavage, polymers that have an identical backbone to Poly(EDOT) with a difference in a molecular weight. The oxidation potentials of **Poly1**, "**Poly3**" and "**Poly4**" are summarized in Table 4.16.

Table 4.16. Electrochemical and absorption data for polymers derived from 1-4.

POLYMER	E (V) ^A	E _{1/2} (V) (vs Ag/AgCl) ^B	λ _{max} (nm)	σ (S/cm)
Poly1	1.600	-0.100	431, 460, 493	53.65±0.35
“Poly3”	1.600	0.150	430, 460, 490	25.25±0.15
“Poly4”	1.000	0.000	432, 460, 485, 520	60.15±1.25

^APotential at which electrolysis was carried out. ^Boxidation half-wave potential of polymer film.

Poly1, **“Poly3”** and **“Poly(4)”** were prepared by controlled potential (i.e. potentiostatic) electrolysis in CH₂Cl₂ containing 1 M of n-Bu₄NBF₄. The concentration of the monomer was 0.01 M. At the end of the electrolysis, a dark film formed on the surface of the electrode. The film was removed from the electrode and washed with 500 ml of CH₂Cl₂ and dried under vacuum for 30 hours. The elemental analysis of **“Poly3”** and **“Poly4”** shows that the amount of silicon present in the polymers is negligible (< 0.3 %), which confirmed the electrochemical and optical results.

Poly1. C₆H₄O₂S₁B_{0.67}F_{2.8}. Calcd. %C: 36.36; %H: 2.04; %S: 16.18, Found. %C: 36.90; %H: 2.64; %S: 18.08.

“Poly3”. C₆H₄O₂S₁B_{0.40}F_{1.6}. Calcd. %C:41.24; %H:2.31; %S: 18.35, Found. %C: 41.13; %H: 2.71; %S: 18.14.

“Poly4”. C₆H₄O₂S₁B_{0.45}F_{1.8}. Calcd. %C:40.24; %H: 2.25; %S: 17.91, Found. %C: 40.07; %H: 2.56; %S: 18.41.

The electrolysis of monomers **1**, **3** and **4** at constant potential led to insoluble dark-blue powders. However, the reduction of the doped state by hydrated hydrazine in CH₂Cl₂ gives yellow undoped polymers. Also, the UV-Vis spectra for the films of **Poly1**, **“Poly3”** and **“Poly4”** on indium tin oxide (ITO) are identical to p(EDOT) described previously. The results of the electrolysis and UV-Vis data are presented in Table 4.16.

The UV-Vis spectra presented in Figure 4.60 shows similar peaks in the range 400-500 nm for all undoped polymers, proving that the backbones of **Poly1**, **“Poly3”** and **“Poly4”** are very similar in nature. The energies of the peaks in **“Poly4”** are somewhat red-shifted relative to **Poly1** and **“Poly3”** suggestive of slightly longer conjugation lengths in neutral **“Poly4”**.

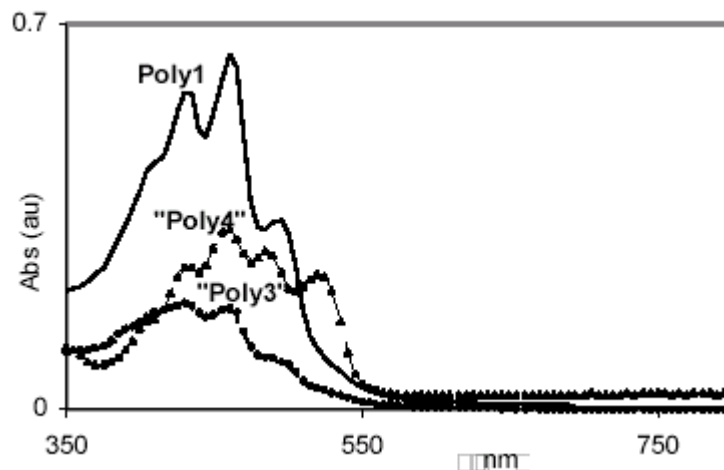


Figure 4.60. Solution absorption spectra of polymers derived from 1-4.

No significant differences were observed in the IR spectra of **Poly1**, **"Poly3"** and **"Poly4"**. All stretches characteristic of p(EDOT) were observed. But, the IR stretches are more resolved for **"Poly3"** and **"Poly4"**.

The electrical conductivity was measured using a four-point method on a pellet. As shown in Table 4.16, **Poly1**, **"Poly3"** and **"Poly4"** are highly conducting, comparable to poly(EDOT) formed via other chemical polymerizations i.e. FeCl₃, or by solid state polymerization.⁴ The maximum conductivity was found to be 60 S/cm for **"Poly4"**. On the other hand, the conductivity of **"Poly3"** (25 S/cm) was ranging by half of that maybe due to less ordering in the backbone of the polymer after the Si-C bond cleavage of the **3⁺**.

4.4.3.3 Conclusions and Future Work

Although the silane-EDOT compounds appear to electropolymerize, the properties of the resulting material strongly suggests that they are in fact polyEDOT, a result of Si-C bond scission during the polymerization. Minor differences in properties between the samples probably arise from differences in molecular weight or morphology. As such new polymer systems have not been achieved.

4.4.4 Amine-Bridged Thiophenes

The success of the sulfur substituent in stabilizing doped forms of the EDOT polymers described in Chapter 2 hinges on the electron donating capabilities of sulfur atoms. With this in mind, nitrogen analogues were targeted on the basis that amines are well known to be powerful electron donating groups in organic chemistry. This section describes recent work on the synthesis and properties of EDOT/amine polymer systems.

4.4.4.1 Synthesis of phenylamine-bridged thiophenes

Different triphenyl-amines mono, di, and tri-substituted by the EDOT moiety **1-3** have been prepared via Stille cross coupling reactions using palladium-phosphines as catalyst. The synthetic procedure of these compounds is summarized in Figure 4.61.

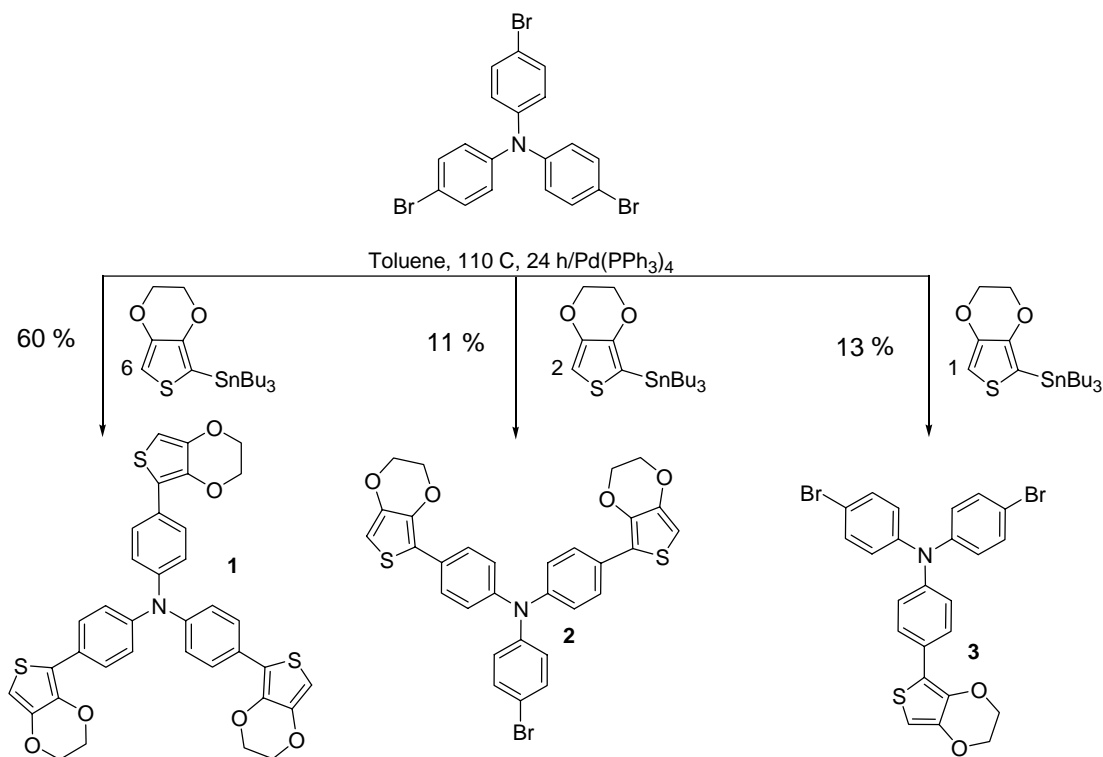


Figure 4.61. Synthesis of EDOT amines **1-3**.

4.4.4.2 Electrochemistry of phenylamine-bridged thiophenes: Electrochemistry of triarylamine model compounds

The electrochemical properties of simple triarylamines were examined in order to aid in the interpretation of the triarylamine-based polymers in subsequent sections.

Triphenylamine (**Ph₃N**) and tris-(4-bromophenyl)-amine (**(BrPh)₃N**) exhibit reversible oxidation waves at oxidation potential of $E^0 = 1.110$ V (vs Ag/AgCl) for **Ph₃N** and $E^0 = 1.280$ (vs Ag/AgCl) for **(BrPh)₃N**. (Figure 4.62).

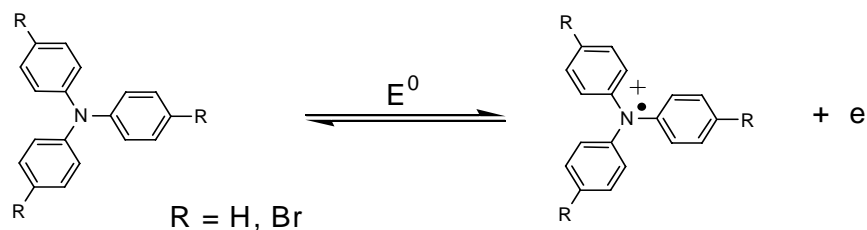


Figure 4.62. Oxidation of triarylamines.

4.4.4.3 Electrochemistry of tris-EDOT/amine 1

The electrochemical oxidation of **1** shows two irreversible waves at 0.750 (oxidation of the amine moiety) and 1.075 V (oxidation of the EDOTs) (vs Ag/AgCl) (Figure 4.63).

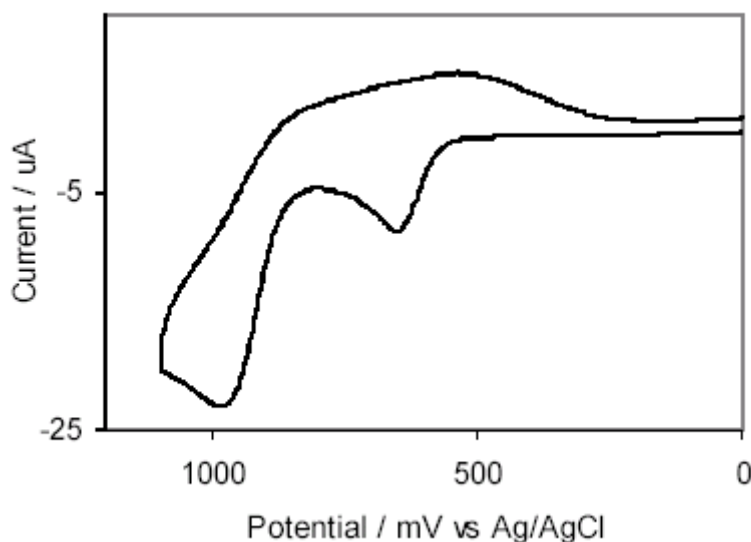


Figure 4.63. CV of tris-EDOT amine 1.

The electropolymerization of **1** via repeated CV cycling at 1.1 V shows a formation of polymer on the surface of the electrode (Figure 4.64)

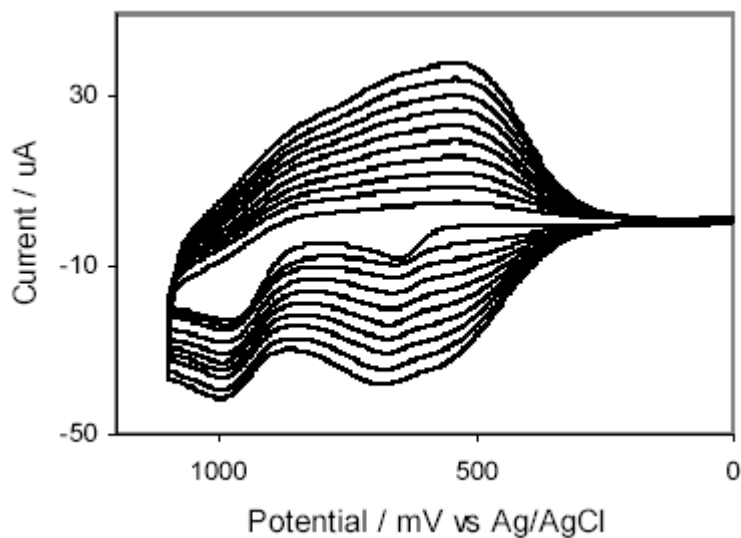


Figure 4.64. Electropolymerization of tris-EDOT amine 1.

The modified electrode in a monomer-free electrolyte solution shows a broad reversible CV wave at $E_{1/2} = 0.640$ V (vs Ag/AgCl) with the oxidation peak current dependent on scan rate (Figure 4.65).

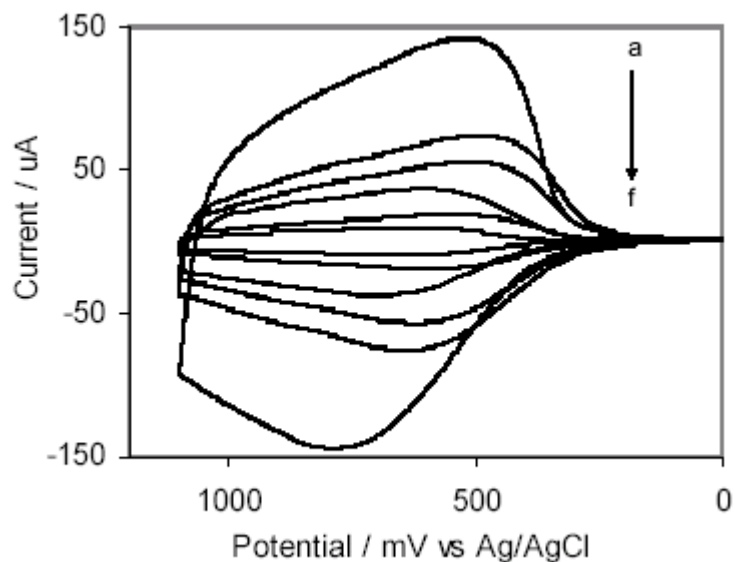


Figure 4.65. CV of poly1 at scan rates: (a) 0.01, (b) 0.025, (c) 0.05, (d) 0.1, (e) 0.15, (f) 0.2 V/s

This polymer is highly stable. The CV cycling (100 scans) of the polymer-modified electrode does not show any change in the oxidation peak current of the polymer. The peak current remained constant after 100 CV scans (Figure 4.66).

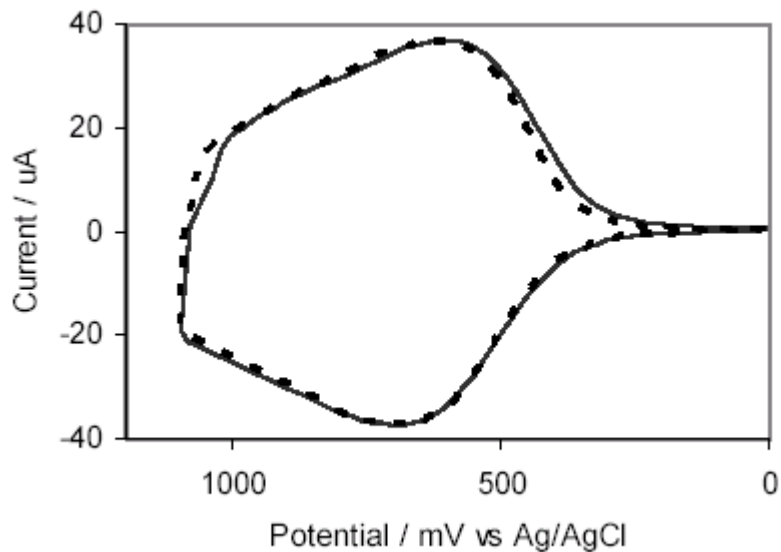


Figure 4.66. CV of Poly1 after one cycle (solid line) and 100 cycles (dashed line).

The optical properties of as-deposited films of Poly1 were studied on an ITO electrode. Figure 4.67 shows the variation of the maximum absorbance with the applied potential. Absorbance maxima and colors of the polymer are summarized in Table 4.17.

Table 4.17. Optical properties of Poly1 films at different potentials.

POTENTIAL (V vs Ag/AgCl)	λ_{max} (nm)	COLOUR
1.1	680, 440	Green
0.0	680, 440	Green-yellow
-0.5	680, 440	Yellow-green
-1.0	440	Yellow

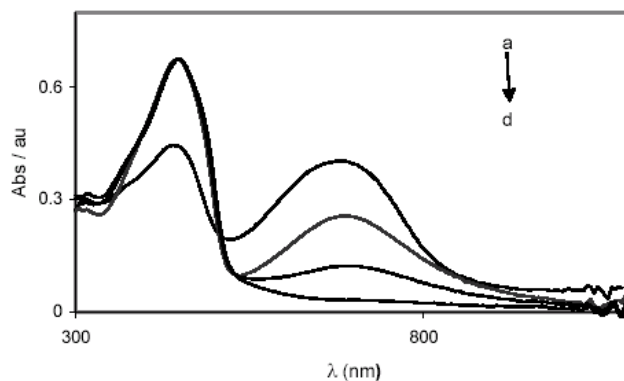


Figure 4.67. UV-Vis spectra of poly1 at different potentials: (a) +1.1V...(d) -1.0V vs. Ag/AgCl.

4.4.4.4 Electrochemistry of bis-EDOT/amine 2

The CV of compound **2** shows two irreversible oxidation waves a $E^1_p = 0.840$ and $E^2_p = 1.160$ V (vs Ag/AgCl) as shown in Figure 4.68. The first oxidation peak corresponds to the oxidation of the amine and the second peak corresponds to the oxidation of EDOT moiety.

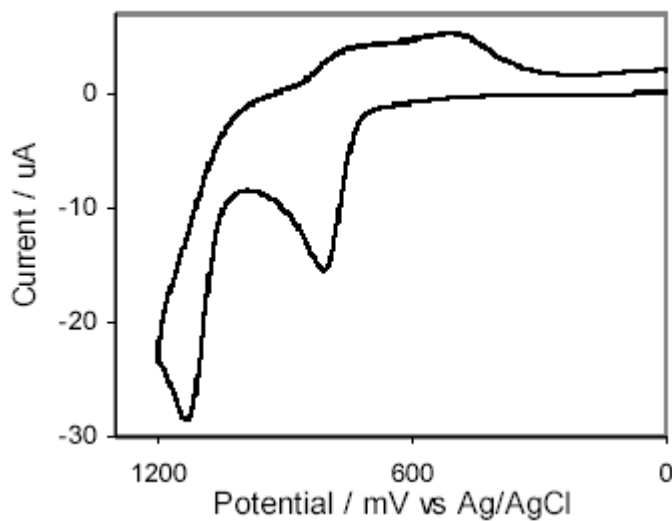


Figure 4.68. CV of bis-EDOT amine 2.

Electropolymerization was performed by cycling the potential beyond the oxidation peak of the monomer (Figure 4.69). The polymer modified electrode in a monomer-free electrolyte solution shows two reversible oxidation waves with oxidation potentials $E_{1/2}^1 = 0.510$ and $E_{1/2}^2 = 0.710$ V (vs Ag/AgCl) as shown in Figure 4.70. The first wave corresponds to the oxidation of the amine and the second wave corresponds to oxidation of EDOT. The oxidation current of the polymer modified electrode remained constant after 100 cycles at 100 mV/s, which reveals the high stability of the polymer.

The higher resolution observed in the oxidation potentials of Poly2 compared to Poly1 is related to the fact that the former is a linear polymer while the latter is heavily cross-linked.

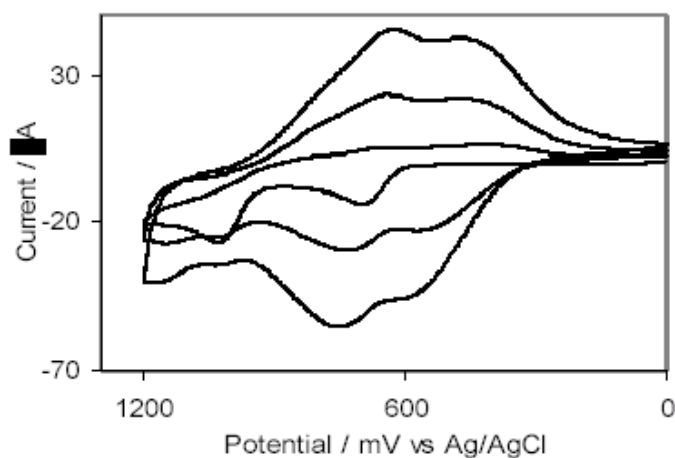


Figure 4.69. Electropolymerization of bis-EDOTamine 2. Y-axis units are in microAmps.

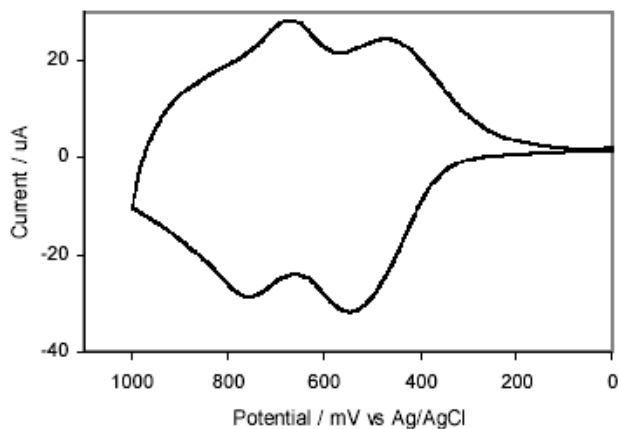


Figure 4.70. CV of film of Poly2.

Poly(2) was deposited on an ITO electrode by constant potential electrolysis at 1.2 V (vs Ag/AgCl). UV-Vis spectra of the film at different potentials are presented in Figure 4.71. At 1.1 V, the polymer is green and shows two peaks at 663 (major) and 447 (minor) nm. At lower potentials, the peak at 663 nm decreased and that at 447 nm increased. At -1 V, the polymer is fully un-doped and the λ_{max} was found to be 444 nm. Table 4.18 shows the optical properties of Poly2 (p(E2N)) at different potentials.

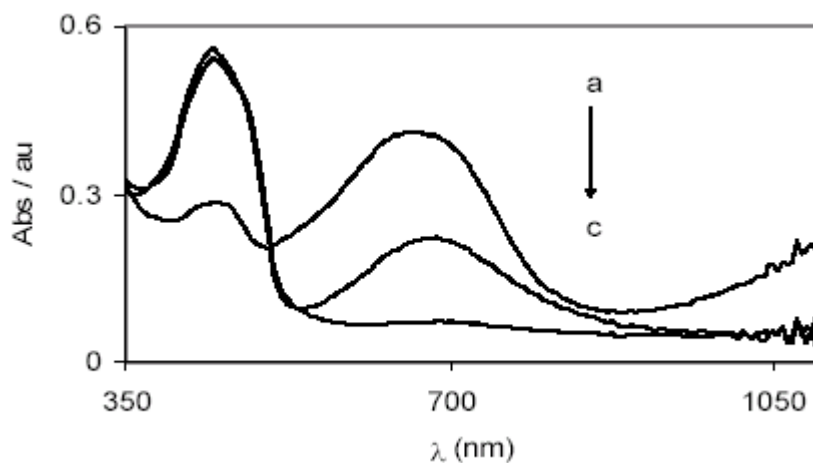


Figure 4.71. Absorption spectra of Poly2 at (a)+1.0V, (b) 0V, and (c)-1V vs Ag/AgCl.

Table 4.18. Optical properties of Poly2 at different potentials.

POTENTIAL (V vs Ag/AgCl)	λ_{max} (nm)	COLOUR
1.2	663, 447	Green
0.0	663, 447	Green-yellow
-1.0	444	Yellow

4.4.4.5 Conclusions and Future Work

The EDOT/amine polymers reported herein have outstanding stability in both doped and undoped forms. They appear to be even more robust than the sulfur-bridged EDOT polymer reported in Chapter 2. The results for the former compounds are extremely encouraging and merit further studies aimed at understanding the differences in behaviour between linear polymer **2** and crosslinked polymer **1**; the latter may prove to have excellent adhesion characteristics. Charge transport properties of the doped polymers also need to be investigated.

4.4.5 Conclusions: Organic Materials

The conducting polymers studied here show merit for the production of radar absorbers as long as long-term stability can be achieved for their properties. Reproducible dispersion of the conductive material in a matrix requires strict control of processing and should be overcome. If these issues cannot be overcome (especially polymer stability) then other materials made be more suitable for absorber fabrication.

Stability and conductivity of the new conducting polymers synthesized in this project need to be further studied. The conductivity of a number of the polythiophene based polymers is too low for making effective microwave absorbers.

4.4.6 Future Work

Future effort with the conducting polymers should focus on material stability and reproducible properties. Other conducting materials should be considered including ferrites for the production of thin broadband absorbers.

4.4.7 References

- (1) R.G. Hicks and M.B. Nodwell, *J. Am. Chem. Soc.* **2000**, *122*, 6746.
- (2) M. Hissler, P.W. Dyer, and R. Reau, *Coord. Chem. Rev.* **2003**, *244*, 1.
- (3) (a) D.L. Simone and T.M. Swager, *J. Am. Chem. Soc.* **2000**, *122*, 9300, and Supporting Information. (b) R.P. Kinsborough and T.M. Swager, *J. Am. Chem. Soc.* **1999**, *121*, 8825.
- (4) H. Meng, D.F. Perepichka, and F. Wudl, *Angew. Chem. Int. Ed.* **2003**, *42*, 658.

5. Permittivity and Permeability Measurement Techniques

The permittivity of the material is far more important for assessing lossy properties than the conductivity, however, the conductivity allows for quick comparison of materials, enabling screening of potential materials. In order to measure the permittivity at X-band frequencies (8.2 – 12.4 GHz) using a waveguide, the materials must be able to fit tightly into the waveguide. Using a vector network analyzer (VNA), as the source, the sample is then irradiated at the appropriate frequencies and the scattering parameters are measured (see Figure 5.1). The permittivity is calculated from the scattering parameters using an algorithm.

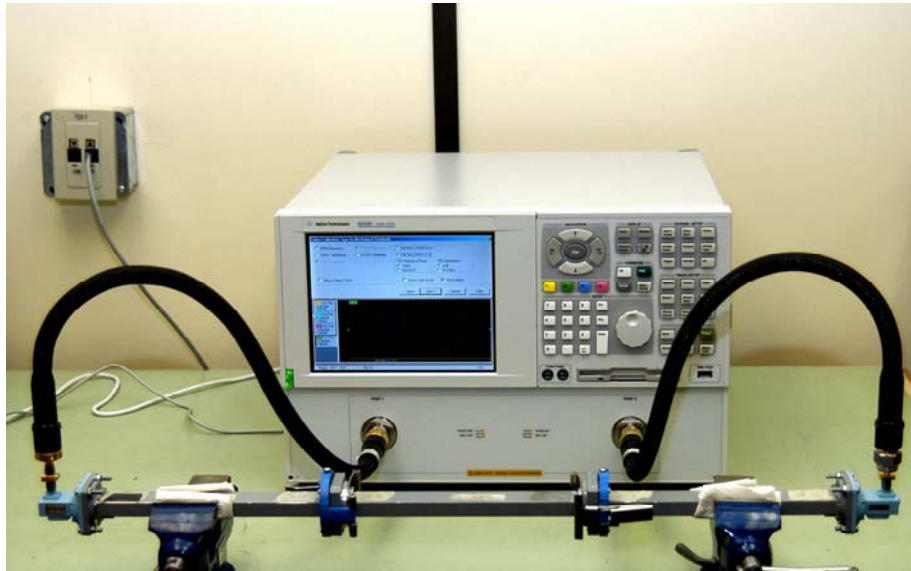


Figure 5.1. Network analyser and waveguide used for measuring S-parameters and fitting permittivity.

In order to measure the permittivity of conducting polymers, which are typically in powder form, one must either deposit the polymer uniformly onto fabric, or disperse uniformly throughout a matrix polymer or coating. In addition to requiring a substrate for mechanical integrity, there is a requirement to reduce the concentration (in the case of composite or coating) or prepare a very thin sample (in the case of fabric), due to the highly conductive nature of the conducting polymers. Pure doped conducting polymers would simply reflect the radiation, as they are metallic in nature.

This contractual research is aimed at development of measurement methods, measurement data processing techniques and actual measurements of the electrical properties (permittivity and permeability) of thin organic polymers at microwave frequencies. The new material samples measured are deposited on a dielectric of low microwave absorption, such as acrylic. Additionally, not mandated by this contract (but essential to the success of future use of the RAM), work has been undertaken on design of radar cross-section reduction techniques.

Measurement Methods

This research was aimed at development of measurement methods, measurement data processing techniques and actual measurements of the electrical properties (permittivity and permeability) of thin organic polymers at microwave frequencies. The new material samples measured are deposited on a dielectric of low microwave absorption, such as acrylic. Additionally, not mandated by this contract (but essential to the success of future use of the RAM), work has been undertaken on design of radar cross-section reduction techniques.

5.1 Overview

Measurement methods for the permittivity and permeability can generally be divided into the free space methods and transmission line methods. Within each of the two categories, two types of measurements can be identified. They are broadband and resonant techniques. Resonant techniques have several advantages for measurements of their samples. Their main advantage is high sensitivity to small changes in the properties and the resultant high accuracy. On the other hand, a separate resonator and sample have to be designed and made for each frequency of interest. Tunable resonators tend to work only in narrow frequency ranges, are expensive, and a decrease in the accuracy accompanies an increase in the frequency bandwidth of a test resonator. There are limitations of resonant methods, which are especially critical for guided wave measurements. For free space measurements at frequencies above 20 GHz, the limitations are less restrictive and tunable resonators provide a reasonably attractive option.^[1-31]

The permittivity and permeability of the (unknown) sample are given by:

$$\varepsilon = \varepsilon_0 \cdot \varepsilon_R^* = \varepsilon_0 (\varepsilon_R' - j\varepsilon_R'')$$

$$\mu = \mu_0 \cdot \mu_R^* = \mu_0 (\mu_R' - j\mu_R'')$$

5.2 Method Selection

It was decided in consultation with the Scientific Authority, that measurements should be performed in X band (8 – 12.4 GHz) for this stage of the project. The following factors were considered.

Availability of the equipment at the University of Victoria and subsequent purchase from the Contract of better accuracy waveguide kit.

Relatively small size of material samples required for testing, which facilitates development of new material.

Reasonably good accuracy expected for thin samples (as their thickness is a small but still reasonable fraction of the wavelength, and the air gaps between the sample and the waveguide are expected to be small with careful machining).

Relative ease of performing the measurement.

Limited thickness of the samples poses a requirement for their support on another material. This necessitates modifications of standard methods to account for the support dielectric. Acrylic was selected as support material because of its low dielectric loss and facility to machine it accurately to fit into the waveguide and to deposit organic and other materials on its surface. The modifications of the standard measurement methods require derivation of the relationships between the measured scattering parameters and the sought electrical properties of test samples (the permittivity and permeability), and careful evaluation of measurement uncertainty. On the basis of these considerations two methods were selected for implementation, namely:

Transmission - reflection methods.

Reflection with two positions of the test sample.

5.3 Transmission – Reflection Method

In the transmission-reflection method (TRM), the test sample deposited on acrylic is placed in the waveguide and Network Analyzer is used to measure, as shown in Figure 5.1. Sample placement in the waveguide and the scattering parameters are related to the complex reflection and transmission coefficients as follows. Designating the permittivity and permeability of a TS by $\hat{\epsilon}_{r1} = \epsilon'_{r1} - j\epsilon''_{r1}$ and $\hat{\mu}_{r1} = \mu'_{r1} - j\mu''_{r1}$, and thickness and d_1 , while ϵ_{r2} and d_2 are the known permittivity and thickness of the support layer. As shown in Figure 5.1, Γ_1 , Γ_2 , and Γ_3 are reflection coefficients between waveguide sections of impedance Z_0 and Z_1 , Z_1 and Z_2 and Z_2 and Z_0 , respectively. It is known that the following relations apply:

$$\Gamma_1 = \frac{Z_1 - Z_0}{Z_1 + Z_0} \quad 5.1$$

$$\Gamma_2 = \frac{Z_2 - Z_1}{Z_2 + Z_1} = -\frac{\Gamma_1 + \Gamma_3}{1 + \Gamma_1\Gamma_3} \quad 5.2$$

$$\Gamma_3 = \frac{Z_o - Z_2}{Z_o + Z_2} \quad 5.3$$

The structure in Figure 5.2 can be represented by five cascaded two-port networks, represented by matrices:

$$S_1 = \begin{bmatrix} \Gamma_1 & 1 - \Gamma_1 \\ 1 + \Gamma_1 & -\Gamma_1 \end{bmatrix} \quad 5.4$$

$$S_2 = \begin{bmatrix} 0 & T_1 \\ T_1 & 0 \end{bmatrix} \quad 5.5$$

$$S_3 = \begin{bmatrix} \Gamma_2 & 1 - \Gamma_2 \\ 1 + \Gamma_2 & -\Gamma_2 \end{bmatrix} \quad 5.6$$

$$S_4 = \begin{bmatrix} 0 & T_2 \\ T_2 & 0 \end{bmatrix} \quad 5.7$$

$$S_5 = \begin{bmatrix} \Gamma_3 & 1 - \Gamma_3 \\ 1 + \Gamma_3 & -\Gamma_3 \end{bmatrix} \quad 5.8$$

where $T_1 = e^{-j\gamma_1 d_1}$ and $T_2 = e^{-j\gamma_2 d_2}$ are the transmission coefficients through the TS and the support material.

The scattering matrix of the whole systems, S, is obtained by cascading the matrices as follows:

$$S = S_1 \diamond S_2 \diamond S_3 \diamond S_4 \diamond S_5$$

where the \diamond operator indicates cascading. The reflection and transmission coefficients of the whole system can be then formed as:

$$S_{11}(f) = \frac{\Gamma_3(1 - T_2^2)(\Gamma_1^2 - T_1^2) + (1 - \Gamma_3^2 T_2^2)\Gamma_1(1 - T_1^2)}{\Gamma_3(1 - T_2^2)\Gamma_1(1 - T_1^2) + (1 - \Gamma_3^2 T_2^2)(1 - \Gamma_1^2 T_1^2)} \quad 5.9$$

$$S_{21}(f) = \frac{T_2(1 - \Gamma_3^2)(1 - \Gamma_1^2)T_1}{\Gamma_3(1 - T_2^2)\Gamma_1(1 - T_1^2) + (1 - \Gamma_3^2 T_2^2)(1 - \Gamma_1^2 T_1^2)} \quad 5.10$$

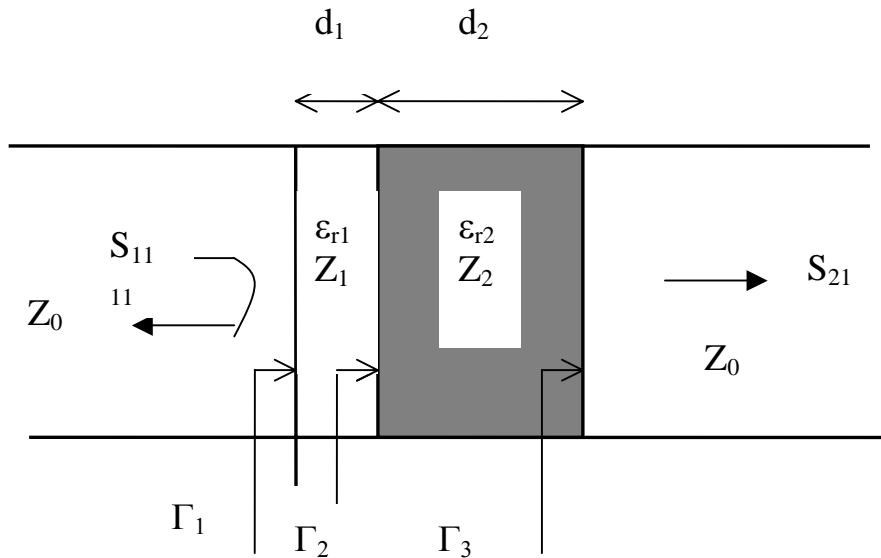


Figure 5.2. Sample placement in the waveguide for transmission – reflection measurements and the equivalent circuit for derivation of the relationship between the measured data and sample parameters.

It should be noted that all the parameters are complex and are functions of $\hat{\epsilon}_r$ and $\hat{\mu}_r$ of the test sample (TS) and the support material. The above shown equations relate the measured quantities, S_{11} and S_{21} to the constrictive properties of the TS. They provide a useful tool for selection of optimum d_2 of the support material for given properties of TS (or in practical situations, the anticipated properties). They can also be used to evaluate uncertainty in the TS permittivity and permeability to the errors in measurements of S_{11} and S_{21} .

5.4 Reflection – Two Position Method

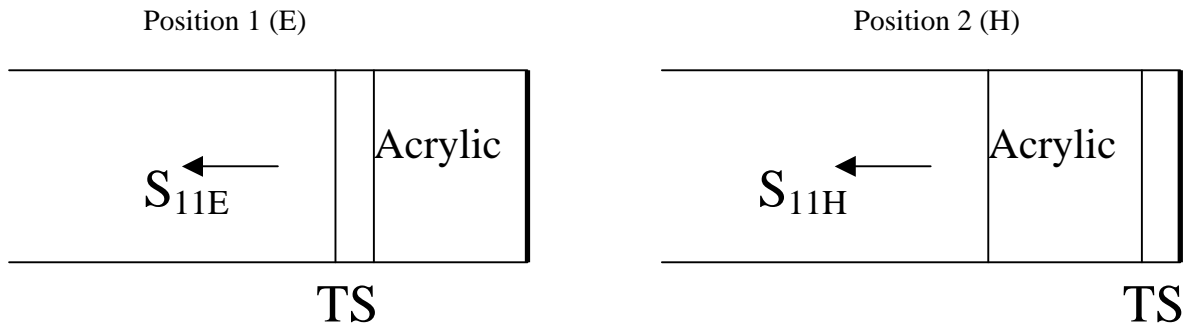


Figure 5.3. Placements of the test sample in the reflection – two-position method

In the reflection – two-positions (R2P) method, as illustrated in Figure 5.3, the TS is placed in two positions. The waveguide is terminated with a short circuit (metallic plate). Position 1 (E) corresponds to the TS being in the maximum of the electric field in the waveguide provided that the acrylic thickness corresponds to the quarter wavelength in the waveguide. In this position the scattering parameter S_{11E} is mainly influenced by the permittivity of TS. In position 2 (H), the TS is in contact with the short, thus placed in the maximum of the magnetic field. Correspondingly, S_{11H} is mostly influenced by the sample permeability. For non-magnetic samples, it suffices to measure the TS in Position E. This method is a modification of a previously described two-position method [2].

To derive the relationships required, referring to Figure 5.4, consider the transmission line model for the short-circuited waveguide. The waveguide shown is divided into three regions as marked. The region 1 (between the short-circuit termination and back face of sample) is filled with a loss less material (Acrylic) of known permittivity and permeability. Region 2 is the TS and region 3 (between the front face of sample and the port 1) is air filled. It is assumed that all the three lengths L_1 , L_2 and L_3 (as marked below) are known with high accuracy.

Using the following relation for a transmission line with loss, the impedance as seen at the short-circuit termination can be transformed to the boundary of region 3 and region 2.

$$Z_{in} = Z_0 \frac{Z_L + Z_0 \bullet \tanh(\gamma L)}{Z_0 + Z_L \bullet \tanh(\gamma L)} \quad 5.11$$

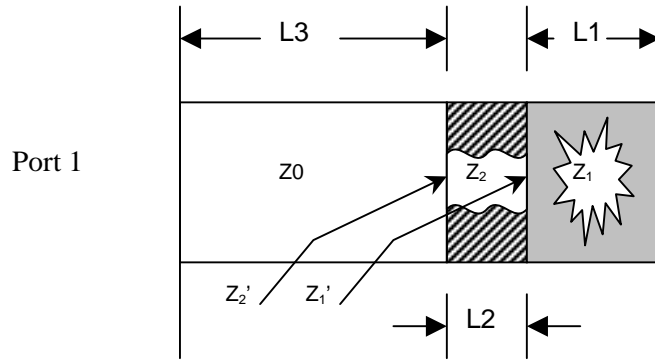


Figure 5.4. Circuit for derivation of the relationship between the scattering parameters and the permittivity and permeability for the T2P method.

Starting from the short-circuit, the impedance (at the short i.e. 0 ohms) is translated to the junction of the back face of unknown sample and the Acrylic material given by Z'_1 ,

$$Z'_1 = Z_1 \bullet \tanh(\gamma_1 L_1) \quad 5.12$$

where Z_1 is the wave impedance in the region 1. In the similar fashion the impedance Z'_1 as seen at the boundary of region 2 and region is translated to the junction of region 3 and front face of the unknown sample, given by

$$Z'_2 = Z_2 \frac{Z'_1 + Z_2 \bullet \tanh(\gamma_2 L_2)}{Z_2 + Z'_1 \bullet \tanh(\gamma_2 L_2)} \quad 5.13$$

$$Z'_2 = Z_2 \frac{Z_1 \bullet \tanh(\gamma_1 L_1) + Z_2 \bullet \tanh(\gamma_2 L_2)}{Z_2 + Z_1 \bullet \tanh(\gamma_1 L_1) \bullet \tanh(\gamma_2 L_2)} \quad 5.14$$

where Z_2 is the wave impedance in the region 2. By definition S_{11} is the reflection coefficient at the junction of region 3 and the region 2 Γ , given by

$$S_{11} = \Gamma = \frac{Z'_2 - Z_0}{Z'_2 + Z_0} \quad 5.15$$

Substituting Z'_2 from equation 5.14

$$S_{11} = \Gamma = \frac{Z_2 \frac{Z_1 \tanh(\gamma_1 L_1) + Z_2 \tanh(\gamma_2 L_2)}{Z_2 + Z_1 \tanh(\gamma_1 L_1) \bullet \tanh(\gamma_2 L_2)} - Z_0}{Z_2 \frac{Z_1 \tanh(\gamma_1 L_1) + Z_2 \tanh(\gamma_2 L_2)}{Z_2 + Z_1 \tanh(\gamma_1 L_1) \bullet \tanh(\gamma_2 L_2)} + Z_0}$$

and after rearranging and letting

$$\Theta_1 = \frac{Z_1}{Z_2} = \frac{\gamma_2 \mu_1}{\gamma_1 \mu_2} \quad \text{and} \quad \Theta_0 = \frac{Z_0}{Z_2} = \frac{\gamma_2 \mu_{01}}{\gamma_0 \mu_2} \quad 5.17$$

where

$$Z_w = j \frac{k\eta}{\gamma} = j \frac{\omega \sqrt{\mu\epsilon} \cdot \sqrt{\frac{\mu}{\epsilon}}}{\gamma} = j \frac{\omega\mu}{\gamma} \quad 5.18$$

$$\gamma = j \sqrt{\frac{\omega^2 \mu_R^* \epsilon_R^*}{c} - \left(\frac{2\pi}{\lambda_c}\right)^2} \quad (19)$$

$$\gamma_0 = j \sqrt{\left(\frac{\omega}{c}\right)^2 - \left(\frac{2\pi}{\lambda_c}\right)^2} \quad (20)$$

Therefore we can rewrite equation 5.17 as

$$S_{11} = \frac{\tanh(\gamma_2 L_2) + \Theta_1 \tanh(\gamma_1 L_1) - \Theta_0 [1 + \Theta_1 \cdot \tanh(\gamma_1 L_1) \cdot \tanh(\gamma_2 L_2)]}{\tanh(\gamma_2 L_2) + \Theta_1 \tanh(\gamma_1 L_1) + \Theta_0 [1 + \Theta_1 \cdot \tanh(\gamma_1 L_1) \cdot \tanh(\gamma_2 L_2)]}$$

5.21

This equation relates the measured complex S_{11} to the lengths and electrical properties of TS and acrylic, the frequency and the cut-off frequency of the waveguide.

5.5 Calibration of Network Analyzer

Network Analyzer used in the measurements (HP 8720C) supports several modes of calibration and there is a variety of calibration kits appropriate for coaxial lines and waveguides. However, only the calibration kits made by Hewlett-Packard have their parameters permanently encoded in the firmware of the instrument. Kits by other vendors have to be entered manually prior to performing the calibration. Less expensive kits from other vendors are used in our measurements. Calibration is a tedious procedure and very prone to entry errors. These errors may render the subsequent measurements completely useless, while the errors are not apparent till the results are computed (and even then the erroneous result is not always apparent). The calibration procedure has to be performed each time the measurement setup is changed

from one type of transmission line to another, e.g. from a coaxial sample holder to a waveguide sample holder. Furthermore, when the instrument is calibrated for a given frequency range, and a different frequency range or a different type of calibration is selected, the correction factors of the previous calibration can only be saved in one of a four internal registers, which in some cases may not be enough. Also, when performing measurements, many different internal functions of the instrument must be set in an unique way. To repeat a given measurement after the instrument has been used for other measurements may require manually changing a number of parameter values to assure they are set the same way as previously.

A set of computer programs was developed and tested for automating calibration kit changeovers and for preserving internal instrument-state and calibration data in computer files. These programs run on a PC connected to Network Analyzer through the GPIB interface. There are three such programs:

- a program for uploading and downloading calibration kit characteristics,
- a program for uploading and downloading the data of a particular calibration, and
- a program for uploading and downloading the internal instrument state.

5.6 Uncertainty Analysis

5.6.1 Reflection-Transmission Method

The term quantifies the indeterminacy in the measurement, and it gives the range of values within the true value lies. It can be defined in an absolute term or as a relative uncertainty, i.e. normalized to the quantity measured (may be expressed as percentage). If a measured variable, e.g. ϵ' , is a function of several independent variables, e.g. $|s_{11}|$, $\arg s_{11}$, $|s_{21}|$, $\arg s_{21}$, thickness, etc., we use the following equations:

$$R = R(x_1, x_2, x_3, \dots, x_n) \quad 5.22$$

where R is the variable for which we want to determine the uncertainty, and x_i , are the independent variables

$$\Delta R = \left[\left(\frac{\partial R}{\partial x_1} \Delta x_1 \right)^2 + \left(\frac{\partial R}{\partial x_2} \Delta x_2 \right)^2 + \dots + \left(\frac{\partial R}{\partial x_n} \Delta x_n \right)^2 \right]^{1/2} \quad 5.23$$

Relative uncertainty is calculated as $\Delta R/R$. Sources of uncertainty in TRM measurements are:

Errors in measuring the magnitude and phase of the scattering parameters.

Uncertainty in sample length.

Uncertainty in reference plane positions.

Line losses and conductor mismatch.

Imperfect calibration, calibration time drift, change in the calibration due to cable flex*.

Gaps between the sample and its holder*.

Coupling to higher order modes*.

* These are often based on estimates.

Additional uncertainties for the two-layer sample:

Acrylic thickness.

Acrylic permittivity.

Acrylic gap.

Uncertainty can be determined from equation 5.23, if S_{11} and S_{21} can be expressed as explicit functions of the scattering parameters. This is not the case for the TRM. Thus, derivatives of interest are obtained by taking implicit derivatives of the scattering parameter equations with respect to the assumed independent variables. The uncertainty due to S_{11} and S_{21} evaluated separately. In this report, we assume that the total uncertainty can be written as

$$\frac{\Delta \varepsilon_{r1}^*}{\varepsilon_{r1}^*} = \frac{1}{\varepsilon_{r1}^*} \cdot \sqrt{\left(\frac{\partial \varepsilon_{r1}^*}{\partial |S_\alpha|} \cdot \Delta |S_\alpha| \right)^2 + \left(\frac{\partial \varepsilon_{r1}^*}{\partial \theta_\alpha} \cdot \Delta \theta_\alpha \right)^2} \quad 5.24$$

$$\frac{\Delta \mu_{r1}^*}{\mu_{r1}^*} = \frac{1}{\mu_{r1}^*} \cdot \sqrt{\left(\frac{\partial \mu_{r1}^*}{\partial |S_\alpha|} \cdot \Delta |S_\alpha| \right)^2 + \left(\frac{\partial \mu_{r1}^*}{\partial \theta_\alpha} \cdot \Delta \theta_\alpha \right)^2} \quad 5.25$$

where $\alpha = 11$ or 21 , superscript * stands for prime (') or double prime(''), $\Delta \theta$ is the uncertainty in the phase of the scattering parameter, $\Delta |S_\alpha|$ is the uncertainty of the magnitude of the scattering parameter. Values of $\Delta \theta$ and $\Delta |S_\alpha|$ are given in the System Performance sheet for HP 8720C. Uncertainties in the permittivity and permeability due to the uncertainty in the sample length are neglected in this paper. From equations 5.24 and 5.25, it can be derived that:

$$\frac{\partial \varepsilon_{r1}}{\partial |S_\alpha|} = \frac{v_\beta}{A+B} \cdot \exp(j\theta_\alpha) \quad 5.26$$

$$\frac{\partial \varepsilon_{r1}}{\partial \theta_\alpha} = j|S_\alpha| \cdot \frac{\partial \varepsilon_{r1}}{\partial |S_\alpha|} \quad 5.27$$

where

$$A = \left(\frac{\partial u_\beta}{\partial \Gamma_1} - S_\alpha \cdot \frac{\partial v_\beta}{\partial \Gamma_1} \right) \cdot \frac{-Z_o Z_1^3}{\eta_o^2 \mu_{r1} (Z_1 + Z_o)^2} \quad 5.28$$

$$B = jd_1 T_1 \cdot \frac{k_o Z_1}{2\eta_o} \left(\frac{\partial u_\beta}{\partial T_1} - S_\alpha \cdot \frac{\partial v_\beta}{\partial T_1} \right) \quad 5.29$$

and

$$\beta = \begin{cases} 1 & \text{for } \alpha = 11 \\ 2 & \text{for } \alpha = 21 \end{cases} \quad 5.30$$

Similarly,

$$\frac{\partial \mu_{r1}}{\partial |S_\alpha|} = \frac{v_\beta}{A+B} \cdot \exp(j\theta_\alpha) \quad 5.31$$

$$\frac{\partial \mu_{ri}}{\partial \theta_\alpha} = j|S_\alpha| \cdot \frac{\partial \mu_{r1}}{\partial |S_\alpha|} \quad 5.32$$

where

$$A_1 = \left(\frac{\partial u_\beta}{\partial \Gamma_1} - S_\alpha \cdot \frac{\partial v_\beta}{\partial \Gamma_1} \right) \cdot \frac{2Z_o Z_1}{\mu_{r1} (Z_1 + Z_o)^2} \cdot \left[1 - \frac{\varepsilon_{r1} Z_1^2}{2\eta_o^2 \mu_{r1}} \right] \quad 5.33$$

$$B_1 = -jd_1 T_1 \cdot \frac{k_o \varepsilon_{r1} Z_1}{2\eta_o \mu_{r1}} \left(\frac{\partial u_\beta}{\partial T_1} - S_\alpha \cdot \frac{\partial v_\beta}{\partial T_1} \right) \quad 5.34$$

Equations 5.24 to 5.34 cannot be solved directly for $\hat{\varepsilon}_1$ and $\hat{\mu}_1$ of the TS and iterative solutions have to be found.

5.6.2 Reflection – Two Positions Method

A similar analysis to that of the RTM method can be performed. Derivation of the equations for this case is in progress.

5.7 Measurement Results

5.7.1 Low Loss Materials (Batch 1)

Till now all measurements were performed with the RTM. Three low loss dielectric samples and one magnetic sample were measured, and the results are illustrated in Figs 5.5 to 5.8.

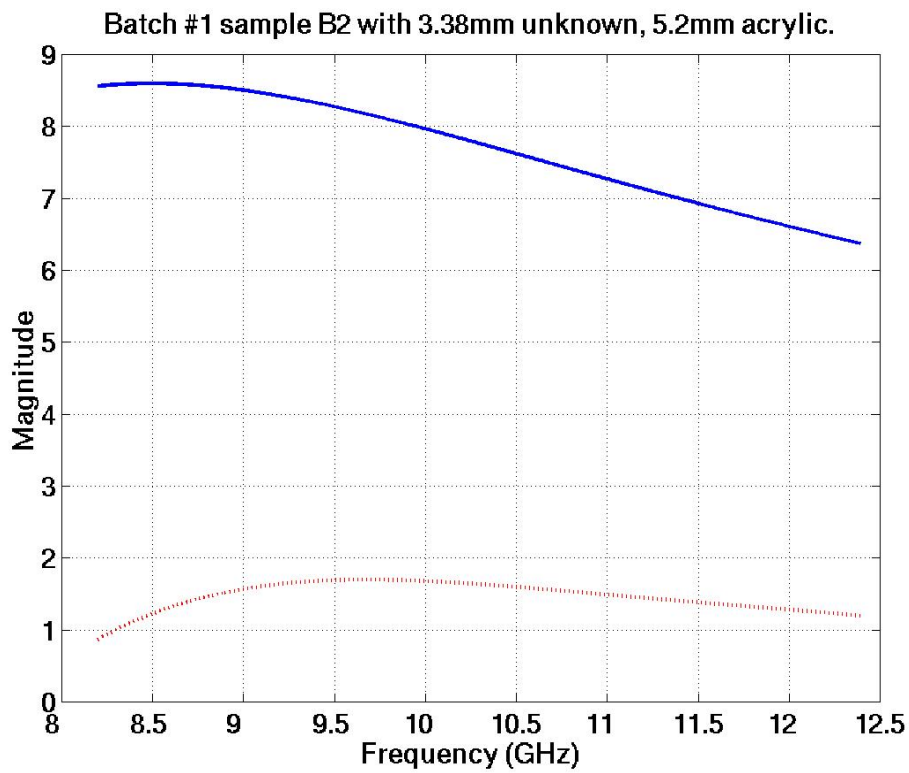


Figure 5.5. The dielectric constant (blue) and loss factor (red); sample B2

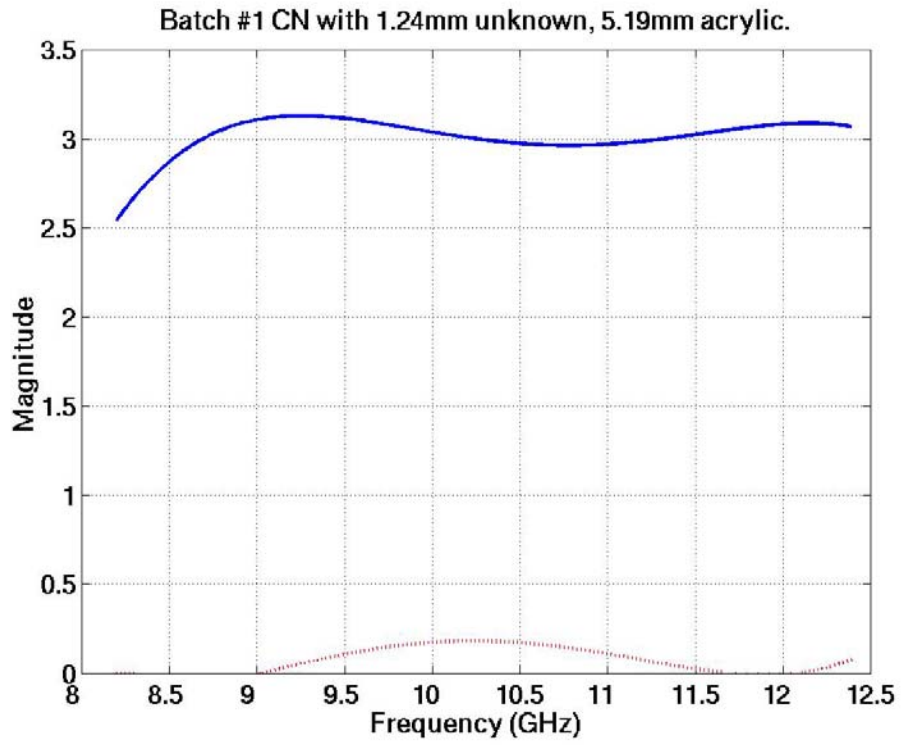


Figure 5.6. The dielectric constant (blue) and loss factor (red); sample CN

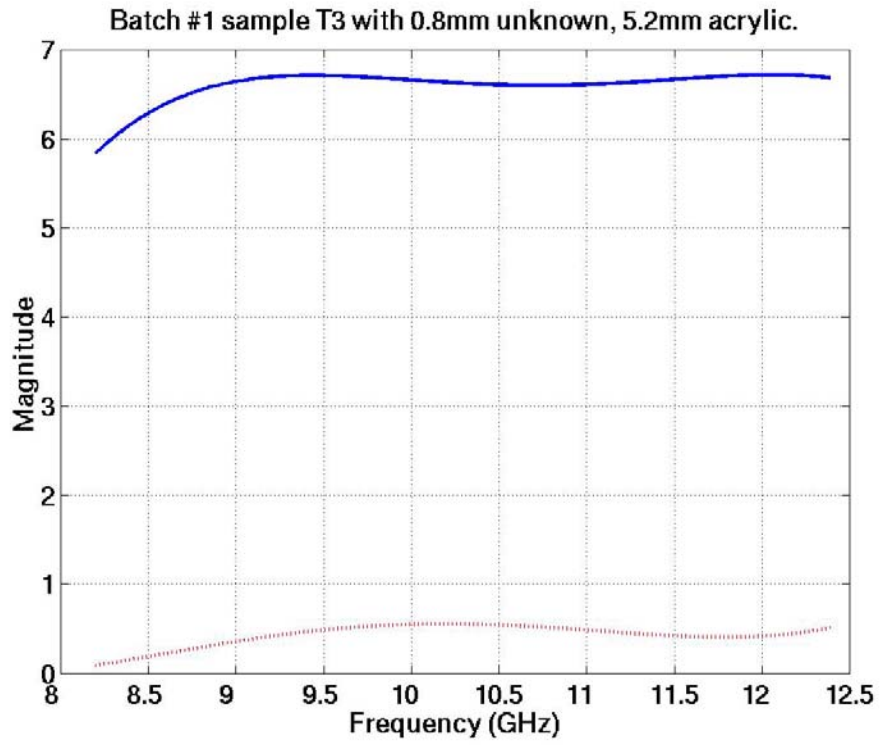


Figure 5.7. The dielectric constant (blue) and loss factor (red); sample T3

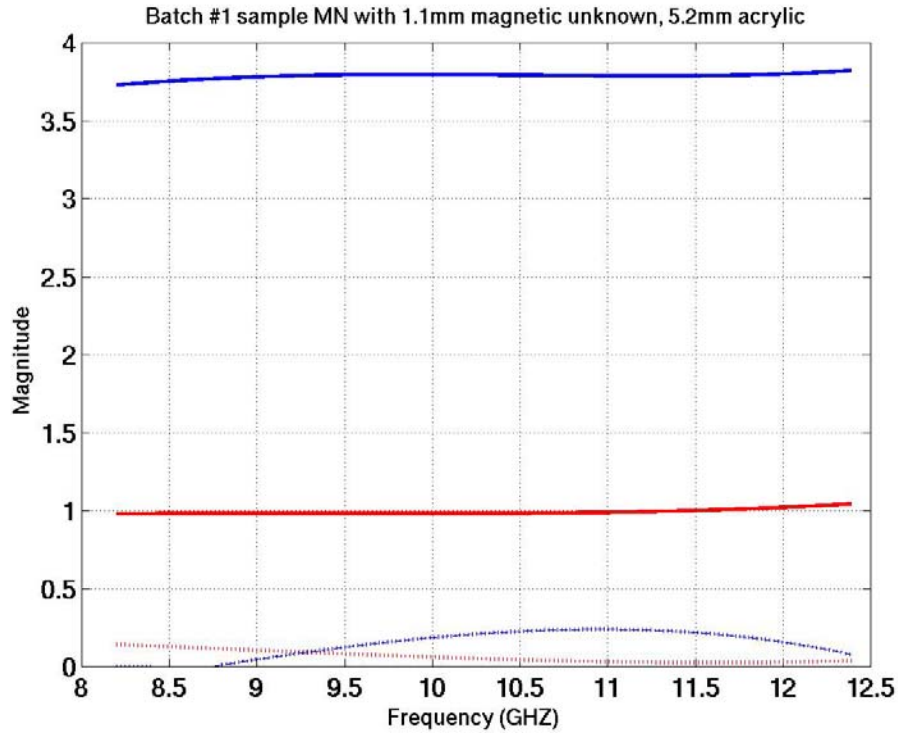


Figure 5.8. The dielectric constant (dark blue, dielectric loss factor (pale blue), permeability, real part (red) and magnetic loss factor (pale red); sample MN

5.7.2 PPy Materials

Six samples containing various percentage of PPy, whose properties are summarized in Table 1, were also measured, and their permittivity is shown in Figs. 5.9 to 5.13. On all graphs, the dielectric constant is shown by solid blue line and the loss factor is shown as dotted red line. In Figs. 5.8 to 5.12, the upper dotted lines show the loss factor that includes the static (DC) conductivity, and the lower lines show only the dielectric loss. Polynomials that approximate the curves are in the form given in equation 5.35, and are summarized in Table 5.2.

$$\epsilon(f) = Af^4 + Bf^3 + Cf^2 + Df + E \quad 5.35$$

Table 5.1. . Samples measured, batch of February 2001

PPy PERCENTAGE	CONDUCTIVITY (S/M)	Acrylic thickness (CM)	Sample thickness (MM)
12.4	52.8	5.78	0.22
18.0	10.9	5.78	0.22
24.8	423.5	5.81	0.24
42.0	552.0	5.81	0.30
56.8	801.3	5.81	0.38

The results shown were obtained an iterative optimization procedure, in which a polynomial is fitted to the measured scattering parameters at all frequencies (400 frequency points within the bandwidth). Because of dependence of the uncertainty values of the scattering parameters on the values of the permittivity, lower total uncertainty may be obtained in some cases if only e.g. S_{21} or S_{11} is used rather than both. The optimization procedure allows for selection of weights for the scattering parameters. Proper selection of the weights can only be made after the approximate values are determined so that the implicit evaluation of uncertainty can be performed.

Uncertainty analysis and measurements by the reflection (two-position) method are in progress.

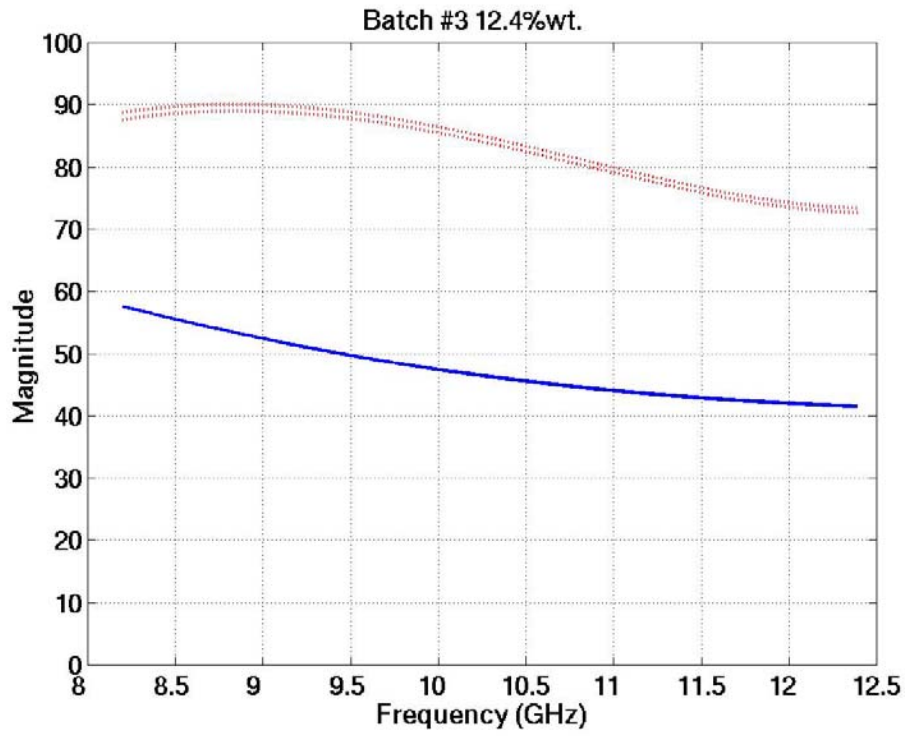


Figure 5.9. Permittivity of 12.4% sample

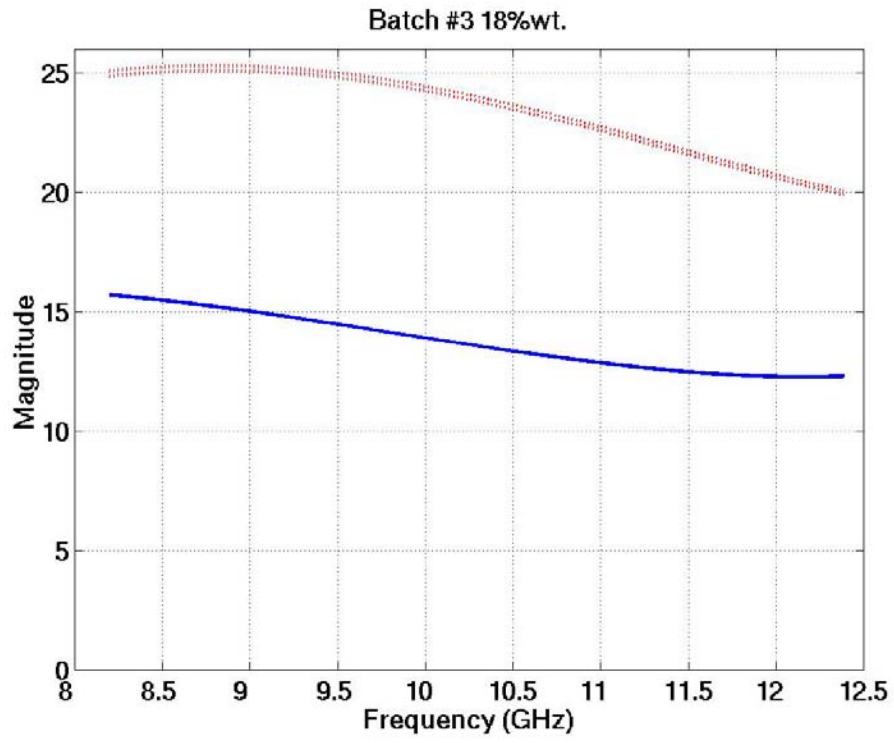


Figure 5.10. Permittivity of 18% sample

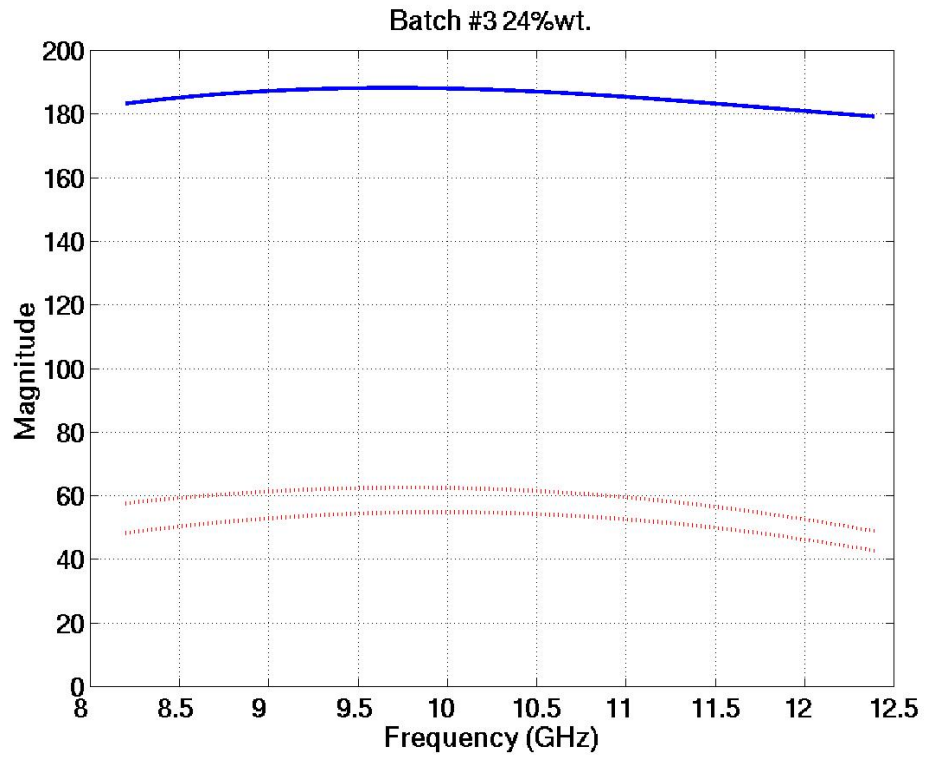


Figure 5.11. Permittivity of 24.8% sample

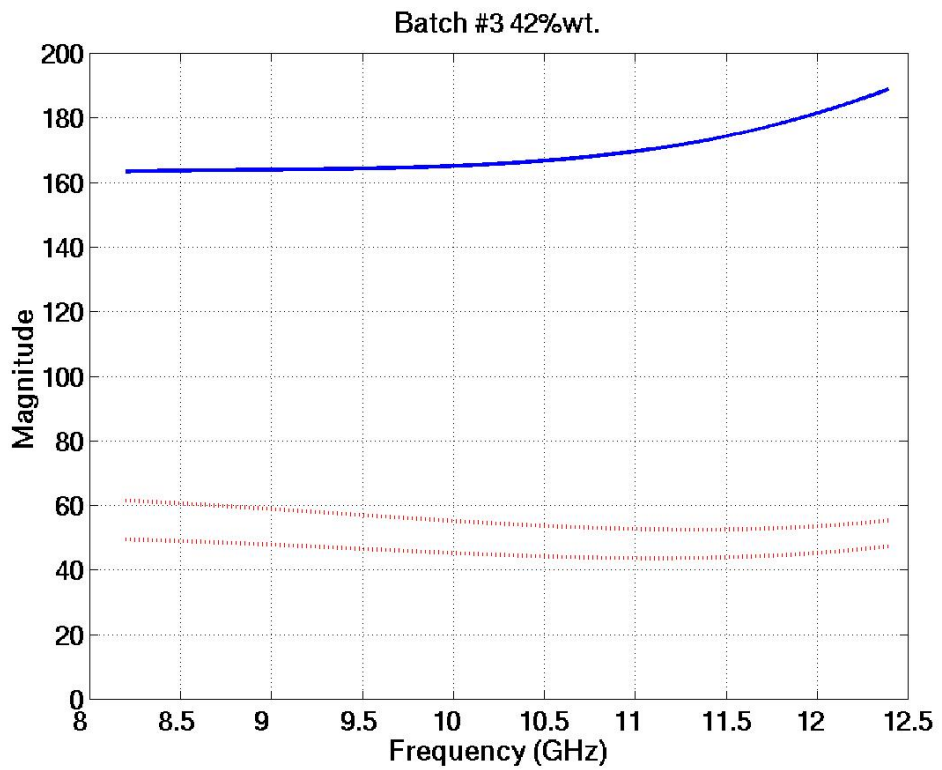


Figure 5.12. Permittivity of 42% sample

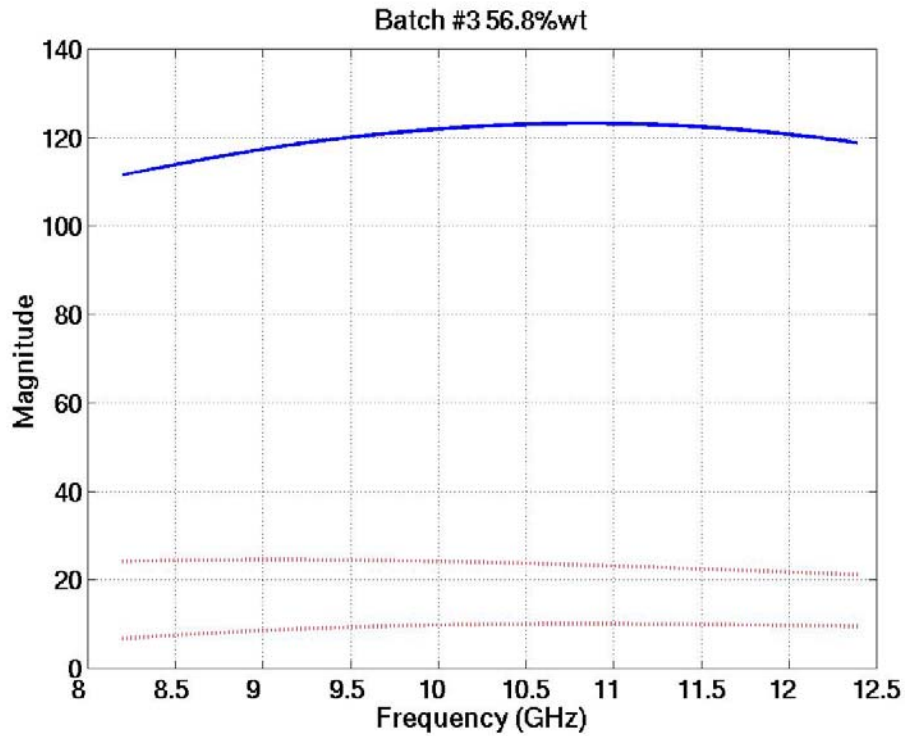


Figure 5.13. Permittivity of 56.8% sample

Table 5.2. Polynomial representation of the material permittivity - coefficients

% weight	ϵ	A	B	C	D	E
12.4	ϵ'	89.33	13.38	-4.467	0.3664	-0.0095
	ϵ''	91.77	-1.979	-10.23	1.337	-0.0472
18.0	ϵ'	2.697	1.906	0.4650	-0.0939	0.0040
	ϵ''	10.27	-1.361	-1.648	0.2180	-0.0074
24.8	ϵ'	15.16	14.04	4.758	-0.6697	0.0226
	ϵ''	32.85	-0.0365	-3.935	0.3978	-0.0099
42.0	ϵ'	45.08	17.66	2.892	-0.6508	0.0305
	ϵ''	-12.33	-7.540	-1.913	0.4035	-0.0180
56.8	ϵ'	11.65	6.735	2.022	-0.1947	0.0036
	ϵ''	2.2442	-1.563	-1.005	0.1338	-0.0044

5.8 Conclusions

In addition to the above mention research uncertainty analysis for the TRM method has been programmed and tested. Code has also been written and tested for the short circuit method and materials measured with both techniques. Development of an iterative procedure to fit the measured permittivity data with Debye relaxation formulas has been started.

Since this section was originally written DRDC Atlantic has established their own measurement facility, using an Agilent 8362B PNA. The code has been upgraded to use all four S-parameters and has been written into a user-friendly GUI format.

5.9 Future Work

Measurement capabilities at other frequency bands need to be developed.

An approximate method for free space measurement of permittivity and permeability is required (to avoid sample deposition on the acrylic and accurate machining required to fit into waveguides, and therefore to accelerate feedback about material properties to the material developers).

Development of uncertainty analysis for permeability analysis.

5.10 References

- (1) Afsar, M. N.; Birch, J. R.; Clarke, R. N. *Proc. IEEE* **1986**, *75*, 183.
- (2) Baker-Jarvis, J.; Janezic, M. D.; Grosvenor, J. H.; Geyer, R. G. "Transmission/reflection and short-circuit line permittivity measurements," NIST, **1993**.
- (3) Baker-Jarvis, J.; Vanzura, E.; Kissick, W. *Microwave Theory and Techniques, IEEE Transactions on* **1990**, *38*, 1096.
- (4) Belhadj-Tahar, N.; Fourier-Lamer, A. *Microwave Theory and Techniques, IEEE Transactions on* **1991**, *39*, 1718.
- (5) Belhadj-Tahar, N.; Fourier-Lamer, A.; de Chanterac, H. *Microwave Theory and Techniques, IEEE Transactions on* **1990**, *2*, 1.
- (6) Busse, G.; Reinert, J.; Jacob, A. F. *Microwave Theory and Techniques, IEEE Transactions on* **1999**, *47*, 297.
- (7) Bussey, H. E. *Proc. IEEE* **1957**, *55*, 1046.
- (8) Champlin, K. S.; Glover, G. H. *J. App. Phys.* **1966**, *37*, 2355.
- (9) Chao, S. *Instrumentation and Measurement, IEEE transactions on* **1986**, *IM-35*, 36.
- (10) Courtney, C. C. *Microwave Theory and Techniques, IEEE Transactions on* **1998**, *46*, 517.

- (11) Courtney, C. C.; Motil, W. *Microwave Theory and Techniques, IEEE Transactions on* **1999**, *47*, 551.
- (12) Domich, P. A.; Baker-Jarvis, J.; Geyer, R. G. *J. Res.* **1991**, *96*, 565.
- (13) Franceschetti, G. *Alta Frequenzia* **1967**, *36*, 757.
- (14) Freeman, M. S.; Nottenburg, R. N.; DuBow, J. B. *J. Phys. E: Sci. Instrum.* **1979**, *12*, 899.
- (15) Friedsam, G. L.; Biebl, M. *Instrumentation and Measuement, IEEE transactions on* **1997**, *46*, 515.
- (16) Galwas, B. A.; Piotrowski, J. K.; Skulski, J. *Instrumentation and Measuement, IEEE transactions on* **1997**, *46*, 511.
- (17) Ghodgaonkar, D. K.; Varadan, V. V.; Varadan, V. K. *Instrumentation and Measuement, IEEE transactions on* **1990**, *39*, 387.
- (18) Goldfarb, R. B.; Bussey, H. E. *Review of Scientific Instrumentation* **1987**, *58*, 624.
- (19) Ligthardt, L. P. *Microwave Theory and Techniques, IEEE Transactions on* **1983**, *MTT-31*, 249.
- (20) Ma, Z.; Okamura, S. *Microwave Theory and Techniques, IEEE Transactions on* **1999**, *47*, 546.
- (21) Mattar, K. E.; Brodwin, M. E. *Instrumentation and Measuement, IEEE transactions on* **1990**, *39*, 609.
- (22) Maze, G.; Bonnefoy, J. L.; Kamarei, M. *Microwave J.* **1990**, 77.
- (23) Ni, E. *Instrumentation and Measuement, IEEE transactions on* **1992**, *41*, 495.
- (24) Nicolson, A. M.; Ross, G. F. *Instrumentation and Measuement, IEEE transactions on* **1970**, *IM-19*, 377.
- (25) Reinert, J.; Busse, G.; Jacob, A. F. *Microwave Theory and Techniques, IEEE Transactions on* **1999**, *47*, 290.
- (26) Sequeira, H. B. *Instrumentation and Measuement, IEEE transactions on* **1990**, *36*, 621.
- (27) Stuchly, S.; Matuszewski, M. *Instrumentation and Measuement, IEEE transactions on* **1978**, *IM-27*, 285.
- (28) Szendrenyi, B. B.; Kazi, K.; Mojzes, I. *Microwave theory and Techniques, Digest* **1988**, *1*, 743.
- (29) Tantot, O.; Chatard-Moulin, M.; Guillon, P. *Instrumentation and Measuement, IEEE transactions on* **1997**, *46*, 519.
- (30) Umari, M. H.; Chodgaonkar, K. D.; Varadan, V. V.; Varadan, V. K. *Instrumentation and Measuement, IEEE transactions on* **1991**, *40*, 19.
- (31) Weir, W. B. *Proc. IEEE* **1974**, *62*, 33.

6. Absorber Design: The Genetic Algorithm

Absorber design has been reviewed in Section 2.6. The design of absorbers using the genetic algorithm is reviewed here. The workings of the genetic algorithm are described and the optimisation of some absorbers is reported.

6.1 Optimisation of Jaumann Layers: Genetic Algorithm

The above optimization methods have produced significant increases in bandwidth and reduction in reflectivity. These methods, however, do not produce the optimal absorbing material, based on a number of factors such as minimum thickness or weight, or whether the solution is a local or global minimum. For these reasons, the Genetic Algorithm (GA) has been investigated as an optimization technique for RAM. Use of the GA is explored in this section and the GA method is reviewed in Section 5.

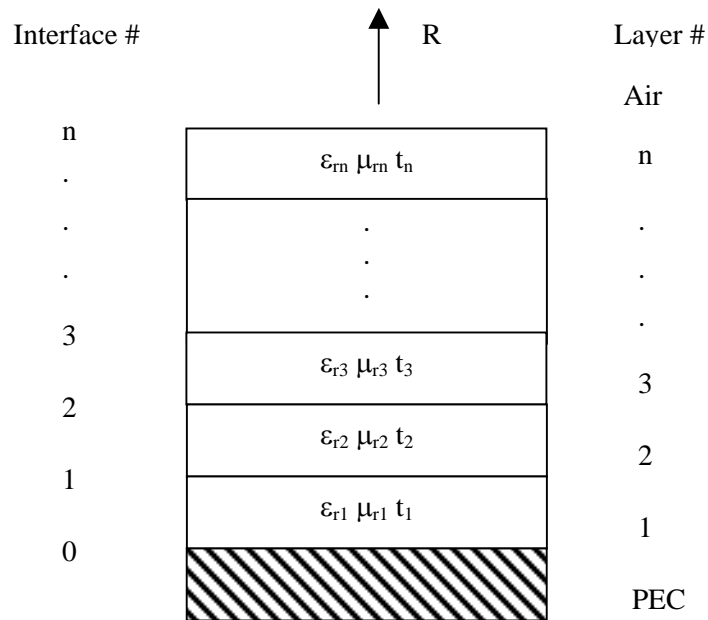


Figure 6.1. Reflectivity from Jaumann absorber layers

A review of the use of genetic algorithms in engineering electromagnetics provides a good description of the genetic algorithm with some examples including the design of microwave absorbers.^[1] Genetic Algorithms were first used in 1993 for the optimization of Jaumann absorbers^[2-4] and built on the approaches used for the optimal control method.^[5] A set of available materials, their frequency dependent optical properties (permittivity and permeability), and the layer thicknesses were used to define a population of absorbers. A genetic algorithm was used to optimise the

absorber design against objective functions including reflectivity, thickness and weight. Both TE and TM polarisations of the reflection coefficient were calculated as well, in order to optimise the absorber as a function of incident angle as well. The reflectivity was calculated using a recursion relationship and the permittivity, permeability of the materials. Pareto fronts for the thickness vs reflectivity were presented.^[6] Several Pareto Genetic Algorithms were compared with the non-dominated sorting genetic algorithm, NSGA, producing the best results.^[6]

The genetic algorithm has also been used to optimise Jaumann absorbers based on transmission line theory.^[7-11] Absorber bandwidth was shown to increase rapidly as a function of the number of resistive layers before asymptotically approaching the maximum bandwidth as the layer number approached infinity.^[11] The optimum sheet resistance profile, assumed to have an exponential form,^[12] was shown to have a sigmoid form with the resistance of the outer layers asymptotically approaching a maximum sheet resistance.^[7,8,11] In these studies the bandwidth was studied as a function of both polarisations so that the absorbers could be optimized for incident angle as well. The bandwidth was defined as

$$BW = 2 \frac{(f_u - f_l)}{(f_u + f_l)} \quad 6.10$$

and the objective function for the combined polarisations as

$$OF = \frac{BW_{||} BW_{\perp}}{(|BW_{||} - BW_{\perp}| + 1)} \quad 6.11$$

The optimised bandwidth for both polarisations was found to be less than that for normal incidence or one polarisation. At oblique incidences up to about 30 degrees the optimum bandwidth was found to remain fairly constant (near the value at normal incidence) before decreasing.^[7] It was found that a two-stage strategy was useful in optimising absorber design. In the first stage an objective function based on the sum of the reflectivity below -20 dB was used to ensure that the -20 dB bandwidth was non-zero. Then in stage two, objective function sought to maximize the bandwidth and ensure that the reflectivity was still below -20 dB.^[7] Absorbers with a protective skin were also optimised^[7] and it was found that with proper choice of the outer layer material the absorber acted as if it had another resistive sheet and therefore had a wider bandwidth. With more than two resistive sheets, shinned absorbers could not be optimised below the -20 dB reflectivity limit, though the bandwidth could be improved for higher reflectivity targets.

The design of active (dynamic) radar absorbers has been investigated by using the genetic algorithm to optimise the absorption over different frequency bands by varying the sheet resistance, the spacer thickness or the spacer permittivity.^[7]

Resistive sheets with capacitive properties have been used for making absorbers.^[13] The optimal design of resistive-capacitive material based microwave absorbers has been studied using the genetic algorithm and transmission line theory.^[14,15] The use of

adaptive mutation has been explored to get out of local minima and to protect designs that are near the global minimum.^[16] The genetic algorithm was also applied to the design of magnetic Dallenbach layers.^[17]

A unique absorber design has been proposed and optimised using a genetic algorithm, where patches of material are organised to form a sheet.^[18] These patches are either of the same material with different thicknesses or different materials with the same or different thicknesses.

A variant of the genetic algorithm, the microgenetic algorithm has been used for optimising frequency selective surfaces and circuit analog absorbers.^[19-21] The microgenetic algorithm uses a small randomly generated population for optimisation in the usual manner for a genetic algorithm. Convergence occurs in a few generations and the fittest individual is added to those from previous generations. A new population is then randomly selected. Narrow band Salisbury Screens with circuit analog patterns replacing the resistive sheet have also been considered.^[22-24]

6.2 The Genetic Algorithm

The Genetic Algorithm is a stochastic optimization routine based on Darwin's theory of evolution and genetics.^[25,26] An evolutionary process arrives at the optimized solution over several iterations (generations), by selecting only the best (the fittest) solutions and allowing these to survive and form the basis for calculating the next round of solutions. In this manner the optimization routine evolves the initial solutions to the optimum. Table 6.1 gives an algorithm for a simple genetic algorithm.

Table 6.1. Algorithm for a simple genetic algorithm.

STEP	ACTION
1	Initialize Population of size N, and Rank against fitness of objective functions
2	Start generation loop
3	Select fittest members of population for mating
4	Crossover properties from parents to create offspring
5	Mutate offspring
6	Rank offspring and parents, select fittest individuals for new population of size N.
7	Check for convergence
8	End generation loop

6.2.1 Initiation

In the first step a population of individuals of size N is randomly generated. Each individual is described by a set of variables (genes), which give rise to the overall characteristics of the individual. The set of variables for an individual is termed the chromosome. The chromosome of an absorber is made up of the permittivity, permeability and thickness of each layer of the absorber. The genes of an individual can be coded in a binary form, however, it has been found that using real variables leads to a faster algorithm since the binary format does not need to be coded and decoded.^[7]

An objective function uses the chromosome (variable description) of an individual in order to calculate its characteristics (ie a solution for optimization). The characteristics are then used as a monitor of the fitness of an individual. Reflectivity, bandwidth and absorber thickness are examples of objective functions that can be used in absorber optimization. Generally the designer is trying to achieve the lowest reflectivity over the widest frequency range for the thinnest absorber possible.

The final step for the initial population is to rank the fitness of the individuals. This is accomplished by comparing the fitness of each individual. If there is only one objective function a simple sort of the fitness will rank the individuals. Now the initial population is created and the evolutionary loop is ready.

6.2.2 Selection

The first step in evolution is to select from the population members for mating so that their genes carried down to their children in the next generation. Darwin's theory of evolution states that the fittest members of a population will most likely to survive and hence propagate their genetic information to future generations. This has led to several selection strategies that favour the fittest members of the population.

6.2.2.1 Decimation Selection

In this strategy the fitness obtained from the objective function is used to rank the superiority of the individuals in a population. Any individuals with fitness lower than a cut-off point are dropped from the population and the remainder are randomly paired for mating. The disadvantage of this simple method is that genes contained in the unfit individuals are lost early on and diversity is lost. This may cause the algorithm to converge to a good solution as determined by the good traits of the initial population, however, it may not be the optimal solution that may have been achieved by maintaining a diversity of genes in the population. This problem is circumvented in the following strategies.

6.2.2.2 Roulette Wheel Selection

The roulette wheel strategy is stochastic and is based on proportional selection. The probability of selecting an individual is determined by the relative fitness of an individual, (f_i), to the fitness of the whole population, $\sum_i f_i$.

$$p = \frac{f_i}{\sum_i f_i} \quad 6.12$$

The probability of selecting an individual is then assigned a proportional space on a roulette wheel, so that all individuals have a chance to be selected with the fittest individuals having the highest probability of selection. Mating pairs are then obtained from two spins of the wheel.

6.2.2.3 Tournament Selection

Individuals are selected for mating by randomly picking several members from the population and comparing their fitness. The individual with the best fitness is then selected to become one of a mating pair. This strategy will drop the lowest ranked individual from the population, as it can never win the tournament. In all these strategies individuals may be selected for mating more than once.

6.2.3 Crossover

This is one of the operators in the genetic algorithm where the objective is to improve the fitness of the population. The principle is along the lines of genetics where the children of a mating pair will have chromosomes containing genes from each parent. For each mating pair a pair of children is created and these children will have a mix of the parent's genes as determined by the crossover routines and the crossover probability. There are a number of routines for producing crossovers at different points within the chromosome and each crossover event is controlled by a crossover probability. Generally a random number is chosen for the crossover event. If this is number is less than the crossover probability then a gene sequence from parent 1 is given to child 2 and the sequence from parent 2 is given to child 1. The result is children with genes from each parent and potentially a more fit population.

6.2.4 Mutation

The mutation operator is a means of introducing random variations into the population in order to explore new regions of the solution space. A consequence of this is that genes, which were lost earlier in the optimization, are brought back into the genetic makeup of the population. The mutation operator acts in response to a mutation probability, randomly changing a gene to a new value. The mutation probability needs to be kept fairly low ($p_{\text{mutation}} = 0.01-0.1$) so that chromosomes with good fitness are

not quickly lost. The mutation operator is applied to the children from the crossover step.

6.2.5 The New Generation

There are several methods for obtaining the individuals that will form the new population, each of which has implications for the convergence rate and robustness of the genetic algorithm.

6.2.6 Simple Genetic Algorithm

In the simple genetic algorithm, as outlined above, the children at each generation completely replace the parents in the population. A drawback of this technique arises as a result of the probabilistic nature of the selection, crossover, and mutation operators. It is quite possible that the fitness of the children may be lower than that of their parent's generation.

6.2.7 Elitism

Elitism addresses the problem of the children's generation having a lower fitness than their parents. If the highest-ranked individual in the children's generation has a lower fitness than the highest-ranked individual in the parent's generation, then the highest-ranked parent is copied into the new population. The process of preserving the best is elitism and ensures that the fitness increases.

6.2.8 Steady State Genetic Algorithms

The steady state genetic algorithm replaces a portion of the population at each generation with the children. This means that individuals can exist in the population over several generations. A number of techniques exist for the replacement of a portion of the population. The percentage replacement is a variable and various methods of selecting individuals for replacement exist. Replacement of the individuals with the lowest fitness in the parent generation adds elitism to the steady state algorithm.

6.2.9 Pareto Genetic Algorithms

The techniques discussed above are used to find the global optimum solution for a single objective. Often in design work several objectives need to be optimized and it is useful to be able to compare one objective against another. Solutions that present one optimized function against another optimized function are said to be Pareto optimal. Consider the design of a radar absorber. A design criterion will be the minimum thickness while a second criterion will be minimum reflectivity over a frequency band. The optimized result of both of these objective functions will be a line of points (the Pareto front) where for a given reflectivity, there will be no absorber design that is thinner. Armed with this information the designer can explore the trade-

offs that will satisfy the design requirements. Any point that is not on the Pareto front is either not feasible or is an inferior design.

6.3 RAM Design using Resistive Sheets and the Genetic Algorithm

The theory for using determining the reflectivity from resistive sheets is given in sections 2.4 and 2.5.

The absorbers studied in this work consisted of resistive sheets separated by dielectric spacers and a perfect electrical conductor, PEC, for backing. The basic design was evaluated with and without protective layers, where the protective layer was another sheet of the spacer material. Symbolically the absorber designs are shown below, with S_N/R_N forming a spacer/resistive sheet pair. The subscript N refers to the Nth layer.

PEC/ $S_1/R_1/S_2/R_2\dots/S_N/R_N$ /air	unprotected
PEC/ $S_1/R_1/S_2/R_2\dots/S_N/R_N/S_{N+1}$ /air	protected

Spacers had a relative permittivity of $\epsilon_r = 1.0, 1.1$ and 2 , and the thickness of the spacers was calculated so as to center the absorption resonance at 10 GHz. For a spacer with $\epsilon_r = 1.0$, a quarter wavelength separation is required between resistive sheets. As the spacer permittivity increases, the thickness used is $\frac{d}{\sqrt{\epsilon_r}}$. The

thickness of the protective sheet was also a quarter wavelength.

Typically a population of 100 absorbers was optimised for 100 generations with a tournament using 2 participants. The cut-off reflectivity was set at -20 dB. A bandwidth objective function was found to produce absorbers with the widest bandwidth. An assumption has been made that the resistive sheet is very thin.

Reflectivity profiles for 1-7 layer absorbers are shown in Figure 6.2. The absorber designs for these reflectivity curves were produced using the bandwidth objective function (Equation 2.29). There is one fringe (interference minimum) for each resistive sheet in the absorber, and none of the fringes cross the -20 dB reflectivity cut-off. The resistive sheet information pertaining to these absorber designs are summarised in Appendix 4, Tables 4-12.

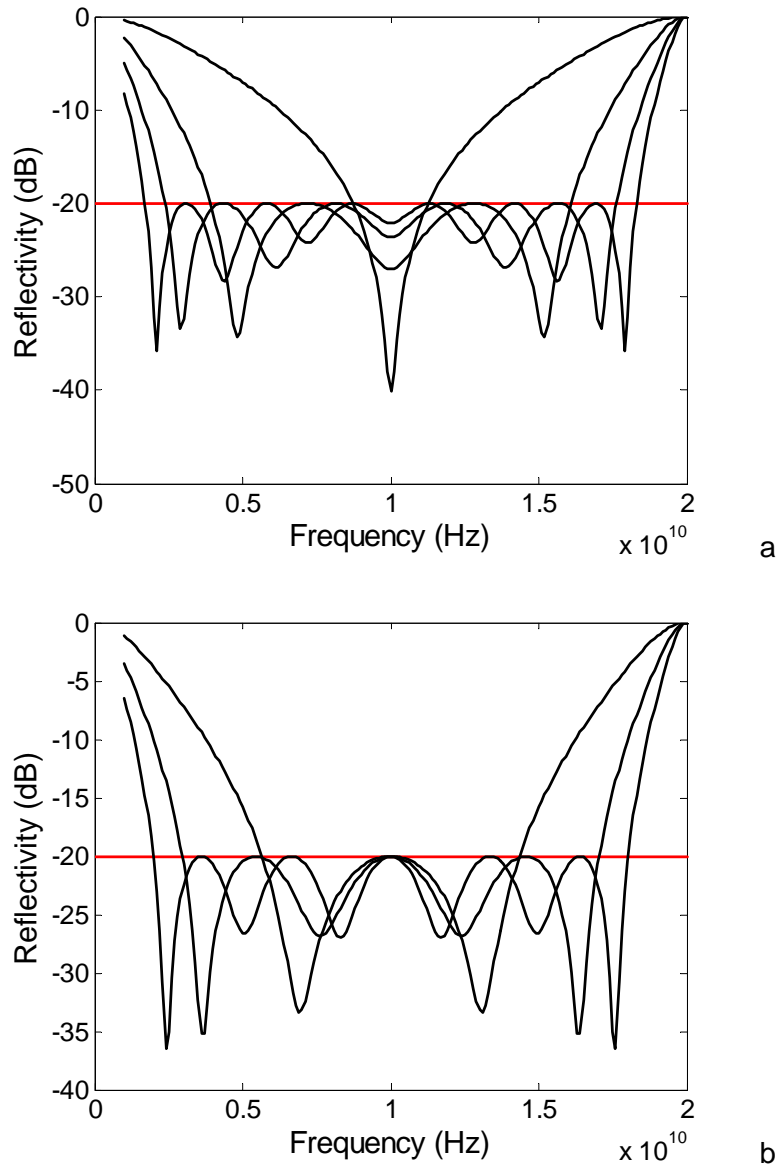


Figure 6.2. Reflectivity of different absorbers over the frequency range for $N= 1, 3, 5,$ and 7 (a) and $N= 2, 4,$ and 6 (b). These absorbers were optimised using the Bandwidth objective function. ϵ_r spacer = 1.0 .

The bandwidth increase as a function of the number of resistive sheets is shown in Figure 6.3. The bandwidth increases with the number of resistive sheets and approaches the maximum bandwidth. The maximum achievable bandwidth, calculated using Eq 2.29 and a frequency span of 1-20 GHz, is about 1.81. The 7 layer absorber design therefore has a bandwidth that is about 90% of the maximum while

the Salisbury screen only offers coverage of about 14% for the frequency range. Absorber thickness is shown in Table 6.2.

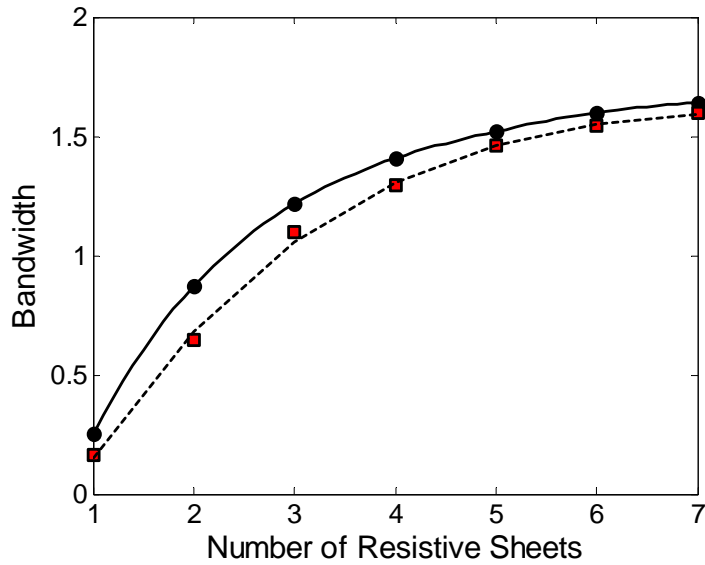


Figure 6.3. Bandwidth of the absorber increases with the number of resistive sheets, N and approaches the maximum bandwidth, (1.81). The bandwidth objective function (solid line) converges on absorber designs with larger bandwidths than does the reflectivity objective function (dashed line). ϵ_r spacer = 1.0.

Table 6.2. Absorber thicknesses and fractional bandwidths.

LAYERS	1	2	3	4	5	6	7
Fraction of Max bandwidth	0.14	0.48	0.67	0.78	0.84	0.89	0.91
Absorber Thickness* (mm)	7.5	15	22.5	30	37.5	45	42.5

* Using a center frequency of 10 GHz and a relative permittivity of 1.0.

The bandwidth of an absorber is a function of the sheet resistance. For $N=1$, the Salisbury screen, the bandwidths all lie on a curve shown in Figure 6.4. For designs below the optimum, there are two values for the sheet resistance that will produce an absorber with the same bandwidth. The different objective functions produced different designs and these are indicated in Figure 6.4. The maximum bandwidth is accurately determined by the bandwidth objective function and has a value of 0.254 for a sheet resistance of $369.3 \Omega/\text{sq}$. The minimum reflectivity occurs at a slightly higher sheet resistance ($376.7 \Omega/\text{sq}$) with a bandwidth of 0.252.

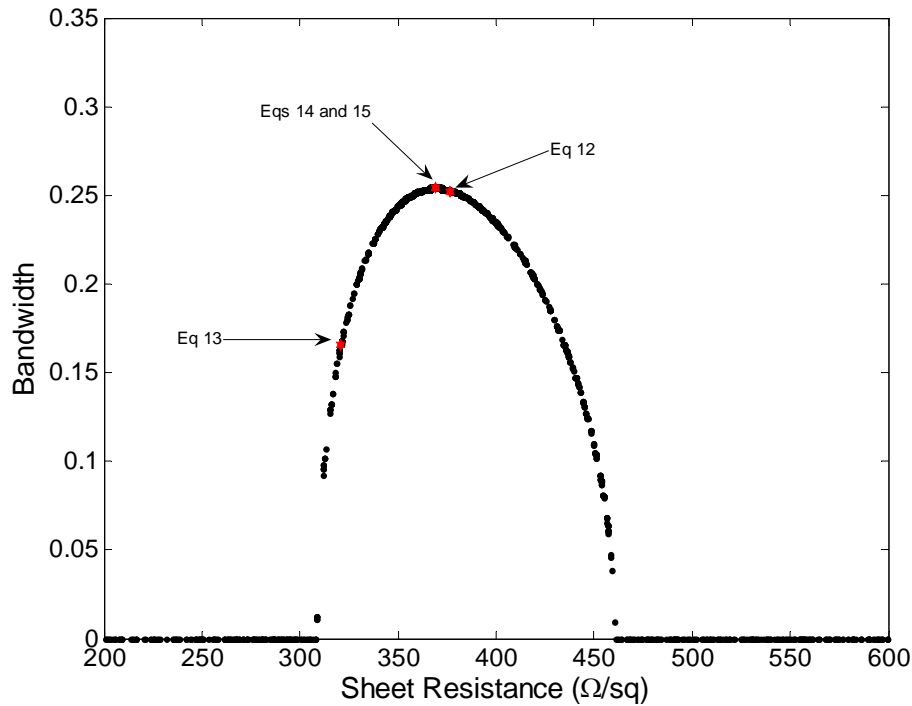
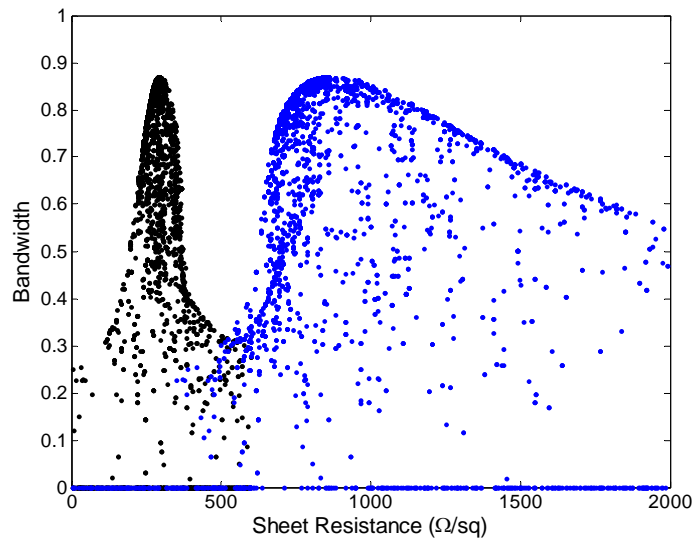
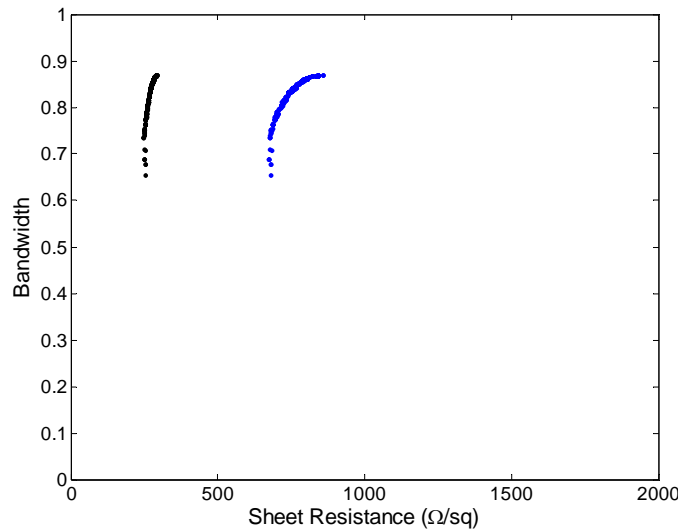


Figure 6.4. Bandwidth as a function of sheet resistance for a Salisbury Screen as determined using the bandwidth objective function. The maximum bandwidth for this absorber is about 0.25 and occurs at a slightly lower sheet resistance (369 Ω/sq) than that which yields the minimum reflectivity (ie 377 Ω/sq), ϵ_r spacer = 1.0.

Adding a second layer to the absorber ($N=2$) increases the complexity of the system. The possible bandwidth solutions to different absorber designs no longer fall onto a curve, but cover a region of space, Figure 6.5. Significant bandwidth is achieved over a narrow distribution of R_1 values and a wider distribution of R_2 values. These results indicate that there are many absorber designs with equal merit (ie with the same bandwidth). The genetic algorithm converges on designs to the lower side of the sheet resistance distribution as shown in Figure 6.5b for the 10th generation, and it is observed that the optimal value is being approached at the top of the curve. The genetic algorithm optimization is stochastic in nature, so premature termination of an optimization will produce different results.



a

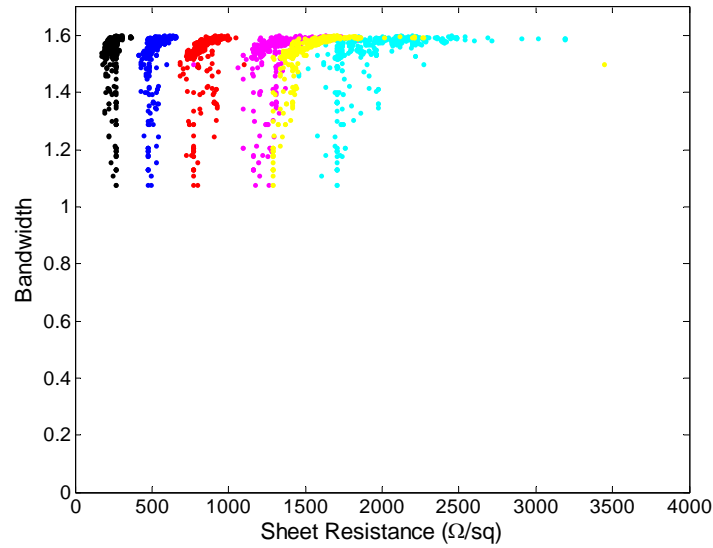


b

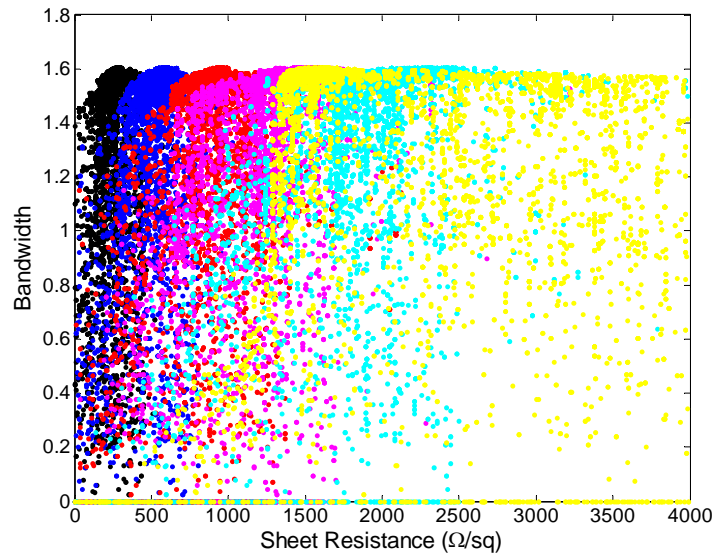
Figure 6.5. Bandwidth as a function of sheet resistance for a 2-layer Jaumann absorber as determined using the bandwidth and reflectivity objective functions (Eq 13). Significant bandwidth is achieved for a small range of R_1 (Black dots) compared to R_2 (Blue dots), the resistive sheet at the air/absorber interface. The maximum bandwidth for this 2-layer absorber is 0.87. Figure 6.5a includes all absorber designs for generations 1-10 while Figure b shows only generation 10. ϵ_r spacer = 1.0.

For larger N absorbers, the solution space for the resistance increasingly overlaps and there is a lack of a pronounced maximum in the resistance profiles, Figure 6.6. It is possible to see in Figure 6.6b that there are absorber designs where the sheet resistances near the PEC interface are larger than those closer to the air interface. As a result there is the potential for absorber designs to arise where the resistance profiles

do not steadily increase toward the air/absorber interface. This is observed in Figure 6.6a, where the yellow points, representing the sheet resistance of the sixth layer, are observed to peak at a lower resistance than the fifth layer (light blue points). Such designs are successful, resulting in wider bandwidth absorbers. It is surmised that this inversion in the resistance profile occurs as a form of impedance matching between the absorber and air.



a



b

Figure 6.6. Resistance profile for a 6 layer Jaumann absorber optimised using the reflectivity and bandwidth objective functions. Generation 4 (a), and 1-50 (b). ϵ_r spacer = 1.0.

6.3.1 Front Protective Layer

The absorbers discussed so far are not very rugged and a more practical design would place a protective layer at the air/absorber interface. This would limit damage to the first resistive sheet or simulate an absorber incorporated into a structural material.

A serendipitous finding is that the absorber bandwidths are greater for those absorbers with a protective layer than those without, Figure 6.7. The difference for this arrangement is not large and decreases as N increases.

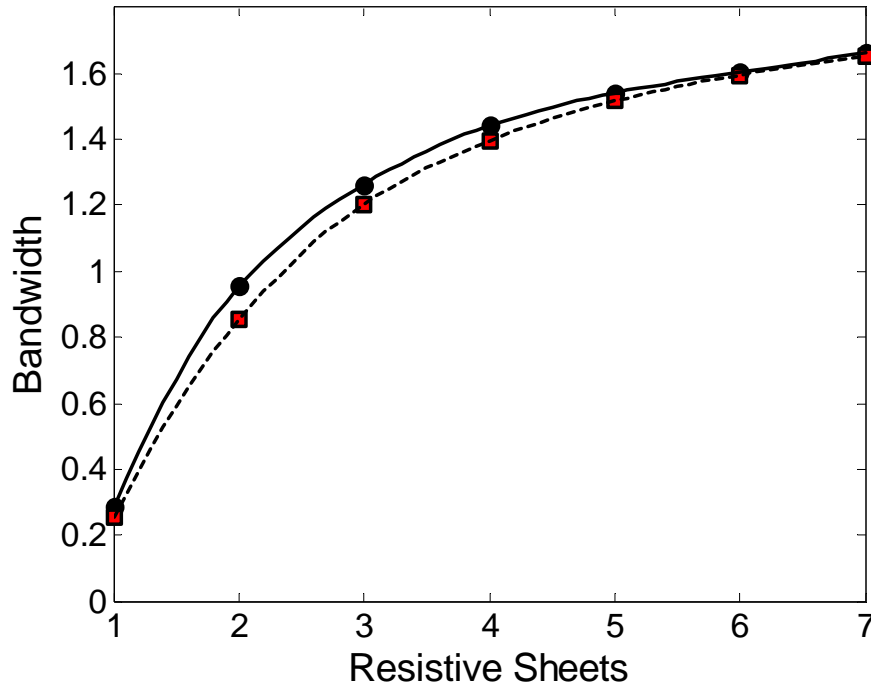


Figure 6.7. Bandwidth improvement as a function of a protective layer at the air/absorber interface. ϵ_r spacer = 1.1. Absorbers optimised using the bandwidth objective function. Solid line absorber with protective layer, dashed line absorber without.

The maximum bandwidth for absorbers with a protective layer is satisfied for a range of R_l , Figure 6.8. For a Salisbury screen, the bandwidth as a function of sheet resistance curve is flat at the maximum bandwidth. This flat region exists for higher order absorbers so that for $N=7$, the maximum bandwidth is achieved for $200 \leq R_l \leq 800$. The optimized resistance profile for an $N=7$ layer absorber with protective layer is shown in Figure 6.9. The reflectivity profiles for this absorber with fixed values of R_l all display the same bandwidth for the above R_l range, though the shape of the reflectivity curves vary below the cut-off. The protective layer appears to no other affect on absorbers with this permittivity.

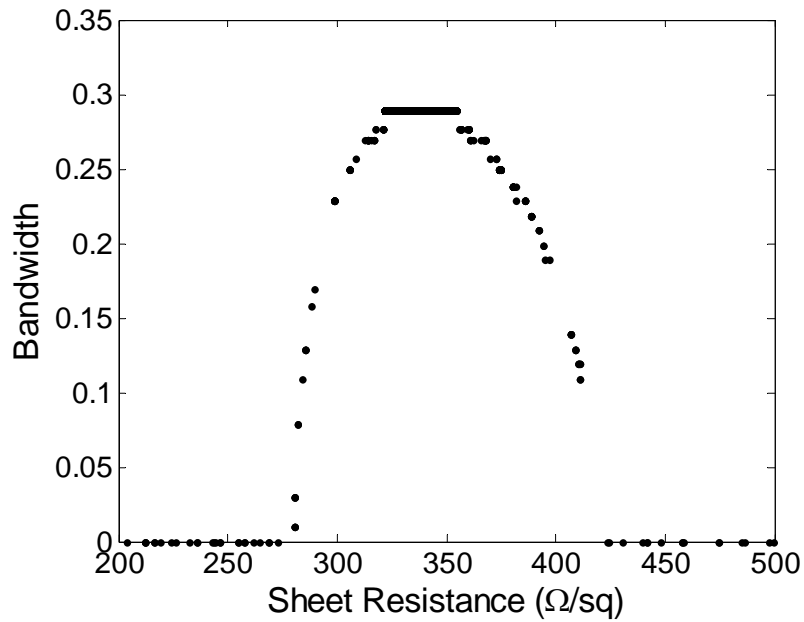


Figure 6.8. The maximum bandwidth is achieved over a wide range of sheet resistances, even for the Salisbury Screen, when a protective layer is placed at the air/absorber interface. ϵ_r spacer = 1.1, bandwidth objective function.

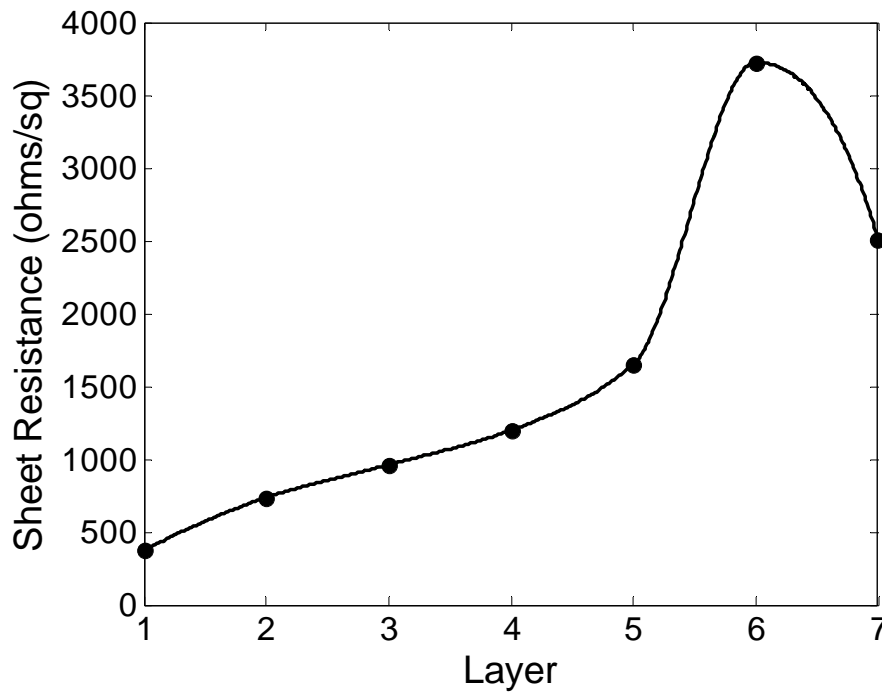


Figure 6.9. The optimised resistance profile for a seven layer absorber with a protective layer. ϵ_r spacer = 1.1.

6.3.2 Spacer Permittivity

For structural absorbers the resistive sheets will be embedded in a matrix (the spacer) where the permittivity is greater the 1.0 or 1.1. Absorber designs with and without protective layers were optimized using the bandwidth objective function. For Salisbury screen designs with no protective layer, increasing permittivity causes a decrease in the bandwidth, Figure 6.10. The bandwidth vs sheet resistance curves are similar to those seen for other Salisbury screen designs, Figure 6.11 a.

The solution space for the higher permittivity, $\epsilon_r = 2$, two-layer absorber design is similar in shape to the lower permittivity absorber Figures 6.11b and 6.4a, respectively. The higher permittivity absorber covers a different resistance range with much larger values of R_2 . For a three-layer absorber, the value of R_3 never peaks even when it is permitted to range up to 50 k Ω /sq, Figure 6.12. Higher order absorbers also fail to converge and their bandwidth remains near 1.0, Table 6.2. The bandwidth of this absorber is smaller than the lower permittivity absorbers.

For a permittivity of 3, the same trend is observed, with smaller bandwidths. An interesting feature is noted, that for absorbers with more layers, the genetic algorithm converges on designs where the outer layers replicate the N=2 design. The resistive sheet adjacent to these last two layers is often very conductive, acting as a short circuit.

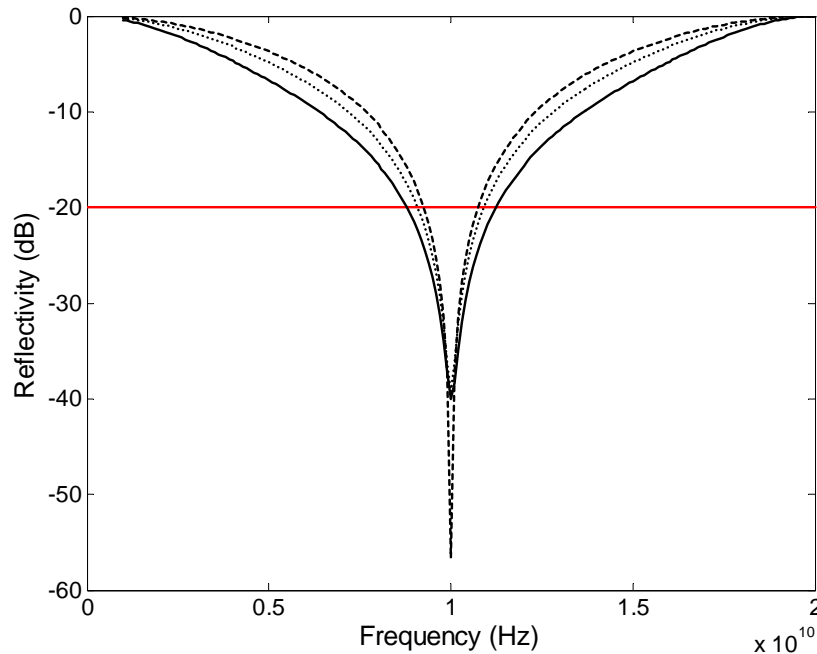
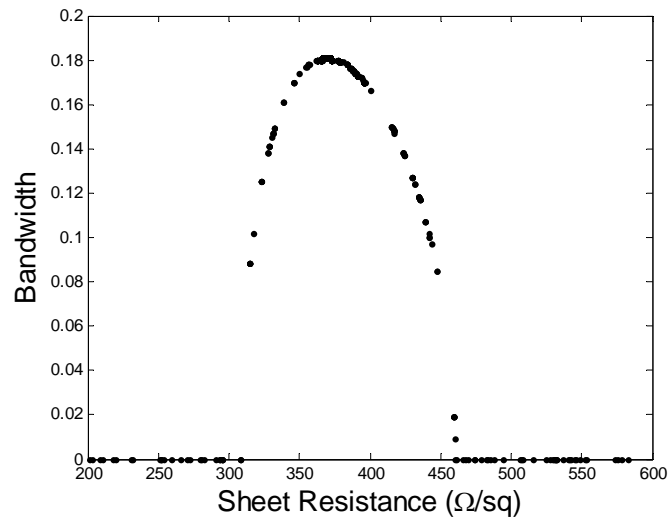
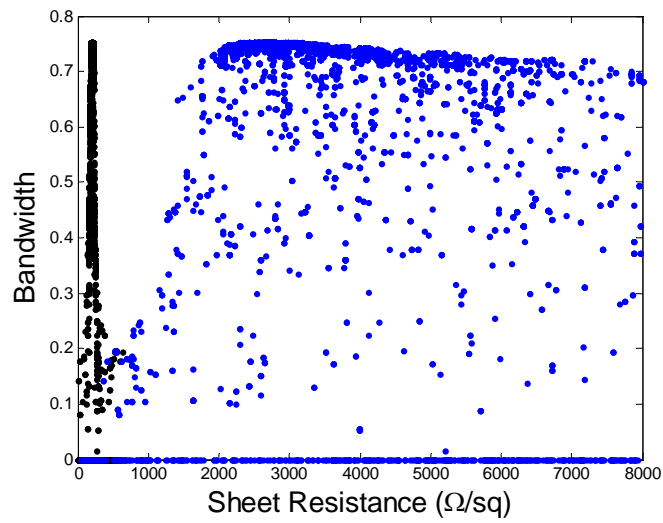


Figure 6.10. Reflectivity profiles for Salisbury screen designs with different spacer permittivity. $\epsilon_r = 1.1$ (solid line), 2 (dotted line) and 3 (dashed line).



a



b

Figure 6.11. Bandwidth vs sheet resistance for one and two layer absorber designs with a spacer permittivity of ϵ_r spacer = 2. The genetic algorithm converges on absorber designs where the bandwidth is smaller than found for lower permittivity materials.

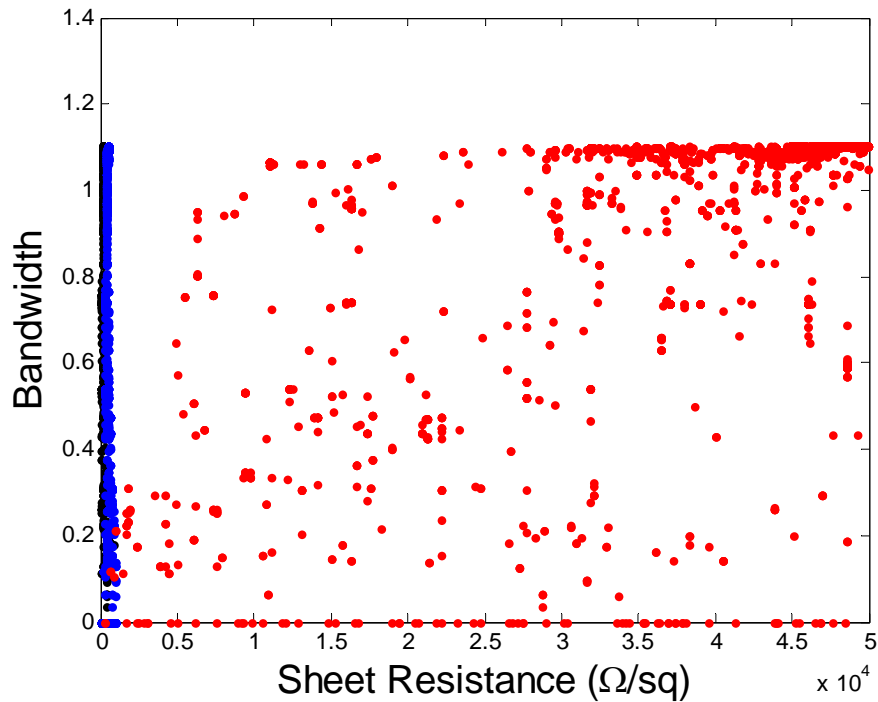


Figure 6.12. Bandwidth vs sheet resistance for a three layer absorber design with a spacer permittivity of $\epsilon_r \text{ spacer} = 2$. The optimum absorber is not achieved with an external sheet resistance of 50 k Ω /sq.

There is no gain in bandwidth for absorber designs with high permittivity spacers and no protective layer, beyond $N = 2$ or 3 at most. These absorbers are a compromise from those with a foam or low permittivity spacer.

6.3.3 Higher Permittivity with Protective Layer

It was already noted that a protective layer increases the bandwidth of an absorber with a low permittivity spacer. This effect is further enhanced for higher permittivity spacers, Figure 6.13. For a permittivity of 2.0, a protected Salisbury screen has two interference fringes and a much wider bandwidth. There is a bandwidth increase of 2.6 times that of the air-spaced Salisbury screen. The reflectivity profile of this protected Salisbury screen is nearly identical to that of the unprotected two-layer absorber with the same permittivity.

This behaviour extends out to $N=3$, after which there is no improvement and absorber designs adopt the $N=2$ design for the outer layers as was seen for higher permittivity absorber designs. In contrast to the unprotected absorbers, the bandwidth vs sheet resistance solution space plots indicate well defined maxima for R_2 and R_3 . Only a small range of resistance values produce the optimum absorber.

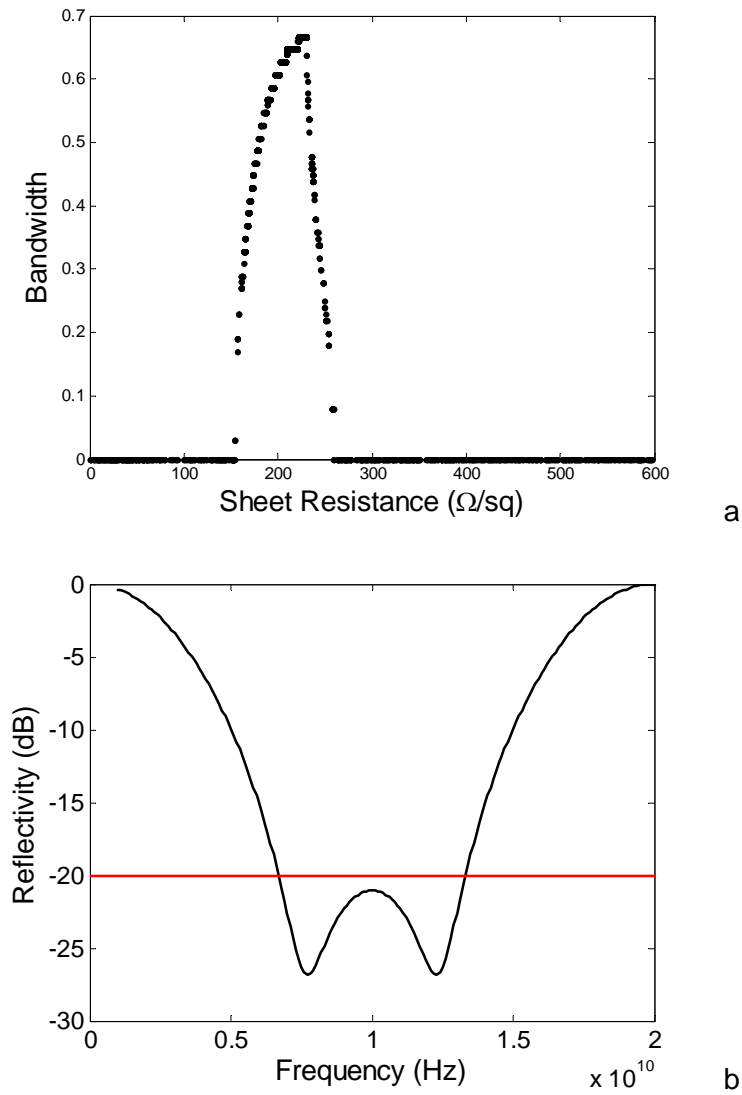


Figure 6.13. Bandwidth vs sheet resistance (a) for a Salisbury screen with a spacer permittivity of ϵ_r spacer = 2, and a protective layer. The optimum absorber design has a much wider bandwidth and appears to have the same reflectivity profile (b) as a two-layer absorber with no protective sheet.

6.4 Conclusions

The design of wideband microwave absorbers requires the use of an optimisation technique due to the complexity of the reflectivity from a multilayered structure. For all the optimisation techniques, the biggest issue is finding the optimal solution without becoming stuck in a local minimum. The methods of simulated annealing and genetic algorithms have been shown to help in avoiding local optima traps. Another issue with the design of multilayer absorbers is the fact that conflicting constraints are

placed on absorber design, such as having thinnest absorber with the lowest reflectivity over the widest bandwidth possible. These constraints are mutually exclusive and so an acceptable design is often a trade off between the constraints. The Pareto Genetic Algorithm calculates a family of optimised design solutions for more than one constraint and can be based on available materials, making it an attractive tool.

The bandwidth of absorbers with layered resistive sheets increases with the number of layers, asymptotically approaching the maximum bandwidth. For a low permittivity spacer the bandwidth reaches about 90% of the maximum with seven resistive sheets. The bandwidth is increased slightly when a protective layer is applied to the absorber. And it is increased considerably when the absorber has a protective layer and higher spacer permittivity. This last effect only extends to 2 or 3 layers after which there is no gain in bandwidth with increase in the number of resistive sheets.

The shape of the resistance profile through the absorber depends on the number of layers and the resistance of the first sheet adjacent to the PEC interface. The resistance profile was found to follow an exponential curve similar to that described by Nortier, except for the outer sheets, where the sheet resistances were less. In certain cases, a range of absorber designs will produce the same near optimal bandwidth. When this occurs the profile depends of the starting resistance, though the trend is to still follow the exponential curve.

The bandwidth optimisation function was found to result in absorber designs with the best properties.

6.5 Future Research

Design of RAM using resistive/capacitive and resistive/capacitive/inductive sheets.

Optimise RAM for a range of incident angles.

Design of RAM from a database of materials using the Genetic Algorithm.

New approach to RAM design using periodic (patterned material) lossy structures as thin layers. This research requires significant investment in development of new tools for structure analysis.

6.6 References

- (1) Johnson, J. M.; Rahmat-Samii, Y. *Antennas and Propagation Magazine, IEEE* **1997**, 39, 7.
- (2) Michielssen, E.; Ranjithan, S.; Mittra, R. *Optoelectronics, IEE Proc.-J* **1992**, 139, 413.
- (3) Michielssen, E.; Sajer, J.-M.; Ranjithan, S.; Mittra, R. *IEEE Transactions on Microwave Theory and Techniques* **1993**, 41, 1024.
- (4) Michielssen, E.; Sajer, J.-M.; Mittra, R. *IEEE* **1993**, 1167.
- (5) Presque, J. J.; Bouche, D. P.; Mittra, R. *Microwave Theory and Techniques, IEEE Transactions on* **1992**, 40, 1789.
- (6) Weile, D. S.; Michielssen, E.; Goldberg, D. E. *IEEE Transactions on Electromagnetic Compatibility* **1996**, 38, 518
- (7) Chambers, B.; Tennant, A. *IEE Proc. - Radar, Sonar Navig.*, **1996**.
- (8) Chambers, B.; Anderson, A. P.; Mitchell, R. J. *Genetic Algorithm in Engineering Systems: Innovations and Applications*, **1995**.
- (9) Chambers, B.; Tennant, A. *Antennas and Propagation*, **1995**.
- (10) Chambers, B.; Tennant, A. *Electr. Lett.* **1994**, 30, 1530.
- (11) Chambers, B.; Tennant, A. *Proceedings of the 16th Annual Meeting on Antenna Measurement Techniques Association*, **1994**.
- (12) Nortier, J. R., Van der Neut, C.A., Baker, D.E. *Microwave Journal* **1987**, 219.
- (13) Wong, T. C. P.; Chambers, B.; Anderson, A. P.; Wright, P. V. *Ninth International Conference on Antennas and Propagation*, **1995**.
- (14) Cheldavi, A.; Kamarei, M. *Microwave Symposium Digest, 1997., IEEE MTT-S International* **1997**, 3, 1555.
- (15) Cheldavi, A. *IEICE Transactions on Fundamentals of Electronics, Communications and Computer Sciences* **1999**, E82-A, 704.
- (16) Foroozesh, A. R.; Cheldavi, A.; Hodjat, F. *Antennas, Propagation and EM Theory, 2000. Proceedings. ISAPE 2000. 5th International Symposium on* **2000**, 227.
- (17) Cheldavi, A.; Kamarei, M. *IEEE Antennas and Propagation Society. International Symposium (1997: Montreal)* **1997**, 3, 1708.
- (18) Qian, J.; Wang, X.; Wu, R.; Pei, M.
- (19) Weile, D. S.; Michielssen, E. *Antennas and Propagation , IEEE Transactions on* **1997**, 45, 343.
- (20) Chakravarty, S.; Mittra, R.; Williams, N. R. *Microwave Theory and Techniques, IEEE Transactions on* **2001**, 49, 1050
- (21) Chakravarty, S.; Mittra, R.; Williams, N. R. *Antennas and Propagation, IEEE Transactions on* **2002**, 50, 284
- (22) Kern, D. J.; Werner, D. H.; Wilhelm, M. J.; Church, K. H. *Microwave and Optical Technology Letters* **2003**, 38, 400.
- (23) Kern, D. J.; Werner, D. H. *Microwave and Optical Technology Letters* **2003**, 38, 61.
- (24) Kern, D. J.; Werner, D. H. *Antennas & Propagation Society International Symposium, 2003.* **2003**, 2, 1119.
- (25) Deb, K.; Pratap, A.; Agarwal, S.; Meyarivan, T. "A Fast and Elitist Multi-Objective Genetic Algorithm: NSGA-II," *Kanpur Genetic Algorithms Laboratory*, **2000**.
- (26) Deb, K. *Multi-Objective Optimization using Evolutionary Algorithms*; John Wiley and Sons: Singapore, **2001**.

7. Circuit Analog Materials

Circuit-analog absorbers have been known to provide superior performance to that of Jaumann absorbers when used to reduce radar cross section (RCS).^[1] Circuit analogs are designed using frequency selective surfaces made of high loss dielectric material. The Dockyard Laboratory is currently developing such materials, and their electrical properties have been measured at the University of Victoria. These materials appear to be good candidates for circuit analog absorbers. However, there is very limited data on modeling behavior of these absorbers. While the design process of a multi-layer structure follows the design of Jaumann structures,^[1] first one needs to obtain the impedance of each constitutive layer.

The objectives of the research reported are:

to investigate the use of the finite difference time domain (FDTD) method as an efficient method to evaluate broad-band impedance of the absorbers, and

to analyze the effects and trends due to dimension changes and electrical property changes of Frequency Selective Surfaces (FSS) constructed from representative materials developed by the Dockyards Laboratory.

7.1 Modeling Software

In house developed Frequency Domain Time Domain (FDTD) code has been used together with a visualization aid called Vezzuto, as illustrated in Figure 7.1.

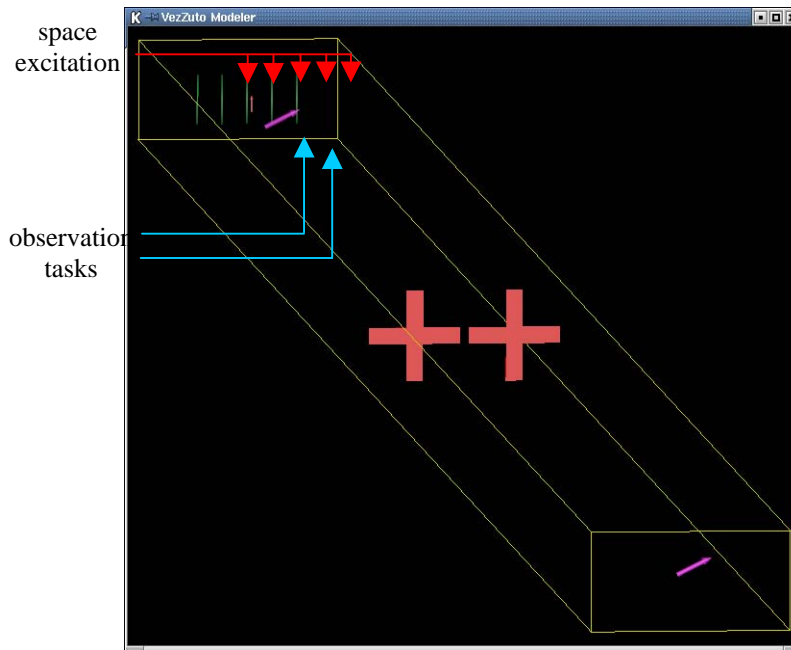


Figure 7.1. View of one structure with Vezzuto software.

Most of the simulations are performed only for normal incidence of the waves. In this case the periodic boundary condition is used, so only few cells of the FSS needs to be included in the computational domain. The remaining two boundaries of the domain are terminated by perfectly matched layers (PML), which limit the reflections below 60 dB. Data are obtained for frequencies between 5 and 20 GHz. The electrical properties are assumed frequency invariant.

The same code can be used for arbitrary angle of incidence. However, because the periodic boundary conditions available are only for normal incidence, the FSS cells have to be placed in wave guiding structures, as described in reference 2,^[2] and used in reference 3.^[3] Alternatively, another code with general periodic boundaries, or our code with an appropriate addition can be used.

Frequency dependence of the electrical permittivity of dielectric materials can be modeled in our code, however the actual behavior of the permittivity materials has only been determined at frequencies from 8.2 to 12.4 GHz. Because of the preliminary

nature and limited scope of this project, the arbitrary-angle wave incidence and dielectric dispersion are not considered.

To compute the impedance \hat{Y}_L , the equivalent circuit of Frequency Selective Surface in free space is used, as shown in Figure 7.2.

The equivalent admittance \hat{Y}_L is:

$$\hat{Y} = \frac{1 - \hat{\Gamma}}{1 + \hat{\Gamma}} \quad (1)$$

where $\hat{\Gamma}$ is the reflection coefficient, and

$$\hat{\Gamma} = \frac{-\hat{Y}_L}{\hat{Y}_L + 2Y_0} \quad (2)$$

The impedance Z_L can be computed from Y_L and plotted on the Smith chart.

$$\hat{Z}_L = \frac{1}{\hat{Y}_L} = -Z_0 \left(\frac{1 + \hat{\Gamma}}{2\hat{\Gamma}} \right) \quad (3)$$

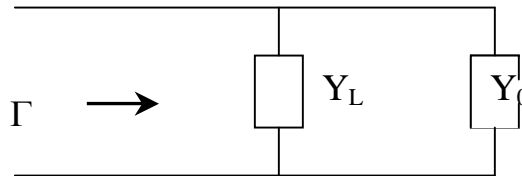


Figure 7.2. Equivalent circuit for the FSS. Admittance of the FSS is Y_L

Different FFS structures have been designed from 7 materials, whose properties, i.e. their relative dielectric constant (ϵ') and their conductivity (σ) are given in Table 7.1. The colors shown in the table correspond to those used in corresponding figures. In all cases the material thickness is 0.1 mm.

Table 7.1. Material properties, permittivity and conductivity.

	MATERIAL & COLOR	DIELECTRIC CONSTANT	CONDUCTIVITY S/M
1.	green	100	200
2.	black	30	100
3.	red	60	150
4.	blue	200	400
5.	yellow	100	400
6.	magenta	100	800
7.	cyan	30	400

7.2 Results and Discussion

For each FSS configuration, the equivalent impedance plotted in the Smith chart, the graphs of the resistance and the reactance are given. Once these results are analyzed, we will see the different parameters that have an influence on the equivalent impedance, because we want to be able to control it. (See Appendix B)

It is well known, that all dimensions of the element of the FSS influence the resonant frequency and thus the impedance of the FSS. Some of the influences and trends can be deduced from the data in Figs. 7.3 to 7.34. Considering the simple structures of type A (Figs. 7.3 to 7.8), it is apparent that the resistance (normalized to that of free space) can be varied from well below to well above that of the free space with dielectric constant ranging from below 30 to above 100, with corresponding values of conductivity, as shown in Table 7.1. Furthermore, the structures are all resonant. The higher the electric properties of the material, the lower the resonant frequency. Also, the more close the spacing of the elements the lower the resonant frequency. An increase in the width of the ribbon forming the cross results in a decrease of the resistance and an increase in the resonant frequency. In summary, this geometry is suitable for design of multi-layer absorbers.

Structures B have been expected to provide an alternative to structures A with less impedance change with frequency and a smaller size of a single element.^[1] Figure 7.35 illustrates the change of impedance with the element length at a frequency of 10 GHz. As expected the resonant length is less than 6 mm. Another parameter controlling the resonant frequency is the gap between the elements. This is illustrated in Figure 7.36. Narrower gap lowers the resonant frequency. However, this dimension plays a less critical role in the resonant control than the length of the element. The ribbon width has only small effect on the impedance, as can be seen from Figures 7.11 to 7.14 for structures B2 and B3, which are identical except for the ribbon width of 0.2 mm (B2) and 0.4 mm (B3).

Addition of a relatively thin (2mm) substrate with a dielectric constant of 4 has a rather large effect on the FSS impedance. This is illustrated in Figures 7.21 and 7.22

for structure B7 (with substrate) as compared with structure B2 (Figures 7.11 and 7.12). Furthermore, the resonant impedance changed also dramatically from much greater than that of free space to much lower.

Structures C illustrate the effects of closer spacing of the FSS elements. Comparing structures A1 (Figures 7.3 and 7.4) and C1 (Figures 7.27 and 7.28), which have the same single elements, but differ in their spatial arrangement, changes in the resonant frequency and resistance at resonance are clearly visible. The advantage of the close element spacing is also shown, namely the less resistance change in frequency. On the other hand the resonant frequency increased, which is not surprising, as the capacitance decreases when the gap between the adjacent elements increases. Structure C3 shows how the effect of the decrease in the capacitance can be offset by an increase in the element length. Similar behavior is shown for the “loop – cross” structures C2 and C4.

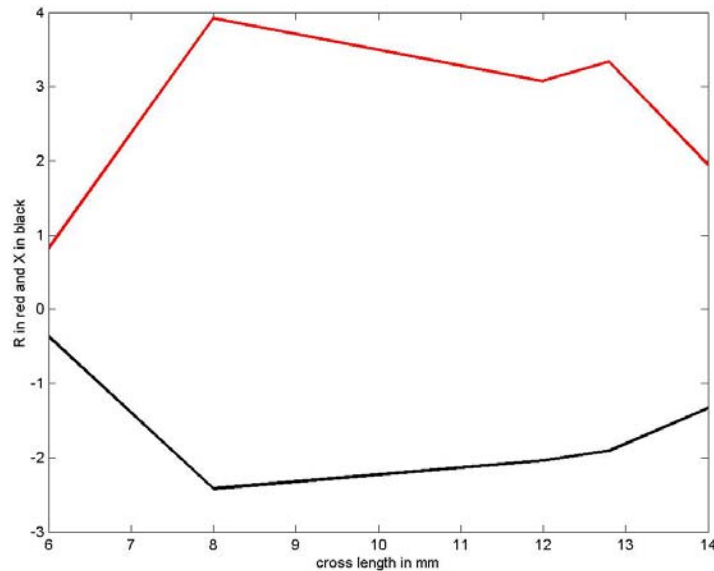


Figure 7.35. Variation of the impedance as a function of the element (cross) length. Material 1.

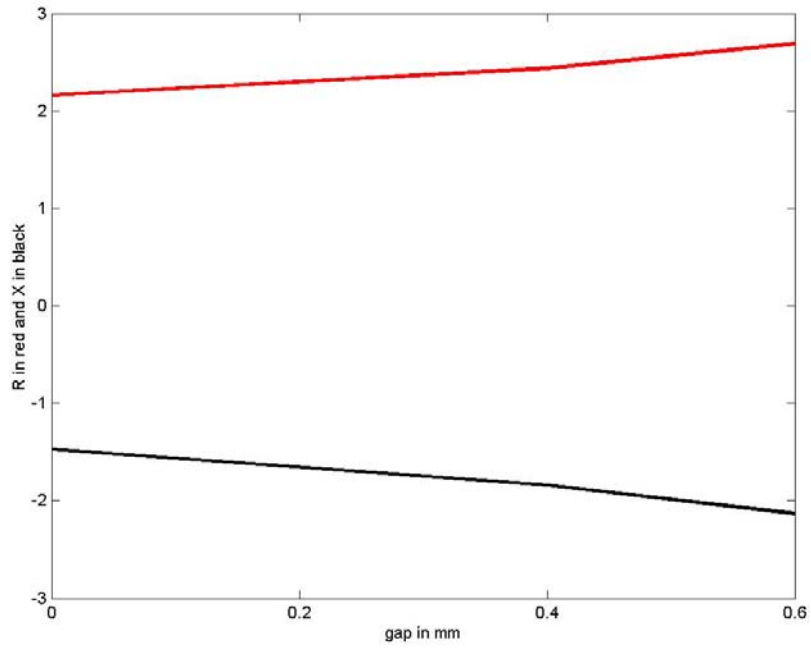


Figure 7.36. Dependence of the resistance (red) and the reactance (black) on the gap width. Material 1, $f=10\text{GHz}$.

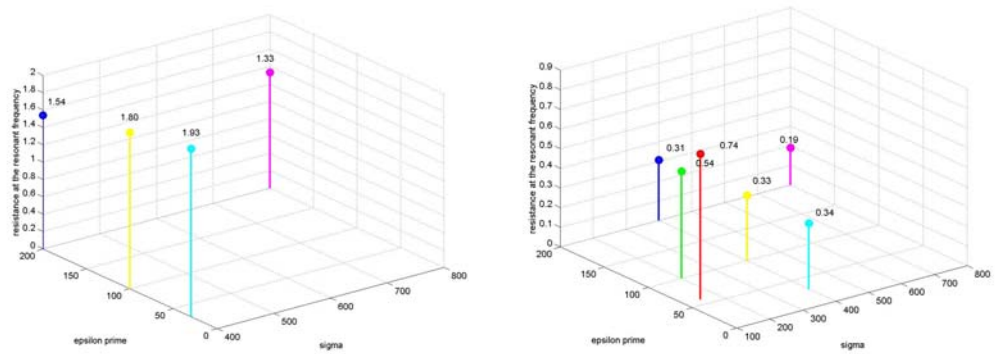


Figure 7.37. Resistance at the resonant frequency for the different materials (for structure B6 on the left side, and for structure C1 on the right side).

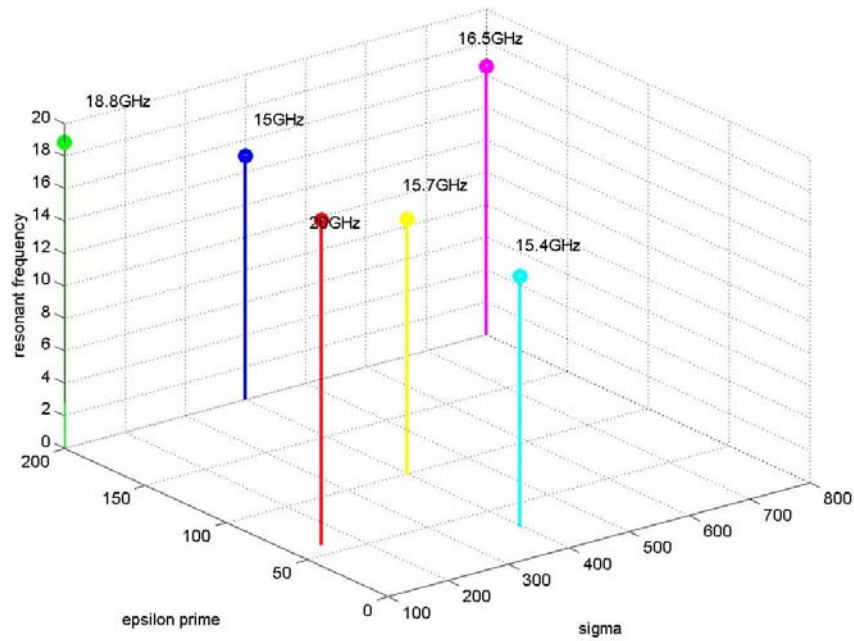


Figure 7.38. Resonant frequency as a function of the permittivity and the conductivity.

Effects of the material properties are rather difficult to quantify on the basis of the data available. Both the dielectric constant and conductivity influence the FSS behaviour. Figures 7.37 and 7.38 show, respectively, the resistance at resonance and resonant frequency, for several materials and structures B6 and C1.

Tables 7.2 and 7.3 give additional illustration of the influence of various dimensions of the FSS on their behavior.

Table 7.2. Dimension influence for structures A

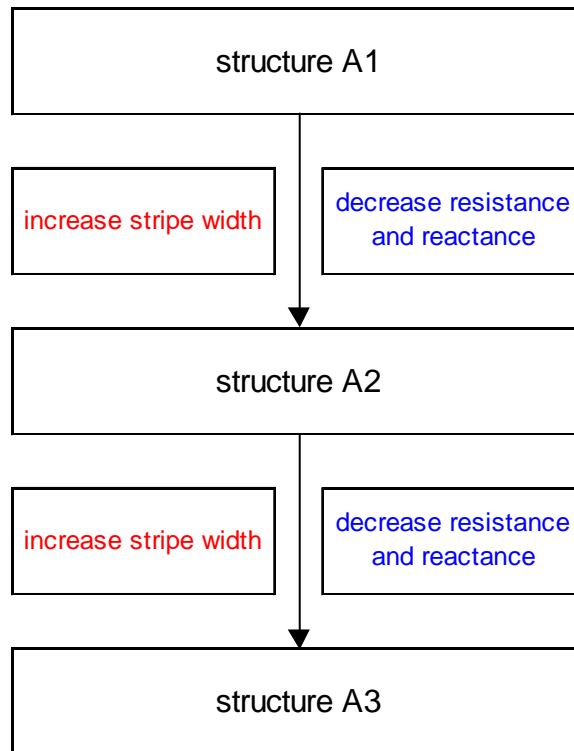
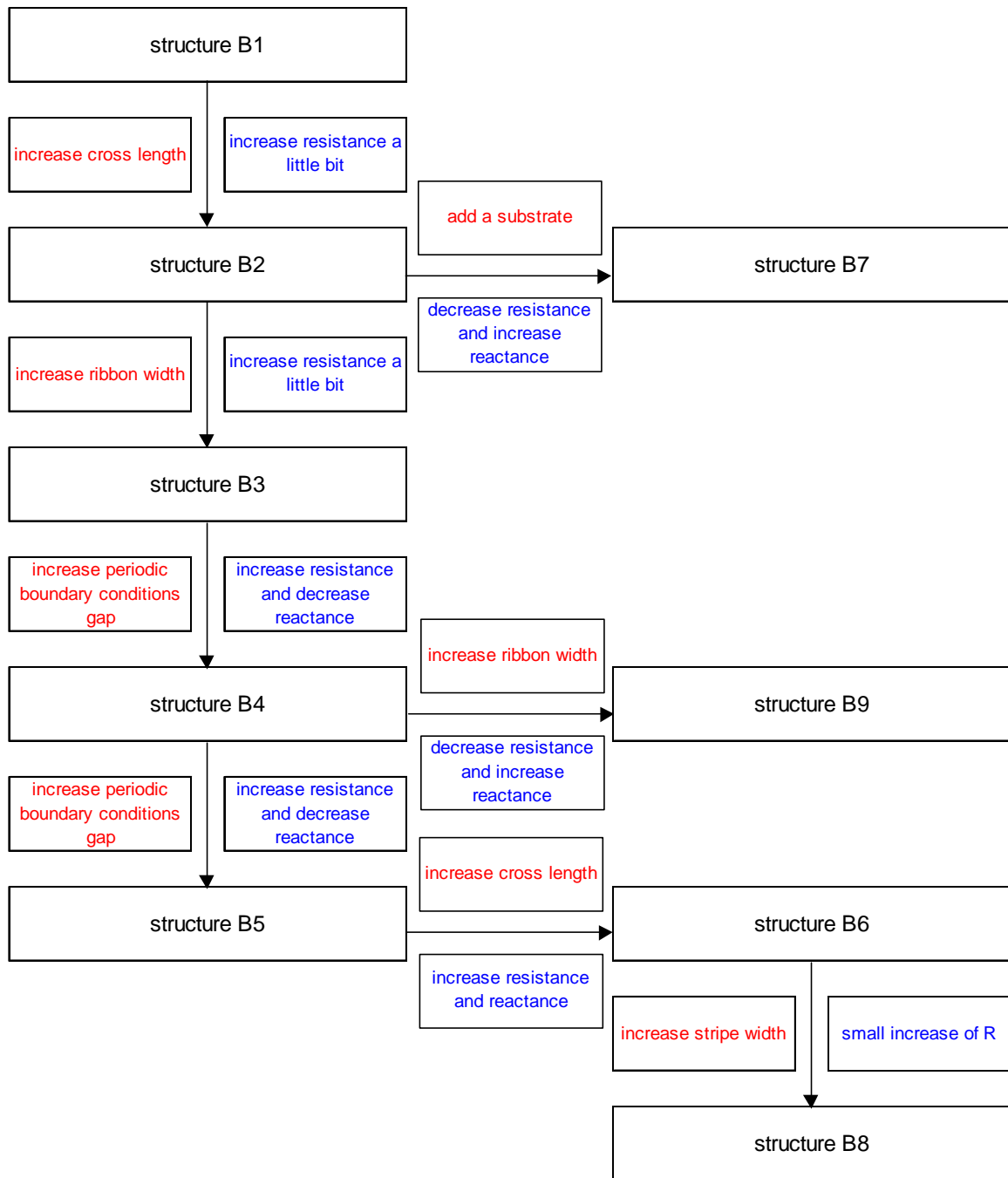


Table 7.3. Dimension influence for structures B



7.3 Conclusion

The preliminary investigations performed, indicate that

The FDTD modeling is suitable for obtaining impedance of FSS surfaces constructed from high loss materials. While the modeling has been performed only for normal incidence, it can also be done for arbitrary angle of incidence. This can be attained either by addition of periodic boundary conditions to the FDTD code, or by modeling the FSS elements in several guided wave structures of appropriate dimensions.

The FDTD modeling allows for inclusion of the layer material layer thickness, as well as the substrate. The impedance is obtained in a broad frequency range in one computation.

The electrical properties of the materials developed by Dockyard laboratory provide means of designing of the FSS of equivalent resistance at resonance varying in the wide range of values. This facilitates design of multi-layer broadband radar absorbers.

There appear to be no specific advantages of one or the other geometry of the two FSS elements investigated. This conclusion may change when arbitrary wave incidence is considered.

7.4 Reference

- (1) Munk, B. A. *Frequency Selective Surfaces*; John Wiley & Sons, Inc.: New York, **2002**.
- (2) Yu, W.; Dey, S.; Mittra, R. *Proc. Antenna Propag. Symp* **1999**, *1*, 594.
- (3) Karkkainen, K.; Stuchly, M. A. *Microwaves, Antennas and Propagation, IEE Proceedings* **2002**, *149*, 248.

8. Summary and Future Work

This TIF set out to develop the capability to design and create radar absorbing materials for reduction of the radar cross section of Canadian Naval platforms. The strategy of developing technical competency in the four key areas of conducting organic materials, property measurement, absorber design and RCS modelling has enabled DRDC to establish a program in radar signature management. Specifically this includes both the development of signature reducing materials and RCS modelling.

From the materials side, organic conducting polymers are readily synthesised with attractive optical properties. Conducting polymer stability and fabrication of materials with consistent properties remain as the challenge for development of successful absorbing materials. Other conductive and magnetic materials should be considered as replacements for the conducting polymers if it is not possible to stabilize them. Methods for fabricating large area materials for coatings and RAM patches need to be explored. The ability to fabricate structural RAM also needs to be investigated.

A facility has been established for measuring the permittivity and permeability of materials in the 8-12 GHz frequency range. This range needs to be extended, uncertainty analysis done for permeability measurements and free space reflectivity measurements made. This latter point is especially required for being able to ascertain the performance of absorbers developed in house.

Absorber design has looked at optimising single layer Dallenbach coatings and multilayer Jaumann absorbers. Absorbers have been designed with a bandwidth of up to 90% of 1-20 GHz frequency range falling below the -20 dB level (or 99% reduction in the reflectivity). The optimization codes need to be upgraded to optimise absorber design as a function of incident angle and for materials containing resistance, capacitance and inductance. Work is also required for designing absorber using a database of frequency dependent permittivity and permeability data measured from real materials. Finally Circuit Analog materials need to be studied in order to produce absorbers that are thinner with better bandwidth. Another new field to move into would be that of Dynamic RAM, were the impedance properties of the materials are varied so that the reflectivity is tuned to different frequency regions.

Appendix A

8.1 Publications related to Research

Huber, T., Saville, P. and Edwards, D., *Investigations into the Polyaniline and Polypyrrole Families of Conducting Polymers for Application as Radar Absorbing Materials*, DRDC Atlantic TM 2003-005

Huber, T.A., *A Literature Survey of Polyaniline, Part 1: Polyaniline as a Radar Absorbing Material*, DRDC Atlantic TM 2003-014

Huber, T.A.; Edwards, D.R., *Polyaniline as a Potential Radar Absorbing Material: Preliminary Experiments*, DRDC Atlantic TM 2003-153

Huber, T.A., Diep, M.N., *Synthesis and Characterization of Polyaniline-Nanostructure Composites*, DRDC Atlantic TM 2003-206

Huber, T.A., *Polymer – Carbon Nanotube Composites, A Literature Review*, DRDC Atlantic TM 2004-091

Makeiff, D. *The Effect of Processing Parameters on the Microwave Absorption by Polyaniline/PMMA Composites*, DRDC Atlantic TM 2004-301.

Makeiff, D. *Microwave Absorption by Polyaniline-coated Polyester Fabrics*. DRDC Atlantic TM 2005-023.

Stuchly, M.A., *Measurements of Radar Absorbing Materials*, March 2001 (DREA CR 2001 – 078) Stuchly, M.A., *Modeling of Circuit – Analog Radar absorbing Material* (DRDC Atlantic CR 2003 – 008)

Campbell, M.; M.A. Stuchly, *Determination of the Complex Permittivity of Thin, High Loss Materials in a Waveguide*. Jan 2003. (DRDC Atlantic CR 2003 – 017) Williams, T.; M. A. Stuchly, P. Saville, *Modified Transmission – Reflection Method for Measuring Constitutive Parameters of Thin, Flexible, High Loss Materials*, IEEE Transactions on Microwave Theory and Techniques, 2003, 51(5), 1560-1566. (DRDC Atlantic SL 2003-010) Saville, P., *Polypyrrole Coated Textiles for Potential RAM Applications: Effect of Fabric Type*, (DRDC Atlantic TM 2003 - 148).

Saville, P., *Reflectivity of Layered Materials: Considerations for Radar Absorbing Materials*, (DRDC Atlantic TM 2004 – 034).

Saville, P., *A Review of Optimisation Techniques for Layered Radar Absorbing Materials: Including the Genetic Algorithm*, DRDC Atlantic TM 2004–260.

Saville, P., *A Review of Optimisation Techniques for Layered Radar Absorbing Materials: Including the Genetic Algorithm*, DRDC Atlantic TM 2004-260.

Leslie, A.; Kopac, M. and Saville, P., *Polypyrrole Stability and Coatings for Radar Absorbing Materials*, DRDC Atlantic TM 2004-299.

Saville, P., *Permittivity Measurement Using the Agilent PNA 8362B: A users guide*, DRDC Atlantic TN 2004-233.

Saville, P., *Review of Radar Absorbing Materials*, DRDC Atlantic TM 2005-003.

Saville, P., *Polypyrrole: Formation and Use*, DRDC Atlantic TM 2005 – 004.

8.2 Conference Presentations

Conducting Polymers as Radar Absorbing Materials: Polyaniline, T.A. Huber and D.R. Edwards, 10th- CF/DRDC MEETING on NAVAL APPLICATIONS OF MATERIALS TECHNOLOGY, Dartmouth, NS, May 2003, SL2003-114

Synthesis and Characterization of Polyaniline-Nanostructure Composites, T.A. Huber and M.N. Diep, Polymer Nanocomposites 2003, Boucherville, PQ, October 2003, SL2003-201

Synthesis and Characterization of Polyaniline-Nanotube Composites, D.A. Makeiff, M.N. Diep, M.C. Kopac, and T.A. Huber, NT04, San Luis Potosi, Mexico, July 2004,

Bajwa, A. T. Williams and M.A. Stuchly. *Design of Broadband Radar Absorbers with Genetic Algorithm*, in *IEEE International Symposium of the Antennas and Propagation Society*, Vol. 4, IEEE, pp. 672--675, 2001

Williams, T. M.A. Stuchly, P.M. Saville *Measurements of the Permittivity and Permeability of Thin Radar Absorber Materials in Waveguides*, Proceedings of the 2002 IEEE Antennas and Propagation International Symposium and USNC/URSI Meeting, June 16-21, San Antonio, Texas 2002. (DREA SL 2001 – 231).

Williams, T., M. A. Stuchly, P. Saville, *Measurements of Thin Radar Absorbing Materials* 2001 IEEE AP-S International Symposium and USNC/URSI National Radio Science Meeting April 2001.

Paul Saville, *Stealth: Materials and Techniques for Signature Reduction*, in the Proceeding DRDC Symposium: Potentially Disruptive Technologies, Ottawa, 14-15 April, 2003. (DRDC Atlantic SL 2003 – 085).

Paul Saville, *Radar Absorbing Materials*, in Proceedings of the 10th CF/DRDC Meeting On Naval Applications Of Materials Technology, Halifax, 13-15 May 2003 (DRDC Atlantic SL 2003 - 119).

Paul Saville, *Stealth: Materials and Techniques for Signature Reduction*, Seminar DRDC Atlantic, 9 May 2003.

Appendix B

'Single' cross-symmetric (structure A)

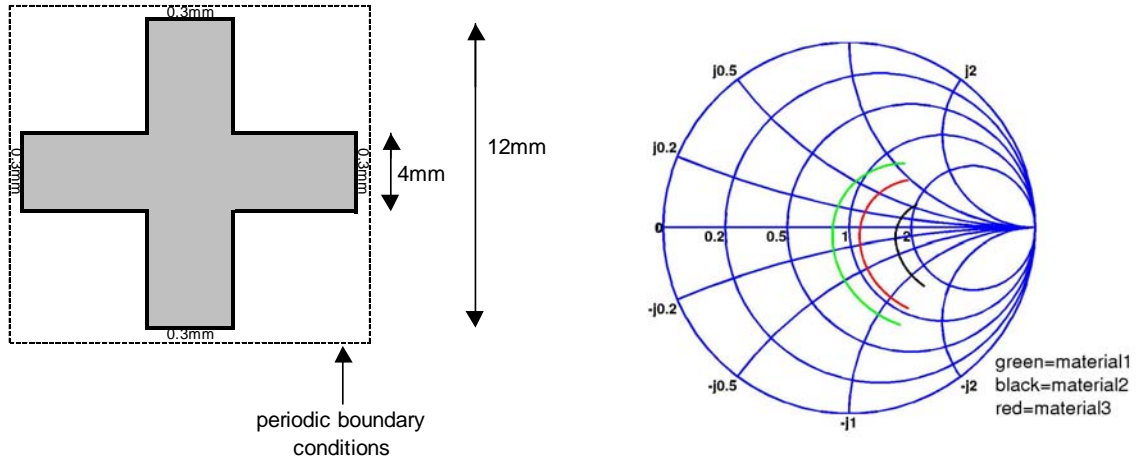


Figure 7.3. Cross dimensions and equivalent impedance plotted in the Smith chart (structure A1).

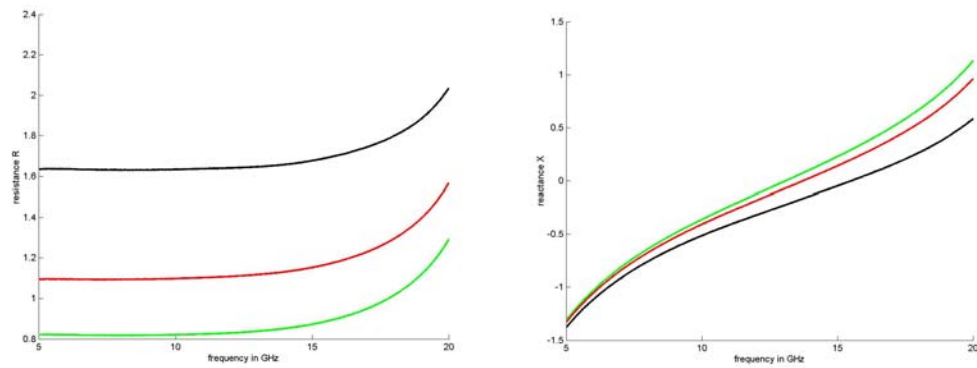


Figure 7.4. Resistance and reactance (structure A1).

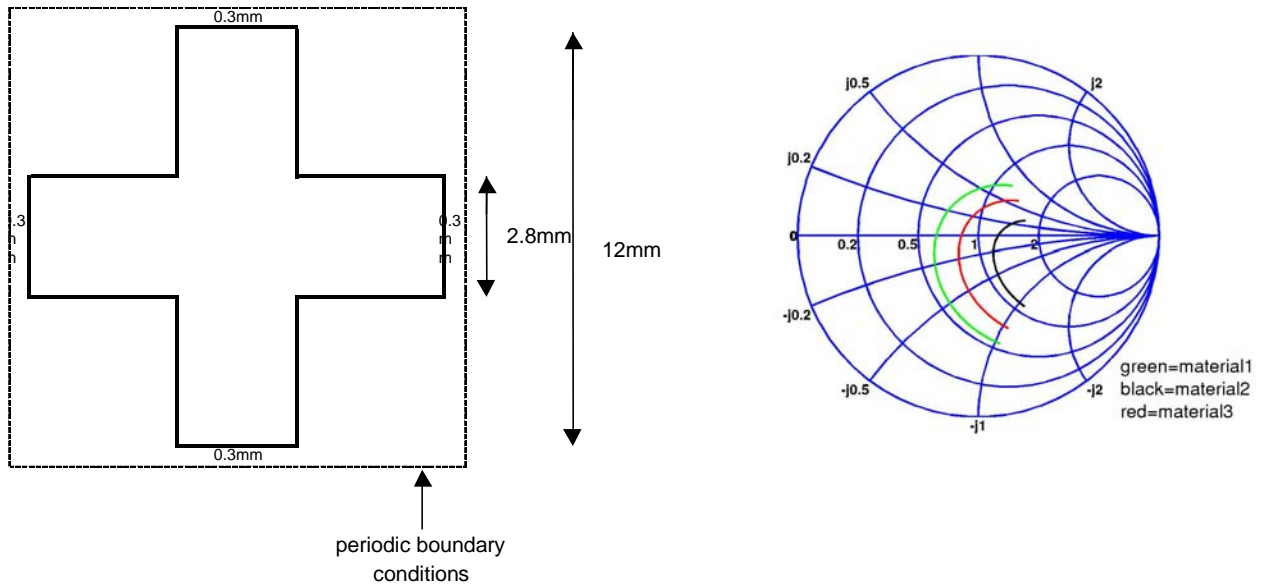


Figure 7.5. Cross dimensions and equivalent impedance plotted in the Smith chart (structure A2).

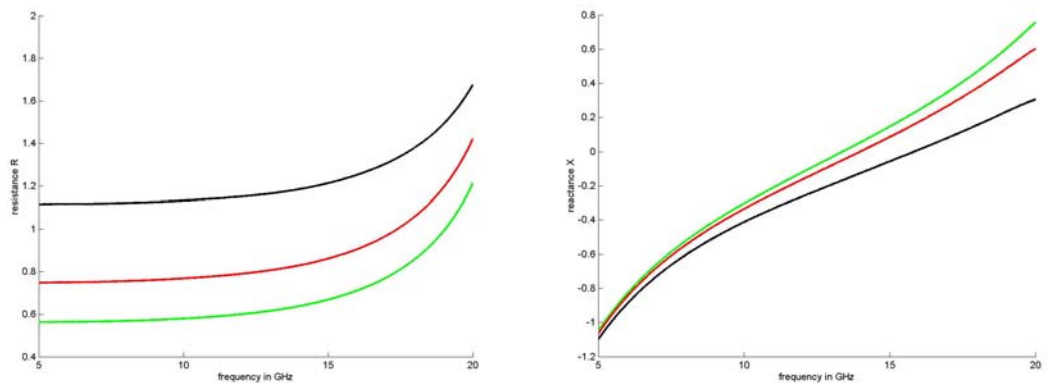


Figure 7.6. Resistance and reactance (structure A2).

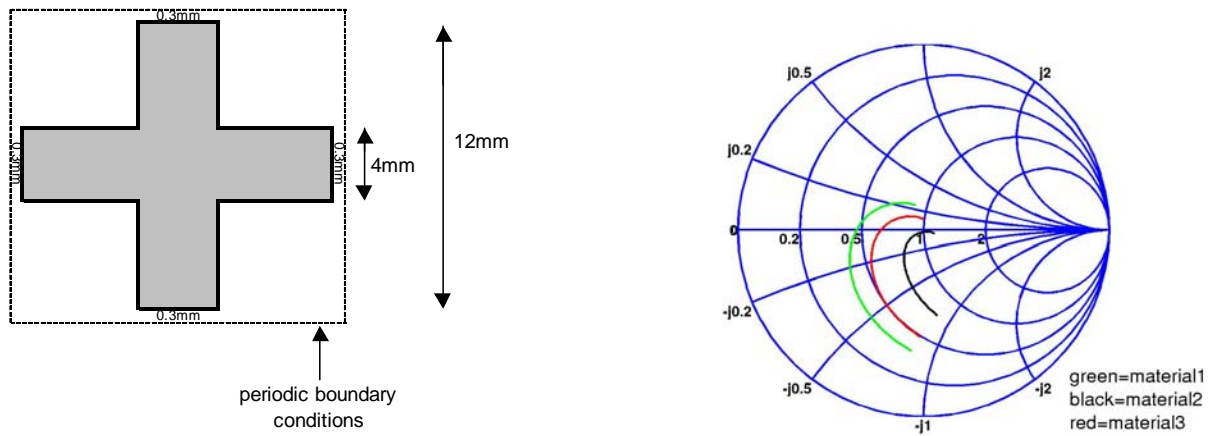


Figure 7.7. Cross dimensions and equivalent impedance plotted in the Smith chart (structure A3).

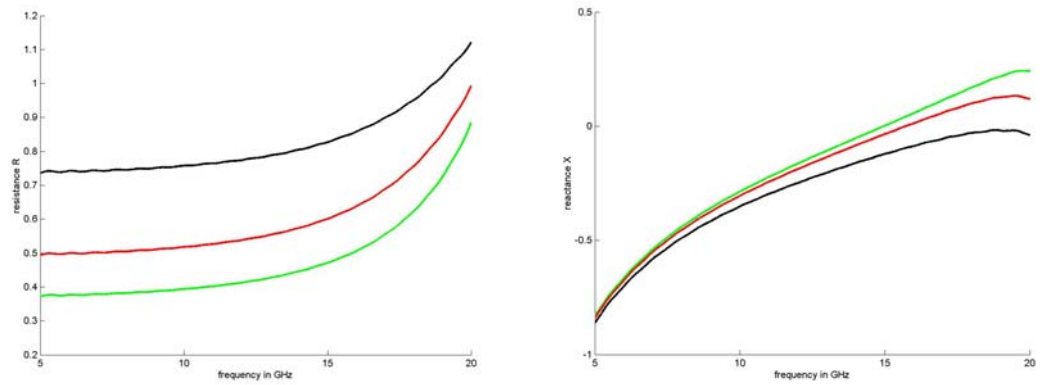


Figure 7.8. Resistance and reactance (structure A3).

'Loop' cross-symmetric (structure B)

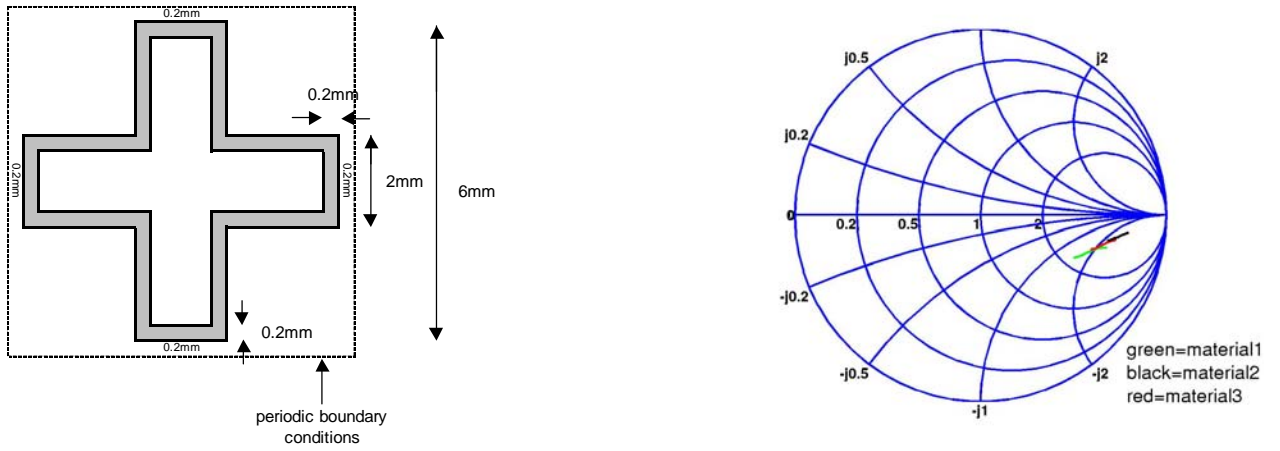


Figure 7.9. Cross dimensions and equivalent impedance plotted in the Smith chart (structure B1).

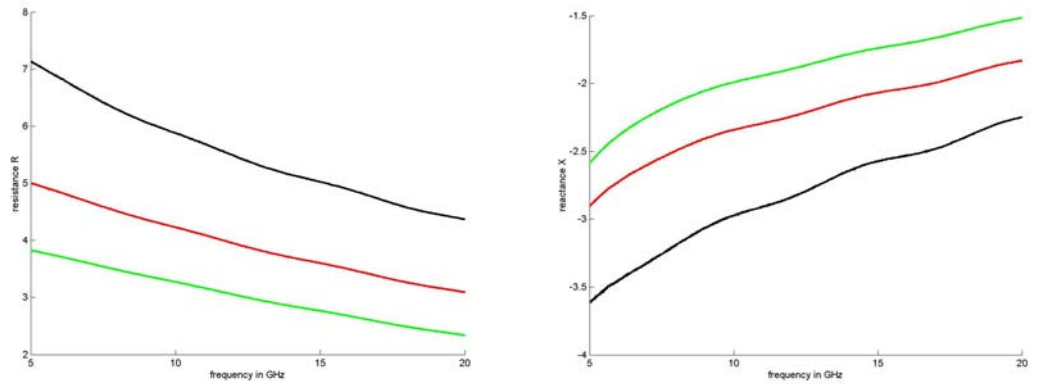


Figure 7.10. Resistance and reactance (structure B1).

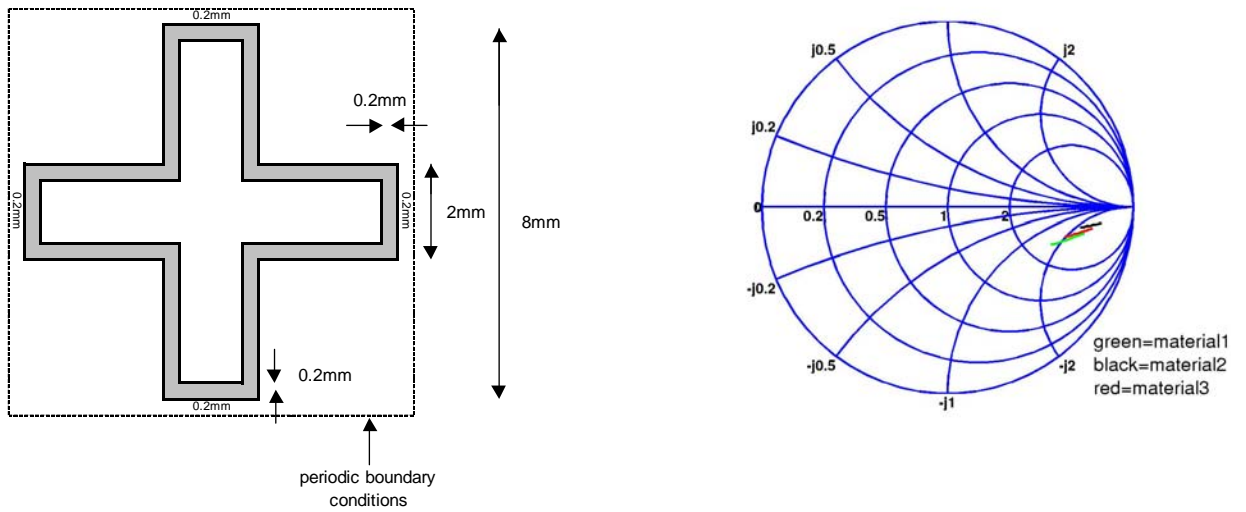


Figure 7.11. Cross dimensions and equivalent impedance plotted in the Smith chart (structure B2).

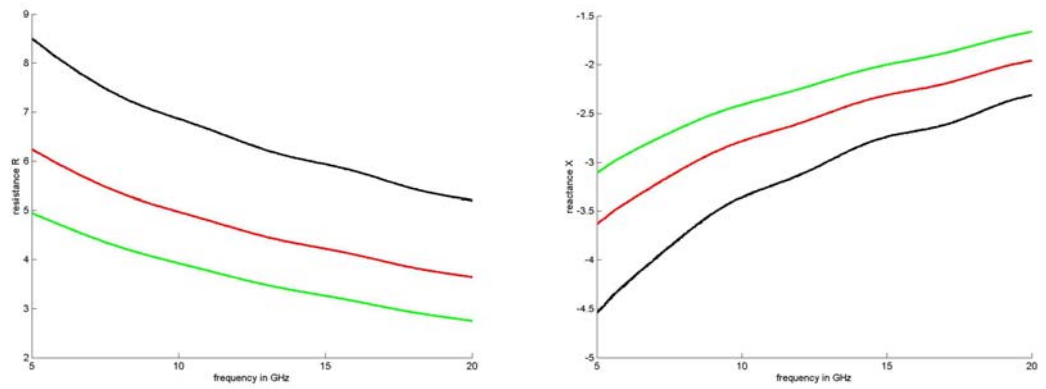


Figure 7.12. Resistance and reactance (structure B2).

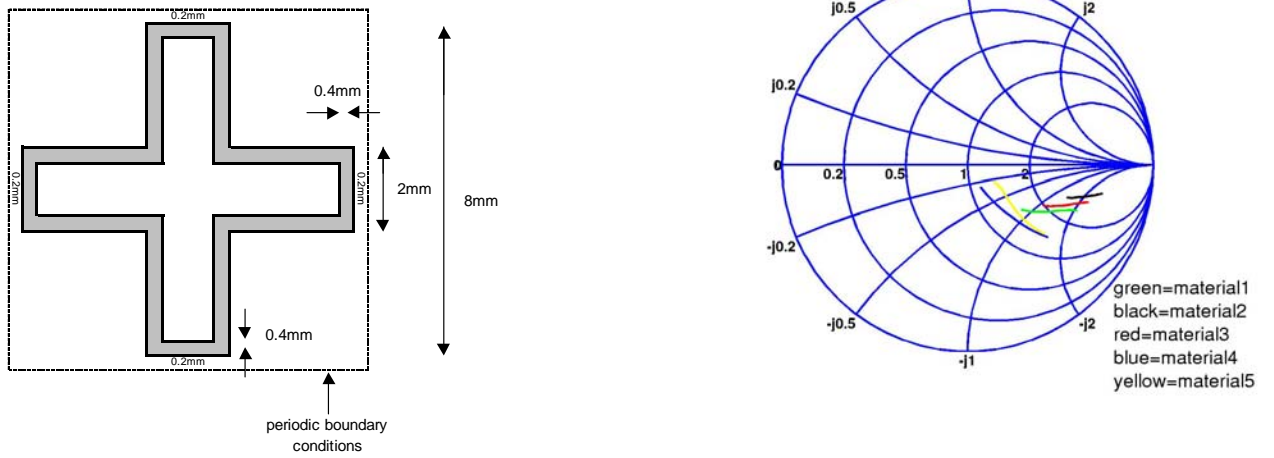


Figure 7.13. Cross dimensions and equivalent impedance plotted in the Smith chart (structure B3).

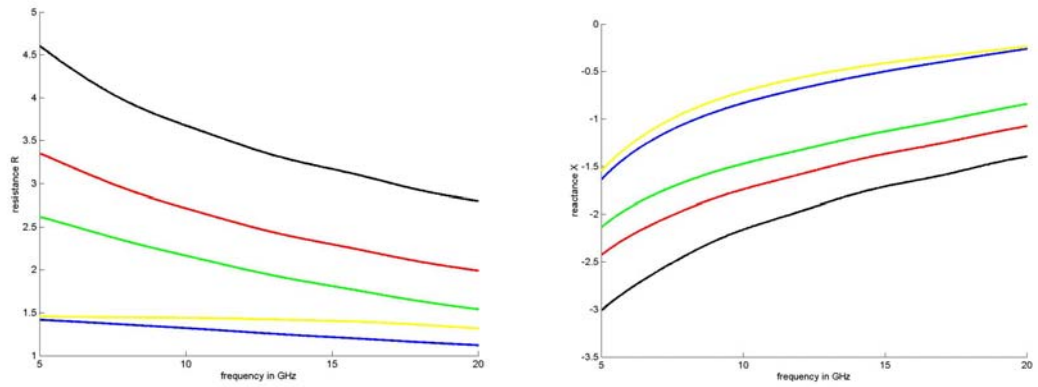


Figure 7.14. Resistance and reactance (structure B3).

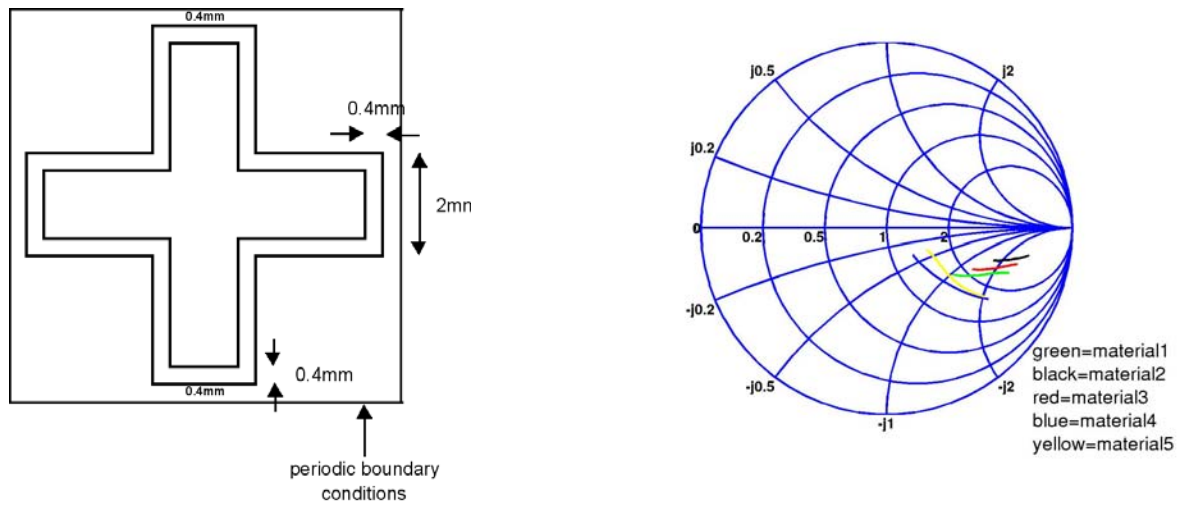


Figure 7.15. Cross dimensions and equivalent impedance plotted in the Smith chart (structure B4).

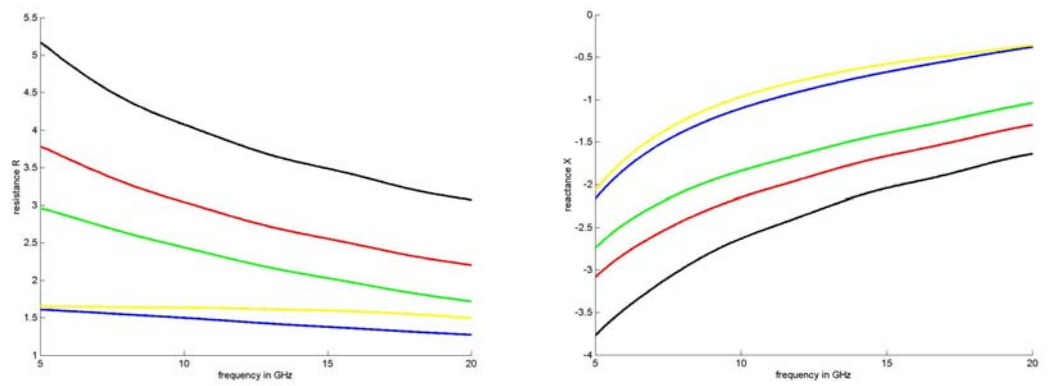


Figure 7.16. Resistance and reactance (structure B4).

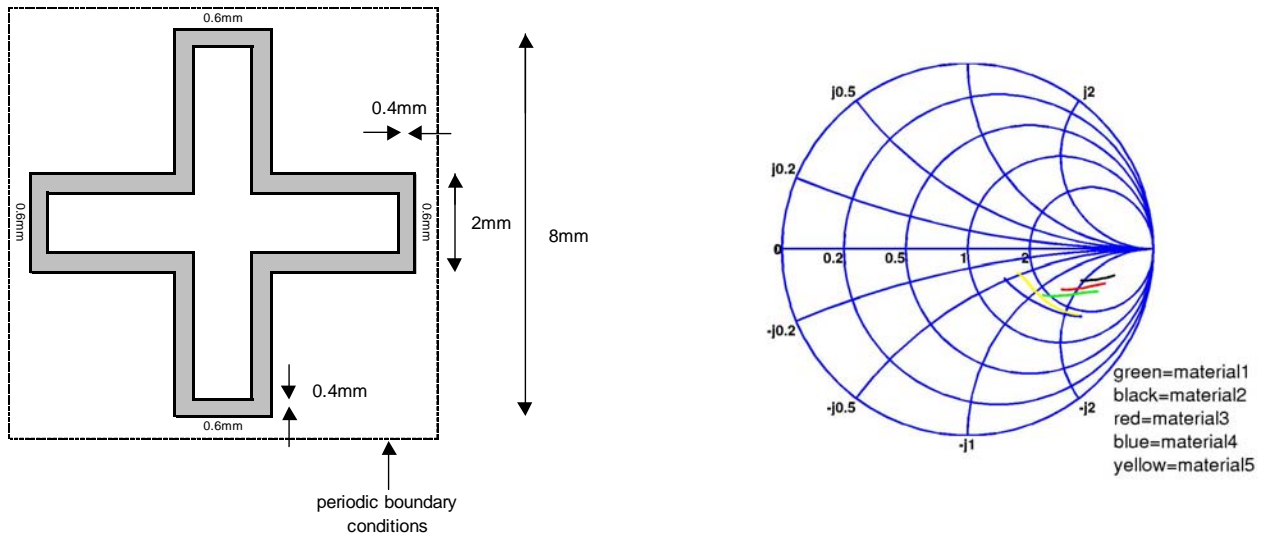


Figure 7.17. Cross dimensions and equivalent impedance plotted in the Smith chart (structure B5).

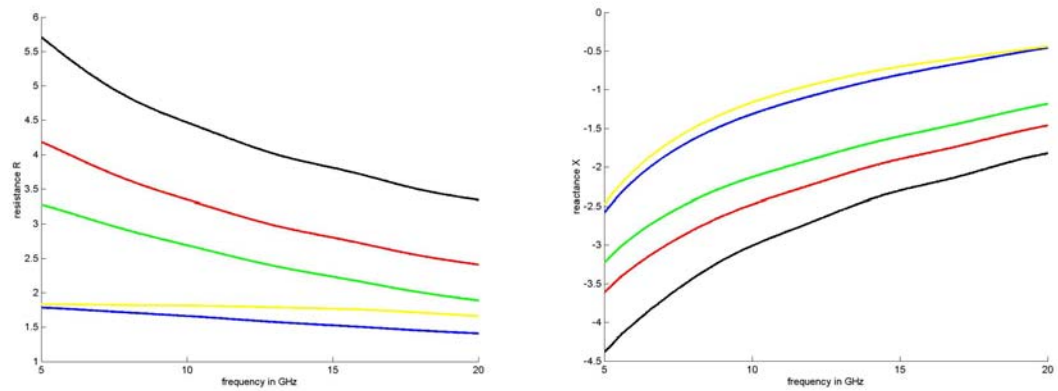


Figure 7.18. Resistance and reactance (structure B5).

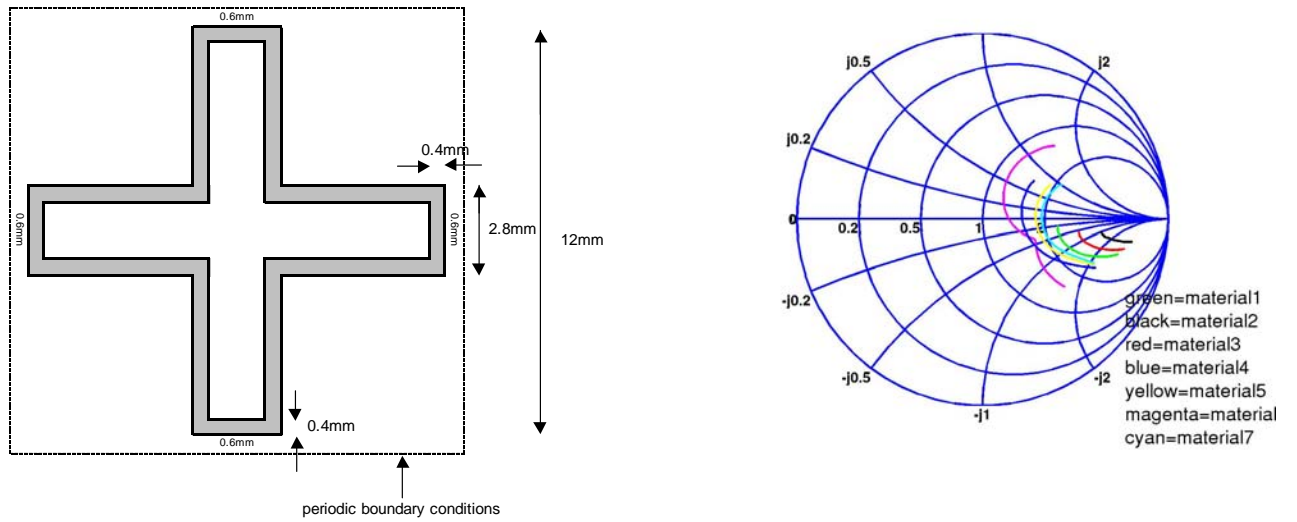


Figure 7.19. Cross dimensions and equivalent impedance plotted in the Smith chart (structure B6).

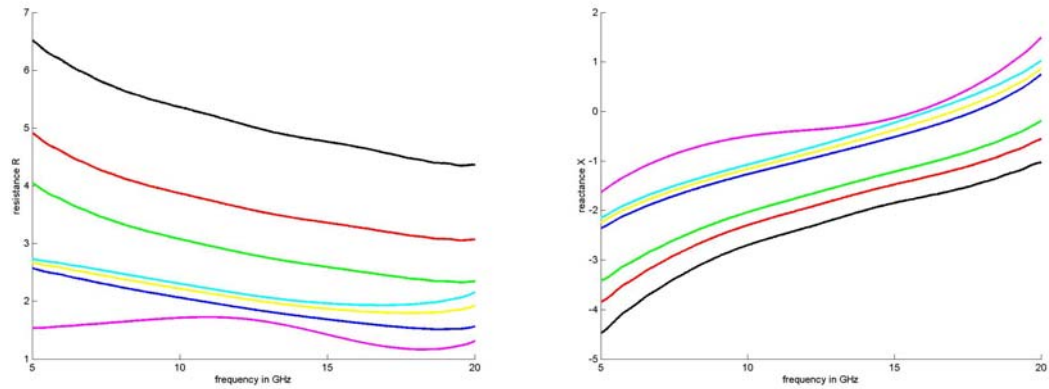


Figure 7.20. Resistance and reactance (structure B6).

Structures B7 to B9 have a dielectric layer located just behind the FSS, to represent a substrate. This layer has $\epsilon' = 4$, and its thickness is 2mm.

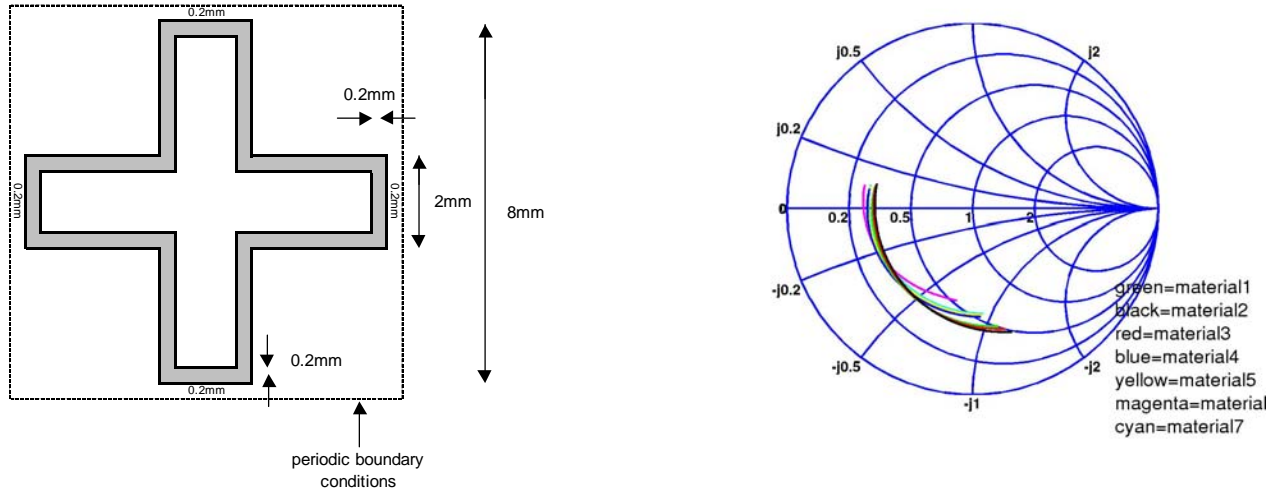


Figure 7.21. Cross dimensions and equivalent impedance plotted in the Smith chart (structure B7).

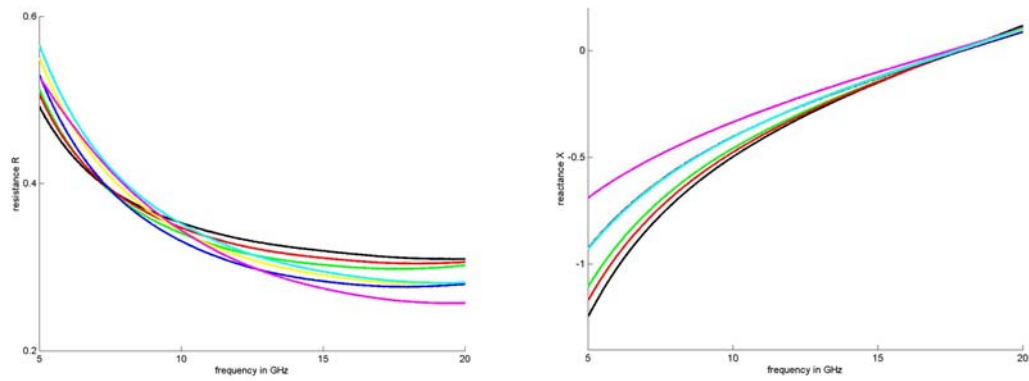


Figure 7.22. Resistance and reactance (structure B7).

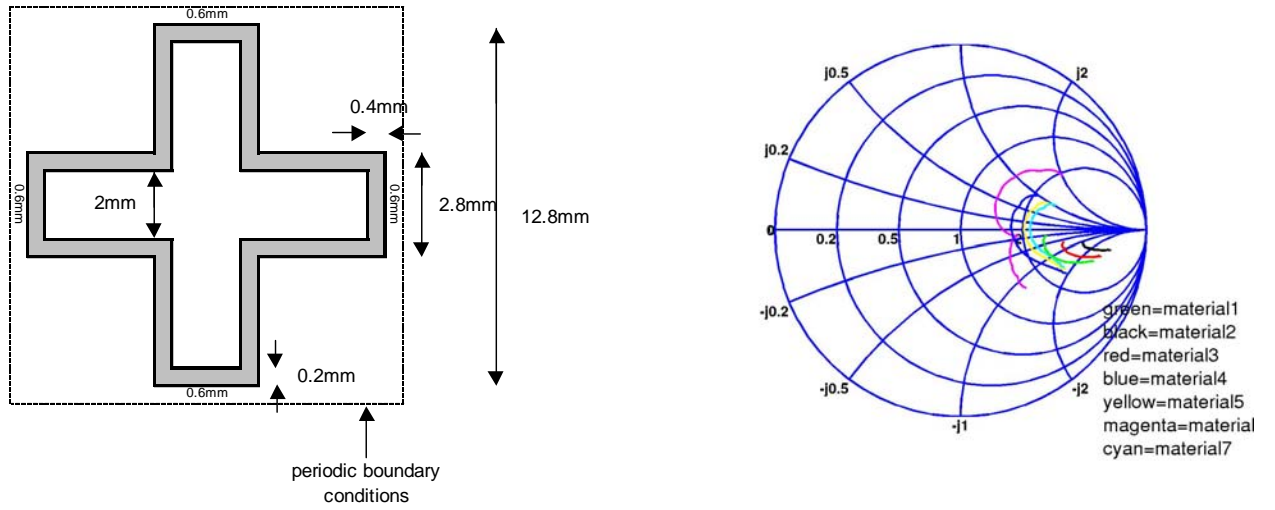


Figure 7.23. Cross dimensions and equivalent impedance plotted in the Smith chart (structure B8).

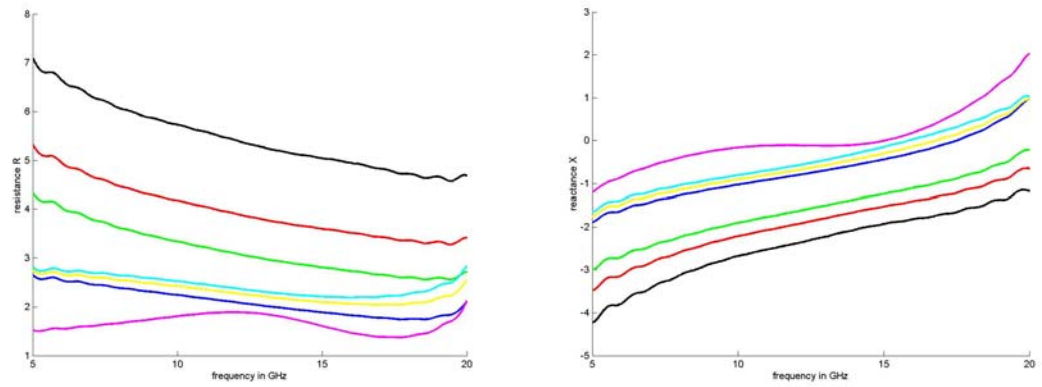


Figure 7.24. Resistance and reactance (structure B8).

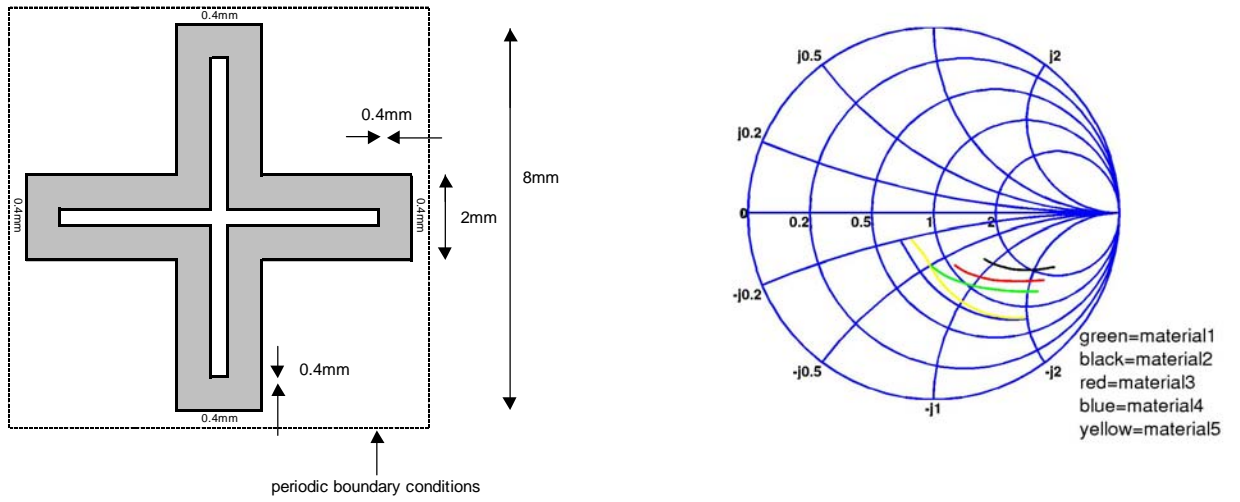


Figure 7.25. Cross dimensions and equivalent impedance plotted in the Smith chart (structure B9).

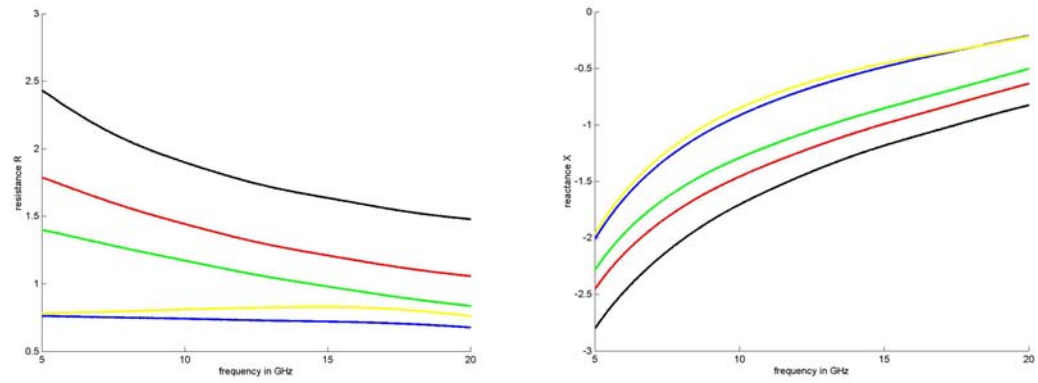


Figure 7.26. Resistance and reactance (structure B9).

FSS with densely arranged elements

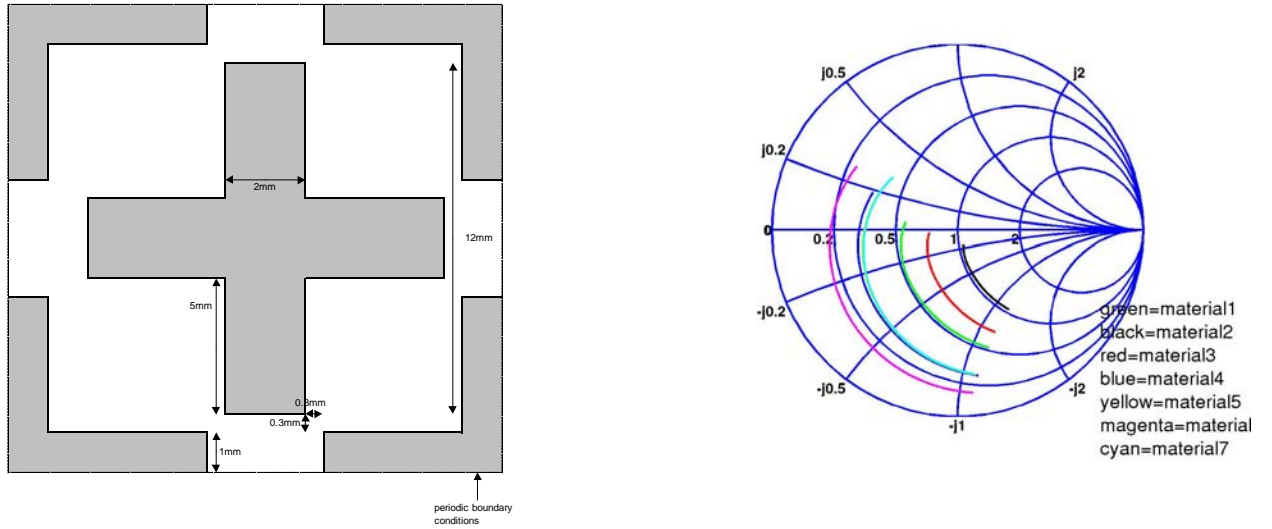


Figure 7.27. Cross dimensions and equivalent impedance plotted in the Smith chart (structure C1).

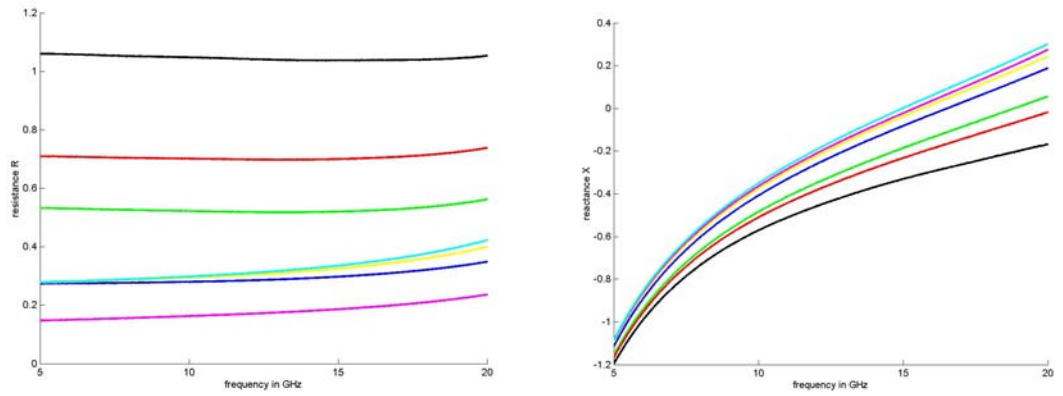


Figure 7.28. Resistance and reactance (structure C1).

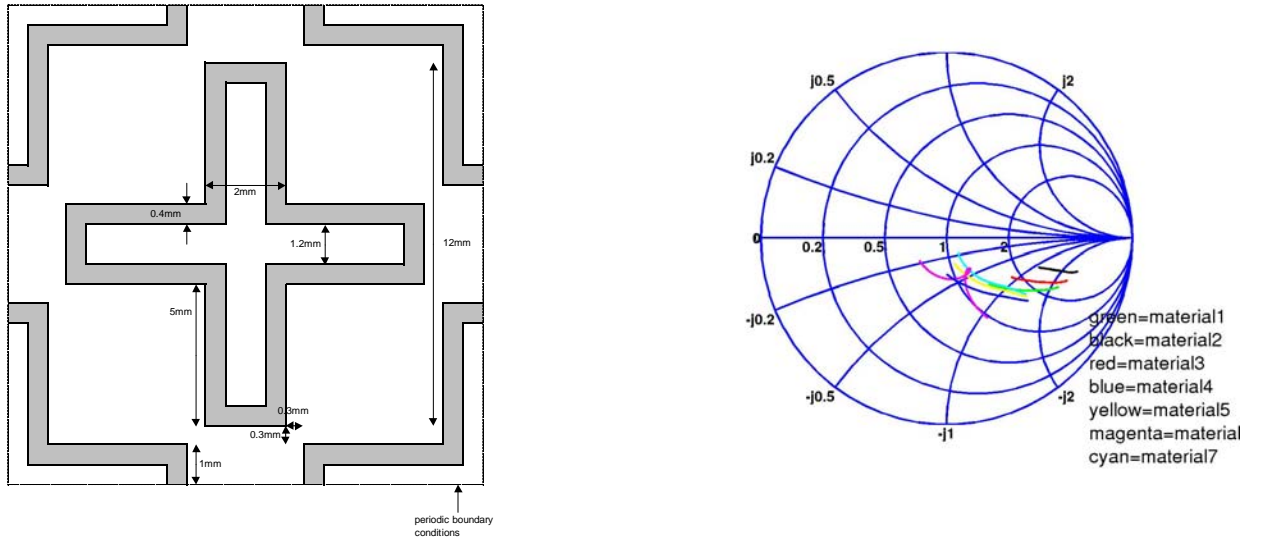


Figure 7.29. Cross dimensions and equivalent impedance plotted in the Smith chart (structure C2).

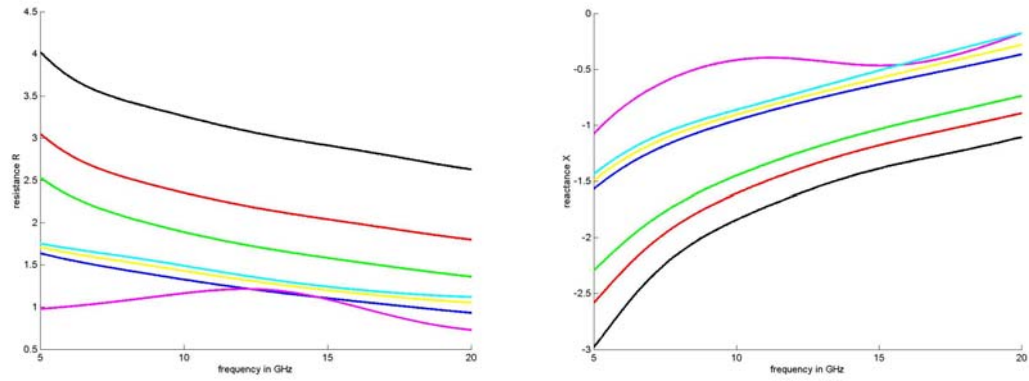


Figure 7.30. Resistance and reactance (structure C2).

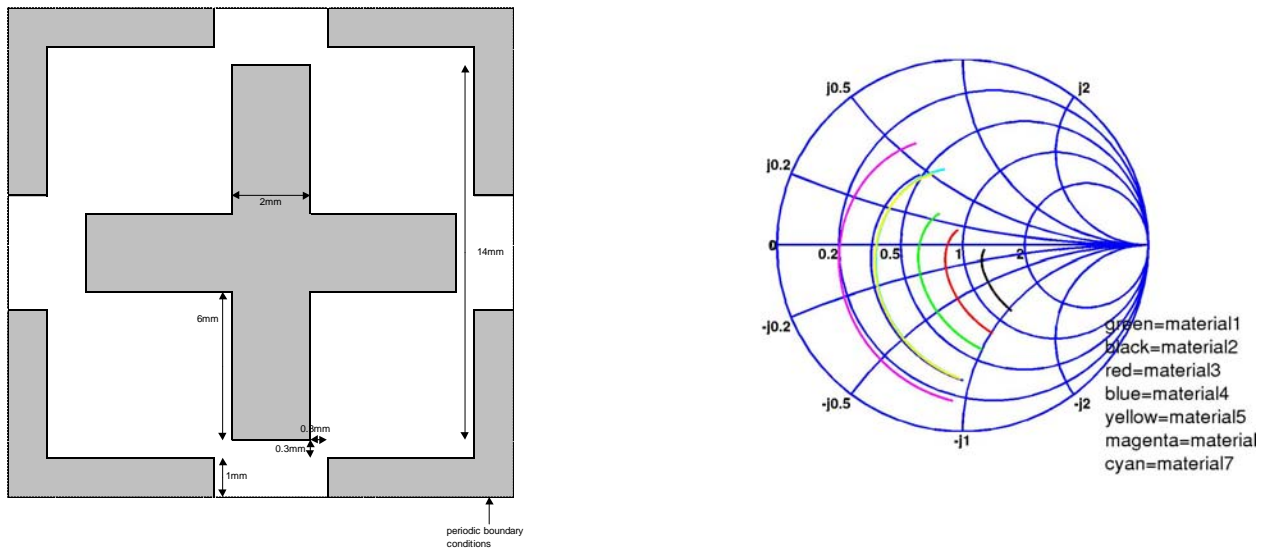


Figure 7.31. Cross dimensions and equivalent impedance plotted in the Smith chart (structure C3).

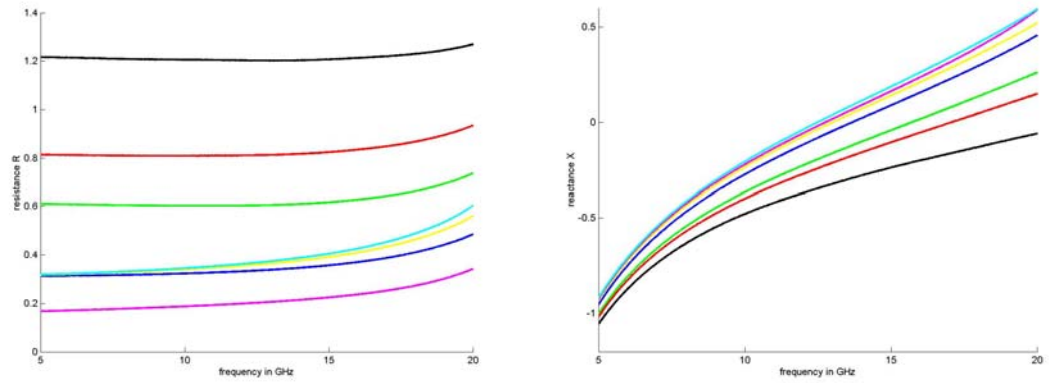


Figure 7.32. Resistance and reactance (structure C3).

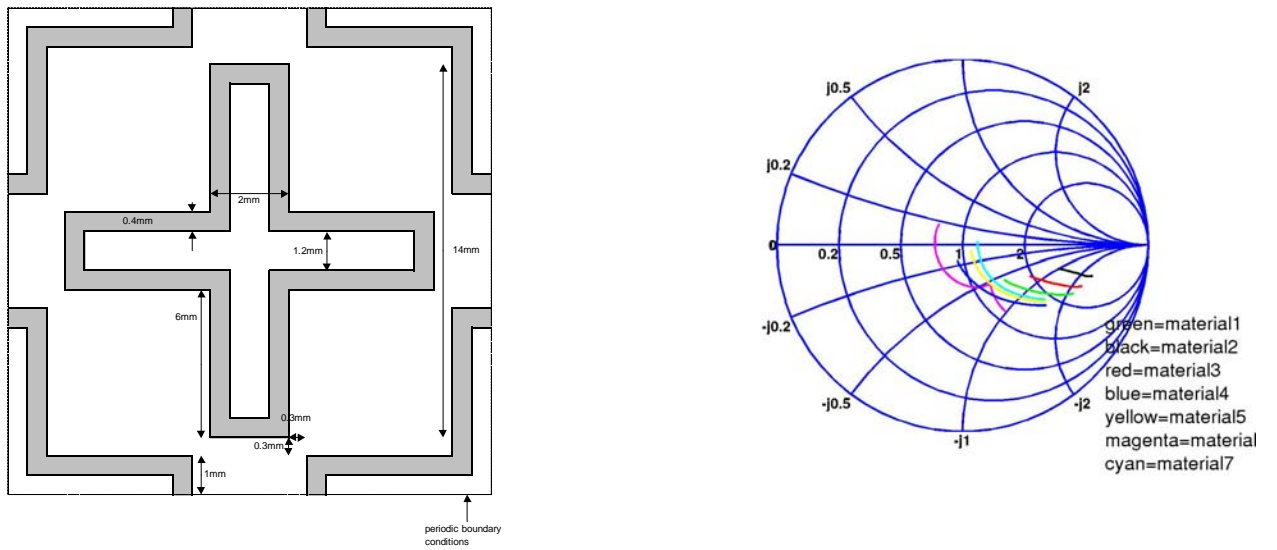


Figure 7.33. Cross dimensions and equivalent impedance plotted in the Smith chart (structure C4).

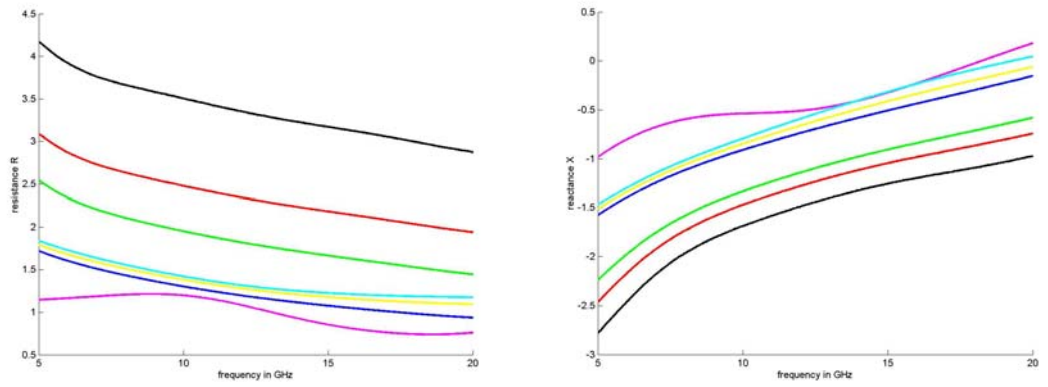


Figure 7.34. Resistance and reactance (structure C4).

Appendix C: Experimental Synthesis of Sulfur-Bridged Thiophenes

Synthesis of Bis(3-hexyl-2-thienyl)sulfide (2)

A 1.6M hexanes solution of *n*-butyllithium (4.0 mL, 6.4 mmol) was added slowly to a stirred solution of 3-hexyl-2-bromothiophene (1.51 g, 6.12 mmol) in THF (40 mL) at -78 °C. The solution was stirred at -78 °C for 1 h and then a solution of bis(phenylsulfonyl) sulfide (0.980 g, 3.13 mmol) in THF (5 mL) was added dropwise over 10 min. After stirring at -78 °C for 3 h, the reaction mixture was allowed to warm to room temperature and stirred for an additional 30 min. The mixture was poured onto water (100 mL), and the aqueous layer was extracted with ether. The combined organics were dried (MgSO₄), filtered, and the solvent was evaporated under reduced pressure. The residue was subjected to column chromatography (silica, pentane) to give **6** as a colourless oil, yield 785 mg (70 %). ¹H NMR (CD₂Cl₂): δ 7.27 (d, *J* = 5.1 Hz, 2H), 6.90 (d, *J* = 5.1 Hz, 2H), 2.75 (t, *J* = 7.7 Hz, 4H), 1.58 (m, 4H), 1.32 (m, 12H), 0.90 (t, *J* = 6.6 Hz, 6H) ppm. ¹³C NMR (CD₂Cl₂): δ 144.4, 135.0, 134.4, 124.7, 32.0, 30.8, 30.7, 29.3, 23.0, 14.2 ppm. MS (LSIMS): *m/z* 366 (M⁺, 100 %). HRMS Calcd for C₂₀H₃₀S₃:366.1510. Found. 366.1503.

Synthesis of Bis(4-hexyl-2-thienyl)sulfide (3)

A 1.6 M hexanes solution of *n*-butyllithium (10.0 mL, 16.0 mmol) was added dropwise to a solution of diisopropylamine (2.24 mL, 16.0 mmol) in THF at 0 °C. After stirring for 30 minutes the solution was cooled to -78 °C and a solution of 3-hexylthiophene **3a** (2.64 g, 15.7 mmol) in THF (60 mL) was added dropwise. The suspension was stirred at -78 °C for 1 h and then a solution of bis(phenylsulfonyl) sulfide (2.48 g, 7.90 mmol) in THF (20 mL) was added dropwise via cannula. After stirring at -78 °C for 3 h, the reaction mixture was allowed to warm to room temperature and stirred for an additional 30 min. The mixture was poured onto water (100 mL), and the aqueous layer was extracted with ether. The combined organic extracts were washed with water and dried (Na₂SO₄). The residue was subjected to column chromatography (silica, pentane) to give **3** as colorless oil, yield 1.90 g (66 %). ¹H NMR (CD₂Cl₂): δ 7.27 (d, *J* = 1.1 Hz, 2H), 6.90 (d, *J* = 1.1 Hz, 2H), 2.75 (t, *J* = 7.7 Hz, 4H), 1.58 (m, 4H), 1.34 (m, 12H), 0.90 (t, *J* = 7.0 Hz, 6H) ppm. ¹³C NMR (CD₂Cl₂): δ 146.9, 129.8, 129.1, 128.0, 32.1, 30.9, 29.5, 29.4, 23.0, 14.2 ppm. MS (LSIMS): *m/z* 366 (M⁺, 100 %). HRMS Calcd for C₂₀H₃₀S₃:366.1510. Found. 366.1503.

Synthesis of Bis(3,4-ethylenedioxy-2-thienyl)sulfide (4)

Bis(3,4-ethylenedioxy-2-thienyl)sulfide **4** was prepared by lithiation of EDOT followed by treatment with bis(phenylsulfonyl)sulfide (*Macromolecules* **2004**, *37*, 2010)

Bis(5-thiophen-2'-yl- 3,4-ethylenedioxy-2-thienyl)sulfide (5)

A solution of **5a** (2.00 g, 6.60 mmol) in THF (30 mL) cooled to -78 °C was treated dropwise with a 1.6M hexanes solution of *n*-butyllithium (4.12 mL, 6.60 mmol). The

resulting bright red solution was stirred for 1.5 h at $-78\text{ }^{\circ}\text{C}$. A solution of bis(phenylsulfonyl) sulfide (1.04 g, 3.30 mmol) in THF (10 mL) was added dropwise via cannula and the resulting yellow solution was stirred at $-78\text{ }^{\circ}\text{C}$ for an additional 30 min. The mixture was poured onto water (100 mL), extracted with diethyl ether and dried (Na_2SO_4). The solvent was removed by rotary evaporation and the residue was purified by column chromatography (silica, 1:1 hexanes/chloroform) to afford a yellow solid. This was recrystallized from methanol/chloroform to give **5** as yellow needles, yield 1.04 g (66%). Mp: $176\text{ }^{\circ}\text{C}$. ^1H NMR (CDCl_3): δ 7.25 (dd, $J = 5.1, 1.5$ Hz, 2H), 7.22 (dd, $J = 3.7, 1.5$ Hz, 2H), 7.01 (dd, $J = 5.1, 3.7$ Hz, 2H), 4.33 (m, 8H) ppm. ^{13}C NMR (CDCl_3): δ 143.9, 136.9, 134.3, 127.3, 124.7, 123.7, 115.7, 104.6, 65.2, 64.9 ppm. HRMS (EI) for $\text{C}_{20}\text{H}_{14}\text{O}_4\text{S}_5$ [M^+]: Calcd: 477.9496. Found: 477.9495. Anal. Calcd. For $\text{C}_{20}\text{H}_{14}\text{O}_4\text{S}_5$: C, 50.19; H, 2.95%. Found: C, 49.94; H, 2.80%.

Synthesis of 2,5-Bis[(2-thienyl)thio]-3-hexyl-thiophene (6)

A solution of 2-thiophenethiol (720 mg, 6.20 mmol) in DMF (5 mL) was added dropwise to a stirred slurry of 3-hexyl-2,5-dibromothiophene **6a** (0.980 g, 3.00 mmol), KOH (368 mg, 6.57 mmol), and copper (I) oxide (230 mg, 1.60 mmol) in DMF (20 mL) at room temperature. The reaction mixture was then stirred at $120\text{ }^{\circ}\text{C}$ for 20 h. The resulting dark brown mixture was cooled to room temperature and poured into 6M HCl (20 mL). Dichloromethane (100 mL) was added to this and the mixture was filtered through a small pad of Celite. The organic layer was separated, washed with water and dried (MgSO_4). Chromatography (silica, hexanes) gave 0.820 g (66 %) of **6** as a colorless oil. ^1H NMR (CD_2Cl_2): δ 7.35 – 7.25 (m, 2H), 7.15 – 7.05 (m, 2H), 6.92 – 6.85 (m, 2H), 6.80 (s, 1H), 2.60 (t, $J = 7.7$ Hz, 2H), 1.50 (m, 2H), 1.25 (m, 6H), 0.80 (t, $J = 7.0$ Hz, 3H) ppm. ^{13}C NMR (CD_2Cl_2): δ 147.8, 138.7, 135.6, 134.0, 133.9, 132.8, 132.5, 132.0, 130.6, 129.5, 127.8, 127.6, 31.9, 30.6, 29.3 (2 CH_2) 22.8, 14.3 ppm. MS (EI): m/z 396 (M^+ , 100%). HRMS Calcd for $\text{C}_{18}\text{H}_{20}\text{S}_5$: 396.0169. Found. 396.0159.

Synthesis of 5,5'-Bis-(thiophen-2-ylsulfanyl)-[2,2'] bithiophene (7)

A solution of 2-thiophenethiol (806 mg, 6.95 mmol) in DMF (5 mL) was added dropwise to a stirred slurry of 5,5'-dibromo-2,2'-bithiophene **7a** (1.10 g, 3.42 mmol), KOH (406 mg, 7.25 mmol), and copper (I) oxide (450 mg, 3.14 mmol) in DMF (50 mL) at room temperature. The reaction mixture was then stirred at $120\text{ }^{\circ}\text{C}$ for 20 h. The resulting dark brown mixture was cooled to room temperature and poured into 6 M HCl (60 mL). Dichloromethane (100 mL) was added to this and the mixture was filtered through a small pad of Celite. The organic layer was separated, washed with water and dried (MgSO_4). Chromatography (silica, pentane) gave 720 mg (54 %) of **7** as a pale yellow solid. Mp: $92\text{ }^{\circ}\text{C}$. ^1H NMR (CDCl_3) δ 7.40 (m, 2H), 7.25 (m, 2H), 7.08 (d, $J = 3.7$ Hz, 2H), 7.00 (m, 2H), 6.96 (d, $J = 3.7$ Hz, 2H) ppm. ^{13}C NMR (CDCl_3): δ 140.9, 136.0, 135.1, 134.1, 133.8, 130.9, 128.3, 124.7 ppm. MS (EI): m/z 394 (M^+ , 100%). Anal. Calcd for $\text{C}_{16}\text{H}_{10}\text{S}_6$: C, 48.69; H, 2.55 %. Found: C, 48.06; H, 2.63 %.

Synthesis of 2,5-Bis-(thiophen-2-ylsulfanyl)- 3,4-ethylenedioxythiophene (8)

A solution of 2-thiophenethiol (1.32 g, 11.3 mmol) in DMF (5 mL) was added dropwise to a stirred slurry of 2,5-dibromomoeDOT **8a** (1.69 g, 5.63 mmol), KOH (624 mg, 11.1 mmol), and copper (I) oxide (936 mg, 3.14 mmol) in DMF (20 mL) at room temperature. The reaction mixture was then stirred at 140 °C for 20 h. The resulting dark brown mixture was cooled to room temperature and poured into 6 M HCl (25 mL). Dichloromethane (100 mL) was added to this and the mixture was filtered through a small pad of Celite. The organic layer was separated, washed with water and dried (MgSO₄). Chromatography (silica, 7:3 dichloromethane/pentane) gave colorless oil. The oil was dissolved in a minimal amount of dichloromethane and a white solid was precipitated by the addition of pentane, yield 1.20 g (57 %). Mp: 50 °C. ¹H NMR (CD₂Cl₂): δ 7.35 (m, 2H), 7.20 (m, 2H), 6.95 (m, 2H), 4.30 (s, 4H) ppm. ¹³C NMR (CD₂Cl₂): δ 143.7, 134.7, 133.6, 130.3, 128.1, 111.3, 65.4 ppm. MS (LSIMS): *m/z* 370 (M⁺, 55 %). Anal. Calcd for C₁₄H₁₀O₂S₅: C, 45.38; H, 2.72 %. Found: C, 45.62; H, 2.62 %.

Synthesis of Bis(5,5'-bithienyl)sulfide (9)

A 10 mL toluene solution containing 2-(tributylstannyl)thiophene (1.85 g, 2.25 mmol), bis(5-bromo-2-thienyl)sulfide **9a** (800 mg, 2.25 mmol) and Pd(PPh₃)₄ (130 mg) was refluxed in the dark for 20 h. After cooling to room temperature, the black mixture was diluted with ether (100 mL) and poured into saturated potassium fluoride (100 mL). The resulting tributyltin fluoride was filtered off and washed with cold ether (3 x 15 mL). The organic phase was collected, washed with brine and dried (Na₂SO₄). The solvent was removed by rotary evaporation and the residue was purified by column chromatography (silica, 1:1 hexane/diethyl ether) to provide a bright yellow solid. This was recrystallized from hexanes/dichloromethane to give **9** as yellow plates, yield 692 mg (85 %). Mp: 96 °C. ¹H NMR (CDCl₃): δ 6.96 – 7.20 (m, 5H) ppm. ¹³C NMR (CDCl₃): δ 141.6, 136.7, 133.9, 133.7, 127.9, 124.9, 124.2, 123.8. MS (LSIMS): *m/z* 362 (M⁺, 100%). Anal. Calcd for C₁₆H₁₀S₅: C, 53.00; H, 2.78; S, 44.22%. Found: C, 52.80; H, 2.81; S, 44.43%.

Synthesis of Bis(5-(3',4'-ethylenedioxythienyl)-thiophen-yl-2)sulfide (10)

A solution of 2-(tributylstannyl)-3,4-(ethylenedioxy)thiophene (2.50 g, 5.80 mmol), **9a** (0.860 g, 2.41 mmol) and Pd(PPh₃)₄ (140 mg) in toluene (15 mL) was refluxed for 20 h. The toluene was removed under vacuum, and the remaining dark yellow residue was dissolved in a minimal amount of dichloromethane. The crude product was precipitated by the addition of hexanes. This material was further purified by column chromatography (silica, 1:1 hexanes/chloroform) to give **10** as a bright yellow solid, yield 890 mg (77 %). Mp: 130 °C. ¹H NMR (CDCl₃): δ 7.10 (d, J = 3.7 Hz, 2H), 7.01 (d, J = 3.7 Hz, 2H), 6.20 (s, 2H), 4.30 – 4.28 (m, 4H), 4.27 – 4.18 (m, 4H) ppm. ¹³C NMR (CDCl₃): δ 142.0, 139.3, 138.1, 133.5, 133.2, 122.8, 109.7, 97.7, 65.2, 64.8 ppm. MS (LSIMS): *m/z* 478 (M⁺, 100%). Anal. Calcd for C₂₀H₁₄O₄S₅: C, 50.19; H, 2.95; S, 33.50%. Found: C, 50.01; H, 2.99; S, 33.68%.

Synthesis of 2,3-Dihydro-7H-thieno[3,4-b][1,4]dioxine-5-thione (11)

EDOT (0.52g, 3.66mmol) was dissolved in a 100mL sidearm flask in 20 mL freshly distilled THF. To this solution there was added nBuLi (2.4mL, 3.84mmol) at RT dropwise via syringe and the resulting pale yellow solution was stirred at RT. After 45 min, a large excess of elemental sulfur (0.2g, 6.23mmol) was added to the stirring solution as a pure powder over 10 min and the resulting deep red solution was stirred with occasional heating for a further 30 min, after which LiAlH₄ was slowly added to the solution in large excess. The reaction mixture was slowly worked up by adding dilute HCl until there was no more sign of any reaction. DCM (100 mL) was added, and the solution was washed with distilled water until the aqueous layer was clear and colorless. The organic layer was dried over MgSO₄, filtered, and concentrated to yield a yellow brown solid which was purified by chromatography over silica (Hex:EtoAc 5:1) and crystallized from benzene and hexanes to yield bright yellow needles, yield 0.35g (55%). Mp: 170-172 °C; ¹H NMR (CDCl₃): δ 4.28 (m, 4H), 3.87(s, 2H).

Polymerization using FeCl₃

General procedure. To a suspension of four equivalent of anhydrous FeCl₃ in 5 ml CHCl₃, was added dropwise a solution of one equivalent of the monomer dissolved in 1 or 2 ml of CHCl₃. After stirring the mixture at room temperature for 3 hours, 100 ml of methanol was added to precipitate the polymer. The mixture was put in the freezer overnight. After filtration, the polymer was washed by 1 L of methanol and dried under vacuum overnight.

Electrochemistry

The oxidation peak measurements (first scan) of thiophene monomers were performed in CH₂Cl₂ containing 0.1 M of n-Bu₄NBF₄. Platinum wire and non-aqueous Ag/Ag⁺ electrode were used as counter and reference electrodes respectively. Platinum electrode (1.6 mm, BAS) was used as working electrode. For electropolymerization deposition of the corresponding polymer, 1 M of n-Bu₄NBF₄ was used as supporting electrolyte because the polymer is more stable on the surface of the electrode (no alteration in the oxidation polymer current was observed after 100 scans at 0.1 mV/s). Silver wire was used as reference electrode.

Appendix D: Phosphorous-Bridged Thiophenes Experimental

General Synthesis of (3,4-ethylenedioxy-2-thienyl) phosphine derivatives

The synthesis of EDOT-substituted phosphines **1-4** is exemplified by the synthesis of **1**. EDOT (1.313 g, 9.25 mmol) was dissolved in THF (50 ml) and treated with *n*-BuLi (1.6 M, 3 ml, 9.36 mmol) at room temperature. After two hours of stirring, the mixture was cooled to -78°C and chlorodiphenylphosphine (3 ml, 3.1 mmol) was added dropwise to the reaction mixture. The mixture was stirred at -78°C for two hours and gradually brought to room temperature. The mixture was then poured into water (100 ml) and extracted using CH_2Cl_2 (2x100 ml). The organic layers were combined and dried over anhydrous MgSO_4 . Removal of the solvent gave a crude product which was purified by chromatography using silica gel and chloroform as the elution. The product was then recrystallized in CH_2Cl_2 /Methanol. In case of thiophene phosphine **5**, it was prepared by reaction of phosphine **1** and MesSCl in the same condition described for the other phosphine thiophene.

(3,4-ethylenedioxy-2-thienyl)diphenylphosphine, EDOT-PPh₂ (1)

Yield 74%. M. Pt. 84°C ; ^1H NMR (CD_2Cl_2 , 300 MHz): δ 4.20 (m, 4H), 6.60 (s, 1H), 7.40 (m, 10H); ^{13}C NMR (CD_2Cl_2 , 125 MHz): δ 64.94 (CH₂), 65.41 (CH₂), 106.22 (CH), 109.95 (C, d, $J = 28.6$ Hz), 128.75 (4CH, d, $J = 6.8$ Hz), 129.23 (2CH), 133.54 (4CH, d, $J = 20.2$ Hz), 137.24 (2C, d, $J = 8.6$ Hz), 142.72 (C, d, $J = 3.7$), 147.01 (2C, d, $J = 18.9$ Hz); ^{31}P NMR (CD_2Cl_2 , 145 MHz): δ -28.12; UV-Vis (CH_2Cl_2): λ_{max} (nm) 274 nm ($16450 \text{ M}^{-1}\text{cm}^{-1}$). HRMS Calcd for $\text{C}_{18}\text{H}_{15}\text{O}_2\text{PS}$: 326.0530. Found: 326.0535. Anal. Calcd. For $\text{C}_{18}\text{H}_{15}\text{O}_2\text{P}$: C, 66.25; H, 4.63; O, 9.80%. Found: C, 66.21; H, 4.17; O, 9.95%.

Bis(3,4-ethylenedioxy-2-thienyl)phenylphosphine, (EDOT)₂PPh (2)

Yield 74%. M. Pt. 137°C ; ^1H NMR (CD_2Cl_2 , 300 MHz): δ 4.20 (m, 8H), 6.60 (s, 2H), 7.40 (m, 5H); ^{13}C NMR (CD_2Cl_2 , 125 MHz): δ 64.91 (2CH₂), 65.42 (2CH₂), 106.31 (2CH), 109.22 (C, d, $J = 25.5$ Hz), 128.62 (2CH, d, $J = 6.8$ Hz), 129.12 (CH), 132.48 (2CH, d, $J = 19.8$ Hz), 136.95 (2C, d, $J = 6.3$ Hz), 142.53 (2C, d, $J = 4$ Hz), 146.90 (2C, d, $J = 20.5$ Hz); ^{31}P NMR (CD_2Cl_2 , 145 MHz): δ -50.5; UV-Vis (CH_2Cl_2): λ_{max} (nm) 274 nm ($21500 \text{ M}^{-1}\text{cm}^{-1}$). HRMS Calcd. For $\text{C}_{18}\text{H}_{15}\text{O}_4\text{PS}_2$: 390.0149. Found: 390.0144. Anal. Calcd. For $\text{C}_{18}\text{H}_{15}\text{O}_4\text{PS}_2$: C, 55.38; H, 3.87; O, 16.39%. Found: C, 54.60; H, 3.89; O, 16.39%.

Tris(3,4-ethylenedioxy-2-thienyl)phosphine, (EDOT)₃P (3)

Yield 77%. M. Pt. 181°C ; ^1H NMR (CD_2Cl_2 , 300 MHz): δ 4.20 (m, 12H), 6.60 (s, 3H); ^{13}C NMR (CD_2Cl_2 , 125 MHz): δ 64.90 (CH₂), 65.43 (CH₂), 106.15 (CH), 108.75 (C, d, $J = 22.6$ Hz), 142.47 (C, d, $J = 4.5$ Hz), 146.14 (C, d, $J = 21.5$ Hz); ^{31}P NMR (CD_2Cl_2 , 145 MHz): δ -50.54; UV-Vis (CH_2Cl_2): λ_{max} (nm) 277 nm ($25450 \text{ M}^{-1}\text{cm}^{-1}$). HRMS Calcd for $\text{C}_{18}\text{H}_{15}\text{O}_6\text{PS}_3$: 453.9768. Found: 453.9757. Anal. Calcd. For $\text{C}_{18}\text{H}_{15}\text{O}_6\text{PS}_3$: C, 47.57; H, 3.33; O, 21.12%. Found: C, 47.07; H, 3.17; O, 21.97%.

2-5-bis(diphenylphosphinyl)-3,4-ethylenedioxythiophene, Ph₂P-EDOT-PPh₂ (4)

Yield 63%. M. Pt. 101 °C; ¹H NMR (CD₂Cl₂, 300 MHz): δ 4.20 (s, 4H), 7.40 (m, 20H); ¹³C NMR(CD₂Cl₂, 125 MHz): δ 65.14 (CH₂), 116.35 (C, d, J = 31.3), 128.74 (CH, d, J = 7.5 Hz), 129.29 (CH), 133.57 (CH, d, J = 20.4 Hz), 136.79 (C, d, J = 8.8 Hz), 146.91 (C, dd, J = 2.9 Hz, J = 17.9 Hz); ³¹P NMR (CD₂Cl₂, 145 MHz): δ -26.5; UV-Vis: (CH₂Cl₂) λ_{max} (nm) 292 nm; (25230 M⁻¹cm⁻¹). HRMS calcd. For C₃₀H₂₄O₂P₂S: 510.0972. Found: 510.0963. Anal. Calcd. For C₃₀H₂₄O₂P₂S: C, 70.58; H, 4.74; O, 6.27; P, 12.13%. Found: C, 67.97; H, 4.48; O, 6.67; P, 11.67%.

2-diphenylphosphinyl-5-mesitylthio-3,4-ethylenedioxythiophene, MesS-EDOT-PPh₂ (5)

Yield 70%. M. Pt. 102 °C; ¹H NMR (CD₂Cl₂, 300 MHz): δ 2.30 (s, 3H), 2.50 (s, 6H), 4.2 (m, 4H), 6.90 (s, 2H), 7.30 (m, 10H); ¹³C NMR(CD₂Cl₂, 125 MHz): δ 21.33 (CH₃), 22.34 (2CH₃), 65.35 (CH₂), 65.37 (CH₂), 110.97 (2C, d, J = 31.6 Hz), 116.00 (2 C), 128.97 (4 CH, d, J = 6.8 Hz), 129.48 (2CH), 129.79 (2 CH) 133.68 (4 CH, d, J = 19.2 Hz), 137.12 (C, d, J = 7.9), 139.65 (C), 142.65 (C, d, J = 3.4 Hz), 143.21 (C), 146.71 (2 C, d, J = 19.2 Hz); ³¹P NMR (CD₂Cl₂, 145 MHz): δ -27.6. HRMS Calcd for C₂₇H₂₅O₆PS₂: 476.1034. Found: 476.1033. Anal. Calcd. For C₂₇H₂₅O₆PS₂: C, 68.04; H, 5.29; O, 6.71; P, 7.93%. Found: C, 67.58; H, 4.96; O, 7.12; P, 6.08%.

Synthesis of *cis*-Mo(CO)₄(PAR₃)₂ (7; PAR₃ ≡ 1)

A solution of **1** (0.652 g, 2 mmol) in CH₂Cl₂ (2 ml) was added dropwise to a stirred slurry of *cis*-Mo(CO)₄(piperidine)₂ (0.380 g, 1 mmol) in CH₂Cl₂ (10 ml) at room temperature. The mixture was stirred overnight and filtered through a pad of silica gel. After filtration, the solution was concentrated and the product was precipitated by the addition of pentane. The complex was isolated as a white solid (yield 43%). M. Pt. 115 °C; IR: ν(CO) 2023, 1924, 1908, 1878 cm⁻¹; ¹H NMR (CD₂Cl₂, 300 MHz): δ 4.10 (m, 8H), 6.60 (d, J = 2.10 Hz, 2H), 7.20 (m, 8H), 7.40 (m, 12); ¹³C NMR (CD₂Cl₂, 125 MHz): δ 64.60 (CH₂), 64.80 (CH₂), 105.50 (CH), 109.80 (C, dd, J = 12.5 Hz), 128.30 (C, t, J = 4.6 Hz), 130.00 (CH) 133.40 (C, t, J = 6.8 Hz), 135.90 (C, dt, J = 15.5 Hz), 143.20 (C, t, J = 3 Hz), 145.70 (C, t, J = 3.7 Hz), 210.20 (C, t, J = 9.4 Hz), 215.6 (C, t, J = 9.3 Hz); ³¹P NMR (CD₂Cl₂, 145 MHz): δ 24.3; Anal. Calcd. For C₄₀H₃₀MoO₈P₂S₂: C, 55.82; H, 3.51; O, 14.87; P, 7.20. Found: C, 54.70; H, 3.67; O, 15.36; P, 7.07%. HRMS Calcd for C₄₀H₃₀MoO₈P₂S₂: 861.9912. Found: 861.9911.

Syntheses of Mo(CO)₅(PAR₃) (8; PAR₃ ≡ 2)

Complex **8** was prepared in an analogous fashion to **9**. Yield 70%. M. Pt. 172 °C; IR: ν(CO) 1946 cm⁻¹; ¹H NMR (CD₂Cl₂, 300 MHz): δ 4.20 (s, 8H) 6.70 (d, J = 2.2 Hz, 2H), 7.40 (m, 3H), 7.60 (m, 3H); ¹³C NMR(CD₂Cl₂, 125 MHz): δ 64.90 (CH₂), 65.30 (CH₂), 106.70 (CH, d, J = 2.4 Hz), 128.8 (CH, d, J = 9.8 Hz), 130.8 (CH), 132.20 (CH, d, J = 13.1 Hz), 135.30 (C, d, J = 39.9 Hz), 143.20 (C, d, J = 6.4 Hz), 146.4 (C, d, J = 8.1 Hz), 206.40 (C, d, J = 9.5 Hz), 211.60 (C, d, J = 24.7 Hz); ³¹P NMR (CD₂Cl₂, 145 MHz): δ 7.6. HRMS Calcd for C₂₃H₁₅MoO₉P₂S₂: 627.8950. Found: 627.8985.

Synthesis of Mo(CO)₅(PAr₃) (9: PAr₃ = 3)

Cis-Mo(CO)₄(piperidine)₂ (1.154 g, 3 mmole) was added to a solution of **3** (0.422 g, 0.9 mmole) in CH₂Cl₂ (10 ml) at room temperature. The mixture was stirred overnight and filtered through a pad of silica gel. The product was isolated by precipitation from pentane. Yield 60%. M. Pt. 202 °C; IR: $\nu(\text{CO})$ 1947 cm⁻¹; ¹H NMR (CD₂Cl₂, 300 MHz): δ 4.10 (m, 8H), 6.60 (d, J = 2.9 Hz, 2H); ¹³C NMR (CD₂Cl₂, 125 MHz): δ 64.70 (CH₂), 65.00 (CH₂), 106.30 (CH), 107.10 (C, d, J = 36.7 Hz), 142.70 (C, d, J = 7.3 Hz), 145.8 (C, d, J = 10.6 Hz), 206.0 (C, d, J = 9.5 Hz), 211.60 (C, d, J = 24.6 Hz); ³¹P NMR (CD₂Cl₂, 145 MHz): δ -8.5; HRMS Calcd for C₂₃H₁₅MoO₁₁PS₃: 691.8569. Found: 691.8618. Anal. Calcd. For C₂₃H₁₅MoO₁₁PS₃ C, 40.01; H, 2.19; O, 25.49; S, 13.93; P, 4.49%. Found: C, 39.99; H, 2.22; O, 25.65; S, 14.34; P, 4.44%.

Synthesis of *cis*-Mo(CO)₄(PAr₃)₂ (10: PAr₃ = 5)

The synthesis procedure was similar to the complex *cis*-Mo(CO)₄(PAr₃)₂ (**7**). Yield 40 %. IR $\nu(\text{CO})$ 2022, 1945, 1927, 1908 cm⁻¹; ¹H NMR (CD₂Cl₂, 300 MHz) δ 2.25 (s, 6H), 2.45 (s, 12H), 4.10 (m, 4H), 4.25 (m, 4H), 6.95 (s, 4H), 7.14 (m, 4H), 7.30 (m, 6H); ³¹P NMR (CD₂Cl₂, 145 MHz) δ 25.28. HRMS Calcd for C₅₈H₅₀O₈S₄P₂Mo: 1162.0919. Found: 1162.0903.

Appendix E: Silicon-Bridged Thiophenes Experimental

Bis-(2,3-dihydro-thieno[3,4-*b*][1,4]dioxin-5-yl)-dimethyl-silane (3).

To a solution of EDOT (2.10 g, 14.8 mmoles) dissolved in 50 ml of THF under argon was added 7.4 ml (14.8 mmoles) of nBuLi (2 M) dropwise. After stirring for 1 hour at room temperature, the mixture was cooled to $-78\text{ }^{\circ}\text{C}$. Dichlorodimethylsilane (0.98 g, 7.6 mmoles) was added dropwise and the mixture was stirred for a further 3 hours at $-78\text{ }^{\circ}\text{C}$ followed by 21 hours at room temperature. The mixture was then poured into 100 ml of water and the product was extracted using 2x100 ml portions of CH_2Cl_2 . The organic layers were combined and dried over MgSO_4 . After evaporation of the solvent, the product was purified by chromatography on silica gel using CH_2Cl_2 as the eluent. The product was colorless and crystallized slowly after a few weeks affording a yield of 75 % (1.9 g, 5.6 mmoles). ^1H NMR (CD_2Cl_2 , 300 MHz): $\delta = 0.60$ (s, 6H), 4.20 m (s, 8H), 6.60 (s, 2H); ^{13}C NMR (CD_2Cl_2 , 75 MHz): $\delta = -1.20$ (2CH_3), 64.70 (2CH_2), 64.80 (2CH_2), 106.10 (2CH), 109.10 (2C), 142.80 (2C), 148.20 (2C); ^{29}Si NMR (CDCl_3 , 100 MHz): $\delta = -16.83$. Mass spectra: LSIMS: 340 (M). HRMS (EI) for $\text{C}_{14}\text{H}_{16}\text{S}_2\text{O}_4\text{Si}$ [M^+]: Calcd: 340.0259. Found: 340.0262.

Dimethyl-bis-(2,3,2',3'-tetrahydro-[5,5']bithieno[3,4-*b*][1,4]dioxinyl)-7-yl)-silane (4)

To a solution of biEDOT (1.52 g, 5.4 mmoles) dissolved in 50 ml of THF under argon was added 2.7 ml (5.40 mmoles) of nBuLi (2 M) dropwise. After stirring for 1 hour at room temperature, the mixture was cooled at $-78\text{ }^{\circ}\text{C}$. Dichlorodimethylsilane (0.38 g, 2.9 mmoles) was added dropwise and the mixture was stirred for a further 3 hours at $-78\text{ }^{\circ}\text{C}$ and then for 21 hours at room temperature. Following that, the mixture was poured in 100 ml of water and the product was extracted using 2x100 ml portions of diethyl ether. The organic layers were combined and dried over MgSO_4 . After evaporation of ether, the crude was dissolved in acetone, and precipitated by adding pentane and freezing the mixture overnight. A pale yellow solid was formed (1.2 g, 1.9 mmoles) in a 70 % yield. ^1H NMR (CDCl_3 , 300 MHz): $\delta = 0.60$ (s, 6H), 4.30 (m, 16H), 6.20 (s, 2H); ^{13}C NMR (CDCl_3 , 75 MHz): $\delta = -0.96$ (2CH_3), 64.68 (2CH_2), 64.83 (2CH_2), 64.97 (2CH_2), 65.22 (2CH_2), 97.94 (CH), 106.48 (2C), 110.43 (2C), 115.84 (2C), 137.50 (1C), 138.01 (2C), 141.48 (C), 147.57 (C); ^{29}Si NMR (CDCl_3 , 100 MHz): $\delta = -17.12$; Mass spectra LSIMS: 620 (M). HRMS (EI) for $\text{C}_{26}\text{H}_{24}\text{S}_4\text{O}_8\text{Si}$ [M^+]: Calcd: 620.0123. Found: 620.0116.

Appendix F: Amine-Bridged Thiophenes

Tributyl-(2,3-dihydro-thieno[3,4-b][1,4]dioxin-5-yl)-stannane

ESnBu₃ (**5**) was prepared according to a procedure reported by Swager (J. Am. Chem. Soc. 1997, Vol. 119, No. 51, 12576) with few modifications: SnBu₃Cl was added to the lithiated EDOT at -78 °C and the mixture was stirred at 50 °C for 2.50 hours.

Tris-(2,3-dihydro-thieno[3,4-b][1,4]dioxin-5-yl)-pheneyl]-amine (1).

The synthesis was performed in toluene at 110 °C for 24 hours in presence of six equivalents of ESnBu₃ (**5**) and Pd(PPh₃)₄ as catalyst. The product was extracted by 2 x 200 ml of CH₂Cl₂. The organic layers were combined and washed by 2 x 100 ml of H₂O and dried over MgSO₄. After evaporation of the solvent, compound **1** was purified by column chromatography on silica gel using CH₂Cl₂/pentane (30/70) as solvent. A yellow solid **1** was isolated (60 %). ¹H NMR (300 MHz, CD₂Cl₂): 4.20 (m, 2H); 4.30 (m, 2H); 6.30 (s, 1H); 7.10 (d, *J* = 8.2 Hz, 2H); 7.10 (d, *J* = 8.2 Hz, 2H). ¹³C NMR (75 MHz, CD₂Cl₂): δ = 65.15 (CH₂); 65.41 (CH₂); 97.27 (CH); 117.56 (C); 124.65 (CH); 127.38 (CH); 128.48 (C); 138.37 (C); 143.00 (C); 146.27 (C). MS (FAB+) *m/z* = 665 (M⁺, 100%).

(4-Bromo-phenyl)-bis-(2,3-dihydro-thieno[3,4-b][1,4]dioxin-5-yl)-pheneyl]-amine (2)

This reaction was performed in the same condition for the synthesis of product **1** using two equivalents of ESnBu₃ (**5**). The reaction seems not being selective; there is a mixture of the different products. Product **1** was isolated by column chromatography on silica gel using CH₂Cl₂/pentane (50/50) as eluent. The product is white yellow. The yield of the reaction was estimated to be 11 %. ¹H NMR (300 MHz, CD₂Cl₂): 4.11 (m, 4H); 4.18 (m, 4H); 6.15 (s, 2H); 6.88 (d, *J* = 8.83 Hz, 2H); 6.96 (d, *J* = 8.82 Hz, 4H). 7.24 (d, *J* = 8.83 Hz, 2H); 7.50 (d, *J* = 8.82 Hz, 4H). ¹³C NMR (75 MHz, CD₂Cl₂): δ = 65.15 (CH₂); 65.43 (CH₂); 97.27 (CH); 115.55 (C); 117.44 (C); 124.49 (CH); 124.83 (CH); 125.96 (CH); 127.48 (CH); 132.77 (C); 138.47 (C); 143.00 (C); 146.23 (C); 147.15 (C). MS (EI) = 605 (M), 368, 264, 111.

Bis(4-bromo-phenyl)-[4-(2,3-dihydro-thieno[3,4-b][1,4]dioxin-5-yl)-pheneyl]-amine (3)

This product was prepared following the procedure described for products **1** and **2** using one equivalent of ESnBu₃. After purification by column chromatography, a white yellow solid was formed. The yield of the reaction is 13 %. This product seems to be less stable than the others. ¹H NMR (300 MHz, CD₂Cl₂): δ = 4.20 (m, 2H); 4.30 (m, 2H); 6.30 (s, 1H); 6.98 (d, *J* = 8.82 Hz, 4H); 7.04 (d, *J* = 8.83 Hz, 2H). 7.38 (d, *J* = 8.82 Hz, 4H); 7.62 (d, *J* = 8.82 Hz, 2H). ¹³C NMR (75 MHz, CD₂Cl₂): δ = 65.13 (CH₂); 65.43 (CH₂); 97.59 (CH); 115.89 (C); 117.27 (C); 124.99 (CH); 126.10 (CH); 127.53 (CH); 129.23 (C); 132.87 (CH); 138.57 (C); 143.00 (C); 145.77 (C); 146.93 (C). MS (FAB+): *m/z* = 542.8 (M⁺).

Appendix G:

The algorithm for calculating the reflectivity, transmission and absorption is given below for calculating the reflectivity as a function of frequency and incident angle.

Define material properties thickness, permittivity, permeability and conductivity for each layer.

Define frequency and incident angle ranges. (Can also define thickness, conductivity, etc to study the effect of those variables).

Calculate the propagation number, γ , and admittance Y for each layer using equations

21 and 39, and the incident angle in each layer using $\theta_n = \arcsin\left(\frac{\gamma_{n-1}}{\gamma_n} \sin \theta_{n-1}\right)$. The

tilted admittance, η , is then calculated using equations 42 and 43 for the transverse electric and transverse magnetic polarizations.

If reflectivity is from an interface: calculate the reflection and transmission coefficients using equations 44 and 45 for each polarization, then calculate the reflectivity and transmittance using equations 46 and 47 and average the polarizations to get the total reflectivity.

If the reflectivity is from layered material: calculate the matrix elements in equation 66, for each layer. If there are more than one layers then multiply the matrices as per equation 78. Calculate r, t for each polarization using equations 69 and 70 with the appropriate tilted admittances. Calculate R and T and A using equations 71-73. If the layered material is mounted on a perfect electrical conductor, then r and t are found using equations 74 and 75, and A is found using equation 76.

List of symbols/abbreviations/acronyms/initialisms

DND	Department of National Defence
Ag/AgCl	Silver / Silver Chloride
CAD	Computer Aided Design
CHCl ₃	Chloroform
CH ₂ Cl ₂	Dichloromethane
CSA	Camphorsulfonic Acid
CV	Cyclic Voltammetry
DBSA	Dodecylbenzenesulfonic Acid
DSC	Differential Scanning Calorimeter
EDOT	3,4-ethylenedioxythiophene
ESE	EDOT – Sulphur - EDOT
FDTD	Frequency Domain Time Domain
FeCl ₃	Ferric Chloride
FSS	Frequency Selective Surface
GA	Genetic Algorithm
HCl	Hydrochloric acid
ITO	Indium Tin Oxide
MWNT	Multi-Walled Nanotube
NMR	Nuclear Magnetic Resonance
PEC	Perfect Electrical Conductor

pEDOT	poly(3,4-ethylenedioxythiophene)
PANI	Polyaniline
PML	Perfectly Matched Layers
PMMA	Polymethylmethacrylate
PPy	Polypyrrole
PTh	Polythiophene
PTSA	<i>p</i> -Toluenesulfonic Acid
R2P	Reflection – Two-Positions
RAM	Radar Absorbing Materials
RCS	Radar Cross Section
SEM	Scanning Electron Microscopy
TEM	Transmission Electron Microscopy
TGA	Thermogravimetric Analyser
TIF	Technology Investment Funded
TS	Test Sample
THF	Tetrahydrofuran
TRM	Transmission-Reflection Method
VNA	Vector Network Analyzer
α	Attenuation constant
B	Magnetic induction in units webers/m ²
β	Phase constant
c	Speed of light in a vacuum,
D	Displacement flux in units of coulombs/m ²
$\frac{\partial}{\partial}$	Time-changing displacement current

δ	Phase shift
E	Electric field strength
E_{\perp}, E_{\parallel}	Electric field strength perpendicular and parallel to the plane of incidence.
ϵ_0, ϵ_r	Permittivity of free space and relative permittivity
η	Tilted admittance
F	Force
f	Frequency in Hz
γ	Propagation number
Λ	Optical path difference
H	Magnetic field strength
i, j	Imaginary number $\sqrt{-1}$
J	Current density
k, \hat{k}	Propagation number, Propagation vector
λ, λ_0	Wavelength in matter and free space, respectively
M	Magnetization
$m_{11}, m_{12}, m_{21}, m_{22}$	Elements of the optical transmission matrix
N	Refractive index
n', n''	Real and imaginary components of the refractive index
P	Electric polarization
q	Charge
R	Reflectance, or reflectivity
r	Reflection coefficient
σ	Conductivity in units of Siemens/m

T	Transmittance
t	Transmission coefficient (also used for time in wave equation).
θ_i	Incident angle
μ_o	Permeability of free space
v	Velocity
ω	Angular frequency
χ_e, χ_m	Electric and Magnetic susceptibility
Y	Optical admittance
Z	Optical impedance

Distribution list

Note No.: DRDC ATLANTIC DLP/

LIST PART 1: CONTROLLED BY DRDC ATLANTIC LIBRARY

3 DRDC ATLANTIC LIBRARY FILE COPIES
3 DRDC ATLANTIC LIBRARY (SPARES)
1 DLP LIBRARY
1 DRDC Ottawa, Dr Satish Kashyap
1 AUTHOR

9 TOTAL LIST PART 1

LIST PART 2: DISTRIBUTED BY DRDKIM 3

1 NDHQ/ DRDKIM 3
(scanned and stored as black & white image, low resolution
- laser reprints available on request)
1 NDHQ/DMSS
1 NDHQ/DMSS 2-5-4
1 NDHQ/DMPPD 4
1 NDHQ/DMRS 7
1 NDHQ/MRCC

6 TOTAL LIST PART 2

15 TOTAL COPIES REQUIRED

Original document held by DRDC ATLANTIC Drafting Office

Any requests by DRDC ATLANTIC staff for extra copies of this document should be directed to the DRDC ATLANTIC LIBRARY.

This page intentionally left blank.

UNCLASSIFIED

DOCUMENT CONTROL DATA (Security classification of the title, body of abstract and indexing annotation must be entered when the overall document is classified)		
1. ORIGINATOR (The name and address of the organization preparing the document, Organizations for whom the document was prepared, e.g. Centre sponsoring a contractor's document, or tasking agency, are entered in section 8.) Publishing: DRDC Atlantic Performing: DRDC Atlantic Monitoring: Contracting:		2. SECURITY CLASSIFICATION (Overall security classification of the document including special warning terms if applicable.) UNCLASSIFIED
3. TITLE (The complete document title as indicated on the title page. Its classification is indicated by the appropriate abbreviation (S, C, R, or U) in parenthesis at the end of the title) Fabrication of Organic Radar absorbing Materials: A Report on the TIF Project. (U)		
4. AUTHORS (First name, middle initial and last name. If military, show rank, e.g. Maj. John E. Doe.) Paul Saville; Trish Huber; Darren Makeiff		
5. DATE OF PUBLICATION (Month and year of publication of document.) May 2005	6a NO. OF PAGES (Total containing information, including Annexes, Appendices, etc.) 311	6b. NO. OF REFS (Total cited in document.)
7. DESCRIPTIVE NOTES (The category of the document, e.g. technical document, technical note or memorandum. If appropriate, enter the type of document, e.g. interim, progress, summary, annual or final. Give the inclusive dates when a specific reporting period is covered.) Technical Report		
8. SPONSORING ACTIVITY (The names of the department project office or laboratory sponsoring the research and development – include address.) Sponsoring: Tasking:		
9a. PROJECT OR GRANT NO. (If appropriate, the applicable research and development project or grant under which the document was written. Please specify whether project or grant.)	9b. CONTRACT NO. (If appropriate, the applicable number under which the document was written.)	
10a. ORIGINATOR'S DOCUMENT NUMBER (The official document number by which the document is identified by the originating activity. This number must be unique to this document) DRDC Atlantic TR 2005-124	10b. OTHER DOCUMENT NO(S). (Any other numbers under which may be assigned this document either by the originator or by the sponsor.)	
11. DOCUMENT AVAILABILITY (Any limitations on the dissemination of the document, other than those imposed by security classification.) Unlimited distribution		
12. DOCUMENT ANNOUNCEMENT (Any limitation to the bibliographic announcement of this document. This will normally correspond to the Document Availability (11). However, when further distribution (beyond the audience specified in (11) is possible, a wider announcement audience may be selected.) Unlimited announcement		

UNCLASSIFIED

UNCLASSIFIED

DOCUMENT CONTROL DATA

(Security classification of the title, body of abstract and indexing annotation must be entered when the overall document is classified)

13. ABSTRACT (A brief and factual summary of the document. It may also appear elsewhere in the body of the document itself. It is highly desirable that the abstract of classified documents be unclassified. Each paragraph of the abstract shall begin with an indication of the security classification of the information in the paragraph (unless the document itself is unclassified) represented as (S), (C), (R), or (U). It is not necessary to include here abstracts in both official languages unless the text is bilingual.)

(U) The fabrication of microwave absorbing materials requires the ability to make materials with well-controlled properties such as shape, thickness, permittivity and permeability. The ability to measure the permittivity and permeability is an essential requirement for designing an optimised absorber. And good optimisations codes are required in order to achieve the best possible absorber designs. In this report, the results from a Technology Investment Funded project on the fabrication of organic radar absorbing materials are presented. The absorbing phase used was based in conducting polymers, which were synthesised and characterised for control and correlation of absorptive properties. The materials made were characterised through measurement of their conductivity and permittivity at microwave frequencies. Methods were then developed for optimising the design of microwave absorbers. A portion of the TIF also focussed on the development of radar cross section modelling software with the capability of determining the radar cross section of a platform with absorbing patches applied.

(U) La fabrication de matériaux absorbant les hyperfréquences exige la capacité de créer des matériaux dont les propriétés sont bien contrôlées, par exemple la forme, l'épaisseur, la permittivité et la perméabilité. La capacité de mesurer la permittivité et la perméabilité est essentielle pour la conception d'un absorbant optimisé. Et de bons codes d'optimisation sont nécessaires pour obtenir le meilleur modèle d'absorbant possible. Le présent rapport décrit les résultats d'un projet sur la fabrication de matériaux organiques absorbants radar, financé par le Fonds d'investissement technologique. La phase absorbante utilisée fait appel à des polymères conducteurs, qui ont été synthétisés et caractérisés pour le contrôle et la corrélation de propriétés absorbantes. Les matériaux fabriqués ont été caractérisés en mesurant leur conductivité et leur permittivité aux hyperfréquences. Des méthodes ont ensuite été définies pour optimiser la conception des absorbants. Une partie du projet portait aussi sur le développement d'un logiciel de modélisation de section efficace radar, capable de déterminer la section efficace radar d'une plate-forme munie de pièces absorbantes.

14. KEYWORDS, DESCRIPTORS or IDENTIFIERS (Technically meaningful terms or short phrases that characterize a document and could be helpful in cataloguing the document. They should be selected so that no security classification is required. Identifiers, such as equipment model designation, trade name, military project code name, geographic location may also be included. If possible keywords should be selected from a published thesaurus, e.g. Thesaurus of Engineering and Scientific Terms (TEST) and that thesaurus identified. If it is not possible to select indexing terms which are Unclassified, the classification of each should be indicated as with the title.)

(U) Radar Absorbing Material, RAM, RCS, Radar Cross Section, conducting polymers, polypyrrole, polyaniline, polythiophenes, carbon nanotubes, coatings, fabric, latex, composites, Dallenbach, Jaumann, Salisbury screen, microwave absorber, optimisation, multilayer, reflectivity, optical properties, conductivity, impedance, permittivity measurement, permeability, impedance, circuit analog, ferrite, magnetic, Tschebyscheff, Equal-Ripple, Genetic Algorithm, frequency dependence, stability, weathering, ageing, vector network analyzer.

UNCLASSIFIED

This page intentionally left blank.

Defence R&D Canada

Canada's leader in defence
and National Security
Science and Technology

R & D pour la défense Canada

Chef de file au Canada en matière
de science et de technologie pour
la défense et la sécurité nationale



www.drdc-rddc.gc.ca